

**Vol.28
No.2
2017**

Al-Mustansiriyah Journal of Science (MJS)

ISSN: 1814-635X (Print), ISSN: 2521-3520 (Online)

Issued by the College of Science, Mustansiriyah University,
Baghdad - IRAQ

Editor in Chief

Prof. Dr. Mohamed Faraj Shather

Managing Editor

Asst. Prof. Dr. Salah Mahdi Al-Shukri

Editorial Board

Asst. Prof. Dr. Ali Hussein Alwan

Asst. Prof. Dr. Olfat Abiad Nief

Asst. Prof. Dr. Eman Ali Hussain

Asst. Prof. Dr. Bahjat Bahlol Kadhim

Asst. Prof. Dr. Yaseen Kadhim Abbas

Dr. Bassam Basim AlKindy

Technical Staff

Maysaa N. Mustafa and Shatha J. Mohammed

Journal website: mjs.uomustansiriyah.edu.iq

E-mail: mustscjo@uomustansiriyah.edu.iq

Mobile: +964 (0) 771 118 4399

Deposit at Iraqi National Library and Archives under the No.278,
1977

Instructions for Authors

Al-Mustansiriyah Journal of Science (MJS)

Manuscript text (first submission) should be double spaced on one side of high quality white A4 sheets (21.6×27.9 cm) with margins of one inch all around the page using Microsoft Word 2007 or 2010 using (doc.) type. The typing in Arabic or English must use (Times New Roman, font size of 14 pt).

The sections should be arranged in the following order: Title Page, Abstract in English, Keywords, Abstract in Arabic, Introduction, Materials and Methods (Experimental), Results and Discussion, Conclusions, Acknowledgments (if any), Abbreviations (if any) and list of References. The head of the sections should be capitalized, bolded and centered and font size of 16pt. (**e. g. Abstract, Introduction, Materials and Methods (Experimental), Results and Discussion, Conclusions, Acknowledgments, References**), and the others (sub-sections) should be in sentence case and bolded as well.

Title Page: Includes the title of the article, author's names with full names and affiliations. The affiliation should comprise the department, college, institution (University or Company), and should be typed as a footnote to the author's name. The e-mail address of the author responsible for correspondence (who is designated with an asterisk *) must be given at the first page under the name and affiliation of authors.

References: All references should be cited in using the appropriate Arabic numerals, which are enclosed in parenthesis (e. g. Polyurethane rigid foams are largely used as insulating materials for their combination of low density, low thermal conductivity and good mechanical properties [1-3].)

A list of references should be given in the end of the manuscript. References should be typed single-spaced and numbered as (IEEE) sequentially in the order in which they are cited in the text. The number of the reference should be given between two brackets [].

❖ **Journal's paper**

[1]. R. Liu and D. Li, "Modification of Archard's equation by taking account of elastic/pseudoelastic properties of materials," *Wear*, vol.251, pp.956-964, 2001.

Books:

[2]. F. Seitz and D. Turnbull, *Solid state physics* vol.7: Academic Press, 1958.

Tables: Tables should be created using the Table tool in MS Word using font size 9 point. Tables should be numbered with Arabic numerals and referred to by number in the Text (e. g. , Table 1, 2, 3... etc.). Each Table should be typed with the legend above the Table.

Figures, Schemes and Diagrams should be numbered in a consecutive series of Arabic numerals in the order in which they are cited in the text (e. g. , Figure 1 or Scheme 1)

Table of Contents

Section: Atmospheric Sciences

- estimation of Dual Polarization Weather Radar Variables 1
DALIA A. MAHMOOD, KAIS J. AL-JUMAILY

Section: Biological Sciences

- Lead Level In Pregnant Women Suffering From Pre- Eclampsia In Baghdad City- Iraq..... 7
ASSALA G. H. AL-SHAMMERY
- External Morphological Study Of The *Sympetrum Fonscolombei* (Selys, 1840) (Odonata: Anisoptera: Libellulidae) In Baghdad..... 11
ASMAA H. AL-HASHMI
- Comparative Study For The Accuracy Of *Helicobacter Pylori* Diagnostic Methods Associated With Some Inflammatory Factors..... 16
EMAN N. NAJI
- A Comparison Of Efficiency Of (Amp) And Its Derivative (Ampaa) Against Some Pathogenic Bacteria..... 29
SUZAN S. HUSSAIN
- Harvesting Of *Chlorella Sp.* By Co-Cultivation With Some Filamentous Fungi..... 35
RANA H. HAMEED AL-SHAMMARI
- Micronucleus Frequency In Buccal Cells Of Males Exposed To Air Pollution In Kufa City..... 43
FARHA A. ALI SHAFI, AQEEL M. ALI AL-LAMI, RAWA ABD AL-AMEER

Section: Chemistry Sciences

- Synthesis, Characterization And Kinetic Study Of Monomeric Complexes Of Cyclohexane-1, 2- Bis (Thiosemicarbazone) With Cobalt (Ii), Nickel (Ii) And Copper (Ii)..... 48
AL-AMEEN BARIZ OMAR ALI
- Synthesis And Characterization Of New Silver (I) N-Heterocyclic Ccarbene Ccomplex Dderived From Imidazol-2-Ylidene Salt 55
MOHAMMED M. HASSON
- Theoretical Study And Biological Activity Of Co(Ii), Ni(Ii), Cu(Ii),Pd(Ii),Pt(Iv) And Cd(Ii) Complexes With2-Thioxoimidazolidin-4-One Derivative 64
SALLAL A. H. ABDULLAH, REHAB A. M. AL HASSANI, ABDUL JABAR K. ATIA, SURA K. IBRAHIM
- Synthesis Of Novel 3-Acetyl N-Methyl-2- Quinolone Derivatives With Expected Antimicrobial Activity 73
GHAZWAN A. SALMAN
- Synthesis, Characterization And Antibacterial Evaluation For Mixed-Ligand Complexes Of Nickle (Ii), Manganese(Ii), Copper(Ii),Cobalt(Ii) And Mercury(Ii) With Tetradentate Schiff Base And 1,10-Phenanthroline 80
REHAB K. AL-SHEMARY, ALI N. NISEAF, AMER. J. JARAD
- Affect The Cross Linking Degree And Polymer Composition On The Mechanical Properties Of Poly (Vinyl Alcohol)/ Pullulan Films 86
SHEMAA A. SOUD
- Development Of Dispersive Liquid-Liquid Microextraction Method Combined With Uv Spectrophotometry For The Determination Of Malathion Pesticide 93
WIJDAN S. KHAYOON

Preparation And Characterization Of TiO_2 Nanostructure By $TiCl_4$ Hydrolysis With Additive Naoh.....	100
RASHED T. RASHEED	
Synthesis And Identification Of Heterocyclic Compounds (Oxazepine, Tetrazole) Derived From Benzidine As Photostabilizing For Poly Vinyl Chloride	108
OLFAT A. NIEF, HAMID G. LAWFAH	
Section: Computer Science	
Fractal Image Compression Based On High Entropy Values Technique.....	119
DOUAA YOUNIS ABBAAS, JAMILA H. SAUD, SHATHA J. MOHAMMED	
Network Intrusion Detection System (Nids) In Cloud Environment Based On Hidden Naïve Bayes Multiclass Classifier.....	134
HAFZA A. MAHMOOD, SOUKAENA H. HASHEM	
Best Approximate Of Vector Space Model By Using Svd.....	143
RAGHAD M. HADI, SOUKAENA H. HASHEM, ABEER T. MAOLOOD	
Hybrid Lossless Image Compression Using Wavelet Transform And Hierarchical Non Linear Prediction	150
RANA T. AL-TIMIMI	
Encryption Of Stereo Images After Compression By Advanced Encryption Standard (Aes).....	156
MARWAH K. HUSSIEN, ALYAA J. JALIL	
Section: Mathematical Sciences	
Comparison Of Bayes Estimators For Parameter And Reliability Function For Inverse Rayleigh Distribution By Using Generalized Square Error Loss Function	162
HUDA A. RASHEED, RAGHDA K. AREF	
Section: Physical Sciences	
Studying The Effect Of Titania Additions On Some Properties Of Porcelain	169
ABBAS K. SAADON, KIREM ALI J., SHATHA H. MAHDI	
Modification Of Iraqi Asphalt 40/50 Properties Using Saw Dust (Sd) And Natural Rubber Latex.....	173
RUSUL M. DARWESH, BALQEES M. AL-DABBAGH, FIRAS A. MOHAMMED	
Structural, Optical, And Morphological Properties Of The Cadmium Oxide Thin Film	179
TAIF S. ALMAADHEDE	
Evaluating Cross Sections Of Gallium Isotopes Production Using Proton And Deuteron Irradiation.....	184
RAGHAD S. MOHAMMED	
Structural Properties Of Nanoparticles TiO_2 /Pva Polymeric Films	188
SAMARA A. MADHLOOM, MAHASIN F. AL-KADHEMY, JEHAN A. SALMAN	
Study Of Nuclear Structures For Nd 148,150,152 A Isotopes By Using Ibm-1.....	196
SALLAMA S. HUMMADI	
Study Stopping Power Collision In One Of Nuclear Element.....	202
SANAR G. HASSAN	

Research Article

Estimation of Dual Polarization Weather Radar Variables

Dalia A. Mahmood, Kais J. Al-Jumaily

Department of Atmospheric Sciences, College of Science, Mustansiriyah University, IRAQ

*Correspondent Author Email: dalia81kitty@yahoo.com

Article Info

Received
07/11/2016

Accepted
12/06/2017

Abstract

Dual polarization weather radar has now become a widely used as instrument in meteorological offices around the world because of its capability in distinguishing different precipitation type and in improving the accuracy of quantitative precipitation estimation. The aim of this work is to estimate the polarimetry radar variables for radars of different frequency bands and study their behavior with rainfall rates.

Calculations of polarimetry radar variables were made on the basis of several assumptions. The results showed that factors at horizontal and vertical polarization, ZH, V, ranges between 20 dBz respectively, and more than 55 dBz for light rain and extreme heavy rain respectively, and radar reflectivity factor at horizontal ZH is greater than radar reflectivity factor at vertical ZV for all rainfall rates. The differential reflectivity, ZDR, also increases with increasing rainfall rates since it is the difference between ZH and Zv.

Calculations of specific differential attenuation indicated that X band radars are seriously attenuated by rain and C band radars are less affected by rain. The specific differential attenuation, S band radars is very small. In addition to this feature, the results showed that the differential phase shift between return signals of horizontal and vertical polarizations for S band radars is much less than those for C and X band radars, and also, the results showed that the co-polarization correlation coefficient for S band the radars is much higher than those of C and X bands.

In order to investigate the accuracy of the calculated polarimetric weather radar variables performed in this research, real radar measurements were used for this purpose. Results indicated that the range of values for calculated polarimetric radar variables are very consistent with range of values for measured variables.

Keywords: Polarization; Radar; Reflectivity; Rainfall.

الخلاصة

أصبح رادار الطقس مزدوج الاستقطاب جهاز شائع الاستخدام في دوائر الارصاد الجوية حول العالم بسبب قابليته في تمييز الأنواع المختلفة من الهطول وتحسين دقة التخمين الكمي للهطول. رادارات الطقس الاعتيادية ترسل وتستلم موجات ذات استقطاب افقي منفرد ويمكنها قياس معدل الهطول فقط. الرادارات المستقطبة ترسل وتستلم موجات كلا الاستقطابين الافقي والشاقولي واضافة لمعدل الهطول لها القابلية في تحديد حجم وشكل ونوع جسيمات الهطول. يهدف هذا البحث الى تخمين متغيرات الرادارات المستقطبة ذات حزم الترددات المختلفة ودراسة سلوك هذه المتغيرات مع معدلات سقوط المطر. تم حساب متغيرات الرادار المستقطب بناء على عدة فرضيات. بينت النتائج بان معاملات الانعكاسية عند الاستقطاب الافقي والاستقطاب الشاقولي ZH, V، تتراوح بين 20 dBz الى أكثر من 55 dBz بالنسبة للأمطار الخفيفة والأمطار الغزيرة جدا على التوالي، وان معامل الانعكاسية عند الاستقطاب الافقي ZH أكبر من معامل الانعكاسية عند الاستقطاب الشاقولي ZV لجميع معدلات الامطار. الانعكاسية التفاضلية ZDR هي أيضا تزداد مع زيادة معدل المطر كونها تمثل الفرق بين ZH و ZV.

دلت حسابات التوهين التفاضلي النوعي بأن الرادارات التي تعمل بالحزمة X تعاني بشدة من التوهين بواسطة الامطار وان الرادارات التي تعمل بالحزمة C هي أيضا تتأثر بالامطار ولكن بشكل اقل. ان التوهين التفاضلي النوعي للرادارات التي تعمل بالحزمة S قليل جدا. إضافة لهذه الخاصية، فان النتائج أظهرت بان فرق الطور التفاضلي بين الإشارات المرتردة عند الاستقطابين الافقي والشاقولي للرادارات ذات الحزمة S اصغر بكثير من فرق الطور عند الحزم X و C، وأيضا بينت النتائج بان معامل ارتباط اشتراك الاستقطاب لرادارات الحزمة S اعلى من معاملات الارتباط للحزم X و C. ولغرض التأكد من دقة حسابات متغيرات رادار الاستقطاب التي تم اجراؤها في هذا البحث، فقد استخدمت قياسات رادار حقيقية لهذا الغرض. وقد دلت النتائج بان مدى قيم متغيرات رادار الاستقطاب متوافقة تماما مع مدى قيم المتغيرات المقاسة.

Introduction

Although weather radars have been in operation

for more than half a century and Doppler weather radars for a few decades, polarimetric weather



radars, which retain Doppler capability, have only recently achieved operational status. Such a choice has been motivated by the capability of polarimetric variables to distinguish different hydrometeor types and to improve the accuracy of quantitative precipitation estimation [1]. The conventional meteorological radar transmits and receives a fixed single polarized wave. Meanwhile, polarimetric radar radiates and receives linear polarization waves which are polarized horizontally and vertically.

The difference of characteristics of backscattered signal due to polarizations directly depends on the shape and orientation of particles. By comparing the signals received from returns at each polarization, one can glean information about the size, shape, and orientation of targets within the radar sampling volume [2].

A large number of publications in the literature deal with theory and observations of weather radar polarimetry. Simulation of dual polarization parameters has also attracted many researchers. Otto [3] inspected the propagation effects influencing polarimetric weather radar measurements attenuation correction. Methods for weather radar measurements at linear horizontal / vertical polarization basis were compared to each other, and identifying the robustly working methods. Kumjian and Ryzhkov [4] studied the impact of size sorting on the S-band polarimetric radar variables by using two idealized bin models. They found that the size sorting produces regions of sparsely concentrated large drops with a lack of smaller drops. Thompson *et al.* [5] derived the bulk electromagnetic scattering properties of precipitation to prove that the extent to which polarimetric radar observations can be used to operate a winter hydrometeor classification algorithm. The results show that the algorithm is able to successfully discern dominant winter hydrometeor types. Jamali [6] examined the applicability of the simple models in estimation of ice mass across the microwave spectral region using three databases consisting of optical properties of some randomly oriented non-spherical ice particles and aggregates.

Materials and Methodos

Polarimetric Radar Variables

Radar echoes are combined signals backscattered by all the hydrometeors within a radar resolution volume at a given range gate. The intensity and

phase of received radar echoes are determined by both scattering and propagation effects. These effects depend on the radar frequency and the size, intensity, phase, shape, structure, and orientation of the hydrometeors. The use of subscripts for polarimetric variables is quite common. In general, letters in lowercase correspond to linear units, while those in uppercase correspond to units in dB. The theoretical equations for the polarimetric radar variables are given below [7] [8] [9].

1- Radar reflectivity factors at horizontal and vertical polarizations ($Z_{h,v}$ or $Z_{H,V}$)

$$Z_{h,v} (mm^6 / m^3) = \frac{4\lambda^4}{\pi^4 |K|^2} \int_{D_{min}}^{D_{max}} |f_{h,v}(\pi, D)|^2 N(D) dD \quad (1)$$

$$Z_{H,V} (dBz) = 10 \log_{10} (Z_{h,v}) \quad (2)$$

2- Differential reflectivity (Z_{dr} or Z_{DR})

$$Z_{dr} = Z_h / Z_v \quad (3)$$

$$Z_{DR} (dB) = 10 \log_{10} (Z_h / Z_v) = Z_H - Z_V \quad (4)$$

3- Co-polar correlation coefficient ($\rho_{h,v}$)

$$\rho_{h,v} = \frac{\int_{D_{min}}^{D_{max}} f_{hh}^*(\pi, D) f_{vv}(\pi, D) N(D) dD}{\sqrt{\int_{D_{min}}^{D_{max}} |f_{hh}(\pi, D)|^2 N(D) dD \int_{D_{min}}^{D_{max}} |f_{vv}(\pi, D)|^2 N(D) dD}} \quad (5)$$

4- Specific differential phase shift (K_{dp})

$$K_{dp} (\text{deg}/km) = \frac{180\lambda}{\pi} \int_{D_{min}}^{D_{max}} \text{Re}[f_{hh}(0, D) - f_{vv}(0, D)] N(D) dD \quad (6)$$

5- Differential phase (Φ_{dp})

$$\Phi_{dp}(r_g) (\text{deg}) = 2 \int_0^{r_g} K_{dp}(r) dr \quad (7)$$

6- Specific attenuation at horizontal or vertical polarization (A_H or A_V)

$$A_{H,V} (dB/km) = 8.686\lambda \int_{D_{min}}^{D_{max}} \text{Im}[f_{h,v}(0, D)] N(D) dD \quad (8)$$

7- Specific differential attenuation (A_{DP})

$$A_{DP} (\text{deg}/km) = A_H - A_V \quad (9)$$

where λ is the radar wavelength; $K = (\varepsilon - 1) / (\varepsilon + 2)$, where ε is the complex dielectric constant of water; D denotes the effective diameter of particle (i. e., hydrometeor); D_{max} (or D_{min}) indicates the maximum (or minimum) D within a radar resolution volume; and $N(D)$ is the Particle Size Distribution (PSD) of all these particles; $f_{hh,vv}$ is the complex scattering amplitude

at the horizontal or vertical polarization, horizontal or vertical and the parameters θ and π for $f_{hh,vv}$ denote the forward-scattering and backward-scattering components, respectively; the notation $|\cdot|$ signifies the complex norm and Re (or Im) indicates the real (or imaginary) part of a complex number; and r denotes the range from radar and r_g is the range for a given range gate. $Z_{h,v}$ represents the energy backscattered by precipitating hydrometeors and depends on their concentration, size, and phase, which have a close connection to precipitation rate and water content. Z_{dr} is directly related to the median size of observed hydrometeors, a parameter used to describe the DSD. K_{dp} is dependent on the raindrop number concentration but is less sensitive to the size distribution than $Z_{h,v}$. Positive K_{dp} values result from a phase lag in the horizontally polarized wave compared with the vertical one. Oblate raindrops (those that have larger horizontal dimensions than vertical) basically cause a slight phase delay, which is more pronounced at horizontal polarization. These three polarimetric measurements can be directly applied for estimating rainfall. The correlation coefficient (ρ_{hv}) indicates how well the backscatter amplitudes at vertical and horizontal polarization are correlated. It is a good indicator of hydrometeor phase (homogenous vs. mixed phase) and data quality. This variable is used for classifying the hydrometeor species of the radar echo. Precipitation can cause strong attenuation (power loss) in radar measurements, depending on the frequency of the radar wave. Specific attenuation (A_H, A_V) and specific differential attenuation (A_{DP}) are two important variables to address how much power has been lost in Z_h, Z_v or Z_{dr} , though they are not directly measured. Values of A_H, A_V , and A_{DP} also have a strong correlation with precipitation rate [7][9].

Methodology

The polarimetric radar variables defined by Equations (1) through (9) were estimated under the following assumptions:

1. Air temperature of 10 °C.
2. Marshall-Palmer raindrop size distribution for raindrop diameters 0.08 to 8 mm and rainfall rates 1 to 100 mm/hr. The distribution is defined as [10]:

$$N(D) = N_o e^{-\Lambda D} \quad (10)$$

Where D is the rain drop diameter, $N(D)dD$ is the number of drops between diameter D and $D+dD$, and N_o is the value of $N(D)$ for $D=0$. For this distribution it was found that $N_o = 0.08 \text{ cm}^{-4}$ and $\Lambda = 41R^{-0.21} \text{ cm}^{-1}$ where R is the rainfall in mm/hr.

3. Rain fall speed formula proposed by Brandes et al. , [11]:

$$v(D) = -0.1021 + 4.932D - 0.9551D^2 + 0.07934D^3 - 0.002362D^4 \quad (11)$$

4. Raindrops are oblate spheroids with 0° canting angle.

All computer codes used in the computations were developed in Matlab®. Calculations of polarimetric radar variables were carried for three commonly used radar frequency bands, namely X band (10 GHz), C band (5 GHz) and S band (3 GHz). To verify the theoretical computations, real polarimetric radar measurements were compared with the results of computations. The data were obtained from NOAA Weather Radar for Research and Experimentation (KOUN) in Norman, Oklahoma, USA. The data were collected for the 13 May 2005 squall-line case.

Results and Discussion

Figures 1 to 3 show the comparisons of Z_H, Z_V , and Z_{DR} for the three bands. Z_H for X band is greater than that of C band and S band has the lowest values among the three bands. Z_V values for X and S band are very comparable but they are notably greater than the values of C bands, especially for rain rates greater than 10 mm/hr. As a consequence, Z_{DR} for X band is greater than those of C and S bands for rainfall rates below 35 mm/hr. beyond this value of rainfall rate, Z_{DR} for C band becomes larger than that for X band.

Figure 4 shows the comparison of A_{DP} for the three bands. It is clear that radars operate at X band are affected seriously by rain attenuation. This leads to degradation of the radar signal as it propagates through rain medium. It is evident

that even light rain affects X band radars. The C band radar waves are less attenuated than X band radar. The S band radar very less attenuated by rain medium and for this reason S band radars are widely used for detecting rain storms.

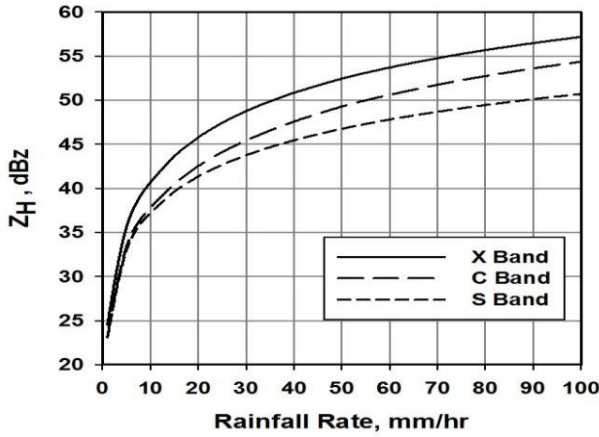


Figure 1: Reflectivity factor at horizontal polarization for X, C, and S bands versus rainfall rate.

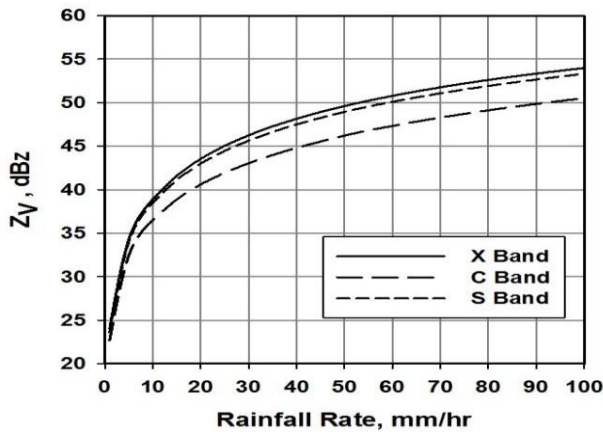


Figure 2: Reflectivity factor at vertical polarization for X, C, and S bands versus rainfall rate.

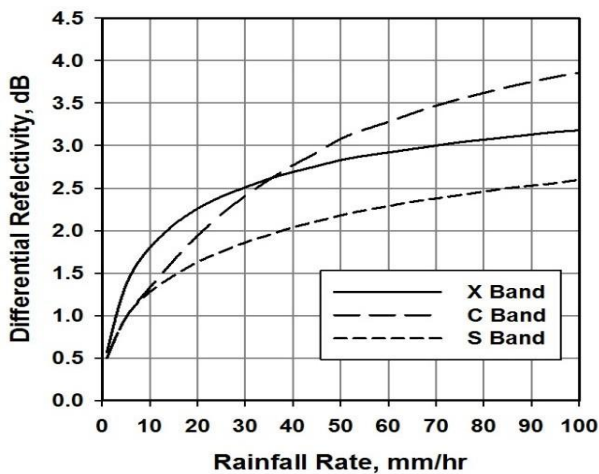


Figure (3): Differential reflectivity for X, C, and S bands versus rainfall rate.

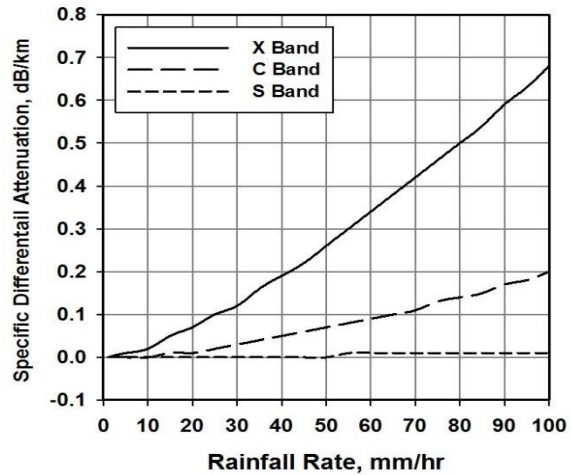


Figure 4: Specific differential attenuation for X, C, and S bands versus rainfall rate.

Figure 5 displays the results of computed specific differential phase shift, K_{DP} . It is obvious that K_{DP} increase linearly with increasing rainfall rates. Light rain produces a phase shift of less than 1 deg/km between horizontal and vertical return of the signals while heavy rainfall, 60 mm/hr for instance, can cause a phase shift of 5, 3, and 1.5 dB/km for radars operating at X, C, and S bands respectively.

Figure 6 shows the results of the calculated co-polarization coefficient, ρ_{hv} , versus rainfall for the three bands. It is seen that ρ_{hv} is more than 0.96 for rainfall rates below 10 mm/hr and that the return signals of S band radars have best ρ_{hv} it is almost constant for all rainfall rates while for radars operating at C band ρ_{hv} decreases gradually to value 0.94 at rainfall rate of 60 mm/hr and then keep constant for rainfall rates higher than this value. For X band radars, ρ_{hv} decreases sharply to less than 0.90 at rainfall rate of 50 mm/hr and then become constant for higher rainfall rates. This suggests that return signals of S band radar are best correlated than return signals of radars operating at other two bands.

In order to investigate the accuracy of the calculated polarimetric weather radar variable performed in this research, real radar measurements were used for this purpose. The measurements were obtained from the University of Oklahoma, Oklahoma, USA S band dual polarization radar (KOUN). The radar is located in Norman near Oklahoma City. The measurements were carried out during a squall-line case on 13 May 2005. Squall lines generally form along or ahead of

cold fronts and drylines and can produce severe weather in the form of heavy rainfall, strong winds, large hail, and frequent lightning. Squall line appears on radar has a shape of a bow echo.

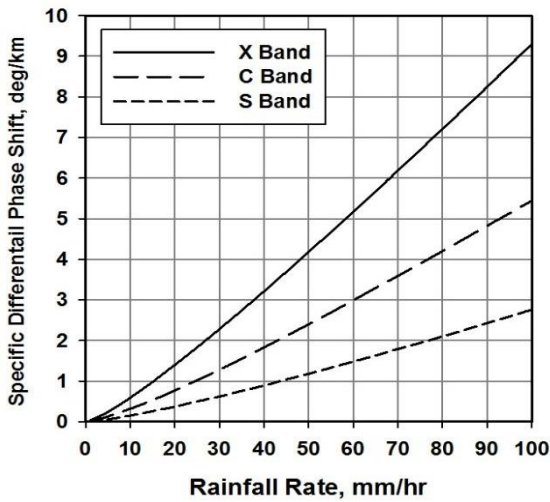


Figure 5: Specific differential phase shift for X, C, and S bands versus rainfall rate.

Figure 7 shows the PPI of Z_H , Z_{DR} , ρ_{hv} , and ϕ_{DP} for this squall-line case study. The bow echo is very apparent on Z_H , and Z_{DR} displays. The bow is located at the head of the storm, just east of the radar site and has high values of Z_H , and Z_{DR} . It is seen that the range of Z_H is between 20 and 55 and the range of Z_{DR} is between 0 and 4. ρ_{hv} is equal to unity all over the storm. ϕ_{DP} ranges between 0 and more than 50 at the edges of the storm. The ϕ_{DP} is the 2-way range integration of K_{DP} . These values of measured polarimetric weather radar are very consistent with the calculated variables obtained in this research.

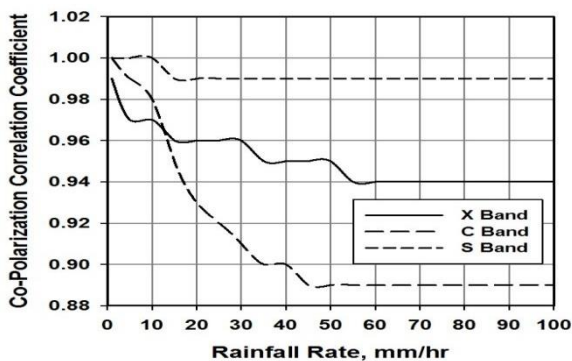


Figure 6: Co-polarization correlation coefficient for X, C, and S bands versus rainfall rate.

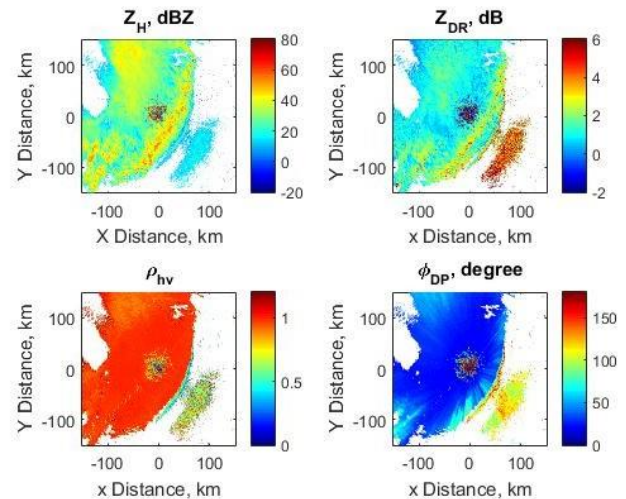


Figure (7): PPI of Z_H (top left), Z_{DR} (top right), ρ_{hv} (bottom left) and ϕ_{DP} (bottom right) for the 13 May 2005 Squall-line case observed by KOUN S band dual-polarization radar.

Conclusions

This paper presents theoretical calculations of dual polarization weather radar variables, aimed at understanding the behavior of these variables for various rainfall rates. Three common radar bands were considered, namely X, C, and S. Calculations were based on Marshall-Palmer raindrop size distribution. Results indicated that differential reflectivity for X band is greater than those of C and S bands for rainfall rates below 35 mm/hr and beyond this value of rainfall rate, ZDR for C band becomes larger than that for X band. It was found that heavy rainfall can cause a differential phase shift of 5, 3, and 1.5 dB/km for radars operating at X, C, and S bands respectively. Results also suggested that co-polarization correlation coefficient suggested that return signals at horizontal and vertical polarizations of S band radar are best correlated than return signals of radars operating at other two bands. Comparisons with real radar measurements showed the calculated radar variables were very consistent with the measured ones.

References

- [1] Sauvage, H. , 1992: *Radar Meteorology*. Artech House Radar Publisher, pp 384.
- [2] Fukao, S. , and K. , Hamazu, 2014: *Radar*

- for *Meteorological and Atmospheric Observations*. Springer, Dordrecht, pp 537.
- [3] Otto, T. , 2011: Propagation effects influencing polarimetric weather radar measurements. Ph. D. Dissertation, der Technischen Universität Chemnitz, Germany, pp 238.
- [4] Kumjian, M. R. , and A. V. Ryzhkov, 2012: The Impact of Size Sorting on the Polarimetric Radar Variables. *J. Atmos. Sci.* , **69**, 2042-2060.
- [5] Thompson, E. J. , S. A. Rutledge, B. Dolan, V. Chandrasekar, and B. L. Cheong, 2014: A dual-polarization radar hydrometeor classification algorithm for winter precipitation. *J. Atmos. Oceanic Technol.* , **31(7)**, 1457-1481.
- [6] Jamali, M. , 2015: Soft model approximation of microwave scattering properties of ice particles. M. Sc. thesis, Department of Earth and Space Science Chalmers University of Technology, Gothenburg, Sweden. pp 87.
- [7] Hong, Y. , and J. J. Gourley, 2015: *Radar Hydrology: Principles, Models, and Applications*. CRC Press, pp 191.
- [8] Bringi, V. N. , and V. Chandrasekar, 2001: *Polarimetric Doppler Weather Radar Principles and Applications*. Cambridge University Press, pp 664.
- [9] Zhang, G. , 2016: *Weather Radar Polarimetry*. CRC Press, pp 304.
- [10] Marshall, J. S. , and W. McK. Palmer, 1948: The Distribution of Raindrops with Size. *J. Meteor.* , **5**, 165-166.
- [11] Brandes, E. A. , G. Zhang, and J. Vivekanandan, 2002: Experiments in rainfall estimation with polarimetric radar in a subtropical environment. *J. Appl. Meteor.* , **41**, 674-685.

Research Article

Lead Level in Pregnant Women Suffering from Pre- Eclampsia in Baghdad City- Iraq

Assala G. H. Al-Shammery

Department of Biology, College of Science, Mustansiriyah University, IRAQ

*Email: Jolanar_20002007@yahoo.com

Article Info

Received
22/12/2016

Accepted
17/04/2017

Abstract

This study was conducted on the number of pregnant women suffering from symptoms of preeclampsia who live in different areas in Baghdad city. These areas were suffering from air pollution by different pollutants in high rates and it was chosen from among these pollutants lead metal which is a high percentage of air pollution where it was observed by measuring the level of lead in blood serum which taken from pregnant women by 40 pregnant women suffering from symptoms of preeclampsia and 20 pregnant women don't suffering from any abnormal symptoms during pregnancy period and classified as control group , so we found marked a significant rise in lead level in comparison with control group reaching ratio of lead in blood of pregnant women which suffering from symptoms of preeclampsia $38.44 \text{ mg/dl} \pm 3.0 \text{ mg/dl}$ in comparison with control group which $14.56 \text{ mg/d} \pm 2.50 \text{ mg/dl}$, this increase may refer to the amount of lead which found in the air and in excess of the normal limit which exposed pregnant women like all people through the overcrowding of roads and use fuel non-environmentally friendly through breathing which effect on pregnant women health, it has been shown on symptoms of preeclampsia from measuring systolic and diastolic blood pressure and measuring of urea in blood, T-test was used at possibility of (0.001) to see the difference between infected samples and control group, therefore this study suggested that a lead is one of the causes of preeclampsia because live in polluted and unhealthy environment.

Keywords: lead, pollution, preeclampsia, symptoms.

الخلاصة

اجريت الدراسة على عدد من النساء الحوامل التي تعاني من اعراض تسمم الحمل والتي يتواجدن في مناطق مختلفة ضمن مدينة بغداد وكانت هذه المناطق تعاني من تلوث الهواء بالملوثات المختلفة وينسب عالية وقد اختير من ضمن هذه الملوثات معدن الرصاص الذي يشكل نسبة عالية من تلوث الهواء حيث لوحظ من خلال قياس مستوى الرصاص في عينة الدم التي اخذت من النساء الحوامل بواقع 40 امرأة حامل تعاني من اعراض تسمم حمل و 20 امرأة لا تعاني من اعراض غير طبيعية خلال فترة الحمل وصنفت ضمن المجموعة الضابطة حيث لوحظ ارتفاع ملحوظ وكبير في مستوى الرصاص بالمقارنة مع المجموعة الضابطة حيث بلغت نسبة الرصاص في الدم لدى النساء الحوامل التي تعاني من اعراض تسمم الحمل $38.44 \text{ mg/dl} \pm 3.0$ بالمقارنة مع المجموعة الضابطة التي بلغت $14.56 \text{ mg/d} \pm 2.50 \text{ mg/dl}$ وهذا الارتفاع قد يعزى الى ارتفاع مستوى الرصاص الموجودة في الهواء والتي تفوق الحد الطبيعي والتي تتعرض لها النساء الحوامل كسائر الأشخاص من خلال ازدحامات الطرق واستخدام الوقود غير الصديق للبيئة من خلال عملية التنفس والتي تؤثر على صحة المرأة الحامل وقد استدل على اعراض تسمم الحمل من خلال قياس ضغط الدم الانبساطي والانقباضي وقياس نسبة اليوريا بالدم وقد استخدمت قيمة T الجدولية عند احتمالية (0.001) لمعرفة معنوية الفروق بين مجموعة العينات المصابة والمجموعة الضابطة. وعليه تشير هذه الدراسة الى ان يكون الرصاص هو احد مسببات مرض تسمم الحمل وهذا يحدث بسبب العيش في بيئة ملوثة غير صحية.

Introduction

Lead is toxic and induces a broad range of harmful effects on various organs including the reproductive system [1] [2] [3].

Lead as a neurotoxic can carry a lethal legacy. Young women who live in Lead –contaminated housing or who were lead-poisoned themselves as youngsters can be passed lead on their unborn fetuses [4]. Lead poisoning remains an urgent public health problem in both developed and developing countries [4].

The main target for lead toxicity is the nervous system, both in adults and children [5] [6].

Long –term exposure during pregnancy to even low concentrations of toxic metals , which have the ability to accumulate, often leads to irreversible damage to fetal developments and maternal morbidities including pre-eclampsia [1] [2] [3]. Environment pollution by lead is worldwide public problem. such as elevated blood level among people living in the polluted areas [7] [8].

Lead is a heavy metal and is highly toxic to plants and cumulative poison to mammals so an important symptoms of lead toxicity is causing central nervous system disorder leading to insomnia like disease which are caused due to the discursive of hemoglobin [7].

Lead is one of the heavy metals people most commonly exposed to in the environment. Lead is not biodegradable and the conference for ecotoxicity of lead are increasing [7] [8].

There are innumerable sources of lead in our environment such as paint, plumbing and water supplies from lead pipes or lead- soldered joints, dust and pint chips from older houses having lead paints, air and soil pollution from leaded gasoline, cooking in leaded pots, newsprint and many other sources [7] [8] [9].

Preeclampsia, the most common medical complication of pregnancy, is associated with oxidative stress with lead elements [7].

Long – term exposure during pregnancy to low concentration of toxic metals, such as lead which have the ability to accumulate, often leads to irreversible damage to fetal and maternal morbidities including pre - eclampsia [7] [9].

Materials and Methods

The study was conducted in several areas, it is choked with traffic throughout the day, and it suffers from air pollution in various pollutants emanating from vehicle exhausts in Baghdad city.

Venous blood samples (5 ml) were taken from each pregnant woman (40 women) does not suffer from any abnormal symptoms during different periods of pregnancy and ranked in the control group.

Twenty pregnant women suffering from symptoms such as high blood pressure continues to rise during the six – hour up to 160/10mmHg during the day. And high proportions of urea in the blood which are less than 50 mg during 24 hours.

The ages of all samples (patients and controls) are converged from (23 - 44) years with periods of pregnancy to every one. All of the samples did not suffer from other overlaps intervention such as heart disease, diabetes and kidney. The systolic blood pressure and diastolics for pregnant women was measured using a standard mercury sphygmomanometer (Accoson, Essex, UK).

The study also included a measurement of the proportion of protein in the blood urea. The samples were taken for pregnant women who completed 22 weeks of gestation at least 5 ml of urine from each pregnant woman in this study after centrifugation for 5 minutes at 3000 rpm for the testing of the present of albumin in urine, 5ml of blood sample was collected from the cubital veins.

The blood was separated after centerfugation for 5 minuts at 3000 rpm and the plasma were stort-ed frozen at 200 C°. Untel analysis was carried out for lead estimation by atomic absorption spectrophotometer model 200A (Buck scientific, East Norwalk, UK) with detection limit of 1 mg /dl was employed for blood lead determination, as described by welz [10]. The digested samples analyzed in duplicates by the atomic absorption spectrophotometer methodology using wavelength of 283 nm, the mean value computed.

Statistical analysis:

Mean \pm standard error were calculated for all treatment. Mean of tests and controls were compared using t – test (using a program of statistic for epidemiology) and p – values were obtained. P value was regarded significant if it is less or equal (0.05). Repeated analyses of standard solution confirmed the methods precision.

Results and Discussion

We found in this research significant increase ($p = 0.001$) in systolic and diastolic blood pressure for 24 hrs with a significant increase ($p = 0.001$) in blood lead level in the serum in the preeclamptic women as compared to normal pregnant women as found in Table 1.

Our results are in keeping with the results of Motawei *et al.* [1] [2] [3] who found same results of correlation between lead level in serum and symptoms of preeclampsia, systolic and diastolic blood pressure in women suffering from preeclampsia in Egypt.

As well our results agree with kasper, *et al* [11] [12] [13] who they found that the lead level in the serum was positively associated with systolic and diastolic blood pressure.

Table 1: Preeclamptic women as compared to the normal pregnant women.

parameter	Preclamptic women	Normal pregnant	p-value
Urea 24 hrs (mg/dl)	40±23	8 ±7.10	0.001
Lead (mg/dl)	38.44±3.0	14.56±2.50	0.001
Systolic blood pressure (mmHg)	180.33±9.22	117.8±8.90	0.001
Diastolic blood pressure (mmHg)	20.19±7.901	8.50±7.90	0.001

Mean ± SD

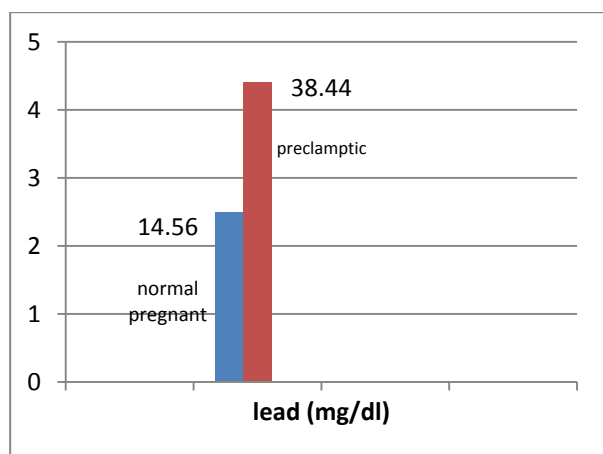


Figure 1: Serum concentration of lead in normal and preclamptic women.

Meanwhile explained Rothenberg et al and Mitra *et al.* [14] [15] found significant positive association between lead level and blood pressure in pregnant women. This is what was said kasper, *et al.* [11] [12] [13] as explained the pregnant women exposure to lead from breathing the air contaminated by leaded gasoline which found in the roads. Exposure to excess toxic elements such as lead in the environmental that increases the production of free radicals, leads to decrease the availability of bioelements necessary for antioxidant defense mechanisms, So acute and chronic low- level lead exposure has been shown to result in adverse health effects [16] [17]. As well our results agree with Line ,et al. who explained the elevated lead level observed in some

rural areas by the fact that some villages are polluted with high concentration of lead in soil and household dust that subsequently carry lead exposure to the population there causing elevated lead level [18] [19] [20].

Air polluted by oxides and minerals more dangerous on human health where through breathing pollutants move by one hundred percent to human blood and features Baghdad city like all cities abundance cars which use fuel have dangerous toxic which include lead which effects significantly on the patients , elderly and pregnant women posing a risk to fetuses ,High lead level in the blood causes anemia and laves of hemoglobin in the blood this may lead to liver kidney and brain damage and it was up to the central nervous system [21].

Conclusions

Through tests conducted in this study and compare with similar studies,it is clear to us that lead which found in high rates in the polluted and unhealthy environment may be a reason of preeclampsia which constitutes a danger on the pregnant woman this lead to the possibility of abortion or may be effect in future on the fetus health.

References

- [1] S. Motawei, S. Attalla, H. Gouda, M. El-Harouny, and A. El-Mansoury, "Lead level in pregnant women suffering from preeclampsia in Dakahlia, Egypt," *International Journal of Occupational & Environmental Medicine*, vol.4, 2013.
- [2] M. Bradbury and R. Deane, "Permeability of the blood-brain barrier to lead," *Neurotoxicology*, vol.14, pp.131-136, 1993.
- [3] A. B. Caughey, N. E. Stotland, A. E. Washington, and G. J. Escobar, "Maternal ethnicity, paternal ethnicity, and parental ethnic discordance: predictors of preeclampsia," *Obstetrics & Gynecology*, vol.106, pp.156-161, 2005.
- [4] L. C. Kenny and D. B. Kell, "Immunological tolerance, pregnancy and pre-eclampsia: the roles of semen microbes and the father," *bioRxiv*, p.198796, 2017.
- [5] O. Akinloye, O. Oyewale, and O. O. Oguntibeju, "Evaluation of trace elements

- in pregnant women with pre-eclampsia," *African Journal of Biotechnology*, vol.9, pp.5196-5202, 2010.
- [6] S. Klitzman, A. Sharma, L. Nicaj, R. Vitkevich, and J. Leighton, "Lead poisoning among pregnant women in New York City: risk factors and screening practices," *Journal of Urban Health*, vol.79, pp.225-237, 2002.
- [7] N. A. Jameil, H. Tabassum, H. A. Mayouf, L. A. Otay, A. A. A. Shenefy, and F. A. Khan, "Identification of predictive marker of prerenal damage in pregnant women with Preeclampsia and women at high risk- A Prospective study conducted in Riyadh, Saudi Arabia," 2014.
- [8] N. Al Jameil, "Maternal serum lead levels and risk of preeclampsia in pregnant women: a cohort study in a maternity hospital, Riyadh, Saudi Arabia," *International journal of clinical and experimental pathology*, vol.7, p.3182, 2014.
- [9] P. Pathak and U. Kapil, "Role of trace elements zinc, copper and magnesium during pregnancy and its outcome," *The Indian Journal of Pediatrics*, vol.71, pp.1003-1005, 2004.
- [10] B. Welz, "Atomic absorption spectrophotometry [English translation by Christopher Skegg]. 2nd comp. rev. ed," ed: Weinheim, Germany, 1985.
- [11] S. Kasperczyk, J. Kasperczyk, A. Ostałowska, J. Zalejska-Fiolka, T. Wielkoszyński, E. Świętochowska, *et al.* , "The role of the antioxidant enzymes in erythrocytes in the development of arterial hypertension among humans exposed to lead," *Biological trace element research*, vol.130, p.95, 2009.
- [12] C. Mosby, W. Glanze, and K. Anderson, "Mosby Medical Encyclopedia, The Signet: Revised Edition," *St. Louis*, 1996.
- [13] J. Neumann, J. Lopuchovsky, and O. Zapletal, "Chemisation, agriculture, pharmacology and toxicology," ed: SZN Praha, 1990.
- [14] S. J. Rothenberg, M. Manalo, J. Jiang, R. Cuellar, S. Reyes, M. Sanschez, *et al.* , "Blood lead level and blood pressure during pregnancy in South Central Los Angeles," *Archives of Environmental Health: An International Journal*, vol.54, pp.382-389, 1999.
- [15] A. K. Mitra, A. Haque, M. Islam, and S. Bashar, "Lead poisoning: an alarming public health problem in Bangladesh," *International journal of environmental research and public health*, vol.6, pp.84-95, 2009.
- [16] A. S. Ettinger and A. M. Wengrovitz, "Guidelines for the identification and management of lead exposure in pregnant and lactating women," 2010.
- [17] A. J. McMichael, G. V. Vimpani, E. F. Robertson, P. A. Baghurst, and P. D. Clark, "The Port Pirie cohort study: maternal blood lead and pregnancy outcome," *Journal of Epidemiology & Community Health*, vol.40, pp.18-25, 1986.
- [18] S. Lin, X. Wang, I. T. S. Yu, W. Tang, J. Miao, J. Li, *et al.* , "Environmental lead pollution and elevated blood lead levels among children in a rural area of China," *American journal of public health*, vol.101, pp.834-841, 2011.
- [19] C. Rusterholz, S. Hahn, and W. Holzgreve, "Role of placentally produced inflammatory and regulatory cytokines in pregnancy and the etiology of preeclampsia," in *Seminars in immunopathology*, 2007, pp.151-162.
- [20] J. Puzas, M. Sickel, and M. Felter, "Osteoblasts and chondrocytes are important target cells for the toxic effects of lead," *Neurotoxicology*, vol.13, pp.783-788, 1992.
- [21] G. Zheng, L. Wang, Z. Guo, L. Sun, L. Wang, C. Wang, *et al.* , "Association of serum heavy metals and trace element concentrations with reproductive hormone levels and polycystic ovary syndrome in a Chinese population," *Biological trace element research*, vol.167, pp.1-10, 2015.

Research Article

External Morphological Study of the *Sympetrum fonscolombi* (Selys, 1840) (Odonata: Anisoptera: Libellulidae) in Baghdad

Asmaa H. Al-Hashmi

Department of Biology, College of Science, Mustansiriyah University, IRAQ

*Email: asmaa_alhashmi80@yahoo.com

Article Info

Received
05/09/2016

Accepted
18/01/2017

Abstract

The specimens were collected from different region in Baghdad / Iraq, by using air net during April 2016. In this study, a morphological characters of *Sympetrum fonscolombi* (Selys, 1840) is include three region of body (head, thorax and abdomen); in addition, male and female genitalia. Such characters were supported by Figured

Keywords: Libellulidae, *Sympetrum fonscolombii*, Morphological study, Baghdad.

الخلاصة

العينات المدروسة جمعت من مناطق مختلفة من بغداد باستخدام الشبكية الهوائية خلال شهر نيسان 2016. في هذه الدراسة، الصفات المظهرية للنوع *Sympetrum fonscolombi* (Selys, 1840) تتضمن ثلاث مناطق من الجسم (الرأس والصدر والبطن) بالإضافة الى السواتين التناسليتين الذكورية والانثوية، وهذه الصفات معززة بالصور.

Introduction

Odonata is one of the ancient groups of winged insects found now; with 5680 present species dragonflies are a comparatively small order of insects [1]. Every known species of Odonata are hunters as adults and larvae, and as such, they are very evaluate for premising biological control over many noxious insects, particularly those with water larvae [2]. This genus *Sympetrum* is already represented in the Iraq by following four species:

Sympetrum fonscolombi (Selys, 1840), *Sympetrum striolatum* (Charpentier, 1840), *Sympetrum depressiusculum* (Selys, 1841) and *S. arena color* Jodicke, 1994 according to list of Kalkman [3]. To Iraqi fauna, the species of *Sympetrum fonscolombi* (Selys, 1840) was recorded by Kalkman, Asahina, Derwesh, Morton and Sage [3] [4] [5] [6] [7]. The species of *S. fonscolombi* (Selys, 1840) was distribution South and East Europe, sometimes reaching Western Europe, the whole of Africa and spreading into Asia as far east as Kashmir. Very extensively distributed in levant the period from April to October [8]. The aim of this study was to make a detail

description for the species *Sympetrum fonscolombi* (Selys, 1840) and afford additional information from these insects to Iraqi fauna.

Materials and Methods

Many specimens of O donate species were collected from different region in Baghdad/Iraq, by using air net during April 2016. The specimens were killed by freezing for 48 hours, and mounting by insect pins. The date and localities of sampling were recorded. The samples of the species were diagnosed by using different taxonomic keys such as: [3] [8] [9] [10] [11] [12] [13] [14].

The morphology of the adults were studied by using dissecting microscope, while the minute parts were studied by preparation of microscope slides, the adults dissected by using two fine pins, then the required parts (the abdomen) put in a beaker 100 ml contains 50 ml water with KOH 10% and placed on fire with shaking for about 10 minutes for dissolving of lipid matters of the body and destroying the muscles. After that it was placed in distilled water for 5 minutes in order to reduce the effect of the alkali. abdomen are

placed in ethyl alcohol 25% and dissected under microscope to obtain the male genitalia, then transferred to ethyl alcohol 50%, 75% and 100% respectively for two minutes of each concentrations to dehydration of water, then placed in Xylol for two minutes, for translucency then placed in Canada balsam to prepare slides for examination under microscope [15].

The binocular dissecting microscope (MB. MARIOBROMA. SRL, Roma) was used to magnificent the morphological features and photographs were taken with a Sony Camera (capacity 12.1 MEGA PIXELS); in addition, some photographs (wing and abdomen) used Samsung galaxy mega, GT-19152.

Results and discussion

Body: Measurements (mm): Male body length of 42, fore wing 33, hind wing 32 (Figure 1); Female body length of 43, fore wing 34, hind wing 33.



Figure 1: body of the adult (male) of *Sympetrum fonscolombei*.

Head:

Labrum yellow, Clypeus silvary, frons yellow and coated with short and pale hairs; a broad black stripe at base of frons; verte convex yellow (Figure 2a).

Occiput pale olivaceous and overed by long and erect pale hairs (Figure 2b). Eyes brown above and pale olivaceous below. In mature specimens, the all face changes bright red (Figure 2c).

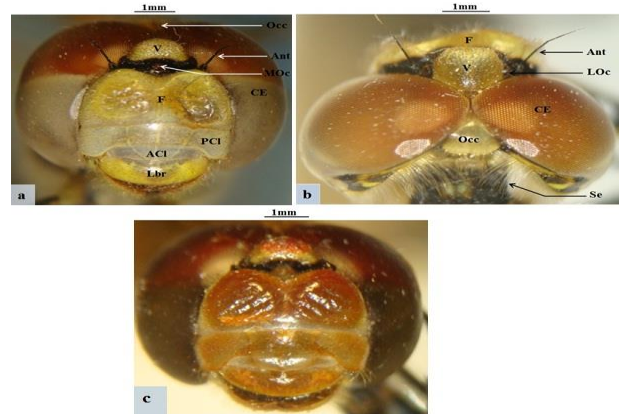


Figure 2: head of *Sympetrum fonscolombei* a: anterior view (teneral specimen); b: posterior view; c: anterior view(mature specimen).

Occ: occiput, Ant: Antenna V: vertex, F: frons; CE: compound eye, ACI: anteclypeus, PCI: post-clypeus, Lbr: labrum, Se: Seta, LOc: Lateral Ocellus, MOc: Median Ocellus.

Thorax:

Prothorax: in dorsal view black. posterior lobe (PL) large, waisted in middle and posterior margin yellow and covered with long, erect and pale hairs(Figure 3a). Synthorax: in lateral veiw yellow-greenish, covered with long hairs, generally no antehumerals, Sutures marked with black, a long black line on humeral suture (Figure 3b).

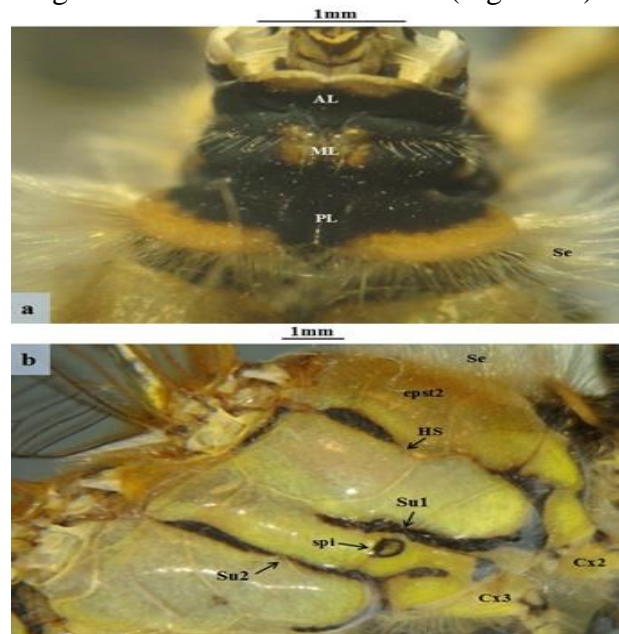


Figure 3: thorax of *Sympetrum fonscolombei*. a: Prothorax (dorsal view); b:Synthorax (lateral view).

AL: Anterior lobe, ML: Median lobe, PL: Posterior Lobe, HS: humeral suture, spi: Spiracle, epst2: mesoepisternum, Su1: Suture 1, Su2: Su-

ture 2, Cx2: Coxa of leg 2, Cx3: Coxa of leg 3, Se: Seta.

Wings:

Wing clear, venation (only main veins) yellow in teneral or red in adults, membranula white, extreme bases of wings possessed with amber yellow; Pterostigma light yellow and boarded with black nervures. Fore wings with 6-½ antenodal crossveins, last antenodal crossvein incomplete. Arculus integrated at origin and situated between the first and second antenodal nervure. Discoidal cell divided to two cells, Discoidal field begins with three cells then parallel and lastly narrows. Triangular cell of the fore wing put vertical sloping to the rear edge of wing, base equal to one-third of the length of outer side. Only one row of cells between IRiii and Rspl. One Cubital crossvein (Cn) occur in each wing (Figure 4).

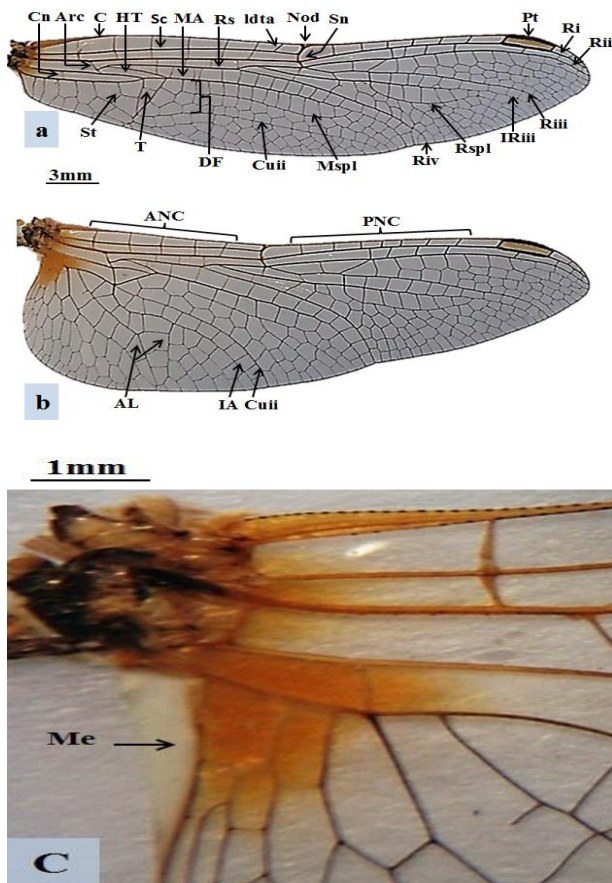


Figure 4: wings of *Sympetrum fonscolombe*, a: fore wing; b: hind wing, c: base of hind wing.

HT: Humeral triangle, Idta: Last discontinued transverse arculus, Ri: 1st Radius vein, Rii: 2nd Radius Vein, Riii: 3rd Radius vein, Riv: 4th Radius vein, IRiii: 1ST Radius vein branch, AL:

Anal loop, MA: Median Arculus, Msp1: Nervulus between Cu and MA, IA:Anal vein, Rs: Radius vein, Arc: Arculus, Nod: Nodus, Rspl: Nervulus between IRiii and Riv, C:Costal vein, ANC:Transverse antenodal nervulus, PNC: Transverse post nodal nervulus, Sc: Subcosta vein, Cn:Transverse Cubital nervulus, Pt:Pterostigma, Sn:Sub nodus, Cuii: Cubital vein, T: Triangular cell, St: Sub triangular cell, DF: Discoidal field, Me: Membranula.

Legs:

Legs black, external surfaces of femora and tibia with bright yellow stripe (Figure 5).

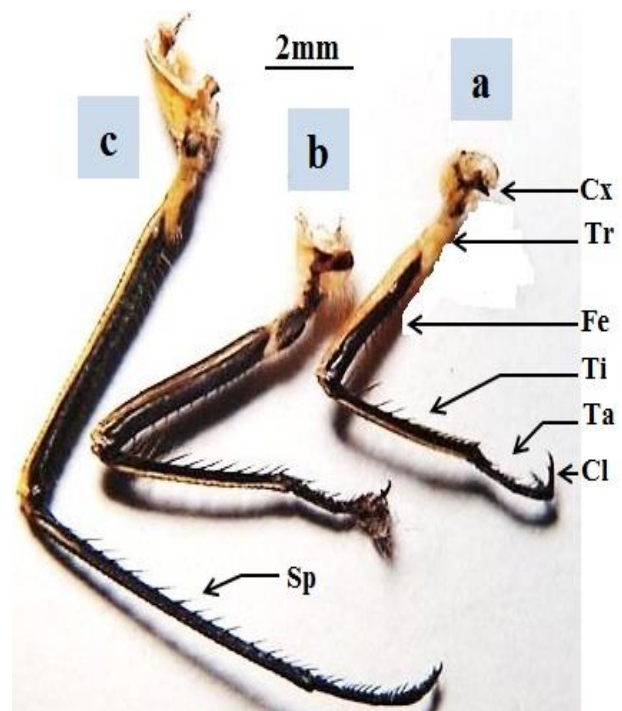


Figure 5: legs of *Sympetrum fonscolombe*: a: Fore-leg; b: Mid-leg; c: Hind-leg Cx: Coxa, Tr: Trochanter, Fe: Femur, Ti: Tibia, Ta: Tarsus, Cl: Claw, Sp: Spin.

Abdomen :

In male: Abdomen bright ochraceous in teneral then turning blood red at maturity (Figure 6a) ; a broad spot black on the dorsum of S₁ and base and sides of S₂ (Figure 6b), also the S_{8,9} with carinal and lateral black straps (Figure 6c). In female: A carinal black spot extant on S₈₋₉ and a fine font on S₁₀ (Figure 9a).

Anal appendages

End abdomen with anal appendages; long, skinny and yellow (later bright red), covered by erect, densely and black hairs (Figure 7a,b).

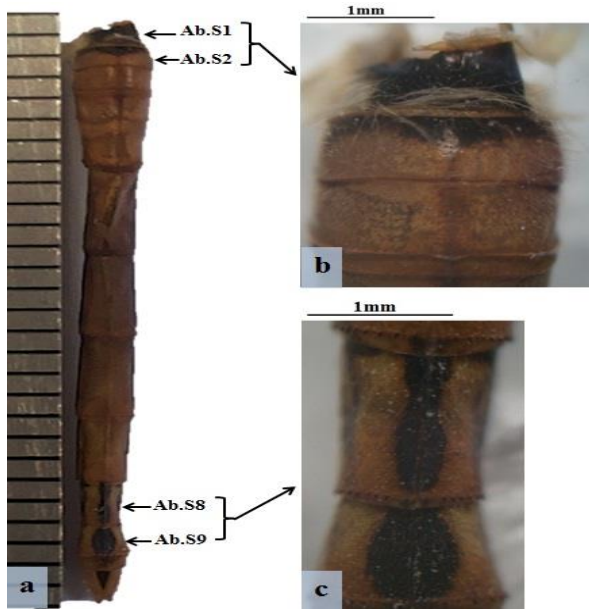


Figure 6: abdomen of *Sympetrum fonscolombei*
 a: the abdomen(dorsal view), b: first segments abdomen(dorsal view); c: end segments of abdomen(dorsal view). Ab. S: abdominal segment.

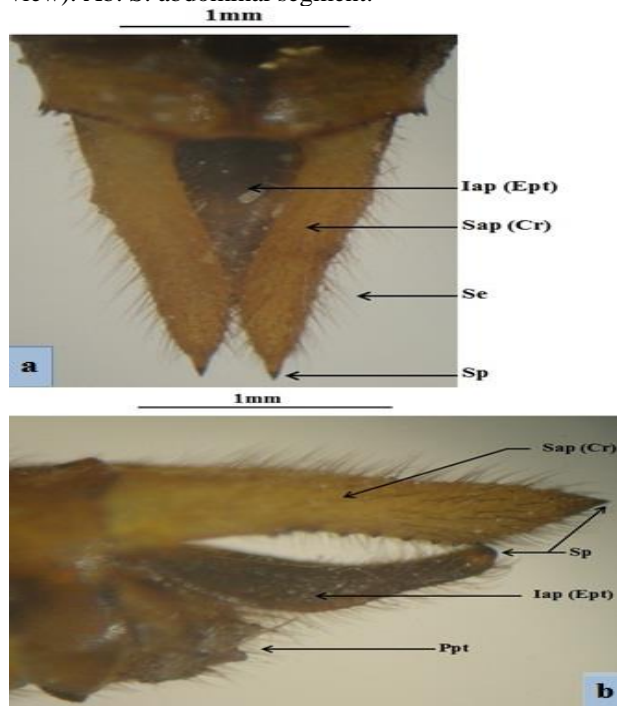


Figure 7: anal appendages (male) of *Sympetrum fonscolombei* a: (dorsal view) , b: (lateral view) Iap- Ept: Inferior anal appendage, Sap-Cr: Superior anal appendage, Sp: Spine, Se: setae, Ppt: paraproct.

Male genitalia:

Lamina anterior: very low in lateral view and black. Hamuli: small, with wide, short outer ramus (Lobe), and much shorter pointed inner ramus (Hook). Genital lobe: yellow, lengthen and hairy (Figure 8a,1b).

(leave 10pt space line here)

Female genitalia:

Vulvar aperture with lips bulgy laterally and a profound U- shaped invagination is found in the mid (Figure 9b).

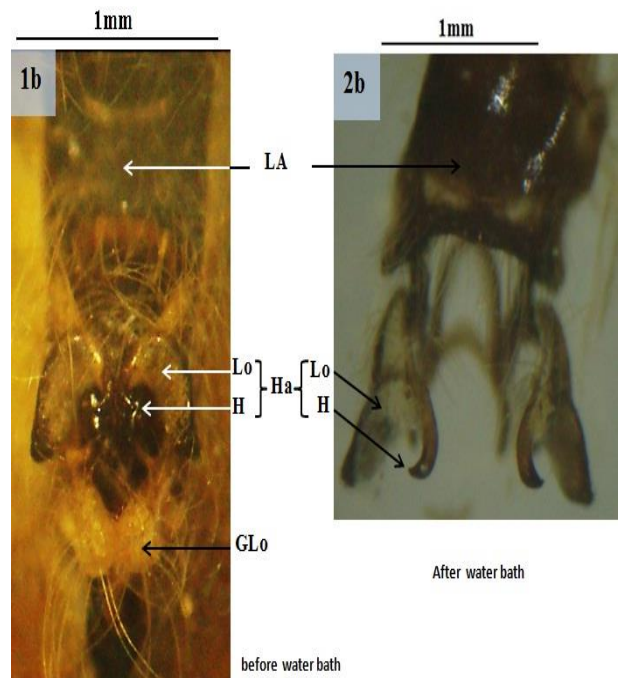
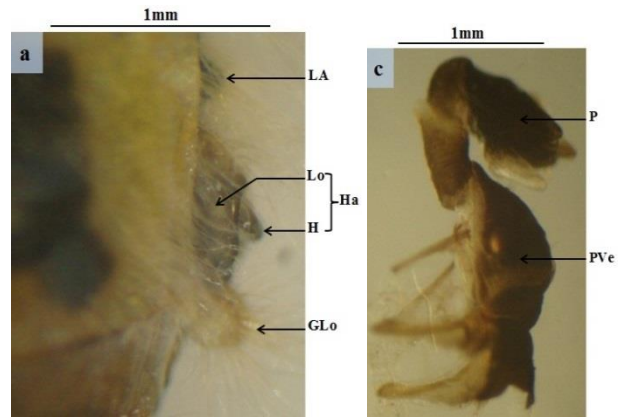


Figure 8: male genitalia of *Sympetrum fonscolombei*, a: lateral view b: ventral view c: penis LA: Lamina anterior, Lo: Lobe, H: hook, GLO: Genital lobe, P: Penis, Ha: Hamula, PVe: Penis Vesicle.

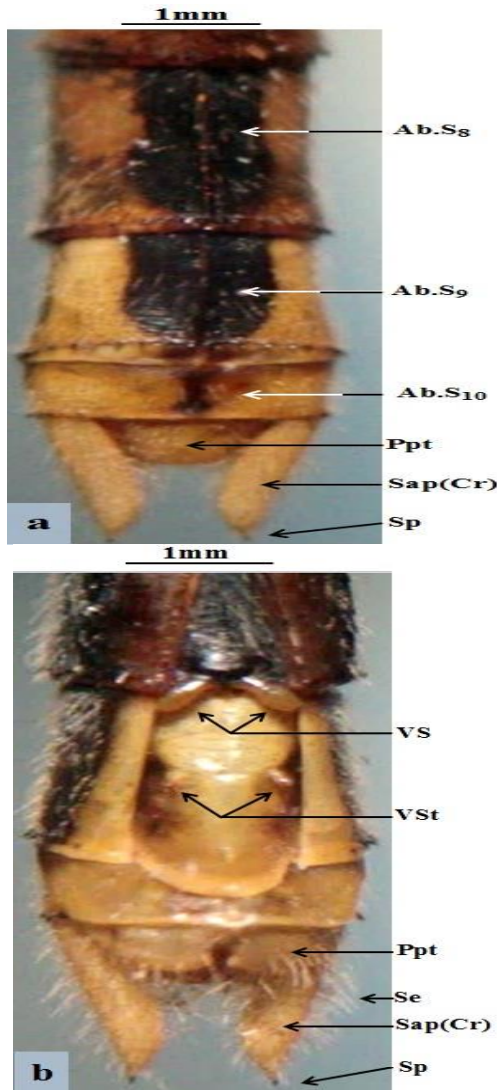


Figure 9: female abdomen and genitalia of *Sympetrum fonscolombii*: a: Abdomen (Dorsal view); b: genitalia (Ventral view) Ab. S: Abdominal Segment, Ppt: Paraproct, Sp: Spine, VS: Vulvar Scale, Sap (cr): Superior appendages, VSt: Vestigial stylet.

References

- [1] Ebrahimi, A. ; Madjzadeh, S. M. and Mohammadian, H. Dragonflies (Odonata) from South-Eastern Iran. *Caspian J. Env. Sci.* , 7(2): 107-112, 2009.
- [2] Heckman, C. W. *Encyclopedia of South American Aquatic Insects, Odonata- Zygoptera.1*: 687 pp. Springer. USA, 2008.
- [3] Kalkman, V. J. Key to Dragonflies of Turkey, including species known from Greece, Bulgaria, Lebanon, Syria, the Trans-Caucasus and Iran. *Brachytron.* , 10(1): 3-82, 2006.
- [4] Asahina, S. The Odonata of Iraq. *Jap. J. Zool.* , 17(1): 17-36, 1973.
- [5] Derwesh, A. I. *Apreliminary List of Identified Insects and Some Arachnids of Iraq. Direct. Gen. Agr. Res. Proj. Baghdad. Iraq. Bulletin 121*: 1-123, 1965.
- [6] Morton, K. J. Odonata Collected in Mesopotamia by the late Major R. Brewitt- Taylor, R. A. M. C. *Ann. Mag. Nat. Hist.* , 9 (5): 293-303, 1920.
- [7] Sage, B. L. Notes on the Odonata of Iraq. *Iraq nat. Hist. Mus. Publs.* , 18: 1-11, 1960.
- [8] Dijkstra, K. D. B and Lewington, R. *Afield guide to the Dragonflies of Britain and Europe.1*: 320 pp. British Wildlife Publishing, Gillingham, 2006.
- [9] De Fonesca, T. *The Dragonflies of Sri Lanka.1*: 303pp, Wildlife Heritage Trust. Colombo, 2000.
- [10] Dumont, H. J. *Odonata of the Levant, Fauna Palestina.5*: 297 pp. Jerusalem, Academy of Sciences and Humanities. Israel, 1991.
- [11] Fraser, F. C. *The Fauna of British India, including Burma and Ceylon, Odonata.3*: 461pp. Taylor and Francis, London, 1936.
- [12] Samways, M. J. *Dragonflies and Damselflies of South Africa.1*: 297 pp. , Pensoft Publishers, Sofia- Moscow, 2008.
- [13] Skvortsov, V. E. *The dragonflies of Eastern Europe and Caucasus: An illustrated guide.1*: 623 pp., KMK Scientific Press Ltd. Moscow, 2010.
- [14] Theischinger, G. *Identification guide to the Australian Odonata.1*: 283p. Department of Environment, Climate Change and Water NSW. Victoria, 2009.
- [15] Ali WK, Khidhir AQS. *Morphological Study of the Sympetrum arenicolor*

Research Article

Comparative Study for the Accuracy of *Helicobacter pylori* Diagnostic Methods Associated with Some Inflammatory Factors

Eman N. Naji

Department of Biology, College of Science, Mustansiriya University, IRAQ

Email: emannatiq@yahoo.com

Article Info

Received
23/02/2017

Accepted
21/05/2017

Abstract

This Study was intended to diagnose *H. pylori* the major causative pathogen in gastro duodenal irritation and ulceration. Different techniques were used invasive tests (histopathological examination, rapid urea CLO test and culture) , while noninvasive tests includes (serological tests and stool antigen) in addition to determination of some immune response factors (IgM , IgG , IgA) as well as (IL – 8 and IFN – γ) in Patients Sera.

According to the results of invasive diagnostic method 30/113 (26.69%) patients were considered to be infected and 83/113(73.31%) patients were considered as noninfected was contrasted with noninvasive diagnostic method 25/113 (22.14%) patients were considered to be infected and 88/113(77.83%) patients were considered as noninfected. In order to get the overall percentage of the infected people included in this study, we merge the results of the two methods ,so we found out that the total infected patients with *H. pylori* diagnosed by invasive and noninvasive methods were 42 /113 (37.2%) while the noninfected 71/113 (62.8) disseminated as 27/68(39.71%) infected male ,which was privileged than the infected female when it was 15/45(33.33%). The high prevalence of *H. pylori* infection in the age group ranging between (46-60) in male and female. Histology (invasive teq.) and ECO rapid test (noninvasive teq.) were considered as the ‘‘best techniques’’ for *H. pylori* detection, in the outlook of its high specificity, sensitivity and because it detected the major number of *H. pylori*-positive patients along with the other techniques used in this work.

The sensitivity, specificity, positive predictive values (PPV) and negative predictive values (NPV) for histology were 100,100,100 and 94.5% , respectively, while for the ECO rapid test they were 96, 93, 91.5, and 97.14%. Culture (invasive teq.) and IgG anti *H. pylori* (noninvasive teq.) coming secondly in the diagnosis of *H. pylori* infection because they detected a little fewer number of infected patients than the first two teq. as noted above. The sensitivity, specificity, (PPV) (NPV) for Culture were 80%, 97% ,96.96% and87.5% and for IgG anti *H. pylori* were 85%, 91%,92.8% and 97.8%. Finally the smallest patient number was obtained from the rest of all the six teq. were used in the present work obtained from the urea CLO test and stool antigen, invasive and noninvasive teq. respectively.

The present research found out that there were a relationship between the results of rapid anti *H. pylori* ECO test, antibody titer in ELFA, immunoglobulin (IgG and IgA) and (IFN- γ) , (IL-8) concentration. Also, all these data were related to the results of the histological changes and the results of the urea CLO test of patients when compared with the noninfected members. These results showed highly significant differences among patient groups in comparison with noninfected group at (P. Value < 0.001). On the other hand, there were no relationship between IgM concentration with any of the other results of diagnostic methods were used may such results considered a first step for determining the susceptibility of infection and to confirm the diagnosis by use one more test in each time especially Histology (invasive teq.) and ECO rapid test (noninvasive teq.) correlated with estimation of (IgG and IgA) and (IFN- γ) , (IL-8) concentration.

Keywords: *Helicobacter pylori*, Gastric ulcer, Invasive test, noninvasive test, immunological parameters.

الخلاصة

تهدف هذه الدراسة الى تشخيص بكتيريا *H. pylori* المسبب الرئيسي لتهيج وتقرح القناة المعدية والاثني عشر باستخدام تقنيات مختلفة شملت الفحوصات المتجاحة (invasive) والتي تضمنت الفحص النسيجي وفحص البوربا والاستنابات والفحوصات غير المتجاحة (الفحوصات المصلية وفحص مستضد البراز) فضلاً عن تحديد بعض عوامل الالتهاب كالأجسام المضادة (IgM , IgG , IgA) والانتروكين 8 والانتروفيرون كما في مصل عينة الدراسة. شارك 113 مريض في هذه الدراسة (68 ذكور و 45 اناث) أخضعوا جميعهم لفحص الناظور المعدي كما تم جمع عينات دم وبراز منهم. اظهرت النتائج ان 30 (69 , 26 %) من مرضى عدوا مصابين و 83 (31 , 73 %) غير مصابين وفقاً لنتائج الفحوصات المتجاحة مقارنة بنتائج الفحوصات غير المتجاحة والتي بينت ان 25 (14,22 %) كانوا مصابين و 88 (83,77 %) غير مصابين و عدت طريقتا الفحص النسيجي (فحص متجاح) والفحص السريع (فحص غير متجاح) هما الافضل للتحري عن الإصابة. ومن اجل التوصل الى النسبة الكلية للمصابين في هذه الدراسة تم دمج نتائج النوعين من الفحوصات وتوصلنا الى ان نسبة المصابين بالبكتريا بطريقتي التشخيص المتجاحة وغير المتجاحة بلغ 113/42 (37.2 %) بينما غير المصابين 113/71 (62.8 %). الظهور الاكبر للبكتريا كان في الفئة العمرية (46-60) في كل من الاناث والذكور. الفحص النسيجي وهو من الفحوصات المتجاحة والفحص السريع ECO وهو من الفحوصات غير المتجاحة اعتبروا افضل تقنية للتحري عن بكتريا *H. pylori* بالنظر لحساسيتها العاليه وخصوصيتها العاليه اضافة الى التحري على اكبر عدد من الحالات الموجبة حيث بلغت الحساسية والخصوصية وقيم التوقع الموجبة وقيم التوقع السالبة للفحص النسيجي 100،100،100،94.5 % على التوالي وبالنسبة لفحص ECO كانت هذه القيم كالتالي 96،93،91.5،97.14 % على التوالي. بالمرتبة الثانية جاء فحصي الاستنابات وهو من الفحوصات المتجاحة مع فحص التحري عن *H. pylori* anti IgG وهو من الفحوصات غير المتجاحة وذلك لان الحالات الموجبة التي تم تشخيصها بهذين الفحصين كانت اقل من الفحصين الاوليين، وقد بلغت قيم الحساسية والخصوصية والتوقع الموجبة والتوقع السالبة لفحص الاستنابات 96،96،97،80،87.5 % على التوالي في حين بلغت بالنسبة لفحص 85 *H. pylori* anti IgG، 91،92.8% و 97.8 % على التوالي. اخيراً فان اقل عدد للحالات الموجبة تم كشفها باستخدام بقية الفحوصات الستة وهي CLO وفحص مستضد البراز. كما وتوصلت الدراسة الى وجود علاقة بين نتائج فحص rapid anti-*H. pylori* Eco test ، *antibody titer in* rapid anti-*H. pylori* Eco test ، وبين تركيز الاجسام المضادة نوع IgG باستخدام تقنية ELFA وبين نتائج الفحص السريع ECO وبين تركيز كل من الاجسام المضادة نوع IgG و IgM وتركيز الانتروكين 8 وانتروفيرون كما في مصل المرضى كما ان هذ النتائج ذات علاقة مع نتائج الفحص النسيجي وفحص CLO وبمعنويه عاليه (P. Value < 0.001). مقارنة بغير المرضى. من جهة اخرى لم نجد علاقة بين تركيز IgM والفحوصات كافه.

Introduction

Helicobacter pylori is a Gram-negative, micro-aerophilic, and small corkscrew-shaped rod, extremely motile bacterium that colonizes just in the mucous layer of the human stomach, is an essential pathogenic factor in chronic energetic gastritis, duodenal and gastric ulcers [1,2], affects more than semi of human population international and is mainly more settled in developing countries[3,4].

H. Pylori in extraordinary in its ability to colonize the stomach, where low pH normally protects against bacterial infection. This bacterium colonizes gastric mucosal cells in the stomach, surviving in the mucous layer that coats the epithelium. The organism is noninvasive, but recruits and activates inflammatory cells, thus causing a chronic inflammation of the mucosa. (*H. pylori* secrete urease, producing ammonium ions that neutralize stomach acid in the vicinity of the organism, thus favoring bacterial multiplication. [5]

There are now several invasive methods for the clinical diagnosis of *H. pylori*, such as histopathology examination (HE), rapid urea (CLO) test, and bacterial culture as well as noninvasive methods such as serology, 13C-urea breath test, and the stool antigen test [6,7]. Regardless of the

fact that several invasive and noninvasive methods exist for the diagnosis of *H. pylori*, none of these have been conventional as a gold standard[9,10]. Infection with this organism induces infiltration of polymorphonuclear and mononuclear leukocytes and enhances the creation of various cytokines in gastric mucosa [9,10]. This development enhanced protein secretion of interleukin (IL) -8 and interferon- γ (IFN- γ) production they can be detected in serum of *H. pylori*-positive gastritis and control. [11,12,13,14]. In addition, concurrent of serum immunoglobulin (IgG), (IgM), and (IgA) antibodies towards *H. pylori* infection can be used to find out the incidence of both acute and chronic infections. [15]. For the earlier description of the significance and occurrence diagnostic methods of *H. pylori* infections associated with the determination of some inflammatory factors this study aimed to diagnose *H. pylori* in patients assumed to have gastric ulcers by both invasive methods includes histopathological examination (HE), rapid urea (CLO) test and culture in addition to noninvasive tests includes serological tests and stool antigen test, or else determine some humoral immune response factors (IgM, IgG, IgA), and detect the (IL-8 and IFN- γ) in patient sera.

Materials and Methods

Patients and Sample collection: The specimens were collected under physician medicine conference during the period between April 2015 and December 2016 from different private clinics and hospitals in Baghdad. One hundred thirteen volunteers consisted of 43 males and 70 females undergoing upper gastroduodenal endoscopy. These patients were admitted to the endoscopy unit of the Gastroenterology division. The patient consisted of participants that satisfied the following criteria: misery from pain with the itchy burning feeling; not having taken *H. Pylori* eradication treatment, antibiotic, or other drug within the last two weeks; and without bleeding and clotting disorders. The patient group was formed from patients in whom biopsy samples were found positive by at least two invasive diagnostic tests, such as histopathology and rapid urease test and/or bacterial culture. The noninfected group was formed of subjects whose biopsy samples were found negative for *H. pylori* by histopathology and rapid urease test and/or culture or if they were found positive by at least two non-invasive method used in this study while the others represent the noninfected group.

Gastric biopsies: biopsies were immediately separated into two portions one of them fixed at 10% buffered formalin to be used for the histopathological examination; the other part was ground at 10.000 rpm for 15 sec with an electric tissue homogenizer. The homogenized tissue separated in to two portions one of them used in rapid urea (CLO) test at the same time as the other parts immediately placed in transport medium in order to use in a bacterial culture.

Blood sample:

Five mL of blood was collected in dry tubs without anticoagulant, after clotting, the sera were obtained by centrifugation (for 10 min at 5000 rpm) divided into aliquots and stored at (-20°C) until used in the serological and immunological test.

Stool samples:

One to two grams of stool sample were collected in a dry cup in order to use it in the stool antigen test.

H. pylori infection diagnostic tests:

Invasive test:

Histopathological examination (HE): For routine histology paraffin embedded tissue blocks were prepared and 5µm thickness sections were mounted on slides for Hematoxylin and Eosin staining. Mucosal ulceration with heavy acute or chronic inflammatory cells infiltrate were detected. Giemsa stain was used to search for bacteria within the tissue [11].

Culture (bacterial isolation): The biopsy portion was put in transport media immediately cultured on Colombia agar plates containing 5% defibrinated sheep blood, 10 mg/L Vancomycin, and 5 mg/L Trimethoprim and incubated in 5% CO₂ incubator (microaerobic conditions) for 3-5 days. Organisms were identified as *H. pylori* by colony morphology of bacteria and their Gram-staining characteristics were studied. Convex semitransparent, 1-2 mm diameter colonies with the positive reaction of catalase, urease, and oxidase [15].

Rapid urea (CLO) test:

The CLO test rapid urease test (Kimberly-Clark/U. S. A) is a variation of the test where the biopsy sample is placed in a medium containing urea.

A marker is then used to determine if a chemical reaction has taken place to suggest the presence of the *H. pylori* bacterium. This reaction takes place (10 min-24 hour) the areas of *H. pylori* hydrolyze urea to release ammonia, which is detected colorimetrically and can be used as a diagnosis of an infestation by the *H. pylori* bacterium. When the CLO test is positive (red color reaction) it is a fairly reliable indicator that the individual is suffering from an infection of this bacterium, while the negative reaction (yellow color reaction) it means that the individual is not infected.

Noninvasive Tests

Rapid Anti *H. pylori* Test:

H. pylori antibodies Rapid Test Device (serum \plasma) was used as a rapid visual immunoassay for the qualitative presumptive detection of specific IgM and IgG antibodies to *H. pylori* in human serum specimens. The procedure was done according to manufacture instructions (ECOTest D-HP-32). The device and the specimens were

brought to room temperature and 75µl from the serum was transferred to the specimen well. Migration of specimen across the resort area in the center of the device will cause coloration (dark red color) of control band and another red band appeared within five minutes in case of a positive result ,while the only red control band appears in the negative results. Invalid: There should always be a purplish red control band in the control region regardless of test results. If a control band is not seen, the test is considered invalid. Deep of the color and time of result appearance was recorded.

Quantitative determination of IgG-class antibodies against *H. pylori* by Enzyme Linked Fluorescent Assay (ELFA)

The Vidas is an automated qualitative test for use of the instruments of the Vidas family. For the detection of anti-Helicobacter pylori IgG antibodies in human serum or plasma using the ELFA technique. The procedure was done according to manufacture instructions of IgG-class antibodies kit (Biomerieux, France).

Faecal antigen test:

The *H. pylori* stool antigen test was performed to detect the presence of *H. pylori* infection in the patient and control groups. Stool samples were analyzed using the ABON *H. pylori* antigen test device (Abon Biopharm, Germany), that is, a lateral flow chromatographic immunoassay for detection of *H. pylori* antigen. A diluted stool sample was dispensed into the sample port of the test device, and the appearance of a colored line after 10 min in the test line region of the strip indicated a positive result.

Determine some humoral immune response factors:

Determination of Human Immunoglobulinse (IgM, IgG and IgA) Turbidimetry method. This method depends on the quantitative determination of human Immunoglobulins IgG, IgA, IgM without sample dilution The procedure was done

according to manufacture an instructions kit (Human, Germany).

Determination of Human Interferon Gamma (IFN- γ) Interferon Gama (IFN- γ) according to the protocol of Human IFN- γ ELISA (Enzyme-Linked Immunosorbent Assay) kit was used for the quantitative measurement of human IFN- γ in serum.

Determination of human (IL-8)

Interlukin-8 (IL-8) estimated according to the protocol of Human (IL-8) ELISA Kit. The IL-8 EASIA is a solid phase Enzyme Amplified Sensitivity Immunoassay performed on microtiter-plate.

Statistical Analysis

Statistical analysis was performed using SPSS v20.0 software (SPSS Inc, Chicago, IL, USA). Differences were considered significant when $p \leq .05$.

Results and Discussion

Subject analysis

One hundred and thirteen people's 68 male (60.18%) age ranges between 30-72 years while median age was 51 and 45 females (39.82%) age ranges between 32-70 years while median age was 48.5 years. Patients were divided into three age groups as listed in the Table 1. All patients were subjected to gastroendoscopy, venous blood and stool samples were collected from patients for diagnostic methods and some immunological tests used in this study.

Determination of *H. pylori* in Patients by invasive and noninvasive diagnostic methods:

Methods that exactly detect *H. pylori* infection in dyspeptic patients are major importance. Direct manifestation of *H. pylori* in gastric biopsy specimens is possible through the use of histological examination with Giemsa staining, culture, and assays for rapid urea (CLO) test. All these endoscopy-based methods require gastric biopsy specimens and are thus classified as invasive methods (7).

Table 1: Descriptive statistics of samples.

Gender	Age /year				Age groups		
	Min.	Max.	Range	Median	30-45	46-60	61-72
No 113 (%)							
Male No.68 (60.18)	30	72	30-72	51	20	43	5
Female No.45 (39.82)	32	70	32-75	48.5	16	27	2

H. pylori infection elicits a local mucosal and a systemic antibody response, circulating IgG antibodies to *H. pylori* can be detected by Enzyme Linked Fluorescent Assay (ELFA) antibody, Rapid anti *H. pylori* ECO20E test and other serological test, these two tests and detect the presence of *H. pylori* antigens shed in the faeces involved in the noninvasive methods were used in this study. The patient group was selected from patients in whom biopsy samples were found positive by at least of two invasive diagnostic tests, and/or if they were found positive by at least of two non-invasive methods used in this study while the others represent the noninfected group (16).

Results of invasive test:

In this study, the presence of *H. pylori* was resolute by invasive techniques (histology, rapid urea

CLO test and culture) of gastric antral biopsy specimens in 113 suspected patients. As shown in table (2) and Figure (1A and B), 17 (15.15%) patients were positive in the three tests, 11 (9.76%) patients were positive in both culture and rapid urea CLO test, 2 (1.78%) patients were positive in both histological examination and culture, otherwise 3(2.56%) patients were found to be positive only in histological examination and, while 2 (1.78%) patients were positive in a bacterial culture. Patients were considered to be infected with *H. pylori* if they were positive in two of the three tests as we noted. So, according to these results of invasive diagnostic method 30/113 (26.69%) patients were considered to be infected and 83/113(73.31%) patients were considered as noninfected.

Table (2): Results of endurance of *H. pylori* in Patients by invasive methods.

Invasive methods			No. (113)	(%)
Histology	Culture	CLO test		
+	+	+	17	15.15*
+	+	-	2	1.78*
+	-	-	3	2.65
-	+	+	11	9.76*
-	-	+	1	0.88
-	+	-	2	1.78
-	-	-	77	68

*Infected groups

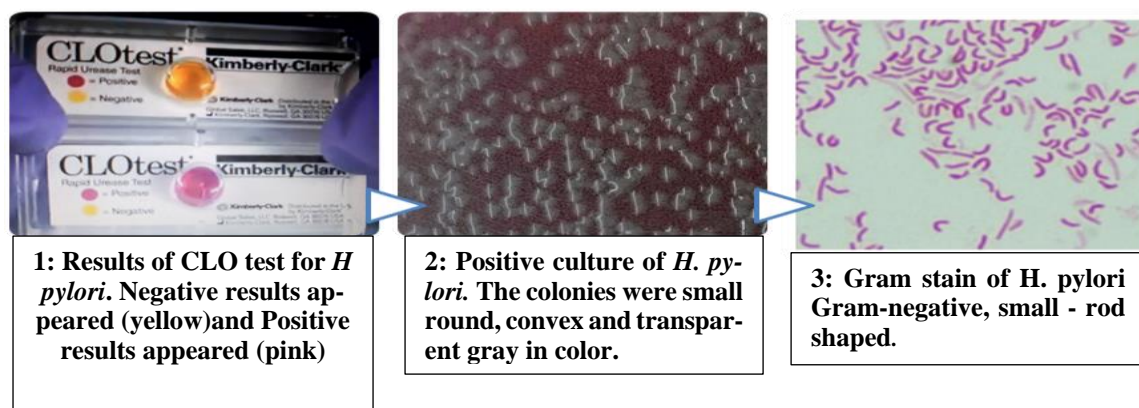


Figure 1: A. The results of 1: urea CLOtest, 2: positive culture of *H. pylori* and 3: Gram stains reaction.

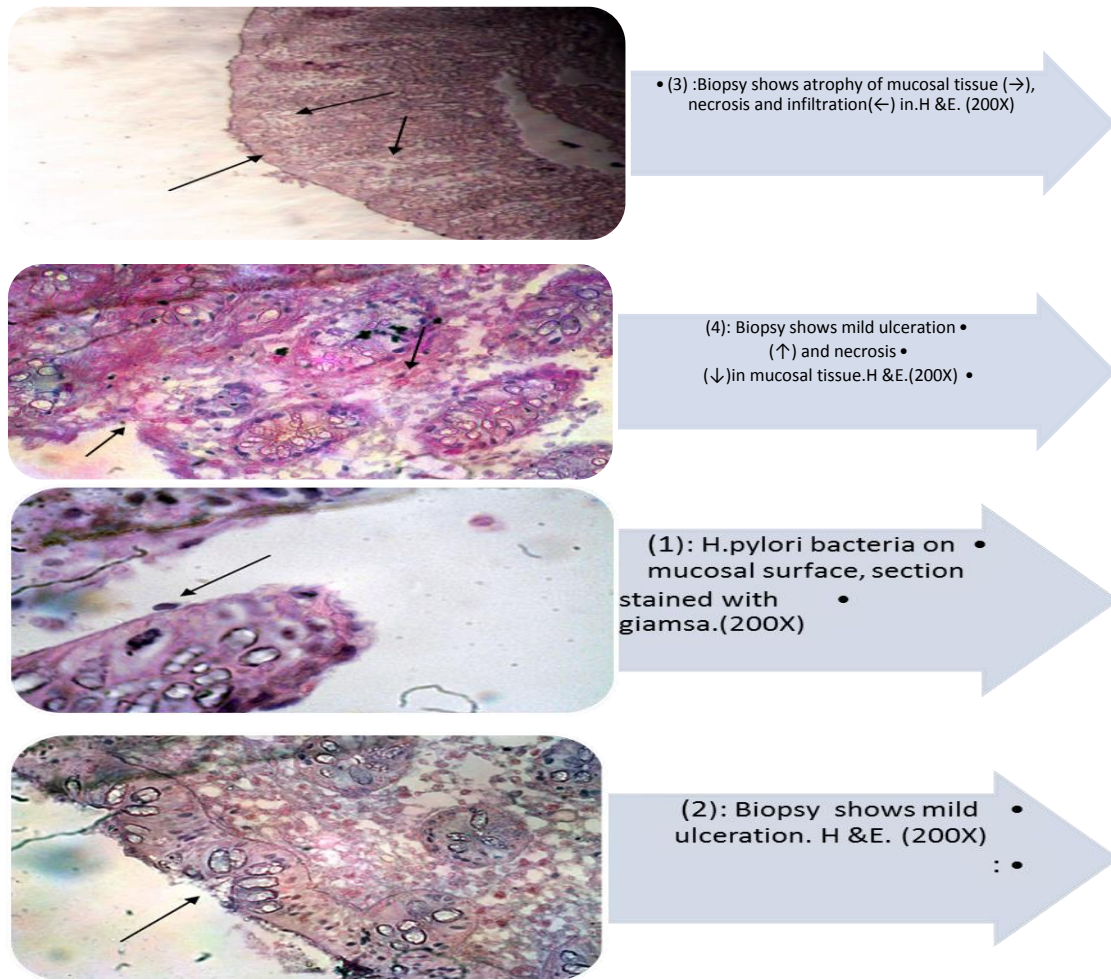


Figure 1: B. Histology (Invasive test) of gastric mucosa.

Results of noninvasive test:

In order to confirm the results we have obtained in determination of *H. pylori* infected patients by invasive method we were undertaking a three of noninvasive techniques as shown in Table 3 Figure 2, 19 (16.9%) patients were only positive in ECO test , 11 (9.76%) were positive in both IgG against *H. pylori* and ECO test, otherwise 13(11.5%) patients were found to be positive in three noninvasive tests and 1 (0.88%) patients were positive in both IgG against *H. pylori* and

fecal antigen test, while 1 (0.88) patients were positive in a Fecal antigen test. Patients were considered to be infected with *H. pylori* if they were positive in two of the three tests as we noted. So, according to these results of noninvasive diagnostic method 25/113 (22.14%) patients were considered to be infected and 88/133(77.83%) patients were considered as non-infected.

Table 3: Results of endurance of *H. pylori* in Patients by noninvasive methods.

(%)	NO (113)	Noninvasive methods		
		Fecal antigen test	IgG against <i>H. pylori</i>	Rapid anti <i>H. pylori</i> ECO test
11.5*	13	+	+	+
9.76*	11	-	+	+
16.9	19	-	-	+

0.88*	1	+	+	-
0.88	1	+	-	-
0.88	1	-	+	-
59.29	67	-	-	-

*Infected groups



Figure 2: The results of noninvasive tests.

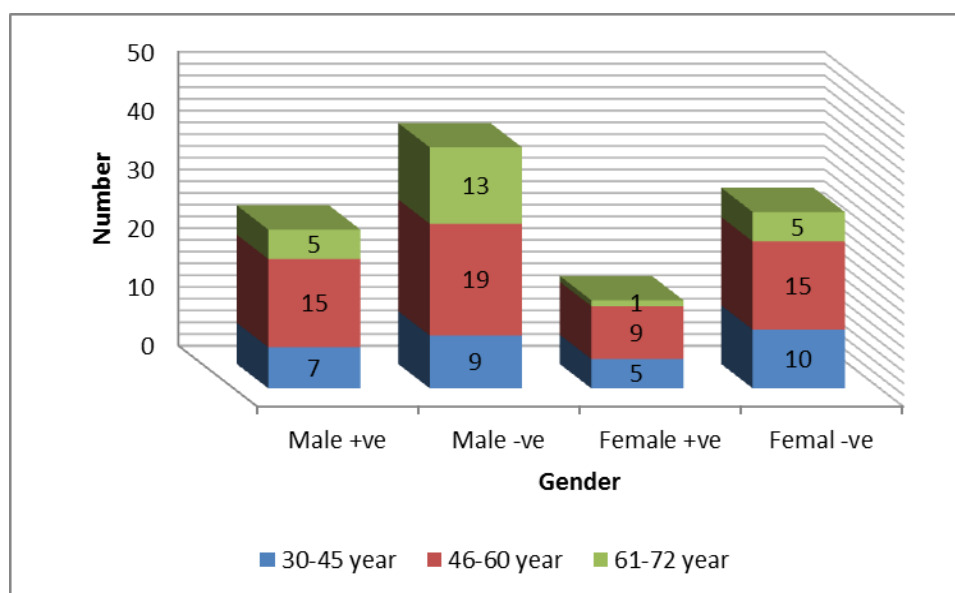
Invasive and noninvasive tests can be used and recommended to correctness for the in vitro diagnosis of *H. pylori*, which has a role in the pathologies of gastritis [17].

In order to get the overall percentage of the infected people included in this study, we merge the results of the two methods (inv. and noninv.) as listed in Table (4) and Figure (3), where it was split percentage and the number of infected patients associated with sex and three age groups. The results showed that the total infected patients with *H. pylori* diagnosed by invasive and noninvasive methods were 42 /113 (37.2%) while the noninfected 71/113 (62.8) disseminated as 27/68(39.71%) infected male, which was privileged than the infected female when it was 15/45(33.33%). The high prevalence of *H. pylori* infection in the age group ranging between 46-60 in male and female were 15/68 (35.71%) and 9/45

(21.43%) respectively, there was highly statistically significant differences at p value (0.02). Our results explained that there is a relation between the age and the incidence of *H. pylori*. The results of the current work disagree with the results of [18] who found that there is no significant difference in *H. pylori* prevalence among patients have the same age range and a different gender, and agree with the study of [19] which showed a very high incidence of *H. pylori* infection in the age group ranging from 41-50 and 51-60 years. The differences among the results might due to some factors such as skin and blood classification, habitates, teaching level and smoking [20].

Table 4: Number and presentages of infected patients with *H. pylori* associated with age groups and gender.

PV	Female NO:45		Male NO:68		Gender Age groups/Years
	Negative NO (%)	Positive NO (%)	Negative NO (%)	Positive NO (%)	
0.05 (S)	10(22.23)	5(11.11)	9(13.3)	7(10.3)	30-45 (No. : 31), M:16 // F:15 46-60 (No. :58), M:34 // F:24 61-72 (No. :24), M:18 // F:6
0.02 (S)	15(33.33)	9(20)	19(27.9)	15(22.1)	
0.01(S)	5(11.11)	1(2.2)	13(19.1)	5(7.4)	
0.01(S)	30(66.67)	15(33.33)	41(60.3)	27(39.7)	Total

Figure 3: The distribution of patients' number infected with *H. pylori* associated with age groups and gender.

The relative results obtained by all the diverse tests used in the current study are listed in table (5), showed that histology (invasive teq.) and ECO rapid test (noninvasive teq.) were considered as the “best techniques” for *H. pylori* detection, in the outlook of its high specificity, sensitivity and because it detected the major number of *H. pylori*-positive patients along with the other techniques used in this work. The sensitivity, specificity, positive predictive values (PPV) and negative predictive values (NPV) for histology were 100, 100, 100 and 94.5%, respectively, while for the ECO rapid test they were 96, 93, 91.5, and 97.14%.

Culture (invasive teq.) and IgG anti *H. pylori* (noninvasive teq.) coming secondly in the diagnosis of *H. pylori* infection because they detected a little fewer number of infected patients than the first two teq. as noted above. The sensitivity, specificity, (PPV) (NPV) for Culture was 80%, 97%, 96.96% and 87.5% and for IgG anti *H. pylori* were 85%, 91%, 92.8% and 97.8%. Finally the smallest patient number was obtained from the rest of all the six teq. were used in the present work they were the urea CLO test and stool antigen, invasive and noninvasive teq. respectively. The sensitivity, specificity, (PPV) (NPV) for these tests was explained in Table 5.

Table 5: The relative accuracy of invasive and non invasive tests for *H pylori* infection.

Test type	Sensitivity %	Specificity %	*PPV %	^NPV %
Invasive test				
Histology	100 %	100 %	100%	94.5%
Culture	80 %	97 %	96.96%	87.5%
Urea CLO test	91 %	89 %	85.71%	98.7%
Noninvasive test				
Rapid ECO test	95 %	94 %	91.5%	97.14%
IgG anti <i>H. pylori</i>	85 %	91 %	92.8%	97.6%
Stool antigen	83 %	89 %	78.9%	96.9%

PPV: Positive predictive value, means that if the test positive, you have a (according to the test type) % chance of actually having the disease ^ NPV: Negative predictive value, means that if the test negative, you have a according to the test type % chance of not having the disease.

In the present study, six techniques were used to detect infection of *H. pylori* in random Iraqi people, including invasive and noninvasive technique. Numerous people get *H. pylori* through childhood, but adults can get it from food and drinks or by get in touch with the saliva or body fluids of infected people. It's further frequent in countries that suffering from contaminated water with sewage [20]. In a study carried by [21], they said that there is no particular test can be considered as the gold standard for the diagnosis of *H. pylori* infection and each technique has its private compensation and discompensation. That is depends on the decreasing sensitivity of each method. The isolation of the bacteria from gastric tissues by culture is difficult because of its low sensitivity The critical troubles In the culture method such as the incubation conditions, media preparing, contamination problems, the slowly reproduction of the bacteria, strain type, technical difficulties and low diagnostic sensitivity of the method (80 % in the current study) , so it has not been used in the routine diagnosis, this result agreed with [23]. Gastric endoscopy is one of the important tests for *H. pylori* diagnoses neither by endoscopy examination and the diagnosis of patients' status or by taking the biopsy that it will be used in the all invasive diagnostic methods used for *H. pylori* infection [24].

In this study , we considered histology on of the "best techniques " for *H. pylori* detection, in the outlook of its high specificity,sensitivity and be-

cause it detected the major number of *H. pylori*-positive patients along with the other techniques used in this work,during histological examination detects lower stage of *H pylori* infection and this bacteria can be found in some sections stained with haematoxylin and eosin, some biopsy shows mild ulceration , atrophy of mucosal tissue , necrosis and infiltration.

The detection of tissue morphological changes because of *H pylori* infection is an important advantage of histology , in addition to the historical record provided, gastric or duodenal sections from biopsies (or even other sections) can be examined at any time[18] [25].

The urea CLO test and low expensive ureas tests are of comparable sensitivity and specificity. This simple tests used for detecting *H pylori* infection but indicate only the presence or absence of infection. Conversely, in this study the sensitivity of urease tests is frequently higher than that of culture (biopsy based technique) because the intact biopsy sample is placed in the media [26]. The CLO test, can consequence in fake positives for numerous reasons, contagion by other bacteria producing urease enzyme, mistaken completion of the CLO test during endoscopy, provisional reduce of bacteria due to antibiotics. As a result, when used alone, this test has low diagnostic concert [27].

For serological identification, rapid ECO test and ELFA are an uncomplicated, inexpensive more modern, successful method and because of their high specificity, sensitivity among other noninvasive test as listed in the Table 4 and can be made on frozined samples in addition this technique available in the private and public laboratories in Iraq. By using fecal antigen test there were no significant association was found

between *H. pylori* stool antigen positivity and the other diagnostic methods were used in this study. However, stool antigen test can be used for diagnosis infection, specifically in children as the easy obtaining of stool sample and the most difficult to make endoscopy [28].

3- Results of Estimation of Immunoglobulins (IgM, IgG, IgA) and Interferon Gamma (IFN- γ) and Interleukin-8 (IL-8).

Estimation of immunoglobulins (IgG, IgA, IgM), Interferon Gamma (IFN- γ) and Interleukin-8 (IL-8) afford useful information for the assessment of convincing disease status. As revealed in the Table 6 the IgG, IgA, titers showed high concentration compared with the noninfected groups, the

statistical analysis showed that there are significant differences at p value (0.001), while there were no statistically differences in IgM titer between the two tested group Table 6. [18] reported an important increase of IgG and IgA titer in *H. pylori* patients' serum, but IgM does not present a further role. While [29] found that IgM has been create to have slight diagnostic efficacy for *H. pylori* infections and is superior only intensely following infection, whereas *H. pylori* infections are common chronic, that is IgM has exceptionally low sensitivity. Concentration of various cytokines, as well as interferon gamma (IFN- γ) and IL-8, are increased in the stomachs of *H. pylori*-infected patients compared to noninfected.

Table 6: Immunoglobulin (IgM , IgG and IgA) concentration in *H. Pylori* infected and noninfected group.

Study groups	Immunoglobulins levels in serum (mg/dl)		
	IgG Mean \pm SD	IgM Mean \pm SD	IgA Mean \pm SD
Infected (42)	1089.54 \pm 113.73	78.5 \pm 9.3	276.2 \pm 19.4
Noninfected (71)	467.88 \pm 79.53	63.4 \pm 7.98	122 \pm 11.8
P Value	0.001	NS	0.001

The cytokines titers showed that highly significant elevation of both cytokines (INF- γ and IL-8) among patient groups in comparison with non-infected group at (P. Value < 0.001) in Mean \pm SD (140.40 \pm 61.08 and 241.72 \pm 32.80 respectively) with (53.82 \pm 11.49 and 118.69 \pm 29.36 respectively) as a result mentioned in the table (7). The study of [18,29] showed that *H. pylori* induced considerably higher concentration of IFN- γ and IL-8, IFN- γ keeps mucosal inflammation and may encourage disease development to gastric ulcer. Another study [30], showed an increased concentration of IFN- γ in the stomachs of *H. pylori*-infected patients is dependable with the expansion of a Th1- largest response and another study by [31] reported that IL-8 is increased within *H. pylori*-infected mucosa where it localizes to gastric epithelial cells, and levels of IL-8 are directly associated to the strictness of gastritis as well IFN- γ , IL-8 increased values coincided with increased inflammation and with increased *H. pylori* density in humans [32] in addition to in animal model studies [33].

The cytokines titers showed that highly significant elevation of both cytokines (INF- γ and IL-8) among patient groups in comparison with non-infected group at (P. Value < 0.001) in Mean \pm SD (140.40 \pm 61.08 and 241.72 \pm 32.80 respectively) with (53.82 \pm 11.49 and 118.69 \pm 29.36 respectively) as a result mentioned in the table (7). The study of [18,29] showed that *H. pylori* induced considerably higher concentration of IFN- γ and IL-8, IFN- γ keeps mucosal inflammation and may encourage disease development to gastric ulcer. Another study [30], showed an increased concentration of IFN- γ in the stomachs of *H. pylori*-infected patients is dependable with the expansion of a Th1- largest response and another study by [31] reported that IL-8 is increased within *H. pylori*-infected mucosa where it localizes to gastric epithelial cells, and levels of IL-8 are directly associated to the strictness of gastritis as well IFN- γ , IL-8 increased values coincided with increased inflammation and with increased *H. pylori* density in humans [32] in addition to in animal model studies [33].

Table 7: Statistical analysis of Interferon Gamma (IFN- γ) and Interleukin-8 (IL-8) concentration in *H. Pylori* infected and noninfected group.

Study groups	INF- γ pg/ml, Mean \pm SD	IL-8 pg/ml, Mean \pm SD
Infected (42)	254.63 \pm 17.8	2.82 \pm 0.32
Noninfected (71)	23.76 \pm 1.2	0.26 \pm 0.04
P Value	0.001	0.001

The present results found out that there was a relationship between the results of rapid anti *H. pylori* ECO test, antibody titer in ELFA, immunoglobulin (IgG and IgA) and (IFN- γ) , (IL-8) concentration. Also, all these data were related to the results of the histological changes and the results of the urea CLO test of patients when compared with the noninfected members, Such results could might be considered a first step for determining the susceptibility of infection and to confirm the diagnosis by use one more test in each time. On the other hand, there was no relationship between IgM concentration with any of the other results of diagnostic methods used in our study, may be because of IgM antibodies against *H pylori* decrease with older age patients, which, since this is frequently asymptomatic, makes it difficult to identify cases of primary infection [34].

The majority of research merge two methods or further to get a magnificent diagnosis, including invasive or noninvasive methods and/or molecular method to advance diagnosis of *H. pylori* infection [35]. *H. pylori* in extraordinary in its ability to colonize the stomach and adhere to the epithelial cells by producing adhesions and causing gastric and peptic ulceration and other unusual changes, where low ph normally protects against bacterial infection[5]. For the reason that of the severe complicatedness that escort *H. pylori* infection which might have awful penalty ,it is essential to clutch an early diagnosis to pass up the progress of the infection. Many particular methods had been used [36] or newly developed molecular techniques like Multiplex PCR was used for amplication the CagA genes assay to identify *H. pylori* in gastric biopsies [16] [36].

Our results indicate that there were a relationship between the results of rapid anti *H. pylori* ECO

test, antibody titer in ELFA, immunoglobulin (IgG and IgA) and (IFN- γ), (IL-8) concentration. Also, all these data were related to the results of the histological changes and the results of the urea CLO test of patients when compared with the noninfected members, this result showed highly significant differences among patient groups in comparison with noninfected group at (P. Value < 0.001). On the other hand, there were no relationship between IgM concentration with any of the other results of diagnostic methods were used. Such results could might be considered a first step for determining the susceptibility of infection and to confirame the diagnosis by use one more test in each time especialy Histology (invasive teq.) and ECO rapid test(noninvasive teq.) correlated with estimation of (IgG and IgA) and (IFN- γ), (IL-8) concentration.

References

- [1] Graham, D. Y., Malaty, H. M., Evans, D. G., Evans Jr., D. J., Klein, P. D. and Adam, E. Epidemiology of Helicobacter pylori in an asymptomatic population in the United States. Elect of age, race, and socioeconomic status. Gastroenterology; 100: 1495-1501. (1991)[2] Kreiss, C., Blum, A. L. and Malfertheiner, P. Peptic ulcer pathogenesis. Curr. Opin. Gastroenterol; 11:25-31. (1995)
- [3] Correa P, Piazuolo MB. Evolutionary History of the Helicobacter pylori Genome: Implications for Gastric Carcinogenesis. Gut Liver; 6: 21-28. (2012)
- [4] Suzuki H, Saito Y, Hibi T. Helicobacter pylori and Gastric Mucosaassociated Lymphoid Tissue (MALT) Lymphoma: Updated Review of Clinical Outcomes and the

- Molecular Pathogenesis. *Gut Liver*; 3: 81-87. 2009.
- [5] Kienesberger, S., L. M. Cox, A. Livanos, X. S. Zhang, J. Chung, G. I. Perez-Perez, G. Gorkiewicz, E. L. Zechner and M. J. Blaser. Gastric Helicobacter pylori Infection Affects Local and Distant Microbial Populations and Host Responses. *Cell reports*; 14(6): 1395-1407. 2016
- [6] Guarner J, Kalach N, Elitsur Y, Koletzko S. Helicobacter pylori diagnostic tests in children: review of the literature from 1999 to 2009. *Eur J Pediatr*; 169: 15-25. 2010.
- [7] Tian XY, Zhu H, Zhao J, She Q, Zhang GX. Diagnostic performance of urea breath test, rapid urea test, and histology for Helicobacter pylori infection in patients with partial gastrectomy: a meta-analysis. *J Clin Gastroenterol*; 46: 285-292. 2012.
- [8] Frencck RW, Fathy HM, Sherif M, Mohran Z, El Mohammedy H, Francis W, Rockabrand D, Mounir BI, Rozmajzl P, Frierson HF. Sensitivity and specificity of various tests for the diagnosis of Helicobacter pylori in Egyptian children. *Pediatrics*; 118:e1195-e1202. 2006.
- [9] Koletzko S, Jones NL, Goodman KJ, Gold B, Rowland M, Cadranel S, Chong S, Colletti RB, Casswall T, Elitsur Y, Guarner J, Kalach N, Madrazo A, Megraud F, Oderda G. Evidence-based guidelines from ESPGHAN and NASPGHAN for Helicobacter pylori infection in children. *J Pediatr Gastroenterol Nutr*; 53: 230-243. 2011.
- [10] Fan, X-G., Chua, A., Fan, X-J. and Keeling, P. W. N. Increased gastric production of interleukin-8 and tumour necrosis factor in patients with Helicobacter pylori infection. *J. Clin. Pathol*; 48:133-136. 1995.
- [11] Dixon, M. F., Genta, R. M., Yardley, J. H., Correa, P., Participants in the International Workshop on the Histopathology of Gastritis, Houston 1994 Classification, grading of gastritis. The updated Sydney System. *Am. J. Surg. Pathol*; 20:1161-1181. 1996.
- [12] Ando, T., Kusugami, K., Ohsuga, M., Shinoda, M., Sakakibara, M., Saito, H., Fukatsu, A., Ichiyma, S. and Ohta, M. Interleukin-8 activity correlates with histological severity in Helicobacter pylori-associated antral gastritis. *Am. J. Gastroenterol*; 91: 1150-1156. 1996.
- [13] Yamaoka, Y., Kita, M., Kodama, T., Sawai, N., Kashima, K. and Imanishi, J. Expression of cytokine mRNA in gastric mucosa with Helicobacter pylori infection. *Scand. J. Gastroenterol*; 30: 1153-1159. 1995.
- [14] Quiding-Jaaskari, M., Lundin, B. S., Lonnroth, H. and Svennerholm, A. -M. CD4+ and CD8+ T cell responses in Helicobacter pylori-infected individuals. *Clin. Exp. Immunol*; 123: 81-87. 2001.
- [15] Glupczynski, Y. The diagnosis of Helicobacter pylori infection: a microbiologist's perspective. *Rev. Med. Microbiol*; 5:199-208. 1994.
- [16] Lage, A., P. Gogforid, E. Fauconnier, A. Burette, A., Diagnosis of Helicobacter pylori Infection by PCR: Comparison with Other Invasive Techniques and Detection of cagA Gene in Gastric Biopsy Specimens. *J. of Clin Microbiol*; 33(10):2752-2755. 1995.
- [17] Miftahussurur, M., Y. Yamaoka. Diagnostic Methods of Helicobacter pylori Infection for Epidemiological Studies: Critical Importance of Indirect Test Validation. *Biomed Res Int*; 4: 419-423. 2016.
- [18] AK-Jumaily, S., T. Essa, R., H. Muhsin, I., M. Immunological study of gastric-ulcer patients infected with Helicobacter pylori. *World J. of Pharmaceutical Research*, 4(1):320-335. 2014.
- [19] Al-Jubori, S., S. Al_Kademy, M., S. Ali, M., R. Mohamed Ali., A. S. 2016 Occurrence of Helicobacter pylori among Iraqi patients with suspected gastric ulcer: histopathological study for mucosal biopsies. *Advances in Environmental Biology*; 10(7): 224-230. 2016.
- [20] Cover, L., and M. J. Blaser. Helicobacter pylori in health and disease. *Gastroenterology*; 136(6):1863-1871. 2009.
- [21] Patel SK, Pratap CB, Jain AK, Gulati AK, Nath G. Diagnosis of Helicobacter pylori: What should be the gold standard? *World J Gastroenterol*; 20:12847-59. 2014.
- [22] Lee HC, Huang TC, Lin CL, Chen KY, Wang CK, Wu DC. Performance of Routine Helicobacter pylori Invasive Tests in Patients with Dyspepsia. *Gastroenterol Res Pract*; 13:184-889. 2013.

- [23] Gisbert JP, Calvet X, O'Connor A, Mégraud F, O'Morain CA. Sequential therapy for *Helicobacter pylori* eradication: a critical review. *J Clin Gastroenterol*; 44:313-325. 2010.
- [24] Logan, R., Walker, M., M. ABC of the upper gastrointestinal tract Epidemiology and diagnosis of *Helicobacter pylori* infection. *BMJ* ;323(20):920-922. 2001.
- [25] Shah, H., P. Shah, M. Jarag, R. Shah, P. Shah, K. Naik. Prevalence of *Helicobacter pylori* infection in gastric and duodenal lesions as diagnosed by endoscopic biopsy. *Int J Med Sci Public Health*; 5(1): 93-96. 2016.
- [26] Puetz T, Vakil N, Phadnis S, Dunn B, Robinson J. The Pyloritek test and the CLO test: accuracy and incremental cost analysis. *Am J Gastroenterol*; 92: 254-257. 1997.
- [27] Çakmak SK, Tantoglu BH, Onan D, Yorulmaz A, Tamer E, Artüz F. The frequency of *Helicobacter pylori* infection in vitiligo patients. *Pigment Int*;2:81-4. 2015.
- [28] She, C. R. ; Wilson, A. R. and Litwin, C. M. Evaluation of *Helicobacter pylori* Immunoglobulin G (IgG), IgA, and IgM Serologic Testing Compared to Stool Antigen Testing. *Clin Vaccine Immunol*; 16(8): 1253–1255. 2009.
- [29] Bimczok, D. ; Grams, J. M. ; Stahl, R. D. ; Waites, K. B. ; Smythies, L. E. and Smith, P. D. Stromal regulation of human gastric dendritic cells restricts the Th1 response to *Helicobacter pylori*. *Gastroenterology*; 141: 929–38. 2011.
- [30] Holck, S., Nørgaard, A., Bennedsen, M., Permin, H., Norn, S. and Andersen, L. P. Gastric mucosal cytokine responses in *Helicobacter pylori*-infected patients with gastritis and peptic ulcers. Association with inflammatory parameters and bacterial load. *FEMS Immunol. Med. Microbiol*; 36: 175–180. 2003.
- [31] Peek, R. M. ; Jr. ; Fiske, C. and Wilson, K. T. Role of Innate Immunity in *Helicobacter pylori*-Induced Gastric Malignancy. *Physiol Rev*; 90(3): 831–858. 2010.
- [32] Ren, Z., Pang, G., Lee, R., Batey, R., Dunkley, M., Borody, T. and Clancy, R. Circulating T cell response to *Helicobacter pylori* infection in chronic gastritis. *Helicobacter* 5, 135–141. 2000.
- [33] Eaton, K. A., Mefford, M. and Thevenot, T. The role of T cell subsets and cytokines in the pathogenesis of *Helicobacter pylori* gastritis in mice. *J. Immunol*;166, 7456–7461. 2001.
- [34] Ramis, I. B., E. P. Moraes, M. S. Fernandes, R. Mendoza-Sassi, O. Rodrigues, C. R. Juliano, C. J. Scaini, P. E. Almeida da Silva. Evaluation of diagnostic methods for the detection of *Helicobacter pylori* in gastric biopsy specimens of dyspeptic patients. *Braz J Microbiol*; 43(3):903-908. 2012.
- [35] Boklage, S. H., W. M. Allen, V. Ramamohan, D. Mladsi, T. Wang. Impact of patient adherence on the cost-effectiveness of non-invasive tests for the initial diagnosis of *Helicobacter pylori* infection in the United States. Patient preference and adherence;10:45-55. 2016.
- [36] Al-Jubori, S., S. Al_Kademy, M., S. Ali, M., R. Mohamed Ali., A. S. Emergency of *Helicobacter pylori* resistance isolates obtained from Iraqi patients suffering Acute and chronic gastritis *World J Pharm Sci*; 4(7): 18-23. 2016.

Research Article

A Comparison of efficiency of (AMP) and its derivative (AMPAA) against some pathogenic bacteria

Suzan S. Hussain

Department of biology, College of Science, Mustansiriyah University, IRAQ.

*E-mail: suzansaadi@roznamachi@yahoo.com

Article Info

Received
18/10/2016

Accepted
18/01/2017

Abstract

Eugenol (4-allyl-2-methoxyphenol, AMP), is a well known a biologically active phenolic component and essential oil from *Eugenia caryophyllata*, which widely used of Eugenol as an antiseptic and analgesic in dental care, so it is active against oral bacteria associated with dental caries and periodontal disease as well as previous studies have shown the effect of Eugenol antifungal; anti-carcinogenic; anti-allergic; anti-mutagenic activity; antioxidant and insecticidal properties, therefore it can be used in preparation of various food as a flavouring agent and cosmetic.

This study aimed to synthesize derivative new medical material 2-(4-allyl-2-methoxyphenoxy) acetic acid (AMPAA) from eugenol (4-allyl-2-methoxyphenol) (AMP) and investigate the antimicrobial activities of both AMP and derivative component (AMPAA), The minimum inhibitory concentration (MIC); minimum bactericidal concentration (MBC) and sensitivity against six pathogenic bacterial isolates: *Streptococcus. pyogens*; *Enterococcus. faecalis*; *Escherichia. coli*; *Klebsiella pneumoniae*; *Bacillus. subtilis* and *Proteus. mirabilis* with study compare the efficiency for both AMP and AMPAA on the same bacterial isolate obtained from Iraqi hospitals.

In this present study synthesize new medical material (AMPAA) from AMP by reacting sodium eugenate with sodium chloroacetic acid and prepare soluble water from eugenol and its derivative AMPAA to scanning the antimicrobial efficacy against some pathogenic bacteria isolates by two common methods; well diffusion and broth dilution methods.

Results of the present study show all bacterial isolates were sensitive to both AMP and AMPAA in low concentration except *K. pneumoniae*, also 10.0 and 5.0 µg/mL of AMP and AMPAA as MBC for bacterial isolates except *K. pneumoniae* and *P. mirabilis* that's meaning the new derivative compound AMPAA has more efficacy on six bacterial isolate than eugenol (AMP).

By using Well diffusion method all bacterial isolates were sensitive to both (AMP and AMPAA) in low concentration, but *K. pneumoniae* was killed in same concentration, so all isolates have been killed at concentrations between (10 - 50 µg/mL) of new derivative compound (AMPAA), at the same concentration of AMP were killed for *K. pneumoniae* and *P. mirabilis*, as well as all isolates have varying degrees of sensitivity towards both (AMP and AMPAA), whereas all isolates where more sensitive to AMPAA than AMP.

In conclusion, all bacterial isolate were sensitive to both AMP and AMPAA in low concentration except *K. pneumoniae*, also 10.0 and 5.0 µg/mL of AMP and AMPAA respectively conceder as MBC for bacterial isolate except *K. pneumoniae* and *P. mirabilis*, that killed in these concentration, so at the same concentration of AMP and AMPAA bacterial isolates were sensitivity by well diffusion method, whilst its killed by broth method, that's consulate broth method was best than diffusion method.

Keywords: AMP, Eugenol, 4-allyl-2-methoxyphenol, AMPAA, 2-(4-allyl-2-methoxyphenoxy) acetic acid.

الخلاصة

زيت القرنفل (4 الأليل-2-ميثوكسفينول (AMP)، من مركبات الفينولية المعروفة بفعاليتها البيولوجية وهو من الزيوت المشتقة من القرنفل، والتي تستخدم على نطاق واسع كمطهر ومسكن للعناية بالأسنان، كذلك فهو فعال ضد البكتريا التي ترافق تسوس الأسنان وأمراض اللثة، وهناك دراسات سابقة حول تأثيرها كمضاد للفطريات و مضاد سرطاني. مضاد للحساسية؛ مضادة للعوامل المطفرة. وله خصائص مضادة للأوكسدة وقاتل للحشرات (1)، وبالتالي فإنه يمكن أن تستخدم في إعداد الطعام المختلفة كمادة منكهة وفي مستحضرات التجميل (2).

تهدف هذه الدراسة إلى تصنيع مادة طبية جديدة 2- (4-الأليل-2-ميثوفينوكسيس-حمض الخليك (AMPAA) مشتقة من الأوجينول (4 الأليل-2-AMP) والتحقق من نشاطها كمضاد ميكروبي للمادتين AMP و المشتقة (AMPAA)، من خلال دراسة الحد الأدنى للتركيز المثبط (MIC)؛ و الحد الأدنى من التركيز القاتل للبكتريا (MBC) وحساسيه تجاة ستة العزلات

البكتيرية المسببة للأمراض. مع دراسة مقارنة لكفاءة كلا المادتين AMP و AMPAA على نفس العزلات البكتيرية التي تم الحصول عليها من المستشفيات العراقية.

هذه الدراسة تم اشتقاق مادة طبية جديدة (AMPAA) من AMP عن طريق تفاعل eugenate الصوديوم مع حامض الكلوروأسينيك الصوديوم وتحضير محلول مائي من المادة الأولية و المادة الثانية الجديدة التي اشتقت منها. لها قابلية للذوبان. وقد تم دراسة فعاليتها كمضاد ميكروبي ضد بعض أنواع البكتيريا المسببة للأمراض بطريقتي (الانتشار بالحفر والتخفيف المتسلسل).

وقد اظهرت نتائج الدراسة الحالية كل العزلات البكتيرية كانت حساسة لكلا المادتين AMP و AMPAA في تركيز منخفض عدا بكتريا *K. pneumoniae*، وقد وجد ان تركيزي 10.0 و 5.0 ميكروغرام / مل من AMP و AMPAA على التوالي اعتبر كتركيز ادنى قاتل للبكتريا (MBC) لكل العزلات عدا بكتريا *K. pneumoniae* و *P. mirabilis* والتي تم قتلها في هذين التركيزين، وهذا يعني أن المركب المشتق الجديد AMPAA كان اكثر فعالية على عزلات الدراسة من الـ (AMP).

باستخدام طريقة الانتشار كانت كل العزلات البكتيرية حساسة لكلا المادتين (AMP و AMPAA) في تركيز منخفض، ولكنها بنفس التركيز قد قتلت بكتريا *K. pneumoniae*، بالإضافة لذلك فان كل عزلات الدراسة قد قتلت في تراكيز تراوحت بين (10-50 ميكروغرام / مل) للمركب الطبي الجديد المشتق (AMPAA)، غير انه في نفس التركيز من AMP قتلت فقط عزلات بكتريا *P. mirabilis* و *K. pneumoniae*. في حين اعتبرت هذه التراكيز كـ MBC للعزلات الباقية المتضمنه *S. pyogenes*, *E. faecalis*, *B. subtilis* and *E. coli* وكذلك كل العزلات لها درجات متفاوتة من الحساسية تجاه كل من (AMP و AMPAA).

اظهرت نتائج الدراسة ان كل عزلات البكتيريا كانت حساسة لكلا المادتين AMP و AMPAA في تركيز منخفض عدا *K. pneumoniae*، وأيضا كان تركيزي 10.0 و 5.0 ميكروغرام / مل من AMP و AMPAA على التوالي كادنى تركيز قاتل للبكتريا لعزلات عدا *P. mirabilis* و *K. pneumoniae* حيث تم قتلها بهذه التراكيز. وان طريقة التخفيف كانت أفضل من طريقة الانتشار، وكذلك مركب مشتق جديد (AMPAA) هي أكثر تأثير على ستة عزلات بكتيرية من الأوجينول (AMP)، لذلك نوصي بدراسات مستقبلية قد يفتح طريقا جديدا في استخدام المركبات AMPAA و AMP كمضادات حيوية جديدة ضد البكتريا المرضية.

Introduction

Increasing resistance of pathogenic bacteria to many antibiotics, multidrug resistance as well as conventional chemicals were prompting the scientists to search alternative or novel sources such as plants extract and their derivatives as essential oils, that playing important role as bactericidal and bacteriostatic [3]. These activities of plants are extract and their derivatives due to have high level of phenolic derivatives [4]. Thus Eugenol, 4-allyl-2-methoxyphenol (AMP) is main constituent of essential oil obtained from commonly consumed spices such as *Eugenia caryophyllata* or *Syzygium aromaticum* (clove), molecular formula of Eugenol is $C_{10}H_{12}O_2$ with has molecular weight (164.21), as dark yellow viscous oily liquid with a strong clove flavor in normal temperatures, so its slightly soluble in water as well as easily dissolved in organic solvents [5]. This component has widely applied in dentistry, anesthetics, analgesics, anti-inflammatory agents and flavouring agents. Eugenol has been used as antibacterial against *Escherichia coli*, anti-helicobacter and antiproliferative. So, in dentistry, it is employed as an antiseptic, disinfectant and also widely used as an analgesic, as well as in cosmetic and food products as flavoring, antimicrobial, and antioxidant agent [6].

In addition to these antioxidant properties, it protects neurons in culture from toxic events. It has activities of anti-convulsive and hypothermic

agent [7]. Zinc oxide-eugenol materials have been developed for utilization in number of dental applications; they are most widely employed as antibacterial and palliative agent in treatment of the lesions [8].

antiseptic, disinfectant and also widely used as an analgesic, as well as in cosmetic and food products as flavoring, antimicrobial, and antioxidant agent [Hattori *et al.*, 1986].

So eugenol has limit to stabilization and dispersion in aqueous food systems, which causing increasing concentration required for antimicrobial functions, which may lead to phase separation and negatively affect the quality of food [9].

A derivative of eugenol was prepared by reacting sodium eugenate with sodium chloroacetic acid to give, 2-(4-allyl-2-methoxyphenoxy)acetic acid (AMPAA), this derivative was characterized by the available elemental analysis, UV-visible, Infrared absorption spectrophotometry, 1H and ^{13}C NMR spectrometric techniques [10].

Materials and Methods

A- Material:

Sodium hydroxide, Eugenol, sodium chloroacetate from BDH, UK, Mueller-Hinton agar (Difco), and 95 % methanol from Merck, Germany.

B- Instrument:

Melting points were determined with Stuart Scientific melting point SMP₁, England melting

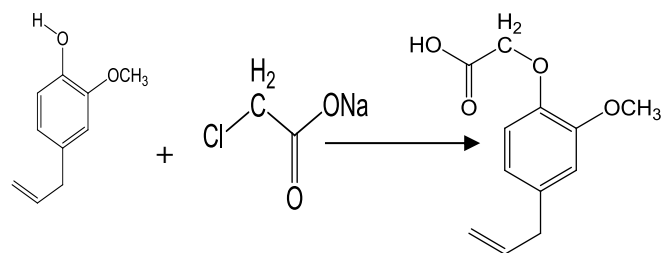
point apparatus. The electronic absorption spectra were recorded in 95 % methanol by using Varian 100 Conc. UV-visible Spectrophotometer with 1.0cm quartz cell immediately after preparing the solutions in range 200-800 nm. Infrared spectra of the compounds were carried out by using KBr pellets in the range of 400-4000 cm^{-1} on Fourier transform Infrared spectrophotometer. The ^1H and ^{13}C NMR spectra were recorded on 300 MHz Bruker DMK-500 NMR Spectrometer by employing TMS as internal standard. Elemental analysis of C, H, and N of complexes were determined by micro analytical methods by Carlo-Erbamicroanalyser (Shimadzu model 8300).

C-Preparation of 2-(4-allyl-2-methoxyphenoxy) acetic acid (AMPAA):

Eugenol (5.0 g, 30 mmol) dissolved in a solution of NaOH (1.4 g., 33 mmol) in 75 mL 95 % ethanol until a clear solution was obtained. The solution was treated drop wise while stirring with a solution of sodium chloroacetate (3.85, 33 mmol) in 30 mL distilled water. The mixture was refluxed for three hour, and cooled to ambient temperature. A solution of 1:1 hydrochloric acid was added slowly until the pH of the solution was below 2.0. Glossy needles of the product were formed after induction time of about 5.0 minutes, and the mixture was left overnight at 4°C. The crystals were filtered over ceramic media, washed with 1:1 of ethanol-diethyl ether mixture, and then dried at 60°C for 3 hours to give a solid crystals m. p 71.5°C, 4.42 gm (65%) of the total product. Found: C, 64.54, H, 6.40 (Theoretical: C, 64.84; H, 6.35). UV-visible λ_{max} (H_2O): 280 nm, FT-IR (KBr disk): 1597 cm^{-1} (m, Ar); 1250-1280 (s, Ar-O-CH₂); 3100-3500 (s, COOH), 1650-1650 (m, C=C); 3000-3100 (m, Ar stretch.). ^1H NMR (300 MHz, CDCl_3): δ 3.25 (2H, d, $J = 6.2$ Hz, CH₂); 3.9 (3H, s, OCH₃); 5.09 (2H, m, =CH₂); 5.50 (2H, s, CH₂-O); 5.91 (1H, m, =CH-); 6.6 - 6.90 (3H, aromatic protons).

Equimolecular quantities of eugenol and sodium chloroacetate react readily to produce the acetic acid derivative of eugenol according to the following equation: The product of 2-(4-allyl-2-methoxyphenoxy) acetic acid was identified with available analytical technique; elemental analysis for C, H, UV-visible, Infrared absorption spec-

trophotometry, ^1H and ^{13}C NMR spectrometric techniques.



Eugenol (AMP) chloroacetate

2-(4-allyl-2-methoxyphenoxy)acetic acid (AMPAA)

D- Bacterial strains:

Test pathogenic bacteria used in this study were stock cultures of standard and local isolates obtained from Al-Yarmuk Teaching Hospital, Baghdad medical City Teaching Laboratories, and Health Center Laboratories in Baghdad. Bacterial isolate as gram-positive bacteria include: *S. pyogenes*, *E. faecalis*, *B. subtilis* and Gram-negative bacteria as: *E. coli*, *K. pneumoniae* and *P. mirabilis*. Cultures of these bacteria were grown in Mueller-Hinton broth at 37°C and maintained on slants of nutrient agar at 4°C. The isolates were identified and checked for their purity on the basis of the following characteristics: morphology of the colonies by microscopical examinations; Gram's stain [11] morphological feature on culture media, and biochemical tests [12] as well as Vietk system.

Antimicrobial activity assay:

Antimicrobial activity was measured by two methods; well diffusion method [13] and broth dilution method [14]. In the well diffusion method, a sterile 8 mm diameter stainless steel borer cylinders were used to make wells in plates of Mueller-Hinton agar, which was spreaded superficial with 100 μL of bacteria at logarithmic plan at a density adjusted to a 0.5 McFarland turbidity standards (10^8 CFU/ mL). The wells were filled with 100 μL of sterilized eugenol (AMP) or its derivative solution 2-(4-allyl-2-methoxyphenoxy) acetic acid (AMPAA) solution at working concentrations of 50 $\mu\text{g}/\text{mL}$. The following dilution were prepared and used for broth methods; 0.1, 0.5, 1.0, 5.0, 10.0, and 25.050

µg/mL. plates were then incubated for 24 hr at 37°C. The results were recorded by measuring zones of growth inhibition (in mm).

Broth dilution method procedure was used to measure Minimal inhibition concentration (MIC) and minimum bactericidal concentration (MBC) of the test solutions. In these experiments, 0.4mL of a suspension containing 1×10^8 CFU/ mL was added to 3.6 mL of susceptibility test broth containing serial two fold dilutions of eugenol and its derivative 2-(4-allyl-2-methoxyphenoxy) acetic-acid (AMPA) in glass test tubes. All tubes were incubated at 37°C for 24 hr before being read, the MIC was considered the lowest concentration of the sample that prevented growth. MBC_s were determined by subculturing, 10 µL from each negative tube and from the positive growth control, MBCs were defined as lowest concentration yielding negative subcultures or only one colony. All samples were examined in duplicate in three separate experiments.

Results and Discussion

By using Broth method the MIC and MBC of AMPA and AMPAA against six pathogenic bacteria were presented in Table 1 and Table 2, all bacterial isolate were sensitive to both AMP and AMPAA at concentration 0.1 µg/mL except *K. pneumoniae* was killed at same concentration, as well as all bacterial isolates were sensitive to 0.5 µg/mL whilst this concentration consider as MIC_s for two isolate : *K. pneumoniae* and *P. mirabilis*. So based on these results all bacterial isolate were killed at concentration range 10.0 to 50.0 µg/mL of AMPAA and same results for same concentration of AMP except *S. pyogenes*, *E. faecalis*, *B. subtilis* that MBC in 10 µg/mL, as well as the concentration (10.0 and 5.0) µg/mL of AMP and AMPAA respectively concenter as MBC for bacterial isolate except *K. pneumoniae* and *P. mirabilis* that killed in these concentration are showed in table (1) meaning the new derivative compound (AMPAA) are more effect on six bacterial isolate than eugenol (AMP).

By using well diffusion method all bacterial isolates were sensitive to both AMP and AMPAA in concentration 0.1 µg/mL except *K. pneumoniae* was killed so all bacterial isolate were sensitive to 0.5 µg/mL whilst this concentration were MIC_s for two isolate (*K. pneumoniae* and *P. mirabilis*). In addition, current results showed all isolates have been killed concentrations of be-

tween (10-50) (µg/mL) of new derivative compound (AMPAA), at the same concentration of AMP were killed for *K. pneumoniae* and *P. mirabilis* whilst considered as MBC for other isolate such as *S. pyogenes*, *E. faecalis*, *B. subtilis* and *E. coli* in Table 2.

Results summarized in both tables 1 and 2 show that all isolates have varying degrees of sensitivity towards both AMP and AMPAA, however at the same time all isolates were more sensitive to AMPAA than AMP, as well as results in both table 1 and 2 appearance at the same concentration of AMP and AMPAA showed sensitive bacteria by well diffusion method, whilst it was killed by broth method, that's consulate broth method is best than diffusion method.

The results of Minimum inhibitory concentration (MIC) showed that *S. pyogenes*, *E. faecalis*, *B. subtilis* and *E. coli* were more sensitive to inhibition of eugenol(AMP) and (AMPAA) at concentration between (0.1 to 1.0) (µg/mL) (Table 1) while its killed in both concentration 25, 50 (µg/mL).

These results of current study is fully compatible with Thosar, et al. (2013) who showed that AMP active at the lowest concentration against many bacteria as *S. aureus* MIC (0.4 µl/mL) while 1 µl/ml of MIC for both *E. coli* and *E. facelis* [15]. So Walsh *et al.*, showed in his study the MIC and MBC of eugenol against the bacteria tested have been proved to be as low concentration [16]. The determination of MIC and MBC of eugenol was necessary to induce death cells at ranging concentrations of these agents.

Also these results of this study shown all isolates have varying degrees of sensitivity towards both (AMP and AMPAA), this difference in sensitivity were study by many researchers as Benniset *al.*, (2001) who showed in his study the eugenol (AMP) exerts causing different envelope damage ,this difference may be explained by the fact that the envelopes of gram negative bacteria and gram positive bacteria do not have the same structure [17], so eugenol effect on lipid of cell membrane for both Gram negative positive pathogenic bacteria [18].

As well as Burt has shown in his studied the mechanical effect of eugenol in degraded bacterial cell wall, damages plasma membrane and membrane protein [8 Burt, 2004], because AMP containing phenol compound which disruption bacterial membrane and causing high leakage of pro-

tein content [14 ; 16 and 18], so the hydrophobicity of eugenol is play as important factor of antibacterial activity via separate lipid from mitochondria and cell membrane causing change in structure as well as increasing the penetrability of the cell membrane [5].

This study was the first time in the world and in Iraq which derivative 2-(4-allyl-2-methoxyphenoxy) acetic-acid (AMPA) by the researcher from Eugenol (AMP) which its known composition and chemical and their effects, so the researcher has found necessary of experimental study on some pathogenic bacteria and comparison effect with AMP.

Conclusions

In conclusion, all pathogenic bacterial isolate were sensitive to both (AMP and AMPAA) in low concentration except *K. pneumoniae*, so (10.0 and 5.0) µg/mL of AMP and AMPAA, respectively considered as Minimum Bactericidal Concentration (MBC) for bacterial isolate except *K. pneumoniae* and *P. mirabilis*, that killed in these concentration, that meaning the new derivative compound (AMPAA) are more effect on six bacterial isolate than eugenol (AMP).

By using well diffusion method all bacterial isolate were sensitive to both (AMP and AMPAA) in low concentration, but *K. pneumoniae* was killed in same concentration. So all isolates had killed a concentration of between (10-50 µg/mL) of new derivative compound (AMPAA), In the same concentration of AMP were killed for *K. pneumoniae* and *P. mirabilis* although considered as MBC for other isolate as *S. pyogenes*, *E. faecalis*, *B. subtilis* and *E. coli*, whilst all isolates have varying degrees of sensitivity towards both AMP and AMPAA, But at the same time all isolate showed more sensitive to AMPAA than AMP. So at the same concentration of AMP and AMPAA showed sensitivity bacteria by well diffusion method, but it's killed by broth method, that's consulate broth method was best than diffusion method.

References

[1] Gayoso, C. W. ; Lima, E. O. ; Oliveira, V. T. ; Pereira, F. O. ; Souza, E. L. and Lima, I. O., (2005), "Sensitivity of fungi isolated

from onychomy-cosisto *Eugenia cariophyllata* essential oil and eugenol. ", *Fitoterapia*, 76:247-9.

- [2] Pisano, M. ; Pagnan, G. ; Loi, M. ; Mura, M. E. ; Tilocca, M. G. ; Palmieri, G. ; Fabbri, D. ; Dettori, M. A. ; Delogu, G. ; Ponzoni, M., (2007). "Antiproliferative and pro-apopto. ", *Appl. Environ. Microbiol.*, 68 (4): 1561-68.
- [3] Abad, M. J. ; Ansuategui, M. and Bermejo, P. (2007). "Active antifungal substances from natural sources. ", *Archivoc*, (207):116–145.
- [4] Cosentino, S. ; Tuberoso, C. I. ; Pisano, B. ; Satta, M. ; Mascia, V. ; Arzedi, E. and Palmas, F., (1999), "In-vitro antimicrobial activity and chemical composition of Sardinian *Thymus* essential oils. ", *Lett. Appl. Microbiol.*, 29(2): 130-135.
- [5] Xiaojun, K. ; Xiwang, L. ; Jianyong, L. I. and Yajun, Y. (2014). Advances in Pharmacological Research of Eugenol. *Curr Opin Complement Alternat. Med.* ; (1):8-11.
- [6] Saravana K., J. and Eko, S. (2012). Antiproliferative and Molecular Mechanism of Eugenol-Induced Apoptosis in Cancer Cells, *Molecules*, 17.
- [7] Wie, M. B. ; Won, M. H. ; Lee, K. H. ; Shin, J. H. ; Lee, J. C. ; Suh, H. W. ; Song, D. K. and Kim, Y. H. (1997). Eugenol protects neuronal cells from excitotoxic and oxidative injury in primary cortical cultures. *Neurosci Lett.* 1997 Apr 4;225(2):93-6.
- [8] Burt, S. A. and Reinders, R. D., 2003. Antibacterial activity of selected plant essential oils against *Escherichia coli* O157:H7. *Letters in Applied Microbiology* 36 (3), 162– 167.
- [9] Burt, S. (2004). "Essential oils: Their antibacterial properties and potential applications in foods a review. ", *Int. J. Food Microbiol.* ; 94(3): 223-53.
- [10] Chen ,H; Jin ,X ; Li ,Y and Tian,J. (2016). Investigation into the physical stability of a eugenol nanoemulsion in the presence of a high content of triglyceride; *RSC Adv.* ,93,(6):91060-91067.



- [11] Hamri ,S ; Rhazri,K. ; Hafid,A. ; Ouchetto,H. ; Hajbi,Y. and Khouili,M. (2013). Clove (*Eugenia Caryophyllata*) Extraction and Synthesis of new Pyrazole Derivatives from Eugenol, *Global Journal of Science Frontier Research Chemistry*, 13 (7): 1-7.
- [12] Sayyah, M. ; Valizadeh, J. and Kamalinejad, M., (2002), "Anticonvulsant activity of the leaf essential oil of *Laurusnobilis* against pentylenetetrazole- and maximal electroshock-induced seizures. ", *Phytomedicine* 9, 212.
- [13] Won, M. H. ; Lee, J. C. ; Kim, Y. H. ; Song, D. K. ; Suh, H. W. ; Oh, Y. S. ; Kim, J. H. ; Shin, T. K. ; Lee, Y. J. and Wie, M. B. (1998). Postischemic hypothermia induced by eugenol protects hippocampal neurons from global ischemia in gerbils, *Neurosci. Lett.*, 254, 101.
- [14] Lambert, R. J. ; Skandamis, P. N. ;Coote, P. J. and Nychas, G. J., (2001), "A study of the minimum inhibitory concentration and mode of action of oregano essential oil, thymol and carvacrol. ", *Appl. Microbiol.*, 91(3):453-462.
- [15] Ultee, A. ;Bennik, M. H and Moezelaar, R., (2002). "The phenolic hydroxyl group of carvacrol is essential for action against the food-born pathogen *Bacillus cereus*. ", *Appl. Environ. Microbiol.*, 68 (4): 1561-68.
- [16] Thosar, N. ; Basak, S. ; Bahadure, R. N. and Monali, R. (2013). Antimicrobial efficacy of five essential oils against oral pathogens: An *in vitro* study., *Eur J. Dent.*; 7(Suppl 1): S71–S77.
- [17] Walsh, S. E. ; Maillard ,J. Y. ; Russel, A. D. ;Catrenich, C. E. ; Charbonneau, D. L. and Bartolo, R. G. (2003). Activity and mechanisms of action of selected biocidal agents on Gram-positive and –negative bacteria, *J. Appl. Microbiol.*, 94: 240-247.
- [18] Bennis, S. ; Chami, F. ; Chami, N. ; Rhayour, K. ; Tantaoui-Elaraki, A. and Remmal, A., (2001), "Eugenol induces damage of bacterial and fungal envelope. ", *Moroccan J. Biol. I*, 33-39.
- [19] Oyedemi, S. O. ; Okoh, A. I. ; Mabinya, L.; Piro9 Chenva, V. G., and Afolayan, A. J., (2009). "The proposed mechanism of bactericidal action of eugenol, α -terpineol and γ -terpinene against *Listeria monocytogenes*, *Streptococcus pyogenes*, *Proteus vulgaris* and *Escherichia coli*. ", *African Journal of Biotechnology*, 8 (7):1280-1286.

Research Article

Harvesting of *Chlorella sp.* by Co-cultivation with Some Filamentous Fungi

Rana H. Hameed Al-Shammari

Department of Biology, College of Science, Mustansiriyah University, IRAQ

*Email: rana_ecology@yahoo.com

Article Info

Received
08/11/2016

Accepted
18/01/2017

Abstract

Algae play a major role as straight producers of biofuels, so expansion of a new harvesting-technology is important to achieve economic feasibility of biofuel production from algae. Fungal pelletization-assisted. Microalgal harvesting has emerged as a new research area for decreasing the harvesting cost and energy inputs in the algae-to-biofuel method. The present study tried to optimize process circumstances as (substrate inputs, process time and pH). Through choice of a robust fungal strain. Four fungal strains (*Aspergillus terreus*, *Trichoderma sp.*, *Mucor sp.* and *Rhizopus sp.*) were screened for their pelletizing efficiency in fresh/supplemented Chu-10 with selected media nutrient (glucose, nitrogen and phosphorous). Results showed that *Aspergillus terreus* was the most efficient strain for pelletizing in the nutrient supplemented Chu-10 with its neutral pH (7) and acidic pH (5). Stimulatingly, *A. terreus* was capable to harvest nearly 100 % of the *Chlorella sp.* cells (1×10^6 spore/ml at optical density (OD) approximately 2.5 initial working algal concentration) within only 24 h. at supplementation of (10 g/l glucose, 2.5 mg/l aNH_4NO_3 and 0.5 mg/l mK_2HPO_4) also performed well at lower glucose level (5 g/l) can also result in similar harvesting but its need relatively higher incubation time. The procedure kinetics in term of harvesting index (H. I) as well as the variation of residual glucose and pH with time was also studied. The mechanism of harvesting process was studied through microscopic examination. *A. terreus* strain investigated in this study could emerge as an efficient, sustainable and economically viable tool in microalgae harvesting for biofuel production and time conservation.

Keywords: Co-cultivation, *Chlorella sp.*, Harvesting, Filamentous fungi.

الخلاصة

تلعب الطحالب دوراً رئيسياً كمنتج مباشر للوقود الحيوي، لذلك يجب تطوير تكنولوجيا حصاد جديدة ضرورية لتحقيق الجدوى الاقتصادية لإنتاج الوقود الحيوي من الطحالب لذا برز دور الفطريات لحصاد الطحالب الدقيقة كساحة أبحاث جديدة لتقليل تكاليف الحصاد في إنتاج الطحالب للوقود الحيوي. انجزت الدراسة الحالية لتحسين ظروف التفاعل (المغذيات الإضافية، وزمن العملية ودرجة الحموضة). اختبر كفاءة أربع عزلات فطرية لحصاد الطحالب وهي *Trichoderma sp.*, *Aspergillus* *Rhizopus sp.*, *sterreus*, *Mucor sp.* : إذ زرعت في وسط Chu-10 الغير محور والمحور باضافة (كلوكوز 10 غرام لتر، نيتروجين 2.5 ملغم لتر، فوسفات 0.5 ملغم لتر) تم اختيار العزلة الأقوى في هذه العملية وهي *A. terreus* إذ أظهرت كفاءة حصاد مقارنة لنسبة 100% بعد 24 ساعة من الحضانة في الوسط المحور المتعادل (درجة حموضة 7) وفي الوسط الحامضي (درجة حموضة 5) إذ زرع العالق الفطري بتركيز 1×10^6 سبور/مل مع عالق الطحالب ذو الكثافة الضوئية ~ 2.5 . تم دراسة معامل الحصاد مع التراكيز المتبقية من الكلوكوز ودرجة الحموضة خلال فترة الحضانة إذ أظهر الفطر *A. terreus* كفاءة حصاد جيدة بتركيز كلوكوز واطيء (5 غرام لتر) لكنه يحتاج فترة حضانة أطول. تم دراسة ميكانيكية هذه العملية تحت المجهر الضوئي المركب. أظهر الفطر *A. terreus* كفاءة عالية في استخدامه كأداة مجدية في حصاد الطحالب لإنتاج الوقود الحيوي باقل كلفة وعدم هدر الوقت.

Introduction

The limitation of non-renewable energy supplies and the serious threat to the environment, alternative energy sources based on biomass appear increasingly attractive [1]. Several candidates appeared to replace the current energy supplies, with no more pollution [2]. Recently microalgae

gained great attention as one of the most promising renewable energy sources [3].

Microalgae produce much larger amounts of "biofuels" in a shorter time than other sources depend on plant wastes and seeds. However, there are several obstacles impeding algae-based biofuel production, from these complica-

tions: microalgae cultivation, harvesting process which contributes to substantial cost and energy demand [4].

The current harvesting approaches as sedimentation, centrifugation, filtration and flocculation had low efficiency due to small sizes and unicellular microalgae [5], thus we need novel harvesting processes.

In nature, associations between microbes particularly in aquatic habitats. Free living algae and fungi coexist in the same habitat without direct structural contact between them, however the physiology and ecology of algal-fungal associations found in freshwater in which algae live as epiphytic on fungi which could be considered a kind of artificial lichen [6], so pelletization characteristic of filamentous fungi could be utilized to harvest microalgae [7].

Recent studies indicate that the pelletization characteristic of filamentous fungi as *Aspergillus oryzae* had a wanted harvesting effect on *Synechocystis* sp., though *Rhizopus oryzae* had no effect [8]. other studies revealed that co-pelletization of *Chlorella vulgaris*. with filamentous fungi could improve biomass production [9]. This study aimed to achieve the following objectives: (1) Screening for the efficient fungal isolate for pelletization in chu-10; (2) exploring the usability of chu-10 for fungal pelletization; (3) selecting a strain with pelletization ability under wide range of pH; and (4) investigating the harvesting kinetics and mechanism (5) reducing the time and glucose inputs required for achieving complete harvesting.

Materials and Methods

Microorganisms isolates and Growth Media

Four filamentous fungal strains, *Aspergillus terreus*, *Trichoderma* sp., *Mucor* sp. and *Rhizopus* sp. were collected from domestic wastewater. (Al-Jaesh canal-Baghdad), and streaked straight on potato dextrose agar (PDA) plates by applying the method designated by [10].

The isolated fungal strains were tested for pellets formation ability by cultivating spores of con-tender strains in 100 ml of PG broth which consist of (4 peptone and 6 glucos g /l for each) and pH 6.0, those which could form pellets were further identified based on mycelia and spores morphological analysis under the microscope and compound- secretion ability grown on the PDA agar plates, depending on the taxonomic key

[11].

Chlorella sp. isolated from Al-Mustansiriyah University garden by Patterson Method [12]. Algal strain identified by using an optical microscope according to [13], this strain had been stably cultivated in our lab under both autotrophic (cultured in chu-10 media) and mixotrophic with (modified chu-10 by adding 10 g /l glucose) modes.

Screening of Pellet Forming Fungal Strains in chu-10 media (PFF)

The method for screening of PFF described by previous study [14], experiments were carried out in 250 ml conical flasks with 100 ml working volume. Two weeks-old *Chlorlla* sp. culture with optical density of ≈ 2.5 at 680 nm) was used as inoculum (10 % v/v). Flasks were inoculated aseptically with fungal spore suspension containing $\approx 1.0 \times 10^6$ spores/ml at inoculum size of (2% v/v), then incubated under shaking (150 rpm) in a bench top orbital shaker at 30°C for 72 h to achieve pelletization. The growth and pelletization were recorded with the visual observations. The chu-10 medium was supplemented with (10g/l glucose) in order to provide carbon source to fungi.

In second set of experiments, glucose and nitrogen (as NH_4NO_3 , 2.5 mg/l) was added to the chu-10 media. The third set of experiment was accomplished with supplementation of phosphate (K_2HPO_4 , 44 0.5 mg/l) in order to adding the glucose and nitrogen with adjusted pH (≈ 6.8) was tested for fungal growth and pelletization. All above flasks were then inoculated and incubated under shaking (150 rpm) at 30 °C for 72 h.

Fungal-algal Pelletization

After the optimization of fungal pelletization process in supplemented chu-10 media, the next study investigated the harvesting of *Chlorlla* sp. by fungal pelletization. *Chlorella* sp. was cultivated in a 250-ml flask using 100 ml sterile chu-10 medium at 25°C. *Chlorella* sp. culture (two weeks-old; $\text{OD}_{680} \approx 2.5$) was used as inoculum at (10% v/v). *Chlorella* sp. cultivation was under light intensity of 4.5 Klux with dark/light cycle of 12 h. After two weeks of growth, flaks (containing microalgal broth) were substituted with optimized media inputs (glucose, NH_4NO_3 and K_2HPO_4) and inoculated with selected fungal spores' suspension (1×10^6 spore/ml). The kinetics of fungal pelletization assisted *Chlorella* harvest-

ing was studied by withdrawing samples after every 3 h for determination of residual suspended algal cells by measuring optical density at 56808 nm (OD_{680}). The harvesting efficiency of the selected fungus was calculated using the harvesting index (HI) calculated as:

$$HI = \left(1 - \frac{\lambda_t}{\lambda_0}\right) \quad (1)$$

Where λ_0 is the OD_{680} of the initial microalgal culture and λ_t is the OD_{680} of the residual algal cells at time t. harvesting efficiency (%) was estimated using the following equation:

$$\text{Harvesting efficiency (\%)} = HI \times 100 \quad (2)$$

Residual glucose concentration was also determined in order to measure the glucose utilization rate of the fungal strains during the algal harvesting process. The residual glucose in the broth was estimated using the "phenol- sulphuric acid method [15] briefly, the powdered biomass (100 mg) was hydrolyzed with 5 ml of 2.5 N hydrochloric acid in boiling water bath for 3 h, cooled at room temperature and neutralized with solid sodium carbonate. After neutralization, an aliquot of 0.1 mL was pipette out in a clean test tube and diluted to 1 ml. After dilution, 1 mL phenol solution and 5 ml of 36N sulfuric acid were added, well mixed and cooled to 25 °C in a water bath.

The optical density of the samples was measured at 490 nm and the total carbohydrates were than calculated using standard calibration curve. Changes in pH were also monitored using pH meter.

Effect of Variation in Glucose Concentration on Fungal–algal Pelletization

According to the hypothesis that fungus can use microalgal biomass as carbon source, attempts were made to decrease the glucose inputs during fungal assisted microalgal harvesting. Depending on the method that achieved by [16], glucose concentration was lowered to 5 and 2.5 g/l, while NH_4NO_3 and K_2HPO_4 concentrations were the same as used previously. High glucose level (15

g/l) was also tested to check if it can further speed up the algal harvesting process. Whenever needed sterile distilled water was used for diluting to maintain the initial OD_{680} at ≈ 2.5 .

The HI and efficiency of algal harvesting through fungal pelletization process was then estimated depending on the (Equation 2).

Mechanism of Fungal Pelletization-Assisted Microalgae Harvesting

The changes in the color of the culture, and the aggregations of suspended *Chlorella* sp. cells in the culture, were monitored. So, to understand the interaction of algae with fungal spores and mycelium, samples from experimental flasks were collected every three hours and visualized under optical microscope (Olympus compound) with objective lenses of 40 \times magnification.

Statistical Analysis

All the tests were achieved in triplicates and results presented here are either mean of triplicate reported as mean \pm standard deviation or with error bars.

Results and Discussion

Screening of Efficient (PFF) in the initial run with fresh chu-10 media without glucose supplementation, it was showed that chu-10 media alone is unable to support growth of any fungal strain. Hence, the glucose supplemented chu-10 media was used for further studies. The pelletization ability of the tested fungal strains in glucose supplemented chu-10 media at different time intervals is shown in (Table 1).

With glucose supplementation, *A. terreus*, *Trichoderma* sp. showed good pelletization within 12h, *Mucor* sp. and *Rhizopus* sp. started to grow within 24h. However, despite the good growth of *Mucor* sp. and *Rhizopus* sp. was not able to pelletize even after 48h (Table 1).

According to microscopic examination, it was observed that the pellets formed were uniform (within fungal strains) with pellet size varying from 0.5 to 1.2 mm, so *A. terreus* was the best.

Table 1: Occurrence of fungal growth and pelletization in fresh /supplemented chu-10 media with glucose (10 g/l), NH_4NO_3 (2.5 mg/l) and K_2HPO_4 (0.5 mg/l).

Time (h)	fresh chu-10 media				Supplemented chu-10 media												
					Glucose (10 g/l) only				Glucose+ NH ₄ NO ₃				Glucose+ NH ₄ NO ₃ +K ₂ HPO ₄				
	At	Tri.	Muc.	Rhi.	At	Tri.	Muc.	Rhi.	At	Tri.	Muc.	Rhi.	At	Tri.	Muc.	Rhi.	
0	-	-	-	-	-	-	-	-	-	-	-	-	-	-	-	-	-
12	-	-	-	-	-	-	-	-	-	-	-	-	-	+	-	-	-
24	-	-	-	-	-	-	-	-	-	-	-	-	-	+	+	G	G
36	-	-	-	-	-	-	-	-	-	-	-	-	-	+	+	G	G
48	-	-	-	-	-	-	-	-	+	-	-	-	-	+	+	G	G
60	-	-	-	-	-	-	-	-	+	-	-	-	-	+	+	G	G
72	-	-	-	-	-	-	-	-	+	+	-	-	-	+	+	G	G

"+" growth with pelletization, "-" no growth, "G" growth without pelletization.

At=*Aspergillus terreus*, Tri. =*Trichoderma* sp., Muc. =*Mucor* sp., Rhi. =*Rhizopus* sp.

Moreover, glucose level of 10 g/l was found to be suitable for proper pelletization of selected fungal strains grown in chu-10. Based on the screening studies, the selected PFF was then tested for growth and pelletization on chu-10 media. In the first set of experiments, chu-10 media (with 10 g/l) was used as nutrient source for fungal pelletization. Interestingly, no pelletization or growth was observed in any flask with fresh chu-10 media (Table 1), even up to extended incubation period of 72 h (table 1). The causes for this could be either (1) the neutral pH of the chu-10 media (≈ 7) or (2) absence of the basic nutrients (N and P) other than glucose, as prolonged cultivation of microalgae in chu-10 media results in utilization of nutrients as well as shift in pH towards alkaline range. At 2.5 and 0.5 mg/l as NO₃³⁻ and PO₄³⁻, respectively, further confirmed the hypothesis of neutral limitation in chu-10 media. Supplementation with NH₄NO₃ and glucose in chu-10 media also did not stimulate the fungal growth and pelletization (table 1) these results agreed with [17] informed that *Rhizopus oryzae* had fast and well pelletization ability when carbon was supplemented to the broth media during co-cultivation with algae, suggesting that organic carbon have profound impact on fungi growth and cell pelletization of filamentous fungi species. Only *A. terreus* showed growth as well as pelletization but after 48 h. Moreover, pelletization in the case of *Trichoderma* sp. was observed in 72 h. The biomass and pellets obtained in both the cases were relatively small as compared with that obtained in fresh chu-10 me-

dia supplemented with same glucose level. However, addition of K₂HPO₄ with NH₄NO₃ and glucose resulted in dramatically enhanced growth and pelletization of the *A. terreus* as fungal pellet were observed within 12 h, *Trichoderma* sp. observed after 24 h (table 1). However, with rest fungal strain, there were growth and no pelletization was observed, even at 72 h. These results established the significance of particular combination of nutrients for fungal growth and pelletization. It is not worthy that in previous attempts on fungal-assisted microalgae harvesting, addition of any inorganic nutrients (N and P) was not reported [18, 19]. At the end of the exponential phase of microalgal growth, no primary nutrients might be available in the chu-10 medium. Thus, it is very unlikely for the fungal strains to grow and pelletize without the addition of primary nutrients along with glucose, as confirmed with current observations.

Such nutrient limitation was possibly not encountered in the study conducted by [20] as fungus was cocultivated with microalgae in nutrient-rich fresh medium. Similarly to [21] utilized pre-cultured fungus (in nutrient medium) to harvest microalgae and hence did not required further addition of any primary inorganic nutrients. Nevertheless, in order to develop a realistic and economically competent harvesting protocol, the availability of data on minimum nutritional demand for fungal pelletization is must. In the present study, only *A. terreus* was able to efficiently pelletize in glucose and nutrient supplemented chu-10, followed by *Trichoderma* sp. with rela-

tively delayed and poor pelletization. No or very little pelletization (and growth) of other tested PFF could be attributed to their inability to survive and pelletize under unfavourable (\approx neutral pH) growth conditions further strengthen the hypothesis that the pH has vital role in fungal growth and pelletization. Similarly [19] also observed the crucial role of pH in fungal pelletization-assisted algal harvesting. However, there is no studies reported earlier on fungal-assisted microalgal harvesting could establish fungal pelletization and harvesting at alkaline pH. However, in the present study, *A. terreus* showed remarkable behavior of ample growth and fast pelletization at the actual pH (\approx 7) of Chu-10. Hence, the growth and pelletization of *A. terreus* was unaffected with variation in pH. The versatile nature of this fungal strain with respect to growth and contaminant removal at various pH has been previously reported by [22, 23]. The acid- and alkali-tolerant characteristics have rendered this organism equally capable of treating acidic electroplating effluent [24] and alkaline textile effluent [22] without the need of any pH adjustment. In this study, the ability of *A. terreus* to pelletize under neutral pH for algal harvesting has been established. Therefore, it can be concluded that *A. terreus* has high potential for microalgal harvesting at any pH, which further strengthens the applicability of this strain at commercial scales. Therefore, *A. terreus* was selected as the most efficient PFF for further studies.

Harvesting Microalgae Using Selected PFF Nutrient supplementation and spore inoculation resulted in an immediate pH drop of chu-10 from initial value of 7 to 6.5 this decline in pH due to the fungal growth, filamentous fungi grow fast and show compound performance when suitable organic carbon is supplied in the medium [17], pH of the chu-10 medium after fungal assisted micro algal harvesting decreases during incubation period and the final pH values were increased as in Table 1, these results confirm the harvesting efficiency was not pH-dependent, unlike previous studies [25, 26] reported that low pH supports micro algal harvesting by fungi. The culture pH is possibly an important factor for the pelletization of fungal spore, but not for the adhesion of *Chlorella* sp. cells to the surface of the

fungal pellet [25]. Significant harvesting phenomenon was observed during the 24 h observation period.

The variation in efficiency of fungal assisted microalgae harvesting process (in terms of HI), residual glucose and pH with time is shown in (Table 2). The fungal assisted micro algal harvesting started within the first 3 h with (\approx 20 % glucose utilization). The harvesting continued at very fast rate up to 12 h (\approx 75 % of glucose utilization) with harvesting efficiency of more than 80 % during this period. After 9 h, harvesting process as well as the glucose utilization continued but at relatively slower rate and resulted in more than 66 % harvesting within 18 h table 2. Eventually, up to 100 % harvesting of microalgal cells was recorded within 24 h with utilization of 86 % of the added glucose (table 2), these results as compared with previous studies on co-cultivation of fungi with microalgae [20] reported about 60 % harvesting of *Chlorella vulgaris* cells in 72 h of co-cultivation system using pre-cultured *Aspergillus niger*. similarly [25] stated the best harvesting of *C. vulgaris* in 418 h at high glucose level (260 g/l) with *Aspergillus* sp.



Figure 1: pictorial illustration of various stages of microalgal-fungal pellet formation at different time intervals. A: *Chlorella* sp. culture at 0 time, B: co-culture after 6 h, C: co-culture after 18 h D: pellet on completion of harvesting after 24 h.

Table 2: Variation in pH, Residual glucose and harvesting ratio (%) and with time (h). data for pH and Residual glucose as (Mean \pm SD).

Incubation time(h)	pH	Residual glucose concentration (g/l)	Harvest ratio (%)
0	6.8 \pm 0.8	10 \pm 0.7	0
3	5.7 \pm 0.1	8.1 \pm 0.18	20
6	4.8 \pm 0.2	5.2 \pm 0.3	41
9	5 \pm 0.8	4.3 \pm 0.3	73
12	5 \pm 0.7	4.1 \pm 0.2	78
15	5.3 \pm 0.2	3.9 \pm 0.1	80
18	5.8 \pm 0.9	3.8 \pm 0.2	90

21	5.6±0.2	3.2±0.1	93
24	6.9±0.1	3.1±0.5	100

As shown (Figure 1) the initially microalgal cells were suspended in medium (0 h). Sooner the fungal spores were germinated, microalgal cells started aggregating (along with fungal biomass) and eventually turned into tightly packed pellets on completion of harvesting process (24 h). These pictures taken at different time intervals, showing the aggregation stages of harvesting process further validated the profile of observed harvesting kinetics. After 24 h, the microalgal fungal pellets settled down at the bottom of the flask with separation of the clear supernatant. The settled pellets were harvested easily by simply decantation of supernatant or filtering through filter paper. Hence, the present study makes an important contribution by depicting the correlations between fungal growth, glucose consumption and accompanied pH change in the medium to best algal harvesting.

The latter will effect of Glucose level variation on *Chlorella* sp. through PFF. It is clear that *A. terreus* was the most efficient in harvesting *Chlorella* sp. from the liquid culture at glucose concentration of (10 g/l). Further attempts were then made to reduce the glucose input in order to make the fungal assisted microalgal harvesting economically feasible at large scale. The variation of HI at different glucose levels is shown in (Figure 2). It was interesting to notice that the reduced glucose level (5 g/l) was enough to support the efficient fungal growth and subsequently the harvesting of microalgal cells at (5 g/l), the recorded harvesting was more than 75 % within 24h. Moreover, 30 % harvesting of microalgal cells was observed approximately in 24h at (2.5 g/l) glucose concentration. Though, the harvesting efficacy was relatively poor at (10 g/l glucose) with own harvesting 93%. Furthermore, as realized from Fig.2, the raised glucose level (1053 g/l) does not have any significant differences from the concentration (10 g/l) on the fungal pelletization assisted algal harvesting progression. As confirmed by [9] the high concentrations of glucose up to (10 g/l) increase productivity of the fungus about (800 mg/l. day⁻¹) which was about seven times higher than the fungal productivity with low glucose concentrations. [26] confirm higher concentrations of glucose increase fungal biomass in the co-culture,

whereas the microalgal biomass in the co-culture was much lower compared with the biomass produced in the pure culture of only microalgae. So it is strong to be determined that although 10 g/l glucose concentration was optimal for 100 % harvesting of microalgal cells within 24 h, the reduced glucose level (5 g/l) can also result in similar harvesting but maybe with relatively higher incubation time. Hence, the efficient microalgal harvesting can be done either at (10 or 5 g/l) glucose concentration, depending up on the time of incubation, similarly to [27] improved the ability of *A. lentulus* to harvest was nearly 100 % of the *Chroococcus* sp. within only 24 h at supplementation of (10 g/l) of glucose also performed well at lower glucose level (5.0 g/l) resulting in 92 % harvesting within 24 h and up to 98 % harvesting within 52 h.

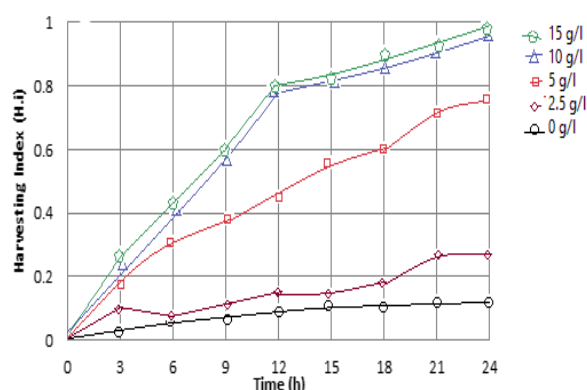


Figure 2: Comparison of H. I % at different glucose concentration (supplemented with 2.5 mg/l NH₄NO₃ and 0.5 mg/l K₂HPO₄) ranging from (0 -15 g/l).

The Possible Mechanism of Microalgal-Fungal Pelletization

The microscopic analysis revealed that in this particular study, the fungal pelletization assisted microalgal. Harvesting mainly talented through coagulative type pelletization (Figure 3). From microscopic observations it is clear that the microalgal and fungal spores coagulated in form of algal-fungal (spore) cluster as soon as the spore germination started. This cluster then turned into "microalgal cell containing fungal hyphal network", which subsequently evolved as algal-fungal pellet after further hyphal growth and binding of more algal cells. Previous studies [26, 27] state that fungal growth in submerged culture undergoes mainly by three phases including micromorphological growth (germ tube elongation), macromorphological growth (pelletization) and fungal cell autolysis. Hence, the fungal as-

sisted microalgal harvesting could result from the interaction of microalgal cells with fungal biomass at any of the above stated stages of fungal pelletization process as described by [14], in the coagulative-type pelletization, germinating spores possibly may cluster together along with the microalgal cell due to germinating spore to spore interaction and spore to microalgal cell interaction. Moreover, in the hyphal–elemental agglomeration, the microalgal cells might bind to the exposed hyphal tips of the germinating spores as soon as the germination starts followed by fungal hyphal growth resulting in its further interaction with other fungal hyphae and microalgal cells and subsequently the formation of algal–fungal pellet.

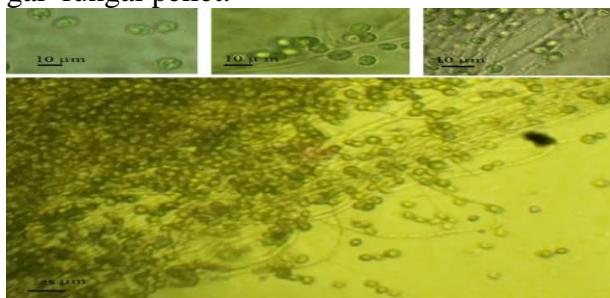


Figure 3: optical microscopic pictures illustrate various stages of fungal pelletization assisted algal harvesting process

It is widely reported that fungal growth (in submerged culture) results in secretion of various metabolites including organic acids, polysaccharides, proteins and enzymes [28, 29]. Hence, the interaction and attachment of microalgal cells to fungal spore and hyphal surface may be facilitated by growth associated metabolite secretion by the fungi.

Conclusions

The present study was focused on the identification of the limiting factors and subsequent optimization of the process of fungal assisted microalgal harvesting. From the present observations, it was found that the fresh chu-10 does not support growth of selected PFF and hence needs to be supplemented with carbon and nutrient sources. Supplementation of the chu-10 media with glucose (10 g/l), NH_4NO_3 (2.5 mg/l) and K_2HPO_4 (0.5 mg/l) was optimal for efficient fungal pelletization of selected strains. Among the tested PFF, only *A. terreus* was efficient to grow and pelletize in the nutrient supplemented chu-

10, irrespective of its pH. Moreover, *A. terreus* resulted in nearly 100 % harvesting of *Chlorella* sp. from the suspended culture within 24 h. However, the mechanism behind the fungal pelletization-assisted microalgae harvesting was observed to be coagulative type. Based on the above observations, the process of microalgal–fungal pelletization can be summarized in the following possible steps: (1) germination of fungal spore, (2) interaction followed by binding of microalgal cell to active sites (on germinating spore or fungal hyphae) resulting in the nucleation of microalgal–fungal pelletization process, (3) further growth of fungal pellet with more active sites on exposed hyphae and finally (4) binding of microalgal cells on other exposed active sites and completion of pelletization process. This technique is yet to be tested at pilot level in order to replace energy intensive harvesting methods currently being employed at industrial scale. If the investigated process is scaled up and optimized properly, it could be the most efficient and the economically feasible process at industrial scale in the world of microalgal biofuel.

References

- [1] Bahadar, A. ; Khan, M. B. (2013). *Progress in energy from microalgae: A review*. Renewable and Sustainable Energy Reviews, 27: 128–148.
- [2] Valipour, M. ; Mousavi, S. M. ; Valipour, R. and Rezaei, E. (2012). *Air, Water, and Soil Pollution Study in Industrial Units Using Environmental Flow Diagram*. Journal of Basic and Applied Scientific Researches and Essays, 2 : 12365-12372.
- [3] Zhang, W.1. ; Zhao, Y.1. ; Cui, B.1. ; Wang, H.1. and Liu T. (2016). *Evaluation of filamentous green algae as feedstocks for biofuel production*. Bioresources Technology, 220:407-413.
- [4] Rhea, N. A. (2016). *Evaluation of Flocculation, Sedimentation, and Filtration for Dewatering of Algal Biomass*. Theses and Dissertations-Biosystems and Agricultural Engineering. pp42. http://uknowledge.uky.edu/bae_etds/42.
- [5] Vandamme, D. ; Pontes, S. C. V. ; Goiris, K. ; Foubert, I. ; Pinoy, L. J. J. and Muylaert, K. (2011). *Evaluation of electro-*

- coagulation-flocculation for harvesting marine and freshwater microalgae*. *Biotechnology and Bioengineering*, 108(10):2320-2329.
- [6] Mackay, S. ; Pereira, G. ; Rossi, E. ; gSchwitzgubel, P. and Holliger, C. (2013). *a Pelletization.. of micro-algae by. , made lichen. . formation through co-culture. with filamentous fungi*. SME.5th Swiss Microbial Ecology Meeting. Murten, Switzerland.
- [7] Zhang, J. and Hu, B. (2012). *A novel technique to harvest microalgae via co-culture of filamentous fungi to procedure cell pellets*. *Bioresources Technology*, 114:529–535. doi:10.1016/j. biortech.03.054.
- [8] Choi, Y. N. ; Cho, H. U. ; Utomo, J. C. ; Shin, D. Y. and Park, J. M. (2016). *Efficient harvesting of Synechocystis sp. PCC 6803 with filamentous fungal pellets*. *Journal of Applied Phycology*, 28 (4) :2225–2231.
- [9] Gultom, S. ; Zamalloa, C. ; Hu, B. (2014). *Microalgae harvest through fungal pelletization—co-culture of Chlorella vulgaris and Aspergillus niger*. *Energies*, 7:4417–4429.
- [10] Richard, M. (2003). *Activated sludge microbiology problems and their switch*, in: Proceedings of the 20th Annual US Environmental Protection Agency National Operator Trainers Conference; Buffalo, New York, June 8; US Environmental Protection Agency, Washington. ,. ;l
- [11] Barnett, H. L. and Hunter, B. B. (1972). *Illustrated genera of imperfect fungi*. Burgess Pub. Co., Minneapolis, Minnesota, USA. Barnett H. L. Illustrated Genera of Imperfect Fungi. 2 nd. Ed. Burgess publishing company. 228pp.
- [12] Richmond, A. (2004). *Handbook of.. Microalgal Culture*. Blackwell Science.. Ltd., Oxford, UK.
- [13] Lee, R. E. (2008). *Phycology*. 4th edition. Colorado State University, USA. 550 pp.
- [14] Gultom, S. O. and Hu, B. (2013). *Review of Microalgae Harvesting via Co-Pelletization with Filamentous Fungus*. *Energies*, 6: 5921-5939.
- [15] Dubois, M. ; Gilles, K. Hamilton, JK. ; Rebers, P. A. and Smith, F. (1951). *Method for sugar estimation*. *Nature*, 4265:167-168.
- [16] Prajapati, S. K. ; Kaushik, P. ; Malik, A. ; Vijay, VK. (2012). *Phycoremediation and biogas possible of native algal separates from soil and wastewater*. *Bioresours Technology*, 135:232–238.
- [17] Liao, W. ; Liu, Y. C. ; Frear and Chen, S. (2007). *A new approach of pellet formation of a filamentous fungus – Rhizopus oryzae*, *Bioresources Technology*, 98 : 3415– 3423.
- [18] Poelman, E. ; DePauw, N. and Jeurissen, B. (1997). *Potential of electrolytic flocculation for pH recovery of micro-algae*, *Resources Conservation and Recycling*, 19, pp.1-10.
- [19] Zhou, W. ; Cheng, Y. ; Li, Y. ; Wan, Y. ; Liu, Y. ; Lin, X. and., Ruan, R. (2012). *Novel. fungal pelletization-assisted technology for algae. , harvesting and wastewater. ., treatment*. *Applied Biochemical Biotechnology*, (167):214–228.
- [20] Zhang, J. and Hu, B. (2012). *A novel method to harvest microalgae via coculture of filamentous fungi to form cell pellets*. *Bioresours Technology*, 114:529–535.
- [21] Christenson L. and Sims, R. (2011). *Production and harvesting of microalgae for wastewater treatment, biofuels, and bioproducts*, *Biotechnology Advances*, 29: 686-702.
- [22] Syahiddin, D. ; Hasan, M. and Ramachandran, K. B. (2003). *Effect of pH on growth, spore..., production and spore feasibility of biocontrol agent Trichoderma harzanium in submerged fermentation*. *ASEAN Journal of Chemical engineering*, 3(1):14–18.

Research Article

Micronucleus Frequency in Buccal Cells of Males Exposed to Air Pollution in Kufa City

Farha A. Ali Shafi, Aqeel M. Ali Al-lami, Rawa Abd Al-Ameer

Department of Biology, College of Science, Mustansiriyah University, IRAQ

*Correspondent Author Email: farhaali2009@yahoo.com

Article Info

Received
04/12/2016

Accepted
17/04/2017

Abstract

The aim of the present study is to explore micronuclei recurrence, as a biomarker of genomic damage in buccal cells of individuals living in polluted areas located near to the cement factory in Kufa city. Twenty four apparently healthy males residing in Kufa are enrolled in the present study, their ages between 18-30 years, as control group 24 males with same age are enrolled living in the center of Najaf city a far from cement factory. A sample of the exposed and control groups of buccal mucosa cells was collected during Spring months in 2016. The mean count of cell with micronuclei in buccal cells of the exposed group and control were $(22.33 \pm 0.97; 11.583 \pm 0.85)$ respectively, the mean count of the binucleated cells of the exposed and control groups were $(7.208 \pm 0.71, 10.041 \pm 0.84)$ respectively, a significant difference was detected in the observed frequencies of micronuclei and binucleated cells in the buccal mucosa cells between the exposed and control group. The results indicated that exposure to air pollutants related to cement production induce cytotoxic as well as genotoxic damage in buccal mucosa cells.

Keywords: Kufa, micronuclei, binucleated cells, air pollution.

الخلاصة

الهدف من الدراسة الحالية هو التحري عن تكرار النوى الصغيرة في الخلايا الطلائية المبطنة للفم كمؤشر لمقدار الضرر في المادة الوراثية لمجموعة من سكان منطقة ملوثة بالقرب من معمل أسمنت الكوفة، شملت الدراسة اربعة وعشرون ذكرا من سكان منطقة الكوفة، كانت اعمارهم تتراوح بين 18-30 سنة، كما شملت الدراسة ايضا اربعة وعشرون ذكرا من سكان مدينة النجف وينفس الفئة العمرية وعدت كمجموعة سيطرة. تم جمع العينات من الافراد المتعرضين والسيطرة خلال اشهر ربيع 2016. كان معدل الخلايا ذات النوى الصغيرة في الخلايا المبطنة للفم للأفراد المعرضين والسيطرة $(22.33 \pm 0.97; 11.583 \pm 0.85)$ ومعدل الخلايا ثنائية النواة للأفراد المعرضين والسيطرة $(7.208 \pm 0.71; 10.041 \pm 0.84)$ لوحظ وجود اختلافا معنويا بتكرار ظهور النوى الصغيرة والخلايا ثنائية النواة في الخلايا المبطنة للفم عند مقارنة الافراد المعرضين مع السيطرة. دلت النتائج الى ان التعرض الى ملوثات الهواء المصاحبة لإنتاج الاسمنت يستحث سمية خلوية ووراثية للخلايا المبطنة للفم.

Introduction

Air pollution is a combination of inconsistent concentrations of gases and solid particles in the air. Air pollution and particulate matter are globally recognized as carcinogenic to human [1] [2]. During the previous decades, many literatures have evaluated the genotoxic impacts of air pollution among population residing in areas with medium or high levels of air pollution [3] [4]. Numerous studies have utilized the micronucleus test to determine an association between pollution and cytotoxic and/ or genotoxic effects [5] [6]. In the eighties the buccal cell micronuclei test recommended as a biomarker for genomic damage. Subsequently, this test chosen as convenient biomarker of chromosomal damage cre-

ated by exposure to different environmental pollutants, lifestyle habits in addition to inherited diseases [7]. In the last decade the micronuclei tests in buccal cell have gotten increasing popularity among laboratories working in the field of environmental mutagenesis consequently, the number of published researches based on this biomarker has expanded. Previous research demonstrates that an elevation in the micronucleus score in buccal cells denotes to an increase in risk for malignancy [8] [9]. In Iraq, there are no studies have considered the genomic damage in mucosa buccal cells as micronuclei(MN) score in cells of the population exposed to air pollution. The aim of the present work is to explore micronuclei recurrence, as a biomarker of ge-

onomic damage in buccal cells of individuals living in polluted areas located near to the cement factory in Kufa city.

Materials and methods

The present study includes twenty four apparently healthy males residing in Kufa near cement factory (Al-Kūfa is a town in the south of Baghdad northeast of Najaf city it is situated on the banks of the Euphrates river). Their ages between 18-30 years, as control group 24 males with same age are enrolled living in the center of Najaf city a far from cement factory. All study participants were informed of the study objectives. The data about date of birth, occupational history, health status Lifestyle (smoking, drinking habits and diet) was provided by questionnaire.

A sample of the exposed and control groups of buccal mucosa cells was collected during spring months in 2016. Before cell collection all volunteered were asked to rinse their mouth thoroughly with water to get rid of any unwanted debris. Smooth toothbrushes were used, the head of the toothbrushes was swapped on clean slides, and then samples were fixed with ethanol (90%) for 48 h, and stained with Giemsa for 20 minutes. To count the cells with micronuclei and binucleate cell per 2000 cells for each individual stained slide scanning by light microscope (at 400 X magnification). This procedure was done according to the criteria originally described by Tolbert *et al.* [10] [11].

Statistical Analysis:

To analyze the data The Statistical Analysis System- SAS [12] program was used. Least significant difference –LSD test was used to compare the means of micronuclei and binucleated cells between the studied groups.

Results and Discussion

A cell with micronuclei was differentiated by the presence of one or more than one a small additional nuclei in the cytoplasm (Figure 1). The main finding of the present work was a surprisingly in an elevation score of micronuclei in buccal cells of male living in exposed area. As shown in Table (1) the mean count of cell with micronuclei in buccal cells of individuals from exposed area was (22.33 ± 0.97) . It was significantly higher in comparison with the micronuclei frequency of control subjects ($P < 0.0001$).

According to preceding researches that included adults and children, the range of micronuclei score in buccal cell in unexposed subjects interval of between (3-17 /2000 cell) [13]. Hence, the mean count of cell with micronuclei found in the present study is about two- fold higher than reference value for unexposed individuals. Additionally, the mean value of the binucleated cells of males from exposed area was (10.041 ± 0.84) also significantly higher ($P < 0.01$) in comparison with mean value of binucleated cell in the control subjects.

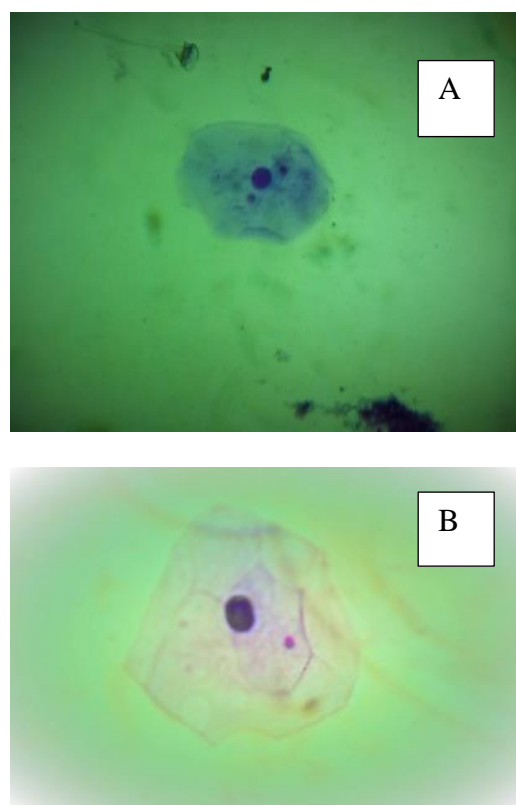


Figure1: A: buccal cell with two micronuclei, B: buccal cell with one micronuclei (400X magnification).

Binucleated cells are cells containing two very close main nuclei instead of one and they are considered marker of cytokinesis failures or cytokinetic faults as a result of aneuploidy [7]. Increased frequency of binucleated cell of the male of exposed area indicated that exposure to air pollutants induce cytotoxic as well as genotoxic damage. Our results are consistent with Jara-Ettinger *et al.* [5] who report a significant increase of binucleated score in Mexican wilder. Al-Kufa cement factory located near urban centers and may create a serious hazard to the environment as well as human health [14].

The main air pollutants related to cement production include: sulfur oxides, nitrous oxides,

carbon oxides, particulates and organic compounds in addition to cement kilns release large amounts of dust which possibly contains large concentrations of heavy metal and particulates [15] [16]. In fact, most of these compounds have mutagenic and / or cytotoxic effects for that reason it is difficult to conclude which of them represent the effects seen in the present work. The result obtained in the present work are in agreement with previous studies Ceretti *et al.* [17] reported that the rate of micronuclei occurrence in epithelial buccal cells significantly associated with concentration of air pollutants, for example, particulate matter (PM10, PM2.5) and nitrous oxide NO₂. Furthermore an increase of micronuclei score has been detected in peripheral blood lymphocytes as well as in buccal mucosa cells of individuals exposed to urban air pollution [3] [4] [6] [18].

As mentioned above, SO₂ is one of the air pollutants related to cement production; previous study documented an increase of chromosomal aberration in lymphocytes of subjects who were occupationally exposed to SO₂. Numerous studies were published which revealed that SO₂ induces DNA instability in laboratory animals as well as in cultured human cells and it was suggested that SO₂ exposure was responsible to increased risk of lung cancer in workers [19] [21]

[22].

Furthermore, the SO₂ also induces genomic instability in plant cells [23]. The impact of cement industry emission on plant production and soil properties has been studied by some researchers, Salama *et al.* [15] documented that cement industry emission includes NO₂, O₃ and SO₂ intensely impact the morphology and physiology of *Datura innoxia* plant., Al-Omran *et al.*, [24] reported an increase of the Cr, Cd, Ni, and Pb in the soil surrounding the cement plant in Saudi Arabia.

The results of present study showed elevation score of micronuclei and binucleated cells in males living near cement factory. It is in consonance with the finding of earlier studies where researchers utilized the micronuclei test in oral cells to detect the genotoxic impact of air pollution in outdoor workers including tunnel worker, street vendors, driver and gas station attendants [18].

In conclusion the results reveal that first, this micronuclei assay can be utilized in monitoring studies second, supports the need to additional researches shed light on the genotoxic and cytotoxic impact of air pollution on population residing in areas with medium or high level of air pollution.

Table (1): Micronucleated and Binucleated cells frequencies in exposed and control males

Parameter /2000 cell	Exposed males 24 (mean ± S. E)	Controls (unexposed males) 24 (mean ± S. E)
Micronucleated cells	22.33 ± 0.97***	11.583 ± 0.85
Binucleated cells	10.041 ± 0.84*	7.208 ± 0.71

Conclusion

References

- [1] WHO Air Quality Guidelines. Global Update 2005. World Health Organization Office for Europe, Copenhagen, Denmark.2006.
- [2] WHO Children’s health and the environment in Europe: a baseline assessment. World Health Organization Regional Of-

fice for Europe, Copenhagen, Denmark.2007.

- [3] Shafi, F. A., AL-Ansari,N., Abdul Majeed, B. Frequency of micronuclei in peripheral blood lymphocytes of healthy individuals: A study from Baghdad, Iraq. World Journal of Experimental Biosciences, 4: 40-48, 2016.
- [4] Kapka L, Baumgartner A ,Ewa Siwin S ,. Knudsen L. E, Anderson D and _zyn’ska D MEnvironmental lead exposure increases micronuclei in children. Mutagenesis, 22 (3) 201–207, 2007.



- [5] Jara-Ettinger AC, López-Tavera JC, Zavala-Cerna MG, Torres-Bugarín O Genotoxic Evaluation of Mexican Welders Occupationally Exposed to Welding-Fumes Using the Micronucleus Test on Exfoliated Oral Mucosa Cells: A Cross-Sectional, Case-Control Study. *PLoS ONE*; 10(8) 2015.
- [6] K. Letaj, I. Elezaj, Q. Selimi and K. Kurtshi The Effects of Environmental Pollution with Heavy Metals in Frequency of Micronuclei in Epithelial Buccal Cells of Human Population in Mitrovica. *Journal of Chemical Health Risks*; 2(3) 1- 4.2012.
- [7] Holland N, bolognesi C, Volders MK, Bonassi S, Zeiger E, Knasmueller S. The micronucleus assay in human buccal cells as a tool for Biomonitoring DNA damage: The HUMN project perspective on current status and knowledge gaps. *Mutation Research*.659,93-08.2008.
- [8] Thomas P, Holland N, Bolognesi C, Kirsch-Volders M, Bonassi S, Zeiger E. Buccal micronucleus cytome assay. *Nat. Protoc.* ; 4(6): 825–837.2009.
- [9] Bonassi, S, Hagmar, L. and Stromberg, U Chromosomal aberrations in lymphocytes predict human cancer independently of exposure to carcinogens. *Cancer Research*; 60, 1619–1625.2000.
- [10] Tolbert PE, Shy CM, Allen JW. Micronuclei and other nuclear anomalies in buccal smears: methods development. *Mutation Research*.271, 69–77, 1992.
- [11] Tolbert PE, Shy CM, Allen JW. Micronuclei and other nuclear anomalies in buccal smears: a field test in snuff users. *Am. J. Epidemiol*.134, 840–850,1991.
- [12] SAS. Statistical Analysis System, User's Guide. Statistical. Version 9.1th ed. SAS. Inst. Inc. Cary. N. C. USA.2012.
- [13] Chen C, Arjomandi M, Qin H, Balmes J, Tager I, et al. Cytogenetic damage in buccal epithelia and peripheral lymphocytes of young healthy individuals exposed to ozone. *Mutagenesis*.21, 131–137.2006.
- [14] Al-Hayali M. K. and AL-Harbawi S. Y. A. Effect of Cement Pollution on Creatinine and Blood Urea in Hamam Al-Alil Factory Workers Haitham L. College of Basic Education Researchers *Journal*,11, 787-797.2007.
- [15] Hediati M. H. Salama, M. M. Al-Rumaih, and M. A. Al-Dosary Effects of Riyadh cement industry pollutions on some physiological and morphological factors of *Datura innoxia* Mill. plant *Saudi Journal Biology sciences*; 18, 227–237,2011.
- [16] Al-Khashman,O,A' Shawabkeh,R. A, Metals distribution in soils around the cement factory in southern Jordan. *Environmental Pollution*,140, 387-394, 2006.
- [17] Ceretti E, Feretti D, Viola GCV, Zerbini I, Limina RM, et al. DNA Damage in Buccal Mucosa Cells of Pre-School Children Exposed to High Levels of Urban Air Pollutants. *PLoS ONE* 9, 387–394,2014.
- [18] A. Nersesyan, Michael, K., Waldherra ,M. Setayesha ,T. Mišika ,M. Wultscha ,G.. Metka F, Gustavo R. Mazzaron B., Siegfried K. Results of micronucleus assays with individuals who are occupationally and environmentally exposed to mercury, lead and cadmium, *Mutation Research*.770, 119-139, 2016.
- [19] Beckman, L., Nordenson, I., Interaction between some common genotoxic agents. *Human Heredity*.36, 397-401.1986.
- [20] Pool, B. L., Janowsky, I., Klein, P., Klein, R. G., Schmezer, P., Vogt-Leucht, G. Zeller, W. J., Effects of SO₂ or NO(x) on toxic genotoxic properties of chemical carcinogens. I. In vitro studies. *Carcinogenesis* 9, 1237-1245.1988.
- [21] Meng, Z., Qin, G., Zhang, B., Bai, J. DNA damaging effects of sulfur dioxide derivatives in cells from various organs of mice. *Mutagenesis*, 19, 465-468.2004.
- [22] Lee, W. J., Teschke, K., Kauppinen, T., Andersen, A., Ja'ppinen, P., Szadkowska Stanczyk, I., Pearce, N., Persson, B., Bergeret, A., Facchini, L. Kishi, R., Kielkowski, D., Rix, B. A., Henneberger, P., Sunyer, Colin, D., Kogevinas, M., Boffetta, P., Mortality from lung cancer in workers exposed to sulfur dioxide in the pulp and paper industry. *Environ Health Perspect*.110, 991-995.2002.
- [23] Miroslav Misík a, Karol Micieta a, Martina Solenska´ a, Katari´na Misíkova a Helena Pisarcikova a, Siegfried Knasmuller b. In

situ biomonitoring of the genotoxic effects of mixed industrial emissions using the *Tradescantia micronucleus* and pollen abortion tests with wild life plants: Demonstration of the efficacy of emission controls in an eastern European city *Environmental Pollution* 145 459-466.2007.

- [24] Abdulrasoul M. Al-Omran, Salem E. El-Maghraby, Mahmoud E. A. Nadeem, Ali M. El-Eter and Salem M. I. Al-Qahtani. Impact of Cement Dust on Some Soil Properties Around the Cement Factory in Al-Hasa Oasis, Saudi Arabia. *American-Eurasian Journal of Agric. and Environmental sciences*, 11, 840-846, 2011.

Research Article

Synthesis, Characterization and Kinetic Study of Monomeric Complexes of Cyclohexane-1, 2- bis (Thiosemicarbazone) with Cobalt (II), Nickel (II) and Copper (II)

Al-Ameen Bariz Omar Ali

Department of Chemistry, College of Science, Mustansiriyah University, IRAQ

*Correspondent Author Email: hero_802007@yahoo.com

Article Info

Received
23/02/2017

Accepted
21/05/2017

Abstract

Cyclohexane-1,2-bis(thiosemicarbazone) (CHTSC) was synthesized via the condensation reaction of cyclohexane-1,2-dione and thiosemicarbazide. Series of metal complexes of the prepared ligand, of general formula $[M(\text{CHTSC})(\text{NO}_3)_2]$, were reported. The prepared coordination complexes were characterized and their structures elucidated using different techniques. These showed that all complexes are octahedral geometries. The kinetics of the formation of these complexes have been investigated using stopped-flow spectrophotometry. These studies revealed that the reactions are completed on the second's timescale with 1st-order dependence (either on the concentration of metal salt or on the concentration of CHTSC).

Keywords: Schiff base ligands, Thiosemicarbazones, Kinetic study.

الخلاصة

تضمن البحث تحضير ليكاند لقاعدة شيف من خلال التفاعل التكثيفي للسياكلوهكسان ثنائي اون والثايسيمي كاربازايد. تم تحضير سلسلة من معقدات العناصر الليكاند المحضر ذات الصيغة العامة $[M(\text{CHTSC})(\text{NO}_3)_2]$. تم تشخيص المعقدات التناسقية المحضرة وتم التوصل الى اشكالها الهندسية باستخدام تقنيات مختلفة. حيث بينت الدراسة بأن جميع المعقدات المحضرة لها شكل هندسي ثنائي السطوح. تمت دراسة حركية تكوين المعقدات والتي أظهرت التفاعل من المرتبة الأولى اعتمادا على كل من تركيز الليكاند او الأيون الفلزّي.

Introduction

Compounds that are containing sulfur and nitrogen atoms (thiosemicarbazones) have received remarkable interests and extensive investigation due to their bonding modes and biological applications [1] [2] [3] [4] [5] [6] [7]. Thiosemicarbazone compounds are also applicable in several fields of inorganic chemistry. The commonly use as: a chelating agent for the formation of metal complexes. Moreover, the metal complexes of thiosemicarbazones have been applied in the field of material sciences such as nonlinear optical (NLO) [7] [8], electrochemical sensing [9], and Langmuir film [10]. During the recent twenty years, so may papers have been published reporting the synthesis and characterization of transition metal complexes with thiosemicarbazones [17]. In this paper, the synthesis, characterization and structural studies of cyclohexane-1,2-bis(3-thiosemicarbazone) (CHTSC) and its metal complexes with different transition metal ions like : Co(II), Ni(II) and Cu(II), are reported. Ki-

netic studies on the formation of the prepared complexes have been also investigated.

Materials and Methods

All reagents that have used in this work were commercially available (Aldrich Co.). Elemental analyses (C, H and N) were carried out on a EuroEA Elemental Analyzer. Electronic spectra were measured in the region (200–1,100) nm for solutions in DMF at room temperature using a Shimadzu, 100 UV–visible spectrophotometer. Infrared spectra were recorded using a Cary 630 FTIR spectrometer equipped with an ATR module. ^1H and ^{13}C NMR spectra were measured in $\text{DMSO}-d_6$ solution with the TMS as an internal standard, using a Bruker 400MHz. Metals were determined using a novaAA 350 flame atomic absorption spectrometer. Conductivity measurements were made with DMF solutions using a Inolab multi 740 digital conductivity meter. Magnetic moments of the prepared complexes were measured at RT using an auto magnetic



susceptibility balance (Sherwood).

Preparation of CHTSC

A mixture of thiosemicarbazide (0.7 g, 8mmol) and cyclohexane-1,2-dione (0.4 g, 4mmol) was dissolved in methanol (30 mL). The solution was heated under reflux for 4 h, during which a yellow precipitate was formed. This solid was filtered off and washed with hot methanol. Yield = 54 %, 0.5g, m. p = 212–214 °C. Elemental analysis, found (calc.), C 37.95 (37.20), H 5.22 (5.42), N 32.20 (32.55) S 25.50 (24.80). ^1H NMR spectrum: δ /ppm: 1.75–2.87 (cyclohexane protons, m, 8H); 7.75 ($\text{H}_2\text{N}-\text{CSH}$, d, 2H); 8.6 (NH, s, 1H); 10.3 ($\text{H}_2\text{N}-\text{C}=\text{S}$, d, 2H); 12.22 (SH, s, 1H). $^{13}\text{C}\{^1\text{H}\}$ NMR spectrum: 20.95–33.5 (cyclohexane carbons); 146.12 (C=N); 178.93 (C=S).

Synthesis of the complexes

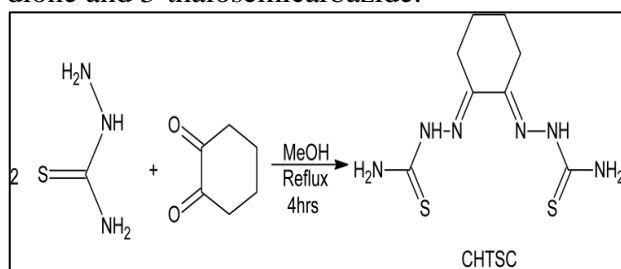
To a solution of CHTSC (0.15g, 0.58mmol) in acetonitrile (40 ml) was added the solution of metal salt (0.58mmol) [$\text{Co}(\text{NO}_3)_2 \cdot 6\text{H}_2\text{O}$, 0.17g ; $\text{Ni}(\text{NO}_3)_2 \cdot 6\text{H}_2\text{O}$, 0.17g ; $\text{Cu}(\text{NO}_3)_2 \cdot 2.5\text{H}_2\text{O}$, 0.13g] in acetonitrile (5ml). A microcrystalline solid was formed immediately. This was filtered off and washed with acetonitrile. Microelemental analysis; yield and other properties for the complexes are listed in Table 1.

Kinetic studies

Applied Photo physics SX.18MV stopped-flow spectrophotometer was used to perform the kinetic studies. The solutions were prepared in MeCN at RT and used within 1 h of preparation. Pseudo-first-order conditions were applied for all experiments with the concentration of CHTSC in an excess over the concentration of the metal ion.

Results and Discussion

N_2S_2 type ligand, CHTSC (Scheme 1), was synthesized by the reaction of cyclohexane-1,2-dione and 3-thiosemicarbazide.



Scheme 1: General route for the preparation of CHTSC.

Different spectroscopic techniques (elemental analysis and IR, ^1H and ^{13}C NMR spectroscopies) were used to characterize the prepared ligand. Characteristic bands have been observed in the IR spectrum of the ligand which mainly belong to NH, NH_2 and C=N functional groups, Table 2. While, several signals are located at the ^1H and ^{13}C NMR spectra of the ligand. These signals correspond to the various proton and carbon nuclei (see Experimental part and Figure 1). The UV–visible spectrum of CHTSC exhibited an intense absorption peak at (28571cm^{-1}) attributable to the ($\pi-\pi^*$) transition.

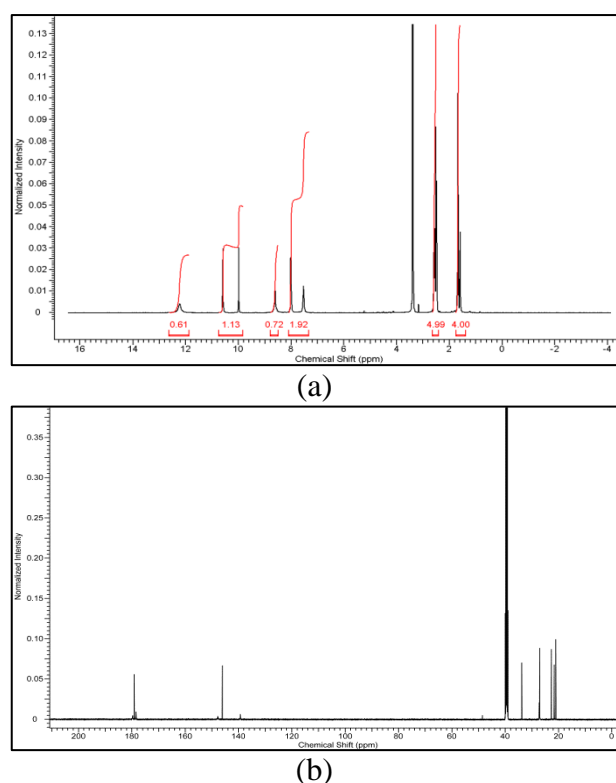
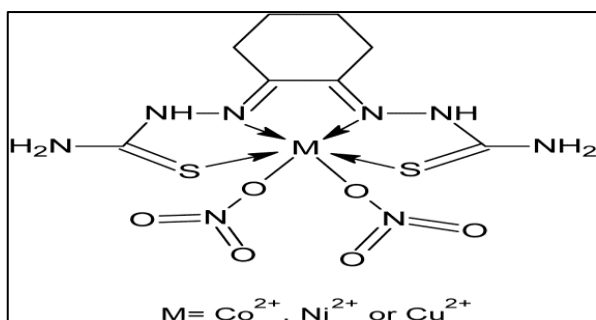


Figure 1: NMR spectra of CHTSC: a) ^1H NMR b) ^{13}C NMR.

The reactions of equimolar amounts of CHTSC with a variety of divalent metal ions ($\text{M} = \text{Co}, \text{Ni}$ or Cu), in a 1:1 stoichiometric ratio, produced rapid deposition of microcrystalline solids. However, the physical properties together with elemental analysis and molar conductivity values, Table 1, give an evidence that all the prepared complexes are neutral with the formulation $[\text{M}(\text{CHTSC})(\text{NO}_3)_2]$.



Scheme 2: Proposed molecular structures of the prepared complexes.

The IR spectrum of the free ligand (Figure 2) shows bands in the region (3420–3110 cm^{-1}), which is attributed to the $\nu(\text{NH})$ and $\nu(\text{NH}_2)$ vibrations. The bands due to $\nu(\text{C}=\text{N})$ and $\nu(\text{C}=\text{S})$ vibrations are located in the regions 1610 and 1360 cm^{-1} , respectively [18]. While, in the spec-

Table 1: Physical properties, elemental analyses and molar conductance values for the prepared compounds.

Compound	Color	Yield (%)	m. p.	Found (Calcd.) (%)					--
				M	S	C	H	N	
[CHTSC]	Yellow	54	212-214	–	25.50 (24.80)	37.95 (37.20)	5.22 (5.42)	33.20 (32.55)	–
[Co(CHTSC)(NO ₃) ₂]	Brown	58	290-293	14.30 (13.37)	15.23 (14.51)	22.30 (21.76)	3.55 (3.17)	26.32 (25.39)	9
[Ni(CHTSC)(NO ₃) ₂]	Brown	56	245-247	13.98 (13.28)	15.12 (14.52)	22.43 (21.79)	4.01 (3.17)	26.12 (25.42)	11
[Cu(CHTSC)(NO ₃) ₂]	Brown	63	233-235	13.92 (14.25)	15.20 (14.36)	22.21 (21.54)	3.88 (3.14)	26.20 (25.14)	13

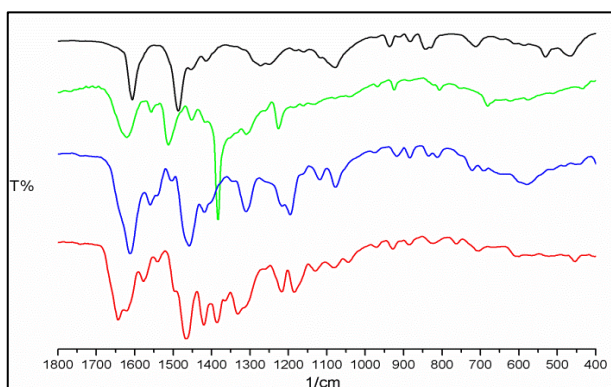


Figure 2: FTIR spectra: CHTSC (black), [Co (CHTSC) (NO₃)₂] (green), [Cu (CHTSC) (NO₃)₂] (blue), [Ni (CHTSC) (NO₃)₂] (red).

In general, hypsochromic shifts of ligand bands were detected in all the electronic spectra of the prepared complexes (Figure 3). The electronic spectrum of the cobalt (II) complex in DMF so-

tra of Schiff base complexes, the $\nu(\text{C}=\text{N})$ mode of ligand is found to shift to higher wave numbers, suggesting the coordination of the azomethine nitrogen to the central metal ion, in agreement with previous studies [19] [20]. In the far infrared region, weak to medium bands have been observed around (610–510), (420–475) and (400–403) cm^{-1} in all the complexes. These could be assigned to the vibrations of $\nu(\text{M}-\text{O})$, $\nu(\text{M}-\text{N})$ and $\nu(\text{M}-\text{S})$, respectively [21] [22] [23]. In addition, the spectra of complexes displayed two characteristic bands at the ranges: (1580 – 1450) cm^{-1} . These are due to the stretching vibrations of NO₃ group [24]. The most important infrared bands of the ligand and its complexes together with their assignments are collected in Table 2.

lution exhibited absorption bands at (18867 cm^{-1}), (15625 cm^{-1}) and (14084 cm^{-1}). These bands can be attributed to the ${}^4\text{A}_{2g}(\text{F}) - {}^4\text{T}_{1g}(\text{P})$, ${}^4\text{A}_{2g}(\text{F}) - {}^4\text{T}_{1g}(\text{F})$ and ${}^4\text{A}_{2g}(\text{F}) - {}^4\text{T}_{2g}(\text{F})$ transitions respectively [25] [26] [27]. Furthermore, the magnetic moment value of this complex is (3.80 BM). These data confirm the octahedral geometry around cobalt atom. Three absorption bands at (24390 cm^{-1}), (15151 cm^{-1}) and (13333 cm^{-1}) were observed in the UV-Vis spectrum of the Nickel (II) complex. These may be assigned to the ${}^3\text{T}_{1g}(\text{F}) - {}^3\text{T}_{1g}(\text{P})$, ${}^3\text{T}_{1g}(\text{F}) - {}^3\text{A}_{2g}(\text{F})$ and ${}^3\text{T}_{1g}(\text{F}) - {}^3\text{T}_{2g}(\text{F})$ transitions respectively [25–27]. The position of these bands together with magnetic moment value (2.9 BM) revealed the octahedral geometry around nickel atom. While, two characteristic absorption bands at (20833 cm^{-1}) and (18181 cm^{-1}) were located in the electronic spectrum of the Copper (II) complex. These bands

can be assigned to the ${}^2B_{1g} - {}^2E_g$ and ${}^2B_{1g} - {}^2B_{2g}$ transitions respectively. The magnetic moment value of this complex is (1.86 BM). These data confirm the octahedral geometry around copper atom [25] [26] [27]. The electronic spectral data, magnetic moment data and molar conductivity of (CHTSC) complexes are listed in Table 3.

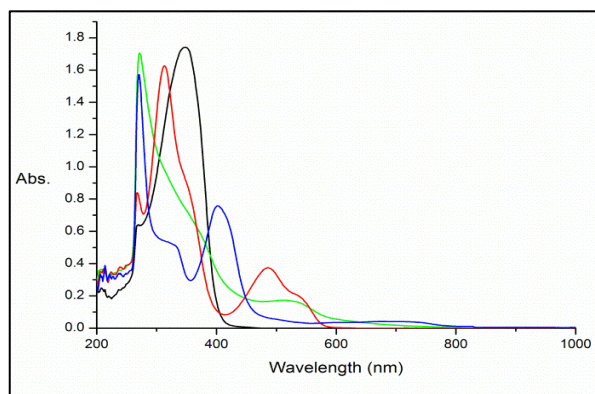


Figure 3: U. V- Vis spectra: CHTSC (black), [Co(CHTSC)(NO₃)₂] (green), [Ni(CHTSC)(NO₃)₂] (blue), [Cu(CHTSC)(NO₃)₂] (red).

Table 2: IR frequencies (cm⁻¹) of the prepared compounds.

Compound	ν_{N-H} , (NH ₂)	$\nu(C=N)$	$\nu(NO_3)$	$\nu(M-O)$	$\nu(M-N)$	$\nu(M-S)$
[CHTSC]	3420, (3225,3150)	1610	-	-	-	-
[Co(CHTSC)(NO ₃) ₂]	3415, (3255,3110)	1622	1550-1450	610	475	402
[Ni(CHTSC)(NO ₃) ₂]	3375, (3300,3150)	1640	1580-1540	510	420	403
[Cu(CHTSC)(NO ₃) ₂]	3390, (3250,3120)	1620	1560,1520	559	450	400

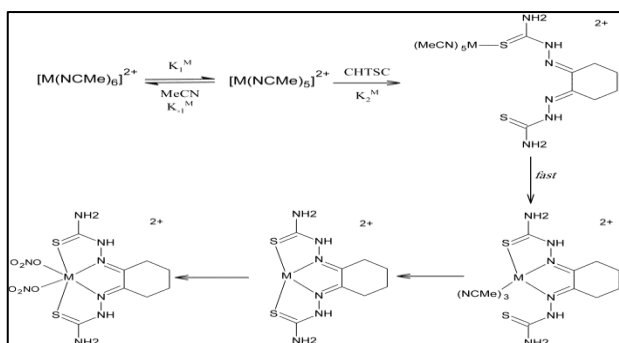
Table 3: Magnetic moments and UV-vis spectral data in DMF solution.

Compound	ν (cm ⁻¹)	Extinction coefficient (ϵ , L mol ⁻¹ cm ⁻¹)	Assignment	μ_{eff} (BM)
[CHTSC]	28571	1750	$\pi-\pi^*$	-
	37735	1570	$\pi-\pi^*$	-
	24390	700	${}^3T_{1g}^{(F)} - {}^3T_{1g}^{(P)}$	-
[Ni(CHTSC)(NO ₃) ₂]	15151	70	${}^3T_{1g}^{(F)} - {}^3A_{2g}^{(F)}$	2.90
	13333	20	${}^3T_{1g}^{(F)} - {}^3T_{2g}^{(F)}$	
	32258	1620	$\pi-\pi^*$	
	28571	900	CT	
[Cu(CHTSC)(NO ₃) ₂]	20833	390	${}^2B_{1g} - {}^2E_g$	1.86
	18181	200	${}^2B_{1g} - {}^2B_{2g}$	
	34482	1700	$\pi-\pi^*$	
	27777	1180	CT	
[Co(CHTSC)(NO ₃) ₂]	18867	180	${}^4A_{2g}^{(F)} - {}^4T_{1g}^{(P)}$	3.80
	15625	60	${}^4A_{2g}^{(F)} - {}^4T_{1g}^{(F)}$	
	14084	15	${}^4A_{2g}^{(F)} - {}^4T_{2g}^{(F)}$	

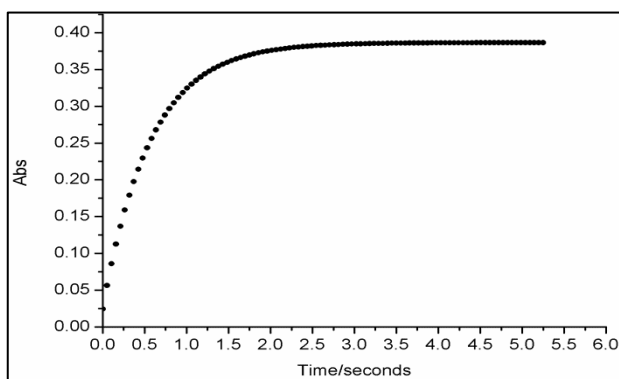
Kinetic studies

Stopped-flow spectrophotometry was used to study the kinetics of the reactions between CHTSC and variety of metal ions: Co (II), Ni(II) or Cu(II). The reactions were studied under pseudo-first-order conditions with [CHTSC] \geq 10[M²⁺]. Figure 4, shows that the absorbance-time traces is fitted to a single exponential curve, which indicates a first-order of the reactions depending upon the concentration of metal ion. This conclusion is confirmed in studies where the concentration of metal ion was varied in the range 0.2–1.0 mmol dm⁻³ with [CHTSC] = 10

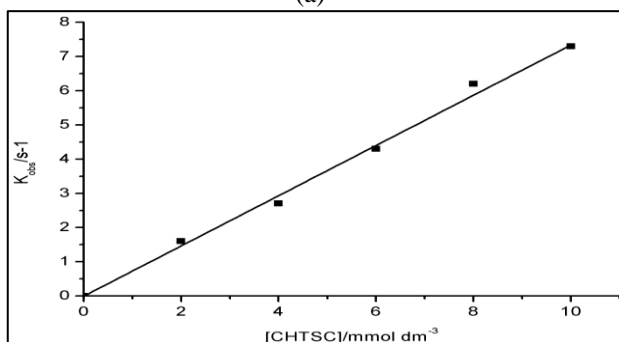
mmol dm⁻³. For each different metal ion, all reactions displaying a first-order dependence on the concentration of CHTSC, as typified by the plot shown in (Figure 4) and the corresponding rate law in Eq. (1). A proposed mechanism for the reactions is shown in scheme 3.



Scheme 3: Proposed mechanism for the reaction of divalent metal ion and CHTSC in MeCN.



(a)



(b)

Figure 4: Kinetic data for the reactions of divalent metal ion with CHTSC in MeCN at RT.

The example shown is for the reaction with Ni²⁺.
a) Shows an absorbance-time curve when [Ni²⁺] = 0.2 mmol dm⁻³ and [CHTSC] = 2 mmol dm⁻³.
b) Shows the first order dependence of k_{obs} on the concentration of CHTSC. Straight line fit to the data is that defined by the equation $k_{obs} = 7.5 \times 10^2 [\text{CHTSC}]$.

$$-d[M^{2+}]/dt = k_a^M [\text{CHTSC}][M^{2+}] \quad (1)$$

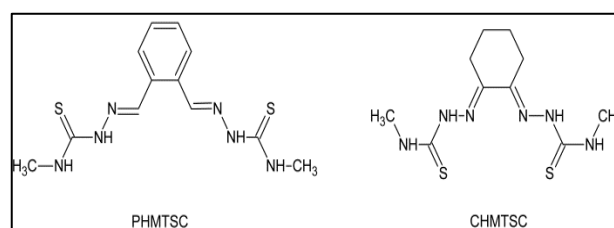
Table 4: Rate constants for the reactions of CHTSC with divalent metal ion in MeCN at RT.

Metal ion M ²⁺	$k_a^M / \text{dm}^3 \text{mol}^{-1} \text{s}^{-1}$
Co	$4.5 \pm 0.5 \times 10^2$
Ni	$7.5 \pm 0.5 \times 10^2$
Cu	$8.3 \pm 0.5 \times 10^2$

$$-d[M^{2+}]/dt = k_1^M k_2^M [\text{CHTSC}][M^{2+}] / k_{-1}^M [\text{MeCN}] + k_2^M [\text{CHTSC}] \quad (2)$$

$$-d[M^{2+}]/dt = k_1^M k_2^M [\text{CHTSC}][M^{2+}] / k_{-1}^M [\text{MeCN}] \quad (3)$$

Previous studies [16] [17] on other Schiff base thiosemicarbazones complexes [M(CHMTSC-2H⁺)] and [M(PHMTSC-2H⁺)] (where PHMTSC and CHMTSC have the structures shown below) have investigated the kinetic of the reactions of PHMTSC or CHMTSC with divalent metal ions. The rate constant k_a^M values for the reactions of CHTSC with metal ions, and the reactions of PHMTSC or CHMTSC with metal ions, are found to be quite close to each other. This may be due to the similarity in back bone structures of such type of ligands (slightly different).



As in PHMTSC and CHMTSC, and also other studies [28], the rate-limiting step of the chelate formation is the initial binding of CHTSC to [M(NCMe)₅]²⁺ by replacing one of the coordinated CH₃CN molecules. The usual intimate mechanism for such a reaction is dissociative and involves initial dissociation of a coordinated solvent from [M(NCMe)_n]²⁺, generating [M(NCMe)_(n-1)]²⁺ containing a vacant site at which CHTSC can bind as shown in (scheme 3). The full rate law for this mechanism is shown in equation (2). When the concentration of CHTSC is small, $k_{-1}^M [\text{MeCN}] > k_2^M [\text{CHTSC}]$ the rate law would simplify to that shown in equation (3), which is of the same form as observed experimentally in equation (1). For each of the reactions studied, the values of $k_a^M = k_1^M k_2^M / k_{-1}^M [\text{MeCN}]$ are presented in Table 4.

References

- [1] Gupta R. P. and Narayana N. L., Synthesis of some Mannich bases of 1-cyclohexylidene-N(1,2-dihydro-2-oxo-3H-indol-3-ylidene) thiosemicarbazones and their antibacterial activity, *Pharmaceutica Acta Helvetiae.*, 1997; 72(1): 43-45.
- [2] Khan S. A., Asiri A. M., Khan A. A., Khan K. A., and Zayed M. A. M., Synthesis of novel schiff bases by microwave irradiation and their in vitro antibacterial activity, *Asian Journal of Chemistry.*, 2013, 25: 8643-8646.
- [3] Casas J. S., García-Tasende M. S., and Sordo J., Main group metal complexes of semicarbazones and thiosemicarbazones, *A structural review*, *Coordination Chemistry Reviews.*, 2000, 209(1): 197-261.
- [4] West D. X., Padhye S. B., and Sonawane P. B., Structural and physical correlations in the biological properties of transition metal heterocyclic thiosemicarbazone and S-alkyl-dithiocarbamate complexes, *Structure Bonding.*, 1991, 76: 1-50.
- [5] E. Liberta and West D. X., Structure Bonding: Antifungal and antitumor activity of heterocyclic thiosemicarbazones and their metal complexes: current status, *Biometals.* 1992, 5(2): 121-126.
- [6] West D. X., Liberta A. E., Padhye S. B. et al, Thiosemicarbazone complexes of copper(II): structural and biological studies, *Coordination Chemistry Reviews.*, 1993, 123(1-2): 49-71.
- [7] Yousef T. A., Abu El-Reash G. M., El-Gammal O. A. and R. A. Bedier, Co(II), Cu(II), Cd(II), Fe(III) and U(VI) complexes containing a NSNO donor ligand: synthesis, characterization, optical band gap, in vitro antimicrobial and DNA cleavage studies, *Journal of Molecular Structure.*, 2012, 1029(12): 149-159.
- [8] Krishnakumar V. and Nagalakshmi R., Crystal growth and vibrational spectroscopic studies of the semiorganic nonlinear optical crystal: bithiourea zinc chloride, *Spectrochimica Acta A.*, 2005, 61(3): 499-507.
- [9] Liu W., Li X., Li Z., Zhang M., and M. Song, Voltammetric metal cation sensors based on ferrocenyl thiosemicarbazone, *Inorganic Chemistry Communications.*, 2007, 10(12): 1485-1488.
- [10] Ying S. -M., Synthesis, crystal structure and nonlinear optical property of a Zinc(II) complex based on the reduced Schiff-base ligand, *Inorganic Chemistry Communications.* 2012, 22:82-84.
- [11] Padhye S., Zahra A., Ekk S. et al, Synthesis and characterization of copper(II) complexes of 4-alkyl/aryl-1, 2-naphthoquinones thiosemicarbazones derivatives as potent DNA cleaving agents, *Inorganica Chimica Acta.* 2005, 358(6): 2023-2030.
- [12] Maurya M. R., Kumar A., Abid M. and Azam A., Dioxovanadium(V) and μ -oxobis[oxovanadium(V)] complexes containing thiosemicarbazone based ONS donor set and their antiamebic activity, *Inorganica Chimica Acta.*, 2006, 359(8): 2439-2447.
- [13] Alomar K., Khan M. A., Allain M., and Bouet G., Synthesis, crystal structure and characterization of 3-thiophene aldehyde thiosemicarbazone and its complexes with cobalt(II), nickel(II) and copper(II), *Polyhedron.*, 2009, 28(7): 1273-1280.
- [14] Ali M. A., Mirza A. H., Chartres J. D., and Bernhardt P. V., Synthesis, characterization and X-ray crystal structures of seven-coordinate pentagonal-bipyramidal zinc(II), cadmium(II) and tin(IV) complexes of a pentadentate N3S2 thiosemicarbazone, *Polyhedron.*, 2011, 30(2): 299-306.
- [15] El-Asmy A. and Al-Hazmi G. A. A., Synthesis and spectral feature of benzophenone-substituted thiosemicarbazones and their Ni(II) and Cu(II) complexes, *Spectrochimica Acta A.*, 2009, 71(5): 1558-1890.
- [16] Al-Karawi A. J. M., Clegg W., Henderson R. and Henderson R. A., Synthetic, structural and kinetic studies on the binding of cyclohexane-1,2-bis(4-methyl-3-thiosemicarbazone) to divalent metal ions (Co, Ni, Cu, Zn or Cd)*, *Dalton Trans.* 2009: 564-570.
- [17] Al-Karawi A. J. M., Synthesis and characterization of a new N2S2 Schiff base ligand and its complexes with nickel(II), cop-

- per(II) and cadmium(II) including the kinetics of complex formation, *Transition Met Chem.* 2009, 34:891-897.
- [18] Silverstein R., Webster F. and Kiemle D; *Spectrophotometric Identification of Organic Compounds.* 7th Ed., New York. John Willy and sons, 2005.
- [19] L Rejane., Leticia, Tania M. and Heloisa B. (1999) *J. Braz. Chem. Soc.* 10:3:18417
- [20] Beraldo H., Boyd L. and West D. (1988) *Trans. Metal. Chem.* 23: 67
- [21] Nakamoto K., *Infrared Spectra of Inorganic and Coordination Compounds*, New York., 1996.
- [22] El-Shazly R., El-Hazmi G., Ghazy S., El-Shahawi M. and El-Asmy A., spectroscopic, thermal and electrochemical studies on same nickel(II) thiosemicarbazone complexes, *Spectro. Chim. Acta.* 2005, 61: 243-252.
- [23] El- said F., El-Asmy A., Kaminsky W. and West D., *Trans. Met. Chem.* ,2003, 28, 954.
- [24] Nakamoto K., *Infrared and Raman Spectra of Inorganic and Coordination Compounds.* ,4th Ed., New York. John Wiley and Sons, 1986.
- [25] Lever A., *Inorganic Electronic Spectroscopy.* New York. 1984.
- [26] Figgis B., *Introduction to Ligand Field.* Publisher, New York. 1966.
- [27] Sutton D., *Electronic Spectra of Transition Metal Complex.*, New York. 1969.
- [28] Tobe M. L. and Burgess J., *Inorganic Reaction Mechanisms.* Ch.7., Longman, Harlow, 1999.

Research Article

Synthesis and Characterization of New Silver (I) N-Heterocyclic Carbene Complex Derived from Imidazol-2-ylidene salt

Mohammed M. Hasson

Department of Chemistry, College of Science, Mustansiriyah University, IRAQ

*Correspondent Author Email: Hassonmm22222@yahoo.com

Article Info

Received
16/05/2016

Accepted
21/05/2017

Abstract

A new *N, N'*-imidazolium salt 1-(2,6-diisopropylphenyl)-3-(4,6-dimorpholino-1,3,5-triazine-2-yl)-1H-imidazol-3-ium chloride) as a precursor of N-heterocyclic carbene ligand was prepared via the reaction of 1-(2,6-diisopropylphenyl)-1H-imidazole) with 1,3,5-triazine derivative bearing morpholine substituent (2,6-dimorpholino-6-chloro-1,3,5-triaziazine). Linear coordinated Ag(I) NHC complex was synthesised via deprotonation of the imidazolium salt and reaction with Ag₂O in darkness at room temperature by in situ method. The complex was synthesised for using as transfer agent to prepare another transition metals complexes by transmetalation method in the future. The imidazolium salt and their silver complex have been characterized by ¹H and ¹³C NMR spectroscopy as well as mass spectrometry.

Keywords: Heterocyclic carbene, Silver complexes.

الخلاصة

تم في هذا البحث تحضير ملح جديد من املاح الاميدازول 1-(2,6-ثنائي ايزوبروبيل فنييل)-3-(4,6-ثنائي مورفولين -5,3,1- ترايزين -2- يل) -H1 - اميدازو -3- ليوم كلورايد. - (4,6 - 3 - (2,6-diisopropylphenyl) - 1) - dimorpholino -1, 3,5-triazine-2-yl) - 1H-imidazol-3-ium chloride) مع التعويض 1-(6,2)-ثنائي ايزوبروبيل فنييل- H اميدازول (2,6 - diisopropyl phenyl -1H- imidazole) مع مركب الترايزين ثنائي التعويض 2 و6- ثنائي المورفولين-6 - كلورو-5,3,1- ترايزين -6 (2,6 - dimorpholine - 6 - chloro-1,3,5-triaziazine). تم استخدام ملح الاميدازول كمصدر لتحضير ليكاند نوع كربين الحلقات الغير متجانسة -N Heterocyclic carbene (NHC) من خلال نزع البروتون من حلقة الاميدازول باستخدام اوكسيد الفضة الاحادية Ag₂O المستخدم كقاعدة لتوليد الكربين و كمصدر للفضة لتحضير معقد الفضة باستخدام الطريقة المباشرة. الغرض من تحضير هذا المعقد هو امكانية استخدامه كناقل لليكاند transfer agent في تحضير بعض العناصر الانتقالية الاخرى باستخدام طريقة transmetalation مستقبلًا. تم تشخيص الملح المحضر ومعقد الفضة باستخدام مطيافية الرنين المغناطيسي وكذلك تقنية طيف الكتلة.

Introduction

N-Heterocyclic carbene (NHC) compounds have got much attention especially when Arduengo synthesized the first free carbene in 1991 [1]. NHC ligands derived from imidazolium salts have received a lot of attention due to the ease of their synthesis. Through modification of the substituents on the nitrogen atoms many imidazolium salts were achieved with a variety of steric properties and asymmetric environment [2], [3], [4], [5], [6], [7], [8], [9].

1,3,5-triazine compound was widely used as a core in synthesis of many compounds due to their reactivity toward nucleophilic substitution

reaction and their ring stability (82.5 K cal/mole) [10] as well as their application in different fields like herbicide production, [11] polymers photostabilizers, [12] and biological properties for example morpholine-s-triazine is used to treat lung and ovarian cancer [13].

Silver N-heterocyclic carbene complexes were synthesized first time in 1993 by Arduengo and his workers. [14]. Due to sensitivity of free carbene toward moisture air and heat. A few number of silver heterocyclic carbene have been prepared by this method as a result of decompose of free carbene ligands [15] [16]. To overcome this obstruction, in situ method was used in synthesis these complexes by using basic silver sources



like Ag_2O in the deprotonation of imidazolium salts. A lot of silver heterocyclic carbene complexes were synthesized by this method due to their easiness of preparation, ambient conditions, and high yield [17] [18]

Silver N-heterocyclic carbene complexes were used as transfer agent for synthesis other transition metals carbene complexes in addition their applications in different fields. [19] [20]

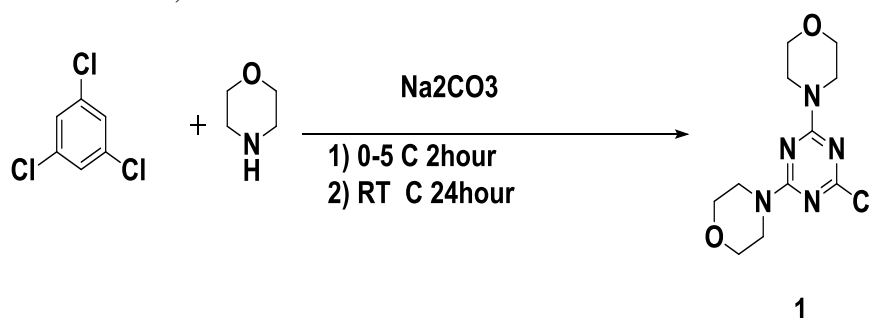
Materials and Methods

Chemical reagents (morpholine $\text{C}_4\text{H}_9\text{NO}$, cyanuric chloride $\text{C}_3\text{N}_3\text{Cl}_3$, Ammonium chloride NH_4Cl , 2, 6-diisopropyl aniline $(\text{CH}_3)_2\text{CH}_2\text{C}_6\text{H}_3\text{NH}_2$, glyoxal $\text{C}_2\text{H}_2\text{O}_2$, formaldehyde CH_2O , and silver oxide Ag_2O were used as received. NMR spectra were obtained using Bruker Avance AMX 250, 400 and JEOL

Eclipse 300 spectrometer, mass spectra were obtained in electrospray (ES) mode. The analysis is performed in the laboratories of School of Chemistry of Cardiff University United Kingdom.

1. Synthesis of 2, 4-di morpholine-6-chloro-1, 3, 5-triazin. [21]

In a round bottom flask cyanuric chloride (9.22 g, 50 mmol) was dissolved in acetone (200 mL) and ice water (200 mL). Morpholine (8.7 g, 100 mmol) was added to the reaction gradually with Na_2CO_3 (10.69 g, 100 mmol). The mixture was stirred ice bath for 2 hours at $0-5^\circ\text{C}$, followed by stirring at room temperature for 24 hours. The white precipitate formed was isolated by filtration and recrystallized from hot ethanol. Yield: 8.8 g (72 %).

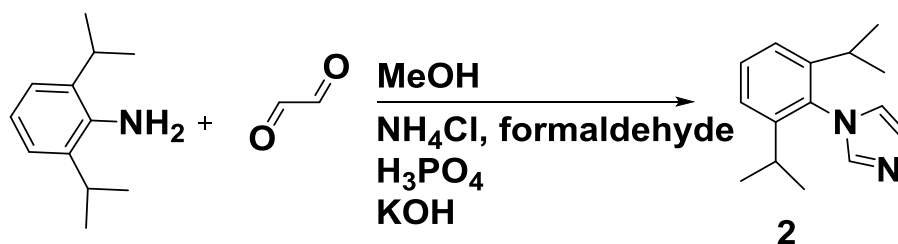


Scheme 1 synthesis of 2,4-dimorpholine-6-chloro-1,3,5-triazine

2. Synthesis of 1-(2,6-diisopropylphenyl)-1H-Imidazole. [22] [23]

2, 6-diisopropylaniline (8.8g, 0.05 mol) in MeOH (25 mL) was stirred with 30% aqueous glyoxal (8.1mL, 0.05mol) for 16 h at room temperature. A bright yellow mixture was formed. NH_4Cl (5.4 g, 0.1 mol) was added followed by 37% aqueous formaldehyde (8 mL, 0.1 mol). The mixture was diluted with MeOH (200 mL) and refluxed for 1 h. H_3PO_4 (7 mL, 85% soln) was added over a period of 10 min. The resulting

mixture was then stirred overnight. After removal of solvent, the dark residue was poured onto ice (200 g) and treated with aqueous 40% KOH solution until $\text{pH} = 9$. The resulting mixture was extracted with EtOAc ($2 \times 200\text{mL}$) and the organic phases were combined and washed sequentially with H_2O and brine solution before drying with anhydrous MgSO_4 . After filtration, the solvent was removed and residue was purified by distillation on a Kugelrohr under vacuum at 240°C .

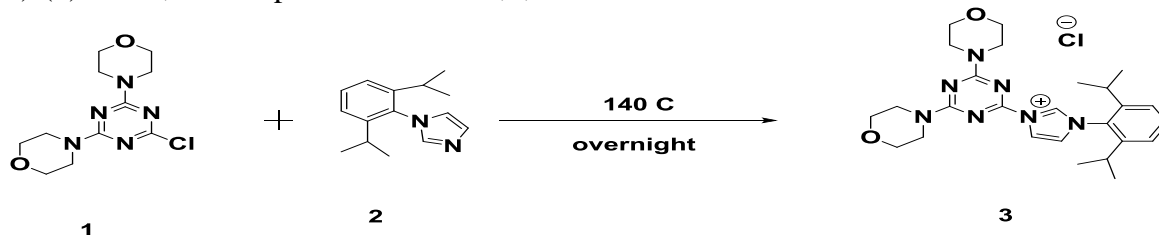


Scheme 2 synthesis of 1-(2,6-diisopropylphenyl) - 1H Imidazole

3. Synthesis of 1-(2,6-diisopropylphenyl)-3-(2,4-dimorpholine-1,3,5-triaz-6-yl)imidazolium chloride.

In a tub pressure a mixture of the 1-(2,6-diisopropylphenyl)-1*H*-Imidazole (0.5 g, 2.1 mmol) (**2**) and 2,6-dimorpholine-chloro-1,3,5-

triazine (**1**) (0.62 g, 2.1 mmol) was stirred at 140 °C overnight. Crud product was dissolved in CH₂Cl₂ (20 mL) and diethyl ether (100 mL) to obtain a white precipitate, yield= 0.89 g (80%).

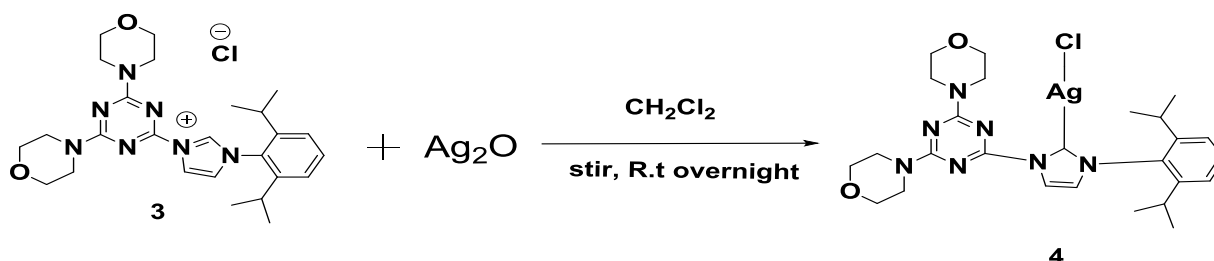


Scheme 3 synthesis of 1-(2,6-diisopropyl)-3-(2,4-dimorpholine-1,3,5-triaz-6-yl)imidazolium chloride

4. Synthesis of [Ag(NHC)Cl]

Imidazolium salt (**3**) (0.41 g, 0.8 mmol) was dissolved in 20mL of CH₂Cl₂ and Ag₂O (0.09 g, 0.4 mmol) was added to the solution, the reaction was stirred under nitrogen for overnight at room

temperature before filtration through celite. The reaction was protected from light by an aluminum foil. The solvent was removed in vacuo and the resulting solid recrystallised (CH₂Cl₂/Et₂O) to produce a whit precipitate



Scheme 4 synthesis of Ag (I) NHC complex

Results and Discussion

Triazine derivative (**1**) (Scheme 1) was prepared according to Dudley method [21] by reaction of 2 equivalent of morpholine with 1 equivalent cyanuric chloride in basic condition to neutralize the hydrogen chloride formed as a side product during the reaction. The recrystallization of crude product was conducted by hot ethanol to produce

a white product with 72% yield. ¹H NMR spectrum confirmed the conversion of cyanuric chloride to secondary amin triazine (2, 4- dimorpholine -6-chloro 1, 3, 5-triazine) by appearance a multiplet at 3.74-3.5 ppm with integration of 16H corresponding to the methylene groups of the morpholine moieties consistent with previous literatures Figure 1 [24].

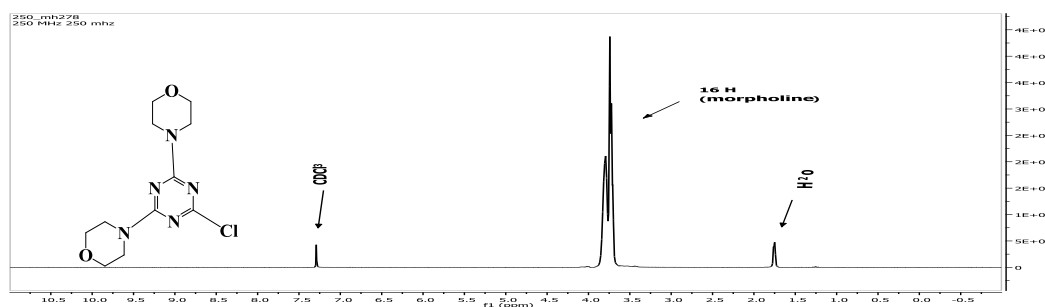


Figure 1: ¹H NMR spectrum of 2,4-dimorpholine -6-chloro- 1,3,5-triazine, **1**.

^{13}C NMR spectra showed two peaks for morpholine in 66.6 and 43.8 ppm in addition two signals in range in 169.7 and 164.4 ppm consistent with carbon atoms of triazine Figure 2. Low resolution mass spectrometry (ES+) was confirmed the formation of compound by appearance of peak at 286 (100%) which can be attributed to the molecular weight of compound $[\text{C}_{11}\text{H}_{16}\text{O}_2\text{N}_5\text{Cl}]^+ [\text{M}+\text{H}]^+$.

1-(2,6-diisopropylphenyl)-1*H*-Imidazole (2) was synthesis by reaction of glyoxal, ammonium

chloride, 1 eq of 2, 6-diisopropylaniline and phosphoric acid in methanol according to previous method (Scheme1) [9,21]. ^1H NMR shows duplet peaks at 1.17 ppm with integration of t 12 H, triplet peak at 2.42 ppm with integration 2H and three singlet peaks at 6.99, 7.31 and 7.52 ppm for imidazole protons as well as doublet peak at 7.29 ppm for *meta*- 2H and multiplet peak at 7.48 ppm for *para*- 1H proton Figure 3.

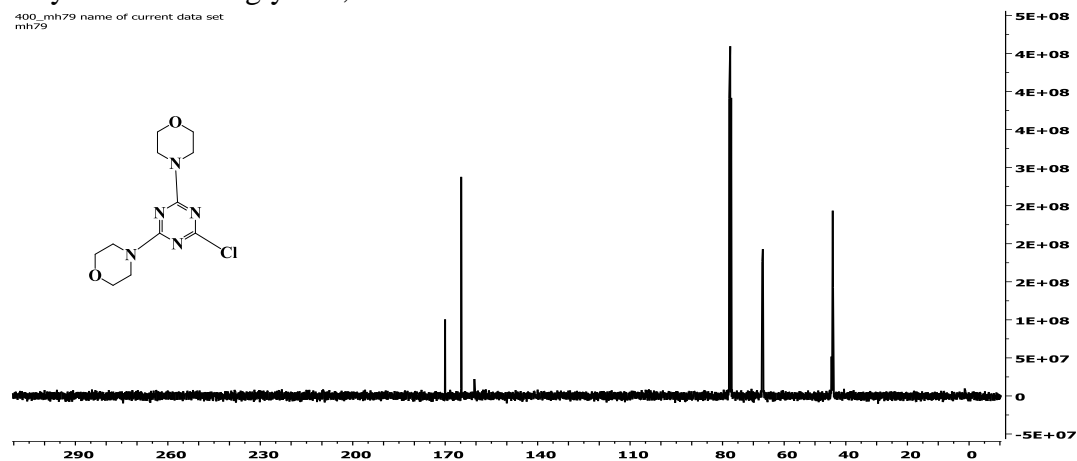


Figure 2: ^{13}C NMR spectrum of 2,4-dimorpholine-6-chloro-1,3,5-triazine, 1

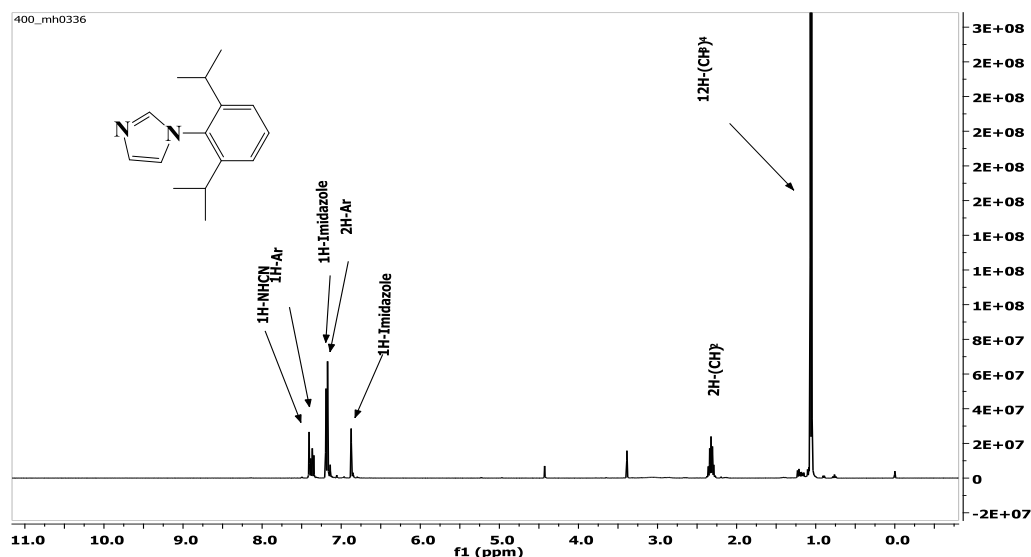


Figure 3: ^1H NMR of 1-(2,6-diisopropylphenyl)-1*H*-imidazole, 2

In order to synthesis the imidazolium salt (3), the corresponding of N-Heterocyclic carbene ligand was synthesised by mixing of 1-(2,6-diisopropylphenyl) imidazole and 2,4-dimorpholine-6-chloro-1,3,5-triazine in pressure

tube in absence of solvent at $140\text{ }^\circ\text{C}$ for overnight, the product was dissolved in dichloromethane and diethyl ether to produce clean powder in yield 70%. ^1H NMR observed two doublet peaks at 1.19 and 1.15 ppm for four methyl

group, multiplet peak at 2.34 ppm with integration 2H for (CH)₂, multiplet peaks in ranges 3.6-3.9 ppm with integration of 16H corresponding to the methylene groups of the morpholine substituents, singlet peaks at 7.78, 8.82 and 10.53

ppm integration to 1H for each peak for imidazole protons, doublet peak and multiplet peak at 7.6 and 7.5 corresponding to 2H in position meta and 1H in Para respectively Figure 4.

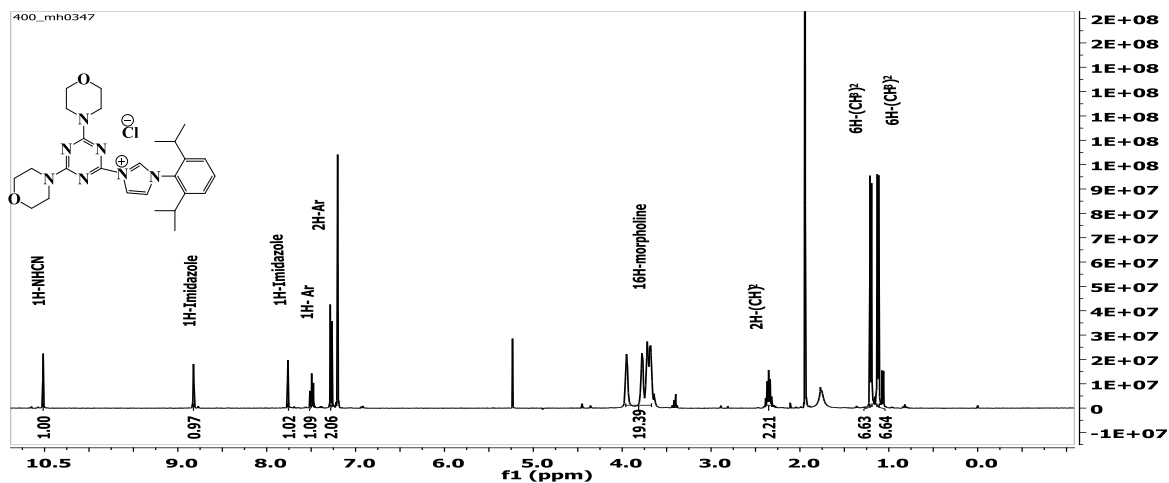


Figure 4: ¹H NMR spectrum of imidazolium salt, 3

¹³C NMR also confirmed the formation of imidazolium salt. peaks were emerged in ranges 120-145 ppm consistent with imidazole ring and aryl carbon atoms, two doublet peaks were emerged at 44.2, 44.6, 66.0, 66.6 ppm corresponding with morpholine carbon atoms, in addition two peaks

at 24.4, 24.6 and 28.7 for methyl groups as well as two peaks in 158.9 and 164.6 observed can be attributed to triazine carbon atoms Figure 5 Mass ES spectrometry gave peak at 478.32 corresponding to [M-Cl]⁺, Figure 6.

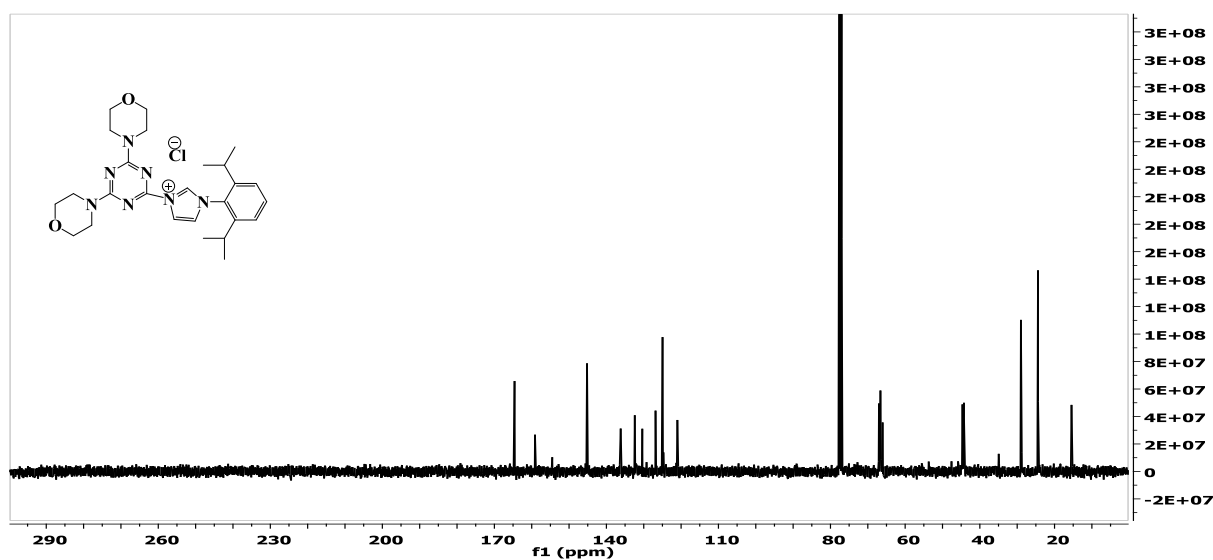


Figure 5: ¹³C NMR spectrum of imidazolium salt, 3

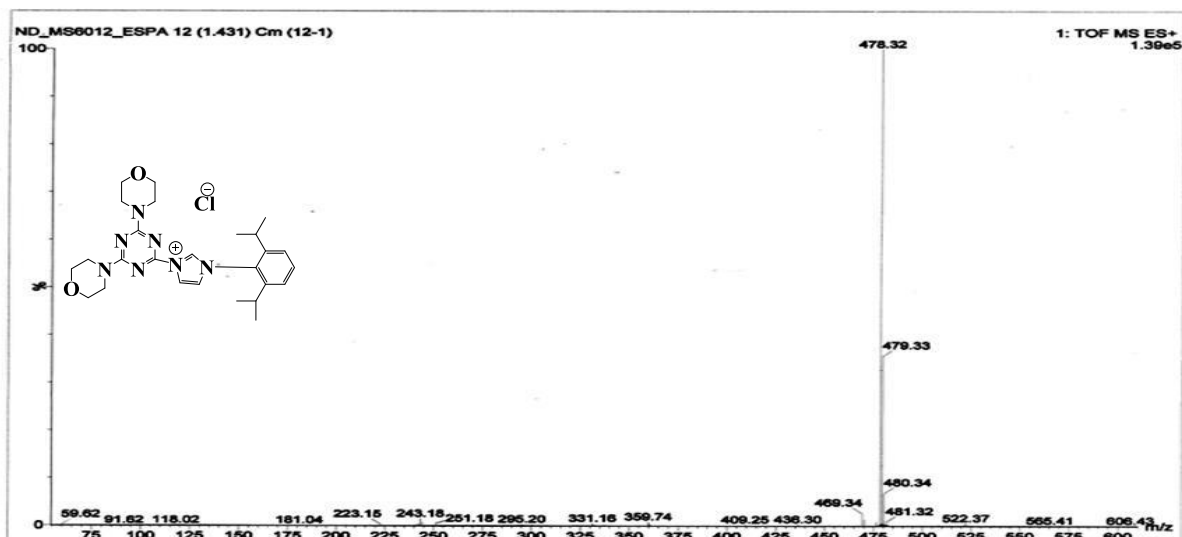


Figure 6: mass spectrum of imidazolium salt, 3

Silver N-heterocyclic carbene complex $[Ag(NHC)Br]$ was synthesised via in situ method [17] [25] by reaction of the imidazolium salt with Ag_2O under ration 2:1% in dry dichloromethane under nitrogen at room temperature overnight, the reaction was protected from light by aluminum foil to avoid the photodecomposition of silver complex.

The reaction was set up by filtration through a pad of celite. The product of crud has been re-

crystallized by diffusion of diethyl ether in concentrated dichloromethane solution of the crude product. The imidazolium salt Deprotonation was confirmed by peak disappearance at 10.53 ppm which attributed to (NCHN) in addition peaks attributed to imidazole ring in position C4 and C5 were moved up field at 6.95 and 8.15 ppm Comparison with the ligand precursors in the ranges 7.8, 8.8 ppm as coordination result with Ag and formation of complex, Figure 7.

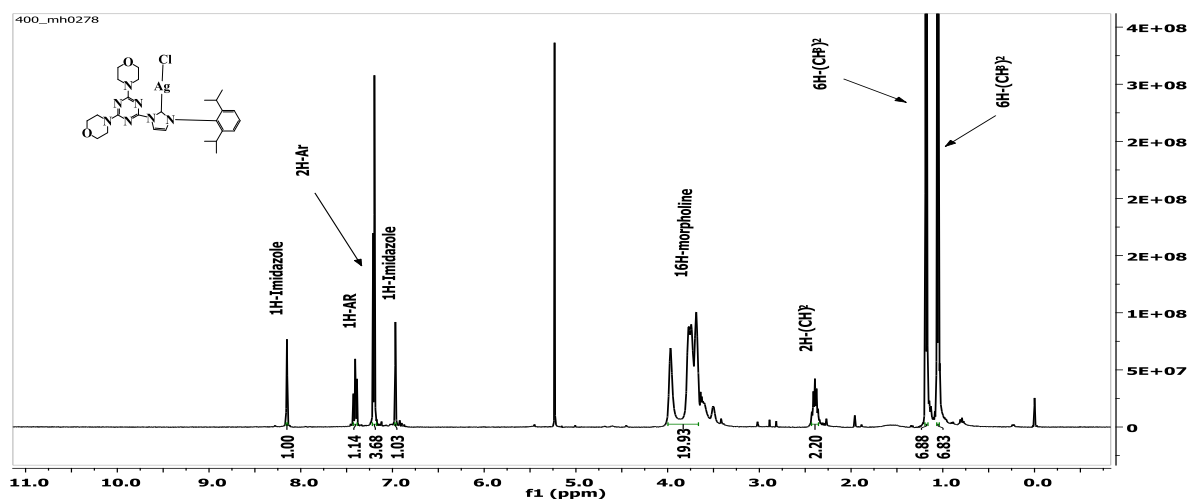


Figure 7: 1H NMR of $[Ag(NHC)Cl]$, 4

The formation of the silver complex was confirmed by the ^{13}C NMR spectrum by disappearance of NHCN peak and the emergence of a weak peak at 187 ppm for Ag-C carbene which consistent with previous literatures. ^{13}C NMR spectrum was observed single peak for Ag-

C instead of two due to fluxional changes between the ionic and neutral complex; for example Internal change between the mono- and bis-carbene species.

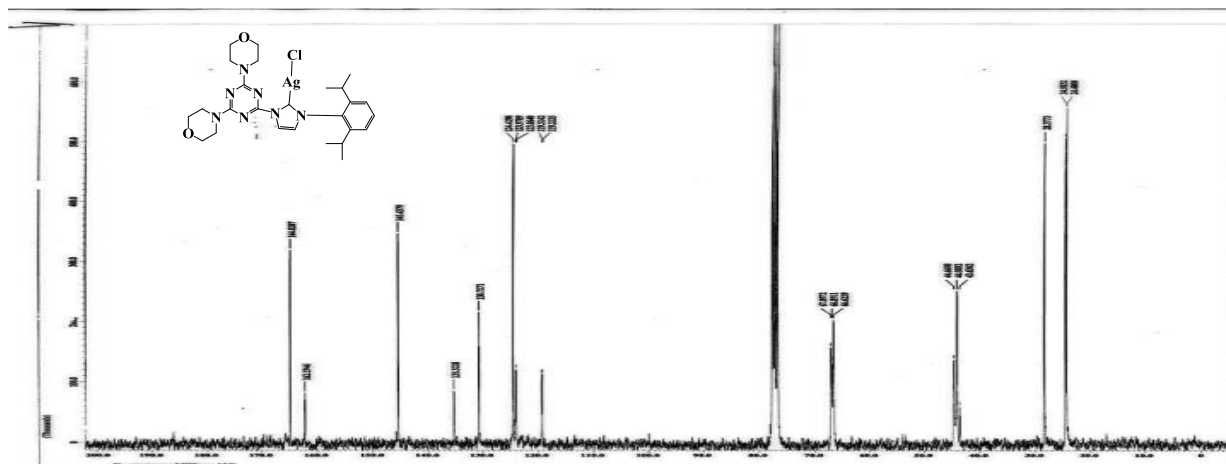


Figure 8: ^{13}C NMR of $[\text{Ag}(\text{NHC})\text{Cl}]$ complex, **4**

Mass spectrum of the silver complex has been found that the complex formed biscarbene structures in gas state with the formula, $[\text{Ag}$

$(\text{NHC})_2]^+$, which is combatable with previous reports in the literature, Figure 9 [26].

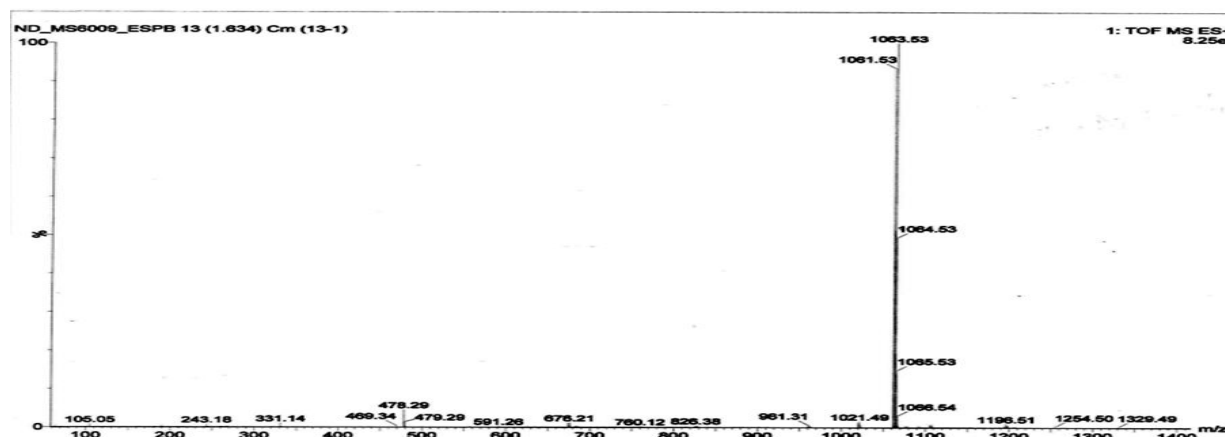


Figure 9: mass spectrum of $[\text{Ag}(\text{NHC})\text{Cl}]$ complex, **4**

References

- [1] Rowan, M. P. ; Cancio, L. C. ; Elster, E. A. ; Burmeister, D. M. ; Rose, L. F. ; Natesan, S. and Chung, K. K. Burn wound healing and treatment: review and advancements. *Critical care*, 2015.19, 243.
- [2] Barret, J. P. ; Herndon, D. N. Effects of burn wound excision on bacterial colonization and invasion. *Plast Reconstr Surg* 2003; 111 (2): 744-50; discussion 751-752.
- [3] McCulloh, R. J. Biomarkers in Sepsis and Severe Infection: Where Immunology Meets Diagnostics.2012. *J Immunodeficient Disor* 2012, 1: 1.
- [4] Castelli, G. P. ; Pognani, C. ; Meisner, M. ; Stuani, A., Bellomi, D. and Sgarbi, L. Procalcitonin and C-reactive protein during systemic inflammatory response syndrome, sepsis and organ dysfunction. *Crit Care*.2004 Aug; 8 (4): R234-42.
- [5] Aabenhus, R.1; Jensen, J. U. Procalcitonin-guided antibiotic treatment of respiratory tract infections in a primary care setting: are we there yet? *Prim Care Respir J*.2011 Dec, 20 (4): 360-7.

- [6] Caliendo, A. M.1; Gilbert, D. N. ; Ginocchio, C. C. ; Hanson, K. E. ; May, L. ; Quinn, T. C. ; Tenover, F. C. ; Alland, D. ; Blaschke, A. J. ; Bonomo R. A., Carroll, K. C. ; Ferraro, M. J. ; Hirschhorn, L. R. ; Joseph, W. P. ; Karchmer T. ; MacIntyre, A. T. ; Reller, L. B. and Jackson, A. F. Infectious Diseases Society of America (IDSA). Better tests, better care: improved diagnostics for infectious diseases. *Clin Infect Dis.*2013 Dec;57 Suppl 3: S139-70.
- [7] Mohan, A. and Harikrishna, J. Biomarkers for the diagnosis of bacterial infections: in pursuit of the 'Holy Grail' *Indian J Med Res.*2015 Mar; 141 (3): 271–273.
- [8] Mokline, A. ; Garsallah, L. ;Rahmani, I. ; Jerbi, K. ; Oueslati, H. ; Tlaili, S. ; Hammouda, R. ; Gasri, B. and Messadi, A. A. Procalcitonin: a diagnostic and prognostic biomarker of sepsis in burned patients. *Ann Burns Fire Disasters.*2015 Jun 30;28 (2): 116-20.
- [9] Rosanova, M. T. ; Tramonti, N. ; Taicz, M. ; Martiren, S. ; Basilico, H. ; Signorelli, C. and Lede, R. Assessment of C-reactive protein and procalcitonin levels to predict infection and mortality in burn children. *Arch Argent Pediatr.* 2015.113 (1), 36-41.
- [10] Kim, H. S. ; Yang, H. T. ; Hur, J. ; Chun, W. ; Ju, Y. S. ; Shin, S. H. and Lee, K. M. Procalcitonin levels within 48 hours after burn injury as a prognostic factor. *Ann Clin Lab Sci.* 2012.42 (1), 57-64.
- [11] Nakae, H. ; Inaba, H. and Endo, S. Usefulness of procalcitonin in Pseudomonas burn wound sepsis model. *Tohoku J Exp Med.*1999 Jul;188 (3): 271-3.
- [12] Tahir, S¹. ; Memon, A. R. ; Kumar, M. and Ali, S. A. Prediction of mortality after major burn: physiological versus biochemical measures. *Wounds.*2009 Jul; 21 (7): 177-82.
- [13] Zarei, M. R.1; Dianat, S. ; Eslami, V. ; Harirchi, I. ; Boddouhi, N. ; Zandieh A. and Rasouli, M. R. Factors associated with mortality in adult hospitalized burn patients in Tehran. *Ulus Travma Acil Cerrahi Derg.* 2011. Jan;17 (1): 61-5.
- [14] Moore, E. C. ; Pilcher, D. V. ; Bailey, M. J. ; Stephens, H. and Cleland, H. The Burns Evaluation and Mortality Study (BEAMS): predicting deaths in Australian and New Zealand burn patients admitted to intensive care with burns. *Journal Trauma Acute Care Surg.* 2013. Aug;75 (2): 298-303.
- [15] Zhao, D. ; Zhou, J. ; Haraguchi, G. ; Arai, H. and Mitaka, C. Procalcitonin for the differential diagnosis of infectious and non-infectious systemic inflammatory response syndrome after cardiac surgery. *J Intensive Care.* 2014. Jun 3;2: 35.
- [16] Klingele, M. ; Bomberg, H. ; Poppleton, A. ; Minko, P. ; Speer, T. ; Schäfers, H. J. and Groesdonk, H. V. Elevated procalcitonin in patients after cardiac surgery: a hint to nonocclusive mesenteric ischemia. *Ann Thorac Surg.* 2015. Apr;99 (4): 1306-12.
- [17] Barati, M. ; Alinejad, F. ; Bahar, M. A. ; Tabrisi, M. S. ; Shamshiri, A. R. ;Bodouhi, N. O. ; and Karimi, H.comparison of WBC, ESR, CRP and PCT serum levels in septic and non-septic burn cases. *Burns.* 2008.34 (6), 770-774.
- [18] Seoane, L. ; Pertega, S. ; Galeiras, R. ; Astola, I. ; and Bouza, T. Procalcitonin in the burn unit and the diagnosis of infection. *Burns.* 2014.40 (2), 223-229.
- [19] Mann, E. A. ; Wood, G. L. ; and Wade, C. E. Use of procalcitonin for the detection of sepsis in the critically ill burn patient: a systematic review of the literature. *Burns.* 2011.37 (4), 549-558.
- [20] Von Heimburg, D., Stieghorst, W., Khorram-Sefat, R. and Pallua, N. Procalcitonin—a sepsis parameter in severe burn injuries. *Burns.* 1998.24 (8), 745-750
- [21] Neely, A. N. ; Smith, W. L. ; and Warden, G. D. Efficacy of a rise in C-reactive protein serum levels as an early indicator of sepsis in burned children. *J Burn Care Rehabil.* 1998.19 (2), 102-105.
- [22] Alkazaz F. F. ; Abdulsattar S. A. ; Farred F. A. and Mahmood S. J. Risk factor of metabolism alteration in burn patients. SENRA Academic Publishers, British Columbia, 2014. Vol.8, No.3, pp.3057-3060,
- [23] Jeschke, M. G. ; Finnerty, C. C. ; Kulp, G. A. ; Kraft, R. ; and Herndon, D. N. Can we use C-reactive protein levels to predict se-

vere infection or sepsis in severely burned patients? *International Journal of Burns and Trauma*, 2013.3 (3), 137-143.

- [24] Lavrentieva, A. ; Kontakiotis, T. ; Lazaridis, L. ; Tsotsolis, N. ; Koumis, J. ; Kyriazis, G. ; and Bitzani, M. Inflammatory markers in patients with severe burn injury. What is the best indicator of sepsis? *Burns*, 2007.33 (2), 189-194.
- [25] Neely, A. N. ; Fowler, L. A. ; Kagan, R. J. ; and Warden, G. D. Procalcitonin in pediatric burn patients: an early indicator of sepsis? *Journal Burn Care Rehabil*, 2004.25 (1), 76-80.
- [26] Sachse, C. ; Machens, H. G. ; Felmerer, G. ; Berger, A. ; and Henkel, E. Procalcitonin as a marker for the early diagnosis of severe infection after thermal injury. *J Burn Care Rehabil*, 1999.20 (5), 354-360.

Research Article

Theoretical Study and Biological Activity of Co(II), Ni(II), Cu(II), Pd(II), Pt(IV) and Cd(II) Complexes with 2-Thioxoimidazolidin-4-one Derivative

Sallal A. H. Abdullah¹, Rehab A. M. Al Hassani², Abdul Jabar K. Atia², Sura K. Ibrahim³

¹ Department of Applied Science, Chemistry Division, University of Technology, IRAQ

² Department of Chemistry, College of Science, Mustansiriyah University, IRAQ

³ Department of Chemistry, College of Science for Women, Baghdad University, IRAQ

*Correspondent Author Email: rehabalhassani@yahoo.com

Article Info

Received
01/09/2016

Accepted
17/04/2017

Abstract

The work contains a theoretical treatment of the prepared ligand (3-[(Z)-(4-nitrophenyl) methylidene] amino)-2-thioxoimidazolidin-4-one [L] and their metal complexes [S₁-S₆] in the gas phase. Hyperchem-8 program has been used to determine structural geometries of ligand and their metal complexes. The electrostatic potential (E_p) of the ligand was calculated, furthermore binding energy (ΔE_b), the heat of formation (ΔH_f), vibration spectra and bond length for the ligand and their metal complexes were calculated by PM3 methods at 298K°. The theoretically calculated data were agreed with those found experimentally. The antibacterial activity for free ligand and its metal complexes (S₁-S₆) were studied against two selected micro-organisms [(*Staphylococcus aureus*) as gram positive] and [(*Escherichiacoli*) as gram negative]. The minimal inhibitory concentrations (MIC) have been also studied to determine the low concentration for inhibition. The antibiotics (Amoxicillin and Ampicillin) have been chosen to compare their activity with those of the new compounds. Furthermore the antifungal activity against two microorganisms (*Candidaalbicans*) and (*Aspergillusflavus*) were studied for all compounds. The results showed great activity of the complexes relative to that of free ligand.

Keywords: 2-thioxoimidazolidin-4-one, complexes, theoretical study, biological activity.

الخلاصة

تضمن هذا العمل معالجة نظرية للليكاند المحضر (3-[(Z)-(4-nitrophenyl)methylidene]amino)-2-: [L] والثيوإيميدازوليدين-4-ون (thioxoimidazolidin-4-one) ومعقداته [S₁-S₆] في الطور الغازي. استخدم برنامج (Hyperchem-8) لاستنتاج الأشكال الهندسية للليكاند ومعقداته. تم حساب حرارة تكوين (ΔH_f) والجهد الإلكتروني وسناتيك (E_p) وطاقة التناصر (ΔE_b) والأطياف الاهتزازية وأطوال الأواصر لكل من الليكاند ومعقداته وباستخدام دالة PM3 وعند درجة حرارة 298K°. ووجد بأن هنالك توافقاً كبيراً بين القيم العملية والنظرية. تم تقويم الفعالية المضادة للبكتيريا للليكاند [L] ومعقداته [S₁-S₆] واختير نوعان من البكتيريا موجبة الصبغة (*Staphylococcus aureus*) وسالبة الصبغة (*Escherichiacoli*). تم دراسة أقل تركيز يحدث عندها التثبيط (MIC) وتمت مقارنة فعالية المركبات المحضرة مع نوعين من المضادات الحيوية (*Amoxicillin* و *Ampicillin*). كما تم إجراء التقويم الحيوي للليكاند ومعقداته ضد نوعين من الفطريات (*Candidaalbicans*) و (*Aspergillus flavus*). وقد أظهرت النتائج الفعالية العالية للمعقدات مقارنة بالليكاند.

Introduction

Thioxoimidazolidin is a five membered heterocyclic ring with two nitrogen atoms and contain two groups, thion (C=S) and carbonyl (C=O) at position, 2 and 4, respectively [1] [2]. Thioxoimidazolidin are biologically active molecules widely used in medicine as drugs [3] [4] [5] [6]. It is also an effective medication for the treat-

ment of some type of cancer [7] [8] as well as it is may be used as fungicides and herbicides [9] [10]. In literature there are some papers studies the crystal structure and hydrogen bonding interaction of 2-thioxoimidazolidin-4-one [11] [12]. In our previous work [13] the Schiff base [L], and its metal complexes [S₁-S₆] have been prepared and investigated using different chemical tech-



niques, as well as molar ratio method measurement in solution gave comparable results with those obtained from solid state studies. Continuing the studies on free ligand and its complexes. This paper reports here the theoretical studies in the gas phase was done by using semi-empirical method in order to show the most stable conformation. The study aims to calculate the binding energy, heat of formation for all the structures geometries to find the most active sites of the [3-[(Z)-(4-nitrophenyl) methylidene] amino]-2-thioxoimidazolidin-4-one [L] by using the electrostatic potential calculations. The vibrational frequencies of the free ligand [L] and their metal complexes have been carried out in order to compare the results with the experimental vibrational frequencies to make assignment of the most diagnostic bands.

The biological activities for free ligand [L], and its metal complexes [S₁-S₆] were employed in the present study to show the effect of introducing the azomethian group in the (2-thioxoimidazolidin-4-one) ring to compare the biological activity of the ligand and their complexes with the main ring structure.

This paper reports here the theoretical studies in the gas phase was done by using semi-empirical method in order to show the most stable conformation. The study aims to calculate the binding energy, heat of formation for all the structures geometries to find the most active sites of the [3-[(Z)-(4-nitrophenyl) methylidene] amino]-2-thioxoimidazolidin-4-one [L] by using the electrostatic potential calculations. The vibrational frequencies of the free ligand [L] and their metal complexes have been carried out in order to compare the results with the experimental vibrational frequencies to make assignment of the most diagnostic bands. The biological activities for free ligand [L], and its metal complexes [S₁-S₆] were employed in the present study to show the effect of introducing the azomethian group in the (2-thioxoimidazolidin-4-one) ring to compare the biological activity of the ligand and their complexes with the main ring structure.

Materials and Methods

(A)-Theoretical treatment

Hyperchem is a sophisticated molecular modeler; it is a powerful computational package, that is known for their quality and ease of use [14] [15]. It can plot orbital wave functions resulting from

semi-empirical quantum mechanical calculations, the total charge density or the total spin density and the electrostatic potential can be determined during semi-empirical calculation, this information is useful in determining reactivity and correlating calculation results with experimental data.

1-Computational methods:

- Semi-empirical quantum mechanical,
- Molecular mechanics, c) Mopac 2000

2-Types of calculations:

The types of prediction possible of Molecules are [14]: Geometry optimization calculations used energy minimization algorithms to locate Bond distances, stable structures, Molecular dynamics which gave the thermodynamic calculations and dynamic behavior of molecules, Plot the electrostatic potential field (HOMO and LUMO), and Vibrational spectrum (I. R and Raman spectra).

(B)-Study of biological activities for (L) ligand and their Metal Complexes (S₁-S₆)

The bioactivities of the free ligand (L) and its complexes (S₁-S₆) were studied against selected types of bacteria which include (*Escherichia coli*) and (*Staphylococcus aureus*) cultivated in Nutrient agar medium, DMSO was used as a solvent and as a control, the concentration of the complexes of this solvent was (10⁻³M) [15, 16]. The new complexes (S₁-S₆) were tested for their *in vitro* growth inhibitory activity against further pathogenic fungi, i. e., [*Candida albicans* and *Aspergillus flavus*] on potato dextrose agar medium and incubated at 30 °C for 72 hours. DMSO was used as a solvent and as a control for both techniques.

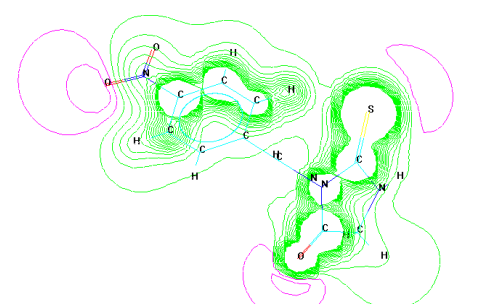
The concentrations of the compounds in this solvent were (10⁻³M). The inhibition of fungal growth expressed in percentage terms, were determined on the growth in test plates compared to the respective control plates.

Results and Discussion

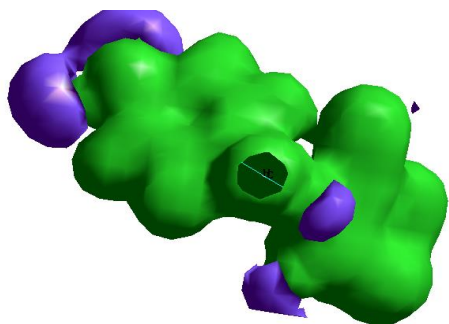
Study Complexes in Gas Stat (Theoretical studies): Electrostatic Potentials:

The electrostatic potential (E. P) describes the interaction of energy of the molecular system with a positive point charge. The active side can be found by calculating (E. P) in a molecule;

positively charged species tend to attack a molecule where the electrostatic potential is strongly negative (electrophonic attack)[14] [17] [18]. The (E. P) of the ligand (L) were calculated and plotted as 2D and 3D contours to investigate the reactive sites of the molecules, Figure1. The results of calculate -ions show that the LUMO of transition metal ions prefer to react with the HOMO of two-donor atoms of sulfur of thion group and nitrogen of the azomithane group for free ligand (L),Figure2.

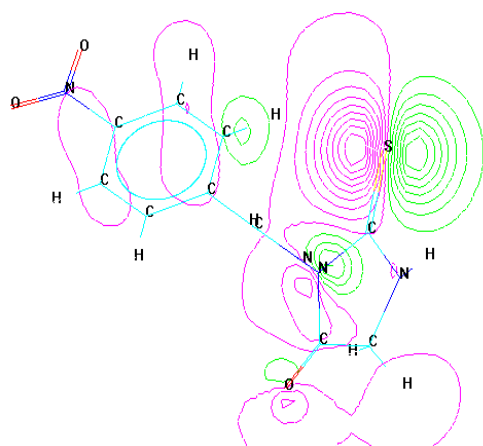


E. P. (L) in 2D

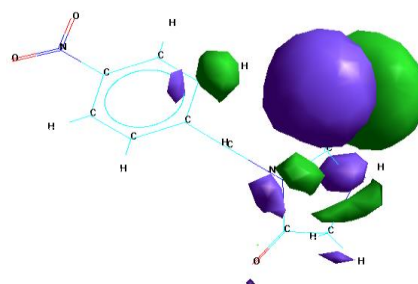


E. P. (L) in 3D

Figure 10 : Electrostatic Potential as 2D&3D Counters for ligand L



HOMO and LUMO in 2D for (L)₂



HOMO and LUMO in 3D for (L)

Figure 11: HOMO and LUMO Sites for the L

Optimized energies: The heat of formation (ΔH_f°), binding energy (ΔE_b), and total energy (ΔE_T) for ligand (L) and its metal complexes (S_1 - S_6) were calculated, by using the semi-empirical (PM3) and (AMBER) methods, Table 1.

Table 1 : Conformation energetic (in KJ. mol⁻¹) for the L and their metal complexes (S_1 - S_6).

No.	PM3			AMBER
	ΔH_f°	ΔE_b	ΔE_T	ΔE_T
L	226	-11573	-291004	
S ₁	-1145	-25476	720062	
S ₂	-425	-24696	743800	
S ₃	1640	-22538	755897	
S ₄	-----	-----	-----	520
S ₅	1124	-22849	681625	
S ₆	1911	-21798	582825	

Optimized vibrational spectra for ligand (L): The vibrational spectra of the prepared ligand (L) and its metal complexes (S_1 - S_6) have been calculated, Table 2. The results of theoret -cally calculated wave numbers for ligand and its complexes showed that some of deviations from the experimental values, these devia -tions are acceptable in theoretical calculations[14] [18] [19] [20] [21] Tables 2.

Table 2: Comparison between the experimental and theoretical vibrational frequencies (cm⁻¹) for free ligand (L) and their metal complexes.

Comp.	$\nu_{\text{N-H}}$	$\nu_{\text{C=N}}$	$\nu_{\text{C=O}}$	$\nu_{\text{C=S}}$	$\nu_{\text{M-N}}$	$\nu_{\text{M-S}}$
L	3329*	1633*	1708*	1099*		
	3404**	1606**	1800**	1030**	-	-
	2.203**	1.681***	5.11***	6.699		
S₁	3336*	1618*	1707*	1072*	535*	462*
	3243**	1609**	1727**	1077**	530**	477**
	2.87***	0.56***	1.158***	0.464***	0.943***	3.114***
S₂	3267*	1614*	1703*	1068*,1076*	530*	458*
	3404**	1592**	1797**	1051**,1088**	532**	455**
	4.02***	1.38***	5.23***	1.62***,1.1***	0.375***	0.659***
S₃	3299*	1619*	1705*	1078*	528*	460*
	3381**	1728**	2000**	1073**	551**	471**
	3.522***	6.195***	14.75***	-0.465***	4.174***	2.335***
S₄	3240*	1608*	1710*	1072*	533*	455*
	3232**	1571**	1671**	1088**	524**	457**
	0.247***	2.36***	2.333***	1.47***	1.171***	0.437***
S₅	3172*	1620*	1708*	1082*	530*	462*
	3200**	1674**	2000**	1111**	552**	457**
	0.88***	3.225***	14.6***	2.61***	3.985***	1.094***
S₆	3240*	1593*	1710*	1051*,1064*	533*	458*
	3263**	1598**	1720**	1044**,1059**	537**	450**
	0.70***	0.31***	0.58***	0.67***,0.47***	0.744***	1.777***

*: Experimental frequencies ** : Theoretical frequencies ***Error %

Optimized geometries of ligand (L) and their metal complexes

Theoretically chosen structures of ligand and its metal complexes have been calculated to find the most possible model building stable structure for ligand and its metal complexes, as shown in Figure 3.

Bond lengths measurements for (L) and their metal complexes

The Gaussian suite of software was employed throughout this study optimizations were carried out for the model systems represented in Figure 4, Table 3, for the free ligand and its metal complexes by using the semi-empirical (PM3) meth-

od at geometry optimization (0.001Kcal/mol). The data results gave excellent agreement with the experimental data [14] [19] [22].

Table 3: Bond length of Ligand and their Metal Complexes.

Comp.	C=N	C=S
L	1.289	1.6224
S₁	1.3126	1.6507
S₂	1.2835	1.6569
S₃	1.3187	1.7627
S₄	1.3261	1.6768
S₅	1.3138	1.7069

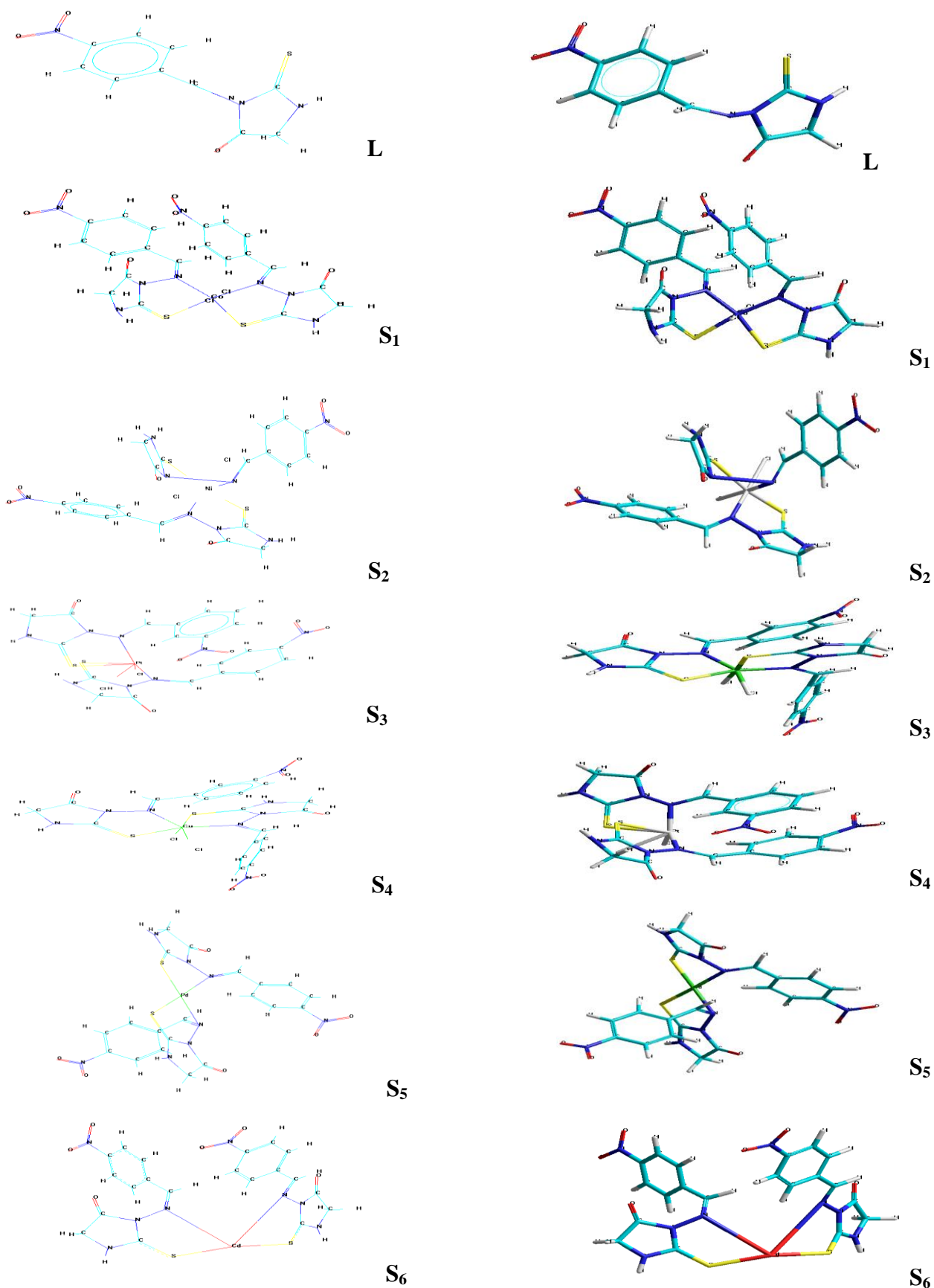


Figure 12: Conformation structure of Ligand (L) and their metal complexes using Hyperchem 8 Program

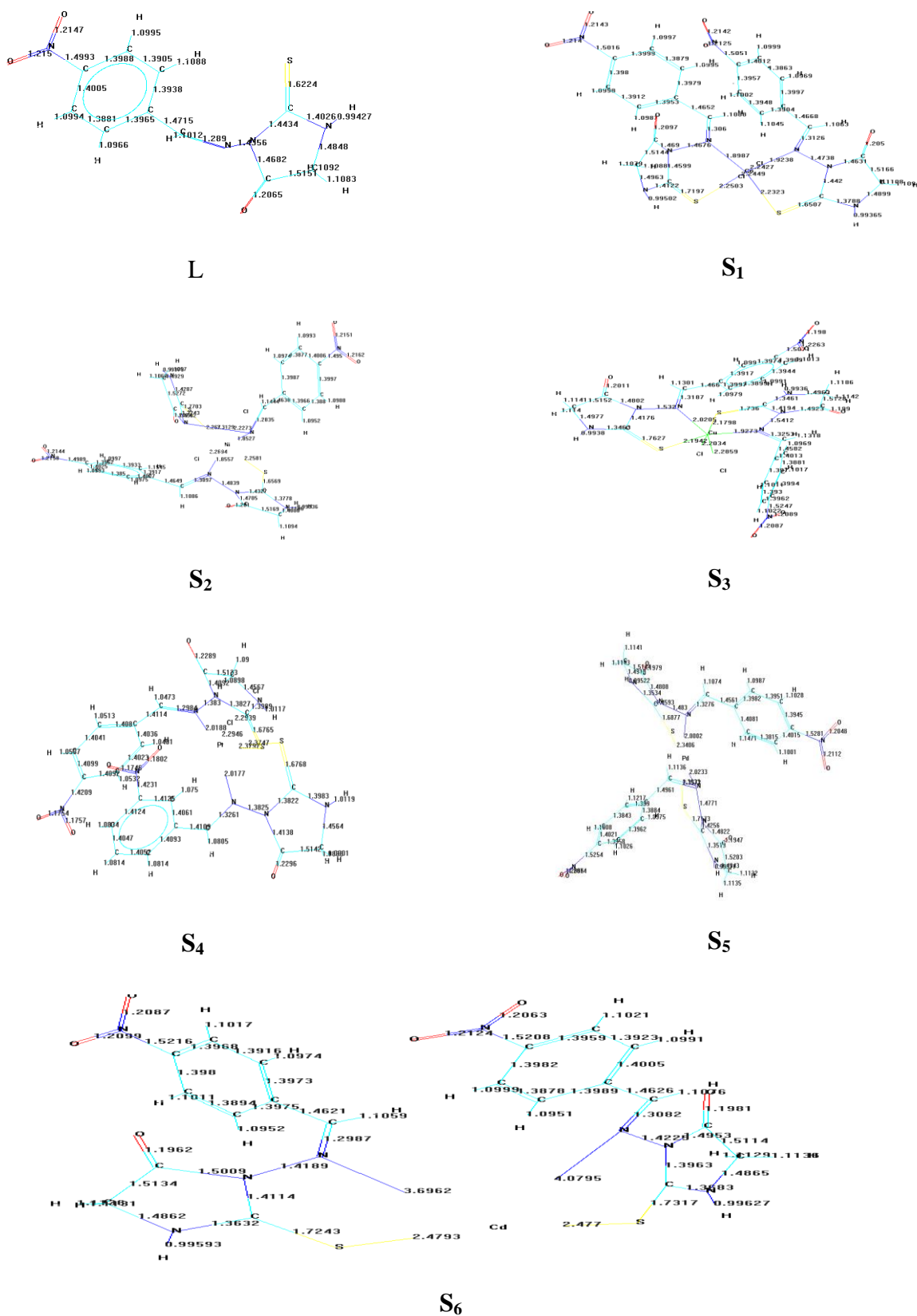


Figure 13: Bond length of Ligand and their metal complexes Using Hyperchem.

Biological Studies

The ligand (L) and their metal complexes (S₁-S₆) were screened *in vitro* for their ability to inhibit the growth of representative [*E. coli*] as gram negative] and [*Staph. aureus*] as gram positive] are shown in Table (4). Also the study was done against (*Candida albicans* and *Aspergillus flavus*) fungus, in DMSO as a solvent, Table 4. As a result from the above mentioned studies, the following points were concluded:

1) The study of antibacterial activities gave that the ligand (L), exhibited high activity against the studied bacteria *Staph. aureus* while against *E. coli*. was moderately active.

2) (S₁-S₆) complexes showed highly active against two types of bacteria compared with the free ligand (L).

3) Results of the antifungal activity of the new compounds, Table 4 showed that the metal ion complexes (S₁-S₆) were more toxic compared with their parent ligand (L) toward the same micro-organism and under the identical experimental conditions. The increase in the antifungal activity of metal chelates may be due to the effect of the metal ion on the normal cell process; these

activities may be explained by Tweedy's Chelation theory [15]. According to this theory the polarity of the metal atom mainly reduce the polarity of metal ions, because of the partial sharing of its positive charge with the donor groups of the ligand, which favors permeation of the complexes through the lipid layer of cell membrane [16, 22].
4) The results of the (MIC) were compared with those of the two antibiotics, Table 5. The new compounds were more active at low concentration, Table 5.

Table 4: Antibacterial and antifungal activities for ligand (L) and their metal complexes (S₁-S₆) (10⁻³ μgm. ml⁻¹)

No.	<i>E. coli</i>	<i>Staph. aureus</i>	<i>Cand. albic</i>	<i>Asper . flav</i>
Con DMSO	-	-	-	-
L	4	6	30	27
(S ₁)	6	8	27	20
(S ₂)	8	10	23	25
(S ₃)	10	12	20	22
(S ₄)	14	16	18	20
(S ₅)	8	10	24	26
(S ₆)	18	14	19	16

Table 5: Minimal inhibitory concentration (MIC) for Schiff base (L) ligand and [S₁-S₆] their metal complexes (μgm. ml⁻¹)

Symb.	<i>Escherichia coli</i>					<i>Staphylococcus aureus</i>				
	0.025	0.05	0.075	0.1	0.5	0.025	0.05	0.075	0.1	0.5
(L)	+	+	(MIC)	-	-	+	(MIC)	-	-	-
(S ₁)	+	(MIC)	-	-	-	+	(MIC)	-	-	-
(S ₂)	+	(MIC)	-	-	-	+	(MIC)	-	-	-
(S ₃)	(MIC)	-	-	-	-	(MIC)	-	-	-	-
(S ₄)	(MIC)	-	-	-	-	(MIC)	-	-	-	-
(S ₅)	+	(MIC)	-	-	-	+	(MIC)	-	-	-
(S ₆)	(MIC)	-	-	-	-	(MIC)	-	-	-	-
Ampicillin	+	+	+	(MIC)	-	+	+	+	+	(MIC)
Amoxicillin	+	+	+	(MIC)	-	+	+	+	+	(MIC)

Conclusion

Hyperchem-8 program has been used to predict structural geometries of all compounds in gas phase. The free ligand (L) and its metal complexes [1-6] show significant antimicrobial activity. The all complexes are found more effective than the free ligand.

References

[1] D. W. Zerong, O. S. Samia and Z. Yulu, "A Simple Synthesis of 2-Thiohyd -antoin, ", *Molecules*, vol.11, pp. : 739-750., 2006.



- [2] A. J. A. Nasser, A. I. Adhulla, R. S. Kumar, J. Selvin "Synthesis of Some 2-Thioxoimidazolidin-4-one Derivatives and its Antimicrobial Activity,," *E-J. Chem.*, vol.7, no. (4), pp. :1320-1325., 2010.
- [3] B. Vinod, D. Selvakumar, and K. K. Bincy "Synthesis, antibacterial and antifungal activities of novel diphenyl hydantoin-carboxamides,," *Int J Pharm Bio Sci*, vol.4, no. (1), p. :759-767., 2013.
- [4] B. Shipra, C. Sumitra, P. Hemali and R. Paras "Synthesis, characterization and antimicrobial activity of some new 2-thioxoimidazolidin-4-one derivatives,," *Ijpcbs*, vol.5, no. (1), pp. :196-202., 2015.
- [5] M. E. Abd El-Fattah, "Synthesis and investigation of mass spectra of 3-substituted-2-thioxoimidazolidin-4-one derivative,," *Ind. J. of Chem.*, vol.45B, pp. : 2523-2533., 2006.
- [6] A. I. Khodair, H. I. El-Subbagh and A. A. El-Emam "Synthesis of certain 5-substituted 2-thiohydantoin derivatives as potential cytotoxic and antiviral agents,," *Boll. Chim Farm.*, vol.136, pp. :561-567., 1997.
- [7] E. Delgado Gerzon, N. Varela Kristal, V. Araque Rohixa, A. Rodríguez Jesús, J. Mora Asiloé and E. Seijas Luis "Synthesis, crystal and supramolecular structure of rac-N-acetyl-2-thiohydantoin-asparagine,," *Avances en Química*, vol.9, no. (1), pp. :3-6., 2014.
- [8] S. Vengurlekar, R. Sharma, P. Trivedi "A Study on the Biological Activity of 2-thioxoimidazolidin-4-ones,," *Let. Drug. Des.*, no. (9), pp. :549-555., 2012.
- [9] B. Shipra, C. Sumitra, P. Hemali and R. Paras "Synthesis, characterization and antimicrobial activity of some new 2-thioxoimidazolidin-4-one derivatives,," *Ijpcbs*, vol.5, no. (1), pp. :196-202., *Ijpcbs*, 2015.
- [10] A. S. Guerra, D. J. Malta, Laranjeira, L. P. Maia, M. B. N. C. Colaço, C. Mdo, S. L. Galdino, R. Pitta, Ida, T. Gonçalves-Silva, "Anti-inflammatory and antinociceptive activities of indoleimidazolidine derivatives,," *Int. Immunopharmacol.*, vol.11, no. (11), p. :1816, 2011.
- [11] A. N. Jamal, A. Idhayadhulla, K. Surendra and J. Selvin "Synthesis of Some 2-Thioxoimidazolidin-4-one Derivatives and its Antimicrobial Activity,," *E-J. Chem.* vol.7, no. (4), pp. :1320-1325., 2010.
- [12] N. M. Aljamali, "Review in Azo compounds and its biological activity,," *Biochem. Anal. Biochem.*, vol.4, no. (2), pp. :1-4., 2015.
- [13] Sallal A. H. Abdullah, Rehab A. M. Al Hassani, Abdul Jabar Kh. Atia, and Ali A. Hussein "Synthesis, characterization, and enzyme activity of Co(II), Ni(II), Cu(II), Pd(II), Pt(IV) and Cd(II) complexes with 2-thioxoimidazolidin-4-one derivative,," *Accepted*.
- [14] D. B. Cook, "Quantum Chemistry,," in *Handbook of Computational Quantum Chemistry*, Vols. [14] D. B. Cook, Hand book of Computational Quantum Chemistry, New York, Oxford univ. Press, 1998:149., New York, Oxford univ. Press, 1998, p. :149.
- [15] J. V. Donald, G. V. Judith and W. P. Charlotte "Principles of Biochemistry,," 3rd Ed., Vols., John-Weily Inc., New York, 2008.
- [16] J. Awetz and A. Delbrgs., Medical Microbiology. John-Weily Inc., 4th Ed., MC Graw Hil-USA. 2007., MC Graw Hil-USA. : John-Weily Inc., 4th Ed., 2007.
- [17] H. Choinacki and F. Pruchnik "Quantum Chemical studies on molecular and Electronic structure of complexes adducts,," *Int. J. Mol. Sci.* vol.2, no. (44), pp. :11-17., 2001.
- [18] G. Mohammad and J. Ahmad "Abinit Investigation of Physicochemical, Thermodynamical and Spectroscopic Characteristics of Hydantoin Structures,," *IJIRSET*, vol.4, no.1, 2015.
- [19] J. J. Stewart "Reviews in Computational Chemistry,," *VCH publishers, New York*, vol.1, no.9, pp. :72-80, 1996.
- [20] R. A. M. AlHassani, "Theoretical studies and Biological activities of new Mannich bases triazole derivative with VO(IV), Co(II), Cu(II), Pd(II), Rh(III), Pt(IV), Zn(II) and Cd(II) ions,," *Al-Mustansiriyah Journal of Science*, vol.22, no. (4), pp. :111-133., 2011.
- [21] R. A. M. Al-Hassani, "Synthesis, Structural, Antimicrobial activities and Theoretical Studies of Some New Trivalent Metal

Complexes with Thiocarbamide Derivative,
,"*International. J. Chem. TechRes.* ,vol.9,no.
(05), pp. :723-737,2016.

- [22] C. Henryk,K. Wojciech and P. Florian, "
Quantum chemical studied on molecular and
electronic structure of some metal complex-
es, " *Int. Mol. Sci.*, vol.2, no. (3), pp. :22-28.,
2001.



Research Article

Synthesis of Novel 3-Acetyl N-methyl-2-Quinolone Derivatives with Expected Antimicrobial Activity

Ghazwan A. Salman

Department of Chemistry, College of Sciences, Mustansiriyah University, IRAQ

*Correspondent Author Email: Ghazwansalman@yahoo.com

Article Info

Received
14/12/2016

Accepted
17/04/2017

Abstract

A series of new 3-Acetyl N-Methyl-2-quinolones oxadiazoles derivatives were synthesized by reaction of 3-acetyl-4-hydroxy-1-methylquinolin-2(1H)-one **3** with ethylbromoacetate to produce compounds **4**. The hydrazinolysis of compound **4** with hydrazine hydrate afforded hydrazide compounds **5**. New Schiff bases **6** were obtained by condensation of compound **5** with different aryl aldehydes. The last step involves refluxing compound **6** with acetic anhydrides to give the corresponding 3-acetyl-N-methylquinolin-2-one oxadiazoles **7**. All the synthesized compounds were characterized on the basis of FT-IR, ¹H-NMR and ¹³C-NMR. The synthesized compounds have been evaluated for antimicrobial activity against Gram-positive and Gram-negative bacteria. Among sixteen synthesized novel compounds, in which five compounds (**7a**, **7b**, **7c**, **7e**, **7g**) exhibited promising Antimicrobial activity as compared to Trimethoprim (100µg/ml).

Keywords: Quinolines, Oxadiazoles, Antimicrobial activity.

الخلاصة

لقد تم تحضير سلسلة جديدة من مشتقات 3-أسيتايل-N-مethyl-2-كوينولين أوكساديازول عن طريق تفاعل 3-أسيتايل-4-هيدروكسي-1-مethyl-2-كوينولينون مع أثيل برومو أسيتيت للحصول على مركبات **4**. تفاعل مركبات **4** مع الهيدرازين هيدريت ليعطي مركبات الهيدرازيد **5**. وتم الحصول على قواعد شف **6** جديدة بواسطة تكثيف مركبات **5** مع الديهايدرات أروماتية متنوعة. الخطوة الأخيرة تضمنت تفاعل غلق لمركبات قواعد شف مع أنهيدريد الحامض للحصول على مشتقات 3-أسيتايل-N-مethyl-2-كوينولين أوكساديازول. وتم تشخيص جميع المركبات المحضرة باستخدام تقنيات FT-IR, ¹H-NMR و ¹³C-NMR. درست الفعالية البكتيرية للمركبات الجديدة المحضرة تجاه بكتريا Gram-positive و Gram-negative. من بين ستة عشر من المركبات الجديدة المحضرة فقط خمسة مركبات (**7a**, **7b**, **7c**, **7e**, **7g**) أظهرت فعالية بيولوجية جيدة بالمقارنة مع دواء Trimethoprim (100µg/ml).

Introduction

Synthesis of functionalized N-methylquinolin-2-one with acyl group in position 3 has found much interest because of their biological properties [1]. A wide spectrum of important pharmacological activities have been associated with 4-substituted 3-acylquinolin-2(1-methyl)-ones [2] [3] [4] [5] [6]. Several derivatives of this heterocyclic class are very interesting in biological activity and was found in many naturally occurring compounds, and also consider as useful intermediates for many medicinal products [7] [8] [9]. It had been reported that N-methyl derivatives of 4-hydroxyquinolin-2-one are possess significant biological activity [10] [11] [12], and many derivatives of 6-methylpyrano [3, 2-c] quinolinone are utilized as pharmaceutical active ingredients e. g. the famous alkaloids: veprisins and flindersins [13] [14].

Over the last few decades 2,5-disubstitued 1,3,4-oxadiazoles have received much attention because of their potential application as antioxidant, antibacterial, antitubercular and insecticidal agents [15] [16] [17] [18]. Herein, we report the first highly efficient total synthesis of seven novel 3-acetyl N-methyl-2-quinolones oxadiazoles derivatives. The chemical structures of the synthesized compounds **7** were characterized by spectroscopic techniques and confirmed. The antibacterial activities of the prepared compounds were investigated.

Materials and Methods

All the chemicals and solvents used in this study were reagent grade and they are available from Sigma-Aldrich and Alfa-Aesar companies. Melting points were determined on a Micro heating table HMK 67/1825 Kuestner (Büchi Apparatus),



Leitz Labolux 12 Pol with heating table Mettler FP 90. Melting points are uncorrected. The FT-IR spectra were obtained using Nicolet 205 FT-IR, Nicolet Protège 460 FT-IR. The ¹H-NMR spectra were recorded on a Bruker AVANCE 250 II (built 2006), Bruker AVANCE 300 II (built 2007) spectrometry, using CDCl₃ as solvent and TMS as internal standard. Thin layer chromatography (TLC) was carried out on Merck Kieselgel 60 F254 on aluminium foil from Macherey-Nagel. Detection was carried out under UV light λ_{max} at 254 nm and λ_{max} at 365 nm. Solutions were evaporated under diminished pressure unless otherwise stated. 3-acetyl-4-hydroxy-1-methylquinolin-2(1H)-one **3** was obtained according to ref. [19].

Preparation of compounds 4-7 Preparation of ethyl 2-((3-acetyl-1-methyl-2-oxo-1,2-dihydroquinolin-4-yl)oxy)acetate (**4**):

A stirred mixture of 3-acetyl-4-hydroxy-1-methylquinolin-2(1H)-one **3** (0.1 mol), anhydrous potassium carbonate (0.1 mol), and ethyl bromoacetate (0.12 mol) was heated under reflux in dry acetone (25ml) for 12 h. The resulting solution was allowed to cool to room temperature, and the produced precipitate was filter off, washed thoroughly with acetone, and then dried under vacuum. Yield 90%; M. p. 210 °C. IR (KBr) [ν, cm⁻¹]: 1735 (C=O_{ester}), 1715, 1692 (C=O_{ketone}), 1285 (C-O_{ester}). ¹H NMR (300 MHz, CDCl₃): δ = 1.27 (t, 3H, CH₃), 2.26 (s, 3H, CH₃ ketone), 3.52 (s, 3H, N-CH₃), 4.25 (q, 2H, CH₂, J = 7.3 Hz), 5.16 (s, 2H, OCH₂), 7.23-7.30 (m, 3H, ArH), 7.49-7.52 (m, 1H, ArH). ¹³C NMR (62.9 MHz, CDCl₃): δ = 16.0, 30.9, 33.1 (3CH₃), 61.0, 65.3 (CH₂), 102.2, 106.2 (C), 120.6, 124.8, 126.3, 128.3 (CH), 129.3, 131.0, 156.9 (C), 167.7 (CO_{ester}), 206.9 (CO).

Preparation of 2-((3-acetyl-1-methyl-2-oxo-1,2-dihydroquinolin-4-yl)oxy)acetohydrazide (**5**):

A solution of compound **4** (0.05 mol) and 80% hydrazine hydrate (0.03 mol) in (25ml) methanol was stirred for 10 h at room temperature. After concentrating the reaction mixture under pressure the residue solid mass washed with methanol and then recrystallized using absolute ethanol to give a yellow solid of compound (**5**). Yield 88%; M. p. : 225 °C. IR (KBr) [ν, cm⁻¹]: 1745, 1705, 1685 (C=O), 3367-3462 (-NHNH₂). ¹H NMR

(250 MHz, CDCl₃): δ = 2.26 (s, 3H, CH₃), 3.56 (s, 3H, N-CH₃), 4.25 (s, 2H, NH₂), 4.95 (s, 2H, OCH₂), 7.21 (d, 1H, J = 8.2 Hz, ArH), 7.49-7.53 (m, 3H, ArH), 8.01 (s, 1H, NH). ¹³C NMR (62.9 MHz, CDCl₃): δ = 29.8, 34.1 (2CH₃), 63.0 (CH₂), 102.2, 107.4 (C), 113.5, 124.7, 125.6, 128.7 (CH), 142.5, 150.8, 155.7, 157.6 (C), 207.5 (CO).

Preparation of (E)-2-((3-acetyl-1-methyl-2-oxo-1,2-dihydroquinolin-4-yl)oxy)-N'-(arylidene)acetohydrazide (**6**):

A stirred solution of hydrazide (**5**) (0.05 mol) and appropriate substituted aldehyde (0.052) in ethanol (25ml) was refluxed for 6 h at boiling temperature. The obtained brownish solution was poured in cold water (50ml). The produced solid was filtered and recrystallized with ethanol.

(E)-2-((3-acetyl-1-methyl-2-oxo-1,2-dihydroquinolin-4-yl)oxy)-N'-(4-bromobenzylidene)acetohydrazide (**6a**). Yield: 80%; M. p. 230 °C. IR (KBr) [ν, cm⁻¹]: 1740, 1708, 1695 (C=O), 1430 (C=N), 3210 (NH). ¹H NMR (250 MHz, CDCl₃): δ = 2.27 (s, 3H, CH₃), 3.43 (s, 3H, N-CH₃), 4.86 (s, 2H, OCH₂), 6.25 (s, 1H, N=CH), 7.25-7.29 (m, 3H, ArH), 7.49-7.53 (m, 3H, ArH), 8.25-8.39 (m, 2H, ArH), 9.99 (s, 1H, NH). ¹³C NMR (62.9 MHz, CDCl₃): δ = 30.9, 34.5 (2CH₃), 67.7 (CH₂), 100.4, 112.2 (C), 120.4, 122.3, 123.5 (CH), 125.9 (C), 126.6, 127.6, 128.5, 129.3, 129.6 (CH), 130.6, 135.7 (C), 136.0 (CH), 145.3, 145.8, 146.5 (C), 206.2 (CO).

(E)-2-((3-acetyl-1-methyl-2-oxo-1,2-dihydroquinolin-4-yl)oxy)-N'-(4-chlorobenzylidene)acetohydrazide (**6b**). Yield: 75%; M. p. 205 °C. IR (KBr) [ν, cm⁻¹]: 1735, 1705, 1692 (C=O), 1530 (C=N), 3211 (NH). ¹H NMR (250 MHz, CDCl₃): δ = 2.36 (s, 3H, CH₃), 3.53 (s, 3H, N-CH₃), 4.67 (s, 2H, OCH₂), 6.29 (s, 1H, N=CH), 7.12 (d, 2H, J = 8.1 Hz, ArH), 7.28-7.38 (m, 3H, ArH), 7.39-7.67 (m, 3H, ArH), 9.85 (s, 1H, NH). ¹³C NMR (62.9 MHz, CDCl₃): δ = 29.1, 30.8 (2CH₃), 67.9 (CH₂), 112.1, 122.1 (C), 123.2, 124.2, 125.0, 126.7, 128.3, 129.3, 130.1, 130.2 (CH), 135.5, 135.8, 135.9 (C), 137.5 (CH), 144.3, 144.6, 159.2 (C), 206.1 (CO).

(E)-2-((3-acetyl-1-methyl-2-oxo-1,2-dihydroquinolin-4-yl)oxy)-N'-(naphthalen-1-

ylmethylene)acetohydrazide (6c). Yield: 82%; M. p.222 °C. IR (KBr) [ν , cm^{-1}]: 1748, 1705, 1690 (C=O), 1485 (C=N), 3222 (NH).¹H NMR (250 MHz, CDCl_3): δ = 2.28 (s, 3H, CH_3), 3.53 (s, 3H, N- CH_3), 4.78 (s, 2H, OCH_2), 8.79 (s, 1H, N=CH), 7.13 (d, 2H, J = 8.2Hz, ArH), 7.28-7.42 (m, 3H, ArH), 7.51-7.72 (m, 3H, ArH), 7.82-7.93 (m, 3H, ArH), 9.87 (s, 1H, NH).¹³C NMR (62.9 MHz, CDCl_3): δ = 29.9, 31.1 (2 CH_3), 67.6 (CH_2), 103.0, 112.1 (C), 120.5, 121.9, 123.4, 123.6, 124.6, 128.3, 129.3, 130.1 (CH), 131.2, 135.5 (C), 136.0 (CH), 142.4, 144.2 (C), 147.3 (CH), 156.8, 158.9, 167.3 (C), 207.3 (CO).

(*E*)-2-((3-acetyl-1-methyl-2-oxo-1,2-dihydroquinolin-4-yl)oxy)-*N'*-(3,4-dimethoxybenzylidene)acetohydrazide (6d). Yield: 77%; M. p.245 °C. IR (KBr) [ν , cm^{-1}]: 1750, 1710, 1695 (C=O), 1480 (C=N), 3100 (NH).¹H NMR (250 MHz, CDCl_3): δ = 2.27 (s, 3H, CH_3), 3.43 (s, 3H, N- CH_3), 3.75 (s, 3H, OCH_3), 3.85 (s, 3H, OCH_3), 5.12 (s, 2H, OCH_2), 7.25 (d, 2H, J = 8.1Hz, ArH), 7.26-7.29 (m, 3H, ArH), 7.49-7.52 (m, 2H, ArH), 8.43 (s, 1H, N=CH), 9.93 (s, 1H, NH).¹³C NMR (62.9 MHz, CDCl_3): δ = 29.7, 31.1 (2 CH_3), 56.2 (2 OCH_3), 67.2 (CH_2), 105.8 (C), 112.1, 123.0, 123.4, 123.5, 126.1, 126.2, 127.9 (CH), 128.3, 129.3 (C), 130.6 (CH), 135.4, 136.0, 145.5, 147.3, 159.8, 167.2 (C), 205.3 (CO).

(*E*)-2-((3-acetyl-1-methyl-2-oxo-1,2-dihydroquinolin-4-yl)oxy)-*N'*-(4-hydroxybenzylidene)acetohydrazide (6e). Yield: 80%; M. p.235 °C. IR (KBr) [ν , cm^{-1}]: 1755, 1712, 1693 (C=O), 1510 (C=N), 3210 (NH).¹H NMR (250 MHz, CDCl_3): δ = 2.41 (s, 3H, CH_3), 3.64 (s, 3H, N- CH_3), 5.14 (s, 2H, OCH_2), 5.74 (s, 1H, OH), 7.09 (d, 2H, J = 8.3Hz, ArH), 7.32-7.39 (m, 3H, ArH), 7.58-7.64 (m, 3H, ArH), 8.17 (s, 1H, N=CH), 9.84 (s, 1H, NH).¹³C NMR (62.9 MHz, CDCl_3): δ = 29.7, 33.6 (2 CH_3), 65.4 (CH_2), 105.1, 112.3 (C), 119.2, 122.3, 122.6, 123.4, 123.5 (CH), 127.3 (C), 127.4, 128.0 (2CH), 128.9 (C), 130.6 (CH), 135.1, 137.5, 157.6, 159.3 (C), 205.1 (CO).

(*E*)-2-((3-acetyl-1-methyl-2-oxo-1,2-dihydroquinolin-4-yl)oxy)-*N'*-(4-

methylbenzylidene)acetohydrazide (6f). Yield: 82%; M. p.200 °C. IR (KBr) [ν , cm^{-1}]: 1755, 1712, 1696 (C=O), 1510 (C=N), 3210 (NH).¹H NMR (250 MHz, CDCl_3): δ = 2.28 (s, 3H, CH_3), 2.41 (s, 3H, CH_3), 3.77 (s, 3H, N- CH_3), 5.21 (s, 2H, OCH_2), 6.96-6.98 (m, 3H, ArH), 7.05-7.06 (m, 2H, ArH), 7.22-7.27 (m, 3H, ArH), 8.33 (s, 1H, N=CH), 9.81 (s, 1H, NH).¹³C NMR (62.9 MHz, CDCl_3): δ = 21.7, 27.5, 30.5 (3 CH_3), 63.8 (CH_2), 103.1, 112.1, 114.1 (C), 120.5, 121.8, 123.4, 123.6, 124.7, 127.7, 127.8 (CH), 129.4, 130.1, 130.6 (C), 131.2 (CH), 142.4, 156.8, 158.2 (C), 206.4 (CO).

(*E*)-2-((3-acetyl-1-methyl-2-oxo-1,2-dihydroquinolin-4-yl)oxy)-*N'*-(4-nitrobenzylidene)acetohydrazide (6g). Yield: 75%; M. p.215 °C. IR (KBr) [ν , cm^{-1}]: 1760, 1715, 1689 (C=O), 1558 (C=N), 3225 (NH).¹H NMR (250 MHz, CDCl_3): δ = 2.27 (s, 3H, CH_3), 3.63 (s, 3H, N- CH_3), 4.92 (s, 2H, OCH_2), 7.04-7.12 (m, 3H, ArH), 7.32 (d, 2H, J = 8.5Hz, ArH), 7.33-7.52 (m, 1H, ArH), 7.53-7.77 (m, 2H, ArH), 8.37 (s, 1H, N=CH), 9.67 (s, 1H, NH).¹³C NMR (62.9 MHz, CDCl_3): δ = 29.6, 30.5 (2 CH_3), 65.5 (CH_2), 103.1, 112.3 (C), 121.7, 122.2, 123.5, 123.6, 125.7, 126.7, 128.4, 128.9 (CH), 129.3, 129.6 (C), 130.5 (CH), 135.6, 136.1, 142.1, 159.2 (C), 207.4 (CO).

Preparation of 3-acetyl-4-((4-acetyl-5-substituted-4,5-dihydro-1,3,4-oxadiazol-2-yl)methoxy)-1-methylquinolin-2(1H)-one (7)

A mixture of compound 6 (0.001), and acetic anhydride (10ml), was stirred for 15 min., and then heated under reflux for 12 h. The hot reaction mixture was poured onto ice water (10ml), and the produced precipitate was filtered off, washed many times with water, and then recrystallized from ethanol and dried [20].

3-acetyl-4-((4-acetyl-5-(4-bromophenyl)-4,5-dihydro-1,3,4-oxadiazol-2-yl)methoxy)-1-methylquinolin-2(1H)-one (7a). Yield: 75%; M. p.245 °C. IR (KBr) [ν , cm^{-1}]: 1715, 1705, 1690 (C=O), 1645 (C=N), 1445 (N-N), 1250 (C-O-C).¹H NMR (250 MHz, CDCl_3): δ = 2.36 (s, 3H, CH_3), 2.55 (s, 3H, CH_3), 3.94 (s, 3H, N- CH_3), 5.67 (s, 2H, OCH_2), 6.29 (s, 1H, H5), 7.11 (d,

2H, $J = 8.1$ Hz, ArH), 7.25-7.29 (m, 3H, ArH), 7.40-7.67 (m, 3H, ArH). ^{13}C NMR (62.9 MHz, CDCl_3): $\delta = 25.5, 29.2, 30.3$ (3CH₃), 67.2 (CH₂), 85.4 (CH), 103.0, 112.2 (C), 114.2 (CH), 121.7 (C), 122.2, 123.4, 123.5, 125.7, 126.6, 128.9, 129.4 (CH), 129.7, 130.5, 130.7, 142.1, 158.2, 159.2 (C), 207.2 (CO).

3-acetyl-4-((4-acetyl-5-(4-chlorophenyl)-4,5-dihydro-1,3,4-oxadiazol-2-yl)methoxy)-1-methylquinolin-2(1H)-one (7b). Yield: 80%; M. p. 230 °C. IR (KBr) [ν , cm^{-1}]: 1720, 1701, 1684 (C=O), 1595 (C=N), 1450 (N-N), 1240 (C-O-C). ^1H NMR (250 MHz, CDCl_3): $\delta = 2.27$ (s, 3H, CH₃), 2.67 (s, 3H, CH₃), 4.06 (s, 3H, N-CH₃), 5.56 (s, 2H, OCH₂), 6.25 (s, 1H, H^{5'}), 7.15-7.38 (m, 3H, ArH), 7.49-7.75 (m, 3H, ArH), 8.25-8.43 (m, 2H, ArH). ^{13}C NMR (62.9 MHz, CDCl_3): $\delta = 21.0, 29.2, 30.8$ (3CH₃), 67.4 (CH₂), 86.0 (CH), 103.0, 112.2 (C), 121.7 (CH), 122.2 (C), 123.5, 123.8, 125.7, 126.7, 128.5, 129.0, 129.3 (CH), 129.7, 130.5, 135.6, 136.0, 142.1, 159.2 (C), 206.2 (CO).

3-acetyl-4-((4-acetyl-5-(naphthalen-1-yl)-4,5-dihydro-1,3,4-oxadiazol-2-yl)methoxy)-1-methylquinolin-2(1H)-one (7c). Yield: 72%; M. p. 232 °C. IR (KBr) [ν , cm^{-1}]: 1715, 1707, 1691 (C=O), 1650 (C=N), 1480 (N-N), 1250 (C-O-C). ^1H NMR (250 MHz, CDCl_3): $\delta = 2.28$ (s, 3H, CH₃), 2.55 (s, 3H, CH₃), 3.78 (s, 3H, N-CH₃), 5.55 (s, 2H, OCH₂), 6.25 (s, 1H, H^{5'}), 7.09-7.25 (m, 3H, ArH), 7.29-7.39 (m, 3H, ArH), 7.40-7.63 (m, 3H, ArH), 7.83 (d, 2H, $J = 8.1$ Hz, ArH). ^{13}C NMR (62.9 MHz, CDCl_3): $\delta = 25.4, 29.2, 30.3$ (3CH₃), 67.2 (CH₂), 85.2 (CH), 103.0, 112.2 (C), 114.0, 121.7, 122.2, 123.5, 123.6, 125.7, 126.6, 128.9, 129.4, 129.8, 130.5 (CH), 130.7, 142.0, 145.3, 145.8, 146.9, 158.2, 159.2 (C), 207.0 (CO).

3-acetyl-4-((4-acetyl-5-(3,4-dimethoxyphenyl)-4,5-dihydro-1,3,4-oxadiazol-2-yl)methoxy)-1-methylquinolin-2(1H)-one (7d). Yield: 80%; M. p. 240 °C. IR (KBr) [ν , cm^{-1}]: 1718, 1700, 1690 (C=O), 1655 (C=N), 1420 (N-N), 1195 (C-O-C). ^1H NMR (250 MHz, CDCl_3): $\delta = 2.29$ (s, 3H, CH₃), 2.53 (s, 3H, CH₃), 3.75 (s, 3H, OCH₃), 3.93 (s, 3H, OCH₃), 4.02 (s, 3H, N-CH₃), 5.52 (s, 2H, OCH₂), 6.43 (s, 1H, H^{5'}), 7.25-7.26 (m, 2H, ArH), 7.27-7.29 (m, 3H, ArH), 7.49-7.52 (m, 2H, ArH). ^{13}C NMR (62.9 MHz, CDCl_3): $\delta = 23.4,$

29.2, 30.3 (3CH₃), 55.2, 55.4 (2OCH₃), 67.2 (CH₂), 86.4 (CH), 102.4, 112.1 (C), 114.1, 120.2, 121.9, 123.5, 123.6, 124.8, 127.7 (CH), 129.4, 130.1, 130.5, 131.2, 147.2, 157.5, 158.2, 159.1 (C), 207.2 (CO).

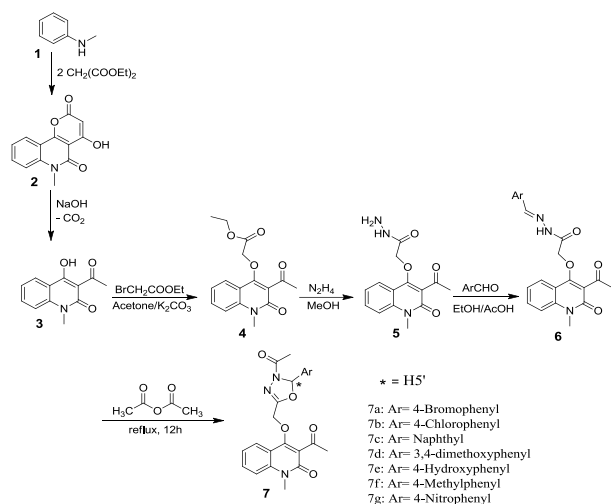
3-acetyl-4-((4-acetyl-5-(4-hydroxyphenyl)-4,5-dihydro-1,3,4-oxadiazol-2-yl)methoxy)-1-methylquinolin-2(1H)-one (7e). Yield: 70%; M. p. 230 °C. IR (KBr) [ν , cm^{-1}]: 1715, 1706, 1690 (C=O), 1651 (C=N), 1401 (N-N), 1200 (C-O-C). ^1H NMR (250 MHz, CDCl_3): $\delta = 2.24$ (s, 3H, CH₃), 2.63 (s, 3H, CH₃), 3.98 (s, 3H, N-CH₃), 5.62 (s, 2H, OCH₂), 5.98 (s, 1H, OH), 6.33 (s, 1H, H^{5'}), 7.11 (d, 2H, $J = 8.3$ Hz, ArH), 7.38-7.39 (m, 3H, ArH), 7.56-7.64 (m, 3H, ArH). ^{13}C NMR (62.9 MHz, CDCl_3): $\delta = 23.9, 29.2, 30.4$ (3CH₃), 67.2 (CH₂), 85.3 (CH), 103.2, 112.2 (C), 114.1, 120.3, 122.3, 123.5, 126.5, 127.6, 129.5 (CH), 130.5, 130.8, 145.7, 146.5, 146.9, 158.2, 159.2 (C), 206.2 (CO).

3-acetyl-4-((4-acetyl-5-(p-tolyl)-4,5-dihydro-1,3,4-oxadiazol-2-yl)methoxy)-1-methylquinolin-2(1H)-one (7f). Yield: 65%; M. p. 215 °C. IR (KBr) [ν , cm^{-1}]: 1718, 1702, 1689 (C=O), 1665 (C=N), 1480 (N-N), 1250 (C-O-C). ^1H NMR (250 MHz, CDCl_3): $\delta = 2.33$ (s, 3H, CH₃), 2.52 (s, 3H, CH₃), 3.57 (s, 3H, CH₃), 4.08 (s, 3H, N-CH₃), 5.67 (s, 2H, OCH₂), 6.29 (s, 1H, H^{5'}), 7.09-7.25 (m, 3H, ArH), 7.28-7.40 (m, 3H, ArH), 7.65 (d, 2H, $J = 8.2$ Hz, ArH). ^{13}C NMR (62.9 MHz, CDCl_3): $\delta = 21.9, 25.4, 29.2, 31.5$ (4CH₃), 67.4 (CH₂), 85.9 (CH), 102.4, 112.1 (C), 120.2, 121.9, 123.5, 123.6, 124.4, 126.5, 127.7, 128.5 (CH), 128.7, 130.2, 131.2, 138.5, 147.3, 157.5, 158.9 (C), 207.9 (CO).

3-acetyl-4-((4-acetyl-5-(4-nitrophenyl)-4,5-dihydro-1,3,4-oxadiazol-2-yl)methoxy)-1-methylquinolin-2(1H)-one (7g). Yield: 77%; M. p. 205 °C. IR (KBr) [ν , cm^{-1}]: 1715, 1705, 1690 (C=O), 1615 (C=N), 1450 (N-N), 1221 (C-O-C). ^1H NMR (250 MHz, CDCl_3): $\delta = 2.33$ (s, 3H, CH₃), 2.77 (s, 3H, CH₃), 3.98 (s, 3H, N-CH₃), 5.61 (s, 2H, OCH₂), 6.41 (s, 1H, H^{5'}), 6.96-6.98 (m, 3H, ArH), 7.07 (d, 2H, $J = 8.2$ Hz, ArH), 7.22-7.27 (m, 3H, ArH). ^{13}C NMR (62.9 MHz, CDCl_3): $\delta = 24.7, 29.2, 31.5$ (3CH₃), 67.7 (CH₂), 85.0 (CH), 103.0, 112.3 (C), 120.3, 121.9, 123.5, 123.6, 124.3, 126.5, 127.8, 128.5 (CH), 128.7, 130.1, 131.2, 138.6, 147.4, 156.9, 158.9 (C), 207.2 (CO).

Results and Discussion

The synthesis of the desired compounds was accomplished according to the representation scheme 1.



Scheme 1: Total synthesis of 3-acetyl-N-methylquinolin-2-one oxadiazoles **7**.

The starting material 3-acetyl-4-hydroxy-1-methylquinolin-2(1H)-one **3** was obtained from known method from aniline **1** and diethyl malonate via the pyronoquinolone **2** and subsequent ring opening with sodium hydroxide followed by spontaneous decarboxylation [19]. Compound **4** was prepared in 90% yield by refluxing ethyl bromoacetate with compound **3** in anhydrous acetone in the presence of anhydrous potassium carbonate. It was observed that the broad band belonging to the OH stretching in compound **3** disappeared in IR spectrum of compound **4** and also signal disappearance of OH proton in ¹H-NMR spectrum of compound **4**. Hydrazinolysis of compound **4** with 80% hydrazine hydrate in methanol at room temperature afforded hydrazide compounds **5** in good yield. The FT-IR spectrum of compound **5** exhibited absorption bands in the region 3342.7-3201.8 cm⁻¹ (belong to hydrazide NH-NH₂) and 1645.7 (amide carbonyl stretching). The ¹H-NMR spectrum showed a singlet due to the -NH proton at δ 8.08 ppm. The -OCH₂ methylene protons appeared as singlet at 4.94 ppm [20]. Heating hydrazide compound **5** with different aryl aldehydes in absolute ethanol in the presence of a

catalytic amount of glacial acetic acid for 5-6 h afforded the corresponding compounds **6**_{a-g}. The evidence for formation of Schiff base is the disappearance of a significant two bands at 3332 and 3150 cm⁻¹ which could be attributed to asymmetric and symmetric stretching vibrations of NH₂ group in compound **5**, and the ¹H-NMR showed disappearance of singlet (NH₂) protons at 4.25 ppm, and displayed a singlet (N=CH) proton at 6.25 ppm in compounds **6**. In the last step for synthesis of target compounds, the compounds **6**_{a-g} then refluxed with acetic anhydride for 8-10 h to give the corresponding substituted 3-acetyl-N-methylquinolin-2-one oxadiazoles **7**_{a-g} in good yields. All the new substituted derivatives of oxadiazoles compounds **7** have been characterized by FT-IR, ¹H-NMR, and ¹³C-NMR spectroscopy, to elucidate their structures. The ¹H-NMR spectrum of compounds **7**_{a-g} exhibited disappearance of singlet N-H proton at 9.8 ppm, and instead, it displayed a methyl protons of the additional acyl group connected to oxadiazole ring appear as a singlet at δ 2.65 ppm. The aromatic protons (both quinolinone and oxadiazolinic) are observed between 7.05 and 7.96 ppm.

Antimicrobial activity [21] [22] [23] [24]: All the synthesized compounds **4-7** have been screened in vitro for their antibacterial activity against gram-positive bacteria *Staphylococcus aureus* (NTCC 11632), *Bacillus subtilis* (ATCC 60511), gram-negative bacteria *Escherichia coli* (ATCC 10536), and the fungus *Candida albicans* (ATCC 2501) at 100 µg/ml concentration by cup-plate agar diffusion method using dimethylsulfoxide as a solvent and using trimethoprim as a reference. After 24 and 48h of incubation at 37^o±1, the antimicrobial activity was determined by measuring the zones of inhibition in mm. The results are summarized in Table (1).

Table 1: In vitro antimicrobial activity of the synthesized compounds at a concentration of 100 µg/ml (zone of inhibition in mm).

Compounds	Zone of inhibition		
	Gram-positive bacteria	Gram-negative	Fungus

			bacteria	
	S. aureus	B. subtilis	E. coli	C. albicans
4	11	07	10	11
5	10	-	12	-
6a	15	17	20	-
6b	11	13	18	-
6c	16	15	21	14
6d	14	12	19	13
6e	09	12	22	-
6g	16	-	18	12
6f	15	-	17	11
7a	21	22	31	18
7b	20	22	30	17
7c	22	24	32	19
7d	16	19	19	-
7e	22	23	31	20
7f	-	-	15	09
7g	21	24	31	20
Trimethoprim	23	26	34	21

-No inhibition zone

When we examine the data of inhibition zone of all compounds against gram-positive bacteria, we observed that compounds **4,5,6_{a-g}** showed poor activity, while compounds **7_{a-g}** showed higher activity against the same bacteria. We noted that compounds **4, 5, 6_{a-g}** also exhibited a moderate activity against E. coli bacteria compared with compounds **7_{a-g}** which appeared a potent bacterial growth inhibition. In the same context, inspection the biological activity results of all synthesized compounds against C. albicans we found similarly that only compounds **7_{a-c, e, g}** showed very good activity compared to the other. The professional antimicrobial activity of compounds

7_{a-c, e, g}, we can be attributed may be to the presence of oxadiazole fragments in the structure of these compounds.

Conclusions

In conclusion, we developed a convenient and high yielding methodology for the synthesis of novel 3-acetyl N-methyl-2-quinolinone oxadiazoles compounds and evaluated for antimicrobial activity. The antibacterial test against gram-positive and gram-negative bacteria performed on the obtained products showed that compounds (**7a, 7b, 7c, 7g**) possess a potent activity as compared to Trimethoprim. The presence of oxadiazole fragments with electron poor substituents in the structure of these compounds may be play a main role of their antimicrobial activity. Suitable molecular modification of these compounds probably generate a powerful antimicrobial agents in future.

Acknowledgment

The supporting of Institute of Chemistry, Rostock university, Rostock, Germany for spectroscopic analysis is gratefully acknowledged. Also we would like to express our sincere gratitude to Mustansiriyah University, College of science for giving me the scientific sabbatical opportunity and financially supporting for one year.

References

- [1] a) Ukita C. ; Mizuno D. Chem. Pharm. Bull **1960**, *8*, 1016; b) Schering Corp. (by Afonso A. ; Weinstein J. ; Gentles M. J. ; Rosenblum S. B.), PCT Int. Appl. WO 92004328, **1992**; Chem. Abstr. **1992**, *117*, 90162r; c) Ukita C. ; Mizuno D. ; Tamura T. ; Yamakawa T. ; Nojima S. ; *J. Chem. Pharm. SOC. Jap.* **1951**, *71* 234; d) Williams D. R. ; Bremmer M. L. ; Brown D. L. ; Antuono J. D. ; *J. Org. Chem.* **1985**, *50*, 2807; e) Wat C. K. ; Innes A. G. ; Smith D. G. ; Wright J. L. C. ; Vining L. C. ; *Can. J. Chem.* **1977**, *55*, 4090; f) Williams D. R. ; Sit S. Y. ; *J. Org. Chem.* **1982**, *47*, 2846; g) Cutler H. G. ; Jacyno J. M. ; *Agric. Biol. Chem.* **1991**, *55*, 2629; h) Tanabe Y. ; Miyakado M. ; Ohno N. ; Yoshioka H. ; *Chem. Lett.* **1982**, 1543; i) Irschik H. ; Jansen R. ; Hopfe G. ; Gert K. ; Reichenbach H. ; *J. Antibiotics* **1985**, *38*, 145; j) Cook L. ; Ternai B. ; Gosh P. ; *J.*

- Med. Chem.* **1987**, *30*, 1017.
- [2] Abass, M. ; Mostafa, B. B. *Bioorg. Med. Chem.* **2005**, *13*, 6133-6144.
- [3] El-Shennawy, A. M. ; Mohamed A. H. ; Abass M. *Medscape J. Med.* **2007**, *9*, 15-33.
- [4] Detsi, A. ; Bouloumbasi, D. ; Prousis, K. C. ; Koufaki, M. ; Athanasellis, G. ; Melagraki, G. ; Afantitis, A. ; Igglessi-Markopoulou, O. ; Kontogiorgis, C. ; Hadjipavlou-Litina, D. *J. Med. Chem.* **2007**, *50*, 2450-2458.
- [5] Rivkin, A. ; Kim, Y. R. ; Goulet, M. T. ; Bays, N. ; Hill, A. D. ; Kariv, I. ; Krauss, S. ; Ginanni, N. ; Strack, P. R. ; Kohl, N. E. ; Chung, C. C. ; Varnerin, J. P. ; 5. Goudreau, P. N. ; Chang, A. ; Tota, M. R. ; Munoz, B. *Bioorg. Med. Chem. Lett.* **2006**, *16*, 4620-4623.
- [6] Tani, M. ; Harimaya, K. ; Gyobu, Y. ; Sasaki, T. ; Takenouchi, O. ; Kawamura, T. ; Kamimura, T. ; Harada, T. *J. Antibiot.* **2004**, *57*, 89-96.
- [7] Snider, B. B. ; Wu X. *Heterocycles* **2006**, *70*, 279-294.
- [8] Ahvale, A. B. ; Prokopcová, H. ; Šefčovičová, J. ; Steinschifter, W. ; Täubl, A. E. ; Uray, G. ; Stadlbauer, W. *Eur. J. Org. Chem.* **2008**, 563-571.
- [9] "Ukrainets, I. V. ; Tkach, A. A. ; Yang, L. Y. *Chem. Heterocycl. compds.* **2008**, *44*, 1347-1354.
- [10] Mohamed, E. A. ; Ismail, M. M. ; Gabr, Y. ; Abass, M. ; Farrag, H. A. *Indian J. Chem.* **1995**, *34B*, 21-26.
- [11] "Mohamed, E. A. ; Ismail, M. M. ; Gabr, Y. ; Abass, M. J. *Serb. Chem. Soc.* **1993**, *58*, 737-743.
- [12] "Stadlbauer, W. ; Badawey, E. ; Hojas, G. ; Roschger, P. ; Kappe, T. *Molecules* **2001**, *6*, 338-352.
- [13] "Watters, W. H. ; Ramachandran, V. N. J. *Chem. Research (S)* 1997, 184-185; *J. Chem. Research (M)* **1997**, 1201-1215.
- [14] "O'Donnell, F. ; Smyth, T. J. P. ; Ramachandran, V. N. ; Smyth, W. F. *Inter. J. Antimicrob. Agents* **2010**, *35*, 30-38.
- [15] Hall, A. ; Brown, S. H. ; Chowdhury, A. ; Giblin, G. M. P. ; Gibson, M. ; Healy, M. P. ; Livermore, D. G. ; Wilson, R. J. M. ; Naylor, A. ; Rawlings, D. A. *Bioorg. Med. Chem. Lett.* **2007**, *17*, 4450-4455.
- [16] "Abdel-Hamid, M. K. ; Abdel-Hafez, A. A. ; El-Koussi, N. A. ; Mahfouz, N. M. ; Innocenti, A. ; Supuran, C. T. *Bioorg. Med. Chem.* **2007**, *15*, 6975-6984.
- [17] " Amir, M. ; Kumar, H. ; Javed, S. A. *Med. Chem. Lett.* **2007**, *17*, 4504-4508.
- [18] "Pastorin, G. ; da Ros, T. ; Bolcato, C. ; Montopoli, C. ; Moro, S. ; Cacciari, B. ; Baraldi, P. G. ; Varani, K. ; Borea, P. A. ; Spalluto, G. J. *Med. Chem.* **2006**, *49*, 1720-1729.
- [19] Wolfgang, S. ; Gerhard, H. *Heterocyclic Chem.* **2004**, *41*, 681.
- [20] Abdullah, S. ; Naceur, H. *Molecules* **2014**, *19*, 911-924.
- [21] Fairbrother RW; Martyn G. *J Clin Pathol* **1951**, *4*, 374-77.
- [22] Gould JC; Bowie JH. *Edinb med J* **1952**, *59*, 178-99.
- [23] Handan A; Oznur A; Seher B; Gulden O; Melten U; Dilek S. *Turk J Chem* **2005**, *29*, 425-35.
- [24] Wolfson J; Hooper DC. *Clini Microbiol Rev.* **1989**, *2*(4), 378-24.

Research Article

Synthesis, characterization and antibacterial Evaluation for mixed-ligand Complexes of Nickle (II), Manganese(II), Copper(II), Cobalt(II) and Mercury(II) with Tetradentate Schiff base and 1,10-phenanthroline

Rehab K. Al-Shemary, Ali N. Niseaf, Amer. J. Jarad

Department of Chemistry, College of Education for Pure Sciences, Ibn-Al-Haitham, University of Baghdad, IRAQ.

*Correspondent Author Email: drrehabalshemary@gmail.com

Article Info

Received
16/05/2016

Accepted
18/01/2017

Abstract

An abstract is a brief summary of a research article, thesis, Schiff base ligand (L) was prepared by the reaction of 4-aminantipyrine with o-phenylenediamine, the prepared ligand characterized by Micro elemental Analysis, FT. IR, UV-Vis, and ^1H , ^{13}C -NMR spectroscopy. complexes of Mn(II), Co(II), Ni(II), Cu(II) and Hg(II) with Schiff base and 1,10-phenanthroline (Phen) have been investigated in aqueous ethanol with (1:1:1) (M:L:Phen). The prepared complexes were characterized using flame atomic absorption, (C. H. N) Analysis, FT. IR and UV-Vis spectroscopic methods as well as magnetic susceptibility and conductivity measurements. From the obtained data the octahedral structure was suggested for all complexes. The biological screening effects of the investigated compounds were tested against the bacterial species (*Staphylococcus aureus*), (*Escherichia coli*), (*Bacillus*) and (*Pseudomonas*) by the good diffusion method.

Keywords: Schiff base, 1, 10-phenanthroline, 4-aminoantipyrine, Mixed ligand complexes.

الخلاصة

تم تحضير ليكاند قاعدة شف من تفاعل 4-امينو انتيبيرين مع اورثوفينيلين ثنائي الأمين، شخصت الليكاند المحضرة بواسطة اطياف الأشعة تحت الحمراء وفوق البنفسجية - المرئية والرنين النووي المغناطيسي للكربون والهيدروجين والتحليل الدقيق للعناصر (C. H. N). حضرت معقدات المنغنيز (II)، الكوبلت (II)، النيكل (II)، النحاس (II) والزنك (II) مع قاعدة شف و1,10-فينانثرولين في وسط ايثانول- ماء وبنسبة (1:1:1) (فلز: ليكاند: فينانثرولين). شخصت المعقدات المحضرة بواسطة التحليل الدقيق للعناصر (C. H. N)؛ تقنية الإتصاص الذري اللفي واطياف الأشعة تحت الحمراء وفوق البنفسجية - المرئية، فضلا عن قياسات التوصيلية الكهربائية والحساسية المغناطيسية، ومن النتائج المحصول عليها تم اقتراح الشكل ثنائي السطوح للمعقدات المحضرة. كما تمت دراسة الفعالية البكتيرية لليكاند والمعقدات المحضرة تجاه انواع مختلفة من البكتريا.

Introduction

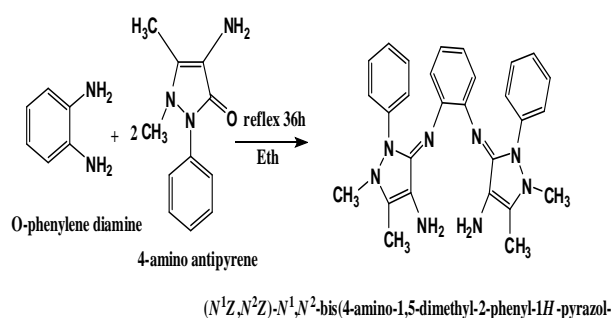
One of the most important derivatives is 4-aminoantipyrine which is deemed from remarkable reagents as its significance in biological [1], pharmacological [2], clinical and analytical applications [3]. Further, they have been investigated due to their diverse biological properties as sedative [4], antifungal [5], ability anti-inflammatory [6], analgesic [7], antibacterial [8], greater DNA binding [9], and antipyretic agents [10]. Amino group in antipyrine as a site of chelation shows highlighting behavior with transition metal ions through covalent or coordinate

[11]. In this work, we are interested to explore preparation and structural design of 4-aminoantipyrine based Schiff base having nitrogen donors, derived from a 4-aminoantipyrine and o-phenylene diamine, and its complexes with Hg (II), Ni (II), Mn (II), Co (II) and Cu (II) metal ions. The antibacterial evaluation of present complexes is also researched against the bacterial types such as (*Staphylococcus aureus*), (*Escherichia coli*), (*Bacillus subtilis*) and (*Pseudomonas aeruginosa*).

Materials and Methods

Preparation of the ligand (L)

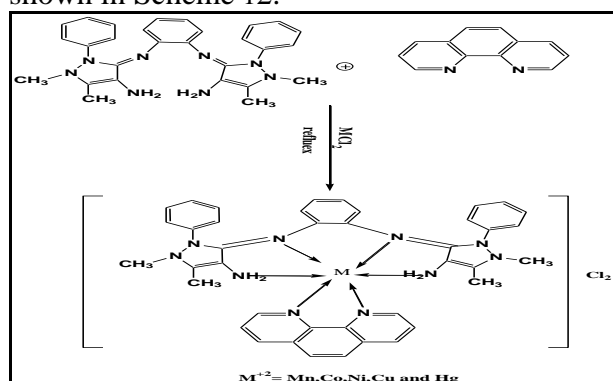
Ethanol solution of 4-aminoantipyrine (4.06g, 0.02mmol) was added to ethanol solution of o-phenylenediamine (1.08g,0.01mmol) with 2 drop glacial acetic acid[8]. The solution mixture was stirred and refluxed for 36 hours, yellow crystalline precipitate observed. The resulting precipitate as filtered off recrystallized from menthol and dried at 50°C. The preparation method of the ligand (L) is represented inScheme 1.



Scheme 1: Preparation method of ligand.

Preparation of Metal Complexes

A aqueous solution of the metal salts containing 0.198g, 0.2388g, 0.238g, 0.170 g and 0.271g (1mmole) of MnCl₂.4H₂O, CoCl₂.6H₂O, NiCl₂.6H₂O, CuCl₂.2H₂O, and HgCl₂ respectively was added gradually with stirring to ethanol solution (0.29g, 1mmol, the complexes precipitate of the ligand, an ethanol solution of (0.18g, 1mmol) of 1, 10-phenanthroline added in each case by using stoichiometric amount (1:1:1) Metal to ligands molar ratio. The mixture was refluxed with constant stirring for 2 hours. The mixture was cooled at room temperature dark precipitate was formed, filtered and recrystallized from ethanol. The preparation method is shown in Scheme 12.



Scheme 2: The expected structure of the metal (II) complexes.

Instrumentation

Melting points were determined on "Gallenkamp melting point Apparatus". Elemental microanalysis C, H, N, was carried out using Euro Vector EA 3000A Elemental Analysis (Italy). FT-IR measurements were recorded on Shimadzu-8300 Spectrophotometer in the range of (4000-400cm⁻¹) as KBr disc. Electronic spectra were recorded using U. V-Vis. Spectrophotometer type (CECIL, England, with quartz cell in rang (200-1000) nm which path length (1cm) at room temperature in ethanol. ¹H and ¹³C-NMR spectra were recorded by using a [Bruker 300 MHz (Switzerland), Chemical shift of were recorded in δ(ppm) unit downfield internal reference (TMS)], using DMSO. Conductivity measurements were obtained from (WTW conductivity meter) by using ethanol of 10⁻³ M concentration at room temperature. The chloride content determined using potentiometric titration method on 686-Titro Processor-665 Dosim A-Metrohm/Swiss. Magnetic properties were performed by using Auto Magnetic Susceptibility Balance Sherwood Scientific instrument at 25°C. Metal analysis of complexes was determined by Atomic Absorption (A. A.) technique. Using a shimadzu PR-5. Oraphic Printer atomic absorption spectrophotometer.

Results and Discussion

The ligand was prepared by condensation reaction between 4-amino antipyrine and o-phenylene diamine. Synthesized ligand (L) was characterized by FT-IR, Elem. Anal (C, H, N) and UV-Vis, ¹H, ¹³C-NMR spectroscopic technique. [1] The solid complexes were prepared by reaction of alcoholic solution of the ligands with the aqueous solution of the metal ions in a (M:L) of (1:1:1). The (C, H, N) analysis with metal contents of these complexes was in good agreements with the calculated values Table 6 includes some physical properties and elemental analysis [2]. Conductivity measurements of complexes were carried out in (10⁻³ M) in dimethylsulphoxide (DMSO) solvent. The molar conductance values are listed in the Table-5. The table reveals that the conductance values of all the metal complexes supporting their 1:2 electrolytic behavior.

NMR Spectra

The ¹H NMR spectrum of ligand Figure 14 in DMSO-d₆ solution shows the following signals:

=C-CH₃ at δ_H 2.15, DMSO at δ_H 2.49, N-CH₃ at δ_H 3.31, NH₂ at δ_H 4.78, C₆H₅ as multiple at δ_H 6.66 ~7.08, Ph-NH- at δ_H 7.82, the data recorded in Table 1[3]. The ¹³C NMR spectrum of ligand Figure-2 in DMSO-d₆ solution shows the signals at: (8.82 for =C-CH₃ group);(34.96 for N-CH₃ group); (40.52 for DMSO);(75.12 attributed to -C-OHgroup); (109.82for=C-N);(123.10~135.86) to 4 benzene rings) and (139.90 for C=C in antipyrine). The peak observed at 164.50 is due to the C=N imine groups for Schiff base[4]. The data tabulated in Table 2:13 CNMR chemical shifts for the ligand (ppm in DMSO-d₆).

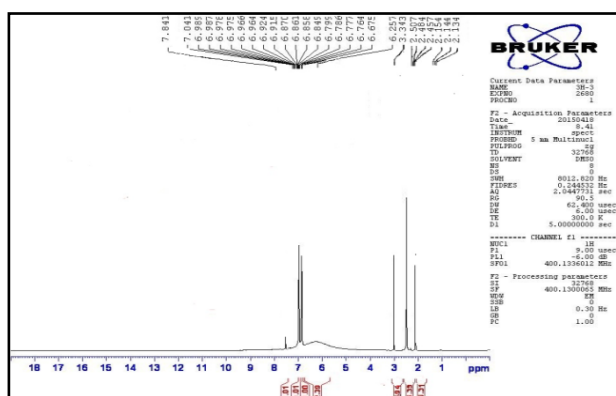


Figure 14: ¹H-NMR spectrum of ligand

Table 1: ¹H NMR chemical shifts for ligand (ppm in DMSO-d₆).

DMSO	CH ₃ -N	CH ₃ -C=	NH ₂	C=C	Ph-NH
2.5	2.16	3.33	4.79	6.67-7.07	7.84

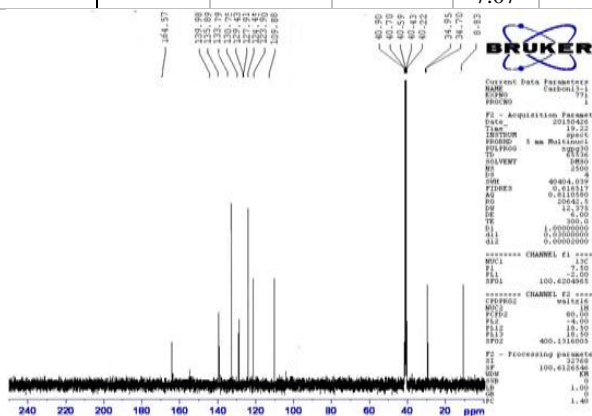


Figure 15: ¹³C-NMR of the ligand.

Table 2: ¹³CNMR chemical shifts for the ligand (ppm in DMSO-d₆).

Compound	NH ₂	ν(C=N) _{imine}	M-N
----------	-----------------	-------------------------	-----

L	3428	1624	-
[Co(phen)(L)]Cl ₂	3339	1615	597
[Ni(phen)(L)]Cl ₂	3261	1608	588
[Cu(phen)(L)]Cl ₂	3377	1618	547
[Mn(phen)(L)]Cl ₂	3265	1610	553
[Hg(phen)(L)]Cl ₂	3348	1616	545
	3274	1608	
	3381	1617	
	3251	1610	

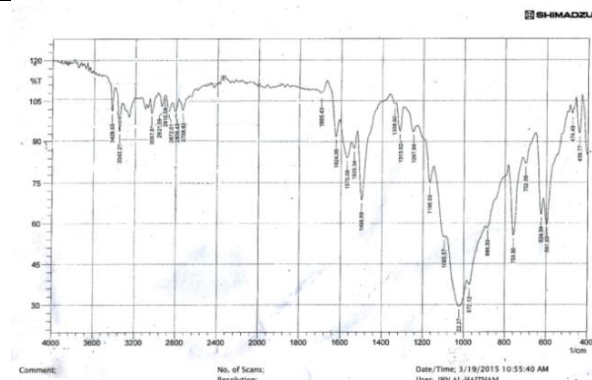


Figure 16: FT-IR spectrum of the lignd

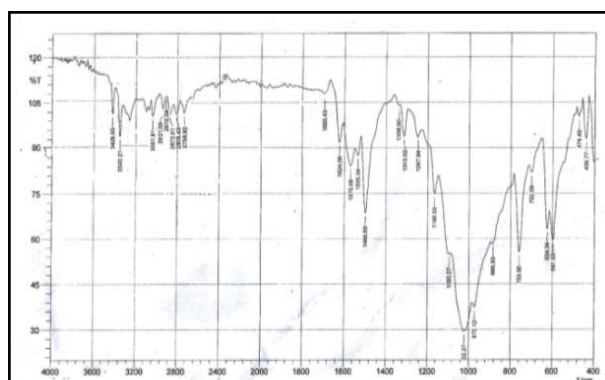


Figure 17: FT-IR spectrum of [Hg(phen)(L)]Cl₂ complexes

Table 1: Diameter of zone of inhibition (mm)

Compound.	<i>Staphylococcus aureus</i>	<i>Escherichia. Coli</i>	<i>Pseudomonas</i>	<i>Bacillus</i>
L	6	7	9	10
[Co(phen)(L)]Cl ₂	12	15	15	11
[Ni(phen)(L)]Cl ₂	14	10	13	10
[Cu(phen)(L)]Cl ₂	13	11	10	15
[Mn(phen)(L)]Cl ₂	18	17	16	12
[Hg(phen)(L)]Cl ₂	15	12	10	19

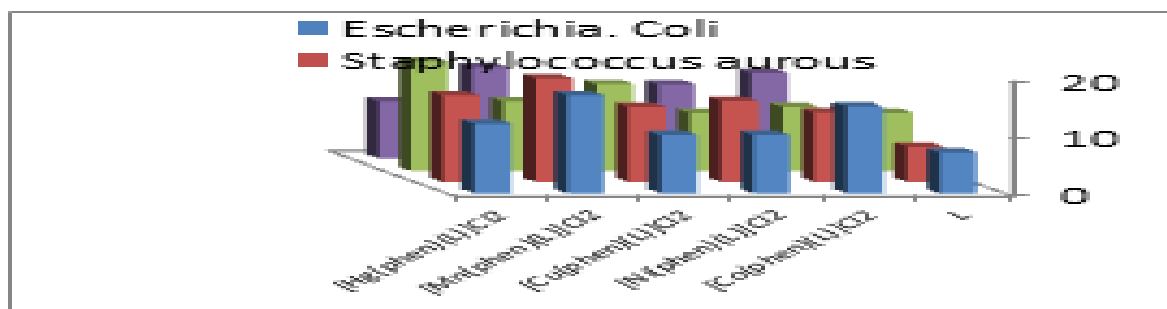


Figure 5: Difference between the antimicrobial activity of ligand and its complexes.

Table 5: Some physical prepared ligand and its complexes and weight of metal salts

Compounds	Formula	Molecular Weight	Colour	Yield %	M. P. °C	%Elemental Analysis Found % (Calculated)			
						C	H	N	M
L	C ₂₈ H ₃₀ N ₈	478.59	pale yellow	65	178	70.00 (70.27)	6.07 (6.32)	23.70 (23.41)	-
[Co(phen)(L)]Cl ₂	C ₄₀ H ₃₈ Cl ₂ CoN ₁₀	788.64	Brown	74	210	61.20 (60.92)	4.76 (4.86)	17.53 (17.76)	7.64 (7.47)
[Ni(phen)(L)]Cl ₂	C ₄₀ H ₃₈ Cl ₂ N ₁₀ Ni	788.40	Brown	76	231	59.52 (60.94)	4.84 (4.86)	17.77 (8.68)	7.29 (7.44)
[Cu(phen)(L)]Cl ₂	C ₄₀ H ₃₈ Cl ₂ CuN ₁₀	791.20	Deep brown	82	236	60.56 (59.07)	4.37 (4.83)	17.41 (17.66)	8.46 (8.01)
[Mn(phen)(L)]Cl ₂	C ₄₀ H ₃₈ Cl ₂ MnN ₁₀	784.64	Light brown	72	227	59.87 (61.23)	4.87 (4.88)	17.73 (17.85)	6.88 (7.00)
[Hg(phen)(L)]Cl ₂	C ₄₀ H ₃₈ Cl ₂ HgN ₁₀	930.24	Off-White	72	227	50.87 (51.64)	4.23 (4.12)	14.73 (15.06)	21.13 (21.56)

Table 6: Electronic spectral data of the ligand and its metal complexes

Compound	μ_{eff}	Λ_m ohm. cm ² mol e ⁻¹	λ_{nm}	ν' wave number cm ⁻¹	(ϵ_{max} molar ⁻¹ cm ⁻¹)	Assignments	Proposed structure
L	-	-	243 312	41152 32051	2278 1245	$\pi \rightarrow \pi^*$ $n \rightarrow \pi^*$	-
1,10-phenanthroline	-	-	202 228 264	49504 43859 37878	2469 2281 1456	$\pi \rightarrow \pi^*$ $\pi \rightarrow \pi^*$ $n \rightarrow \pi^*$	-
[Co(phen)(L)]Cl ₂	4.65	77.4	330 519 654 824	30303 19267 15933 12135	1402 615 209 148	C. T ${}^4T_{1g(F)} \rightarrow {}^4T_{1g(P)}$ ${}^4T_{1g}$ $\rightarrow {}^4A_{2g}$ ${}^4T_{1g}$ $\rightarrow {}^4T_{2g(F)}$	octahedral

[Ni(phen)(L)] Cl ₂	2.47	73.6	333 827	27700 12091	734 213	C. T ³ A _{2g(F)} → ³ T _{2g(F)}	octahedral
[Cu(phen)(L)] Cl ₂	1.85	70.9	338 855	29585 11687	1517 318	C. T ⁴ B _{1g} → ⁴ B _{2g}	octahedral
[Mn(phen)(L)] Cl ₂	5.43	81.0	328 805	30487 12422	1236 436	C. T ⁶ A _{1g(F)} → ⁴ T _{1g(G)}	octahedral
[Hg(phen)(L)] Cl ₂	-	71.6	331 407	30211 24570	1271 629	C. T C. T	octahedral

References

- [1] M. F Tolulope, O. O Olorunfemi, and A. Isaac, "Synthesis and biological properties of N₂O₂ Schiff bases derived from o-phenylenediamine and substituted salicylaldehydes," vol.6, no.6, pp.816-819, 2014.
- [2] M. Aly, A. H Osman., B Abd El-mottled and B. AGouag, "Thermal stability and kinetic studies of Cobalt (II), Nickel (II), Copper(II), Cadmium (II) and Mercury (II) complexes derived from N-salicylide Schiff bases," vol.54, no.4, pp.349-353, 2009.
- [3] F. M. Morad, M. El-jail, S. Mand, B. George, "Preparation, physical characterization and antibacterial activity of Ni (II) Schiff Base complex," vol.1, no.1, pp.72-78., 2007.
- [4] J. Zhang, Y. Tang, J. Q. Xie, Zeng and C. Weihu, "; Study on phenol oxidation with H₂O₂ catalyzed by Schiff base manganese complexes as mimetic peroxides," vol.70, no.10, p.1137-1146, 2005.
- [5] R. a. Y. A. -. D. [5] N. R. J. Jebe, "Synthesis and spectral study of new azo-azomethine dyes and its copper (II) complexes derived from resorcinol, 4-aminobenzoylhydrazone, and 4-amino antipyrine," no.14, 2011.
- [6] M. A Neelakantan, T. Jeyakumar and K. Muthukumar, "spectral, XRD, SEM and biological activities of transition metal complexes of polydentate ligands containing thiazole moiety," pp.71- 628, 2008.
- [7] Z. L. You and H. -L Zhu, "Syntheses, crystal structures, and antibacterial activities of four Schiff base complexes of copper and zinc," vol.630, no.15, pp.2754-2760, 2004.
- [8] M. Golcu, H. Tumer, R. Demirelli, and A. Wheatley " Synthesis, characterization, properties and biological activity, Cd (II) and Cu (II) complexes of polydentate Schiff base ligands," vol.358, no.6, pp.1785-1797, 2005.
- [9] K. D. Karlin and Z. Tyeklar, Bioinorganic chemistry of copper, vol.5th Edition, New York: Chapman and Hal, 1993.
- [10] R. Garg N. Fahmi, and R. V. Singh, " Spectral and biological studies of manganese (II), dioxo molybdenum (VI) and oxovanadium (V) complexes with monobasic bidentate Schiff base ligands," pp.86-670, 2009.
- [11] M. F. El-Ghar, N. T. Abdel-Ghani, Y. Badr, and O. MEI-Brady, " Synthesis, Spectroscopic and Thermal Studies of Co(II), Ni(II), Cu(II), Zn(II), Cd(II) and Hg(II) with Arylazo Derivatives of 5-amino Pyrazole. ," *ISESCO. Science and Technology Vision*, vol.3, pp.58-6, 2007.
- [12] A. Osole, "Antimicrobial activity and spectral, Magnetic and thermal studies of some transition metal complexes of a Schiff base hydrazone containing a quinoline moiety," vol.3, no.9, p.1080, 2007.
- [13] H. Dawood, and N. Jasim, " complexes., Antimicrobial polyester containing Schiff-base metal," *J. Coord. Chem.*, vol.62, no.7, p.1091, 2009.
- [14] E. Arai, Y. Nishida, J. Wasa, H. Urakawa and L. Zhuo, "The synthesis, characterization and antimicrobial activity of N,N'-bis (2-Thiophene carbox amide)-1,3-diaminopropane and N,N'-bis(2-furan-carboxamido)-1,3-diamino propane and

their Cu (II), Zn (II), Co(II) complexes," *Trans. Met. Chem.*, vol.9, pp.1633-1641, 2008.

- [15] H. Hassib and A. A. Razik, "acetyl acetone, Synthesis and characterization of some transition metals complexes of Schiff base derived from benzidine and acetylacetone," *J. Sci. Appl.*, vol.2, no.1, pp.83-90, 2008.
- [16] F. Karipcin and E. Kabalcilar; Spectroscopic and thermal studies on solid complexes of 4-(2-pyridylazo)-resorcinol with some transition metals, *Acta. Chim. Slov.* 2007, 54 : 242-247 2003, p.55.
- [17] G. Eason, B. Noble, and I. N. Sneddon, On certain integrals of Lipschitz-Hankel type involving products of Bessel functions, vol. A247, London: Phil. Trans. Roy. Soc, 1955, pp.529-551.
- [18] J. C. Maxwell, A Treatise on Electricity and Magnetism, 3rd ed. ed., vol.2, Oxford: Clarendon, 1892, pp.68-73.
- [19] I. S. Jacobs and C. P. Bean, "Fine particles, thin films and exchange anisotropy, in Magnetism, vol. III, New York: Academic: G. T. Rado and H. Suhl, Eds, 1963, p.271–350.
- [20] K. Elissa, "Synthesis and characterization of nickel (II), cobalt (II), manganese(II),copper(II),iron(III)and chromium(III) complexes of unsymmetrical salen-type ligand and their application as catalyst for the oxidation of styrene *J. Indian Chem. Soc.*, 2009,10(7) p.86- 697.
- [21] R. Nicole, " Synthesis and characterization of nickel (II), cobalt (II), manganese(II),copper(II),iron(III)and chromium(III) complexes of unsymmetrical salen-type ligand and their application as catalyst for the oxidation of styrene, *J. Indian Chem. Soc.*, 2006,3(8): 60- 69.

Research Article

Affect the Cross Linking Degree and Polymer Composition on the Mechanical Properties of Poly (vinyl alcohol)/ Pullulan Films

Shema A. Soud

Department of Applied Science, University of Technology, IRAQ.

*Correspondent Author Email: shymaa_soud@yahoo.com

Article Info

Received

Revised

Accepted

Published

Abstract

In this study Cross-linked PVA/Pullulan film was prepared. Cross-linking reaction done by addition of glutaraldehyde at different reaction time (10,30and 60) min. Chemical interaction, mechanical, thermal properties, water solubility and film morphology was studied for cross-linked PVA/Pullulan, PVA and Pullulan only. Thus FTIR investigated formation of hydrogen bonding between pullulan and PVA with (GA). Tensile strength, tensile modulus and elongation (%) at break for PVA/Pullulan film was improved with addition of (GA) as the reaction time proceed equivalent with increasing PVA content.

Keywords: Polymer Film, Blend, Mechanical Properties, Crosslinking Reaction.

الخلاصة

في هذه الدراسة تم تحضير الغشاء البوليمري المكون من خلط كل Poly (vinyl alcohol) و Pullulan بنسب وزنيه معينه. تفاعل الارتباط التشابكي تم باضافة العامل الربط (GA) و تم التفاعل بفترات زمنية مختلفة تراوحت بين 10 و 30 و 60 دقيقة. تمت في هذا البحث دراسة تأثير اضافة عامل الترابط التشابكي على العديد من الخصائص الفيزيائية والكيميائية للغشاء البوليمري قبل وبعد اجراء عملية الترابط. حيث تمت دراسة كل من طبيعة الترابط الكيميائي و الخواص الميكانيكية والحرارية وقابلية الذوبان في الماء بالاضافة الى الخصائص المظهرية لسطح الغشاء. حيث اظهرت نتائج FTIR تكون اواصر هيدروجينية بين كل من Poly (vinyl alcohol) و Pullulan نتيجة اضافة العامل الربط ادت الى زيادة التجانس بين البوليمرين. كما ان وجود العامل الربط والزيادة الوزنيه المضافة من Poly (vinyl alcohol) ادت الى تحسنا في الصفات الميكانيكية والتي شملت كلا من [Tensile strength, tensile modulus elongation (%)] للغشاء البوليمري.

Introduction

In recent times, biodegradable polymer has "innovated in biomedical" concept. Introducing of natural polymers results in a biocompatible material with lower mechanical properties. An individual approach to produce biocompatible material with good mechanical properties was to blend biodegradable synthetic polymer with natural polymers as reinforcement agent. [1]. Miscibility is the most significant property of a blending polymer since it affects the morphology and the mechanical properties. Polymer blends are physically mixture of different structural polymers that interact by secondary forces [2]. Such as charge-transfer complexes, dipole-dipole forces and hydrogen bonding to form homogenous polymer mixtures [3] [4] [5]. Addition of cross-links among polymer chains have an effect on

the physical properties such as decrease in the viscosity, Increased Tg, increase strength ,toughness and insolubility of the polymer depending upon the degree of cross linking and presence and absence of crystallinity. Moreover, polymers insolubility was increase [6]. Cross linking can be done by different techniques according upon the structure of the polymer. One of these methods for cross-linking is the polymerization of monomers with functionalities or through irradiation, chemical reactions by adding different chemicals with heating and, sometimes, pressure. In all cases, the chemical structure of the polymer is altered through the cross linking process. [7] [8]. In the chemical cross-linking polymers are cross-linked with many chemical compounds such as glutaraldehyde, formaldehyde, epoxy compounds, dialdehyde [9]

[10] [11]. Pullulan is a water soluble extracellular polysaccharide [12]. Biocompatible, non-toxic, colorless, tasteless, can form transparent and glossy films [13]. Poly (vinyl alcohol) is a biodegradable, biocompatible and water soluble synthetic polymer, material. by reason of its has number of $-OH$ group in each repeating unit, PVA shows a hydrophilic and able to form cross linked film via hydrogen bonding [14] [15] In this study mechanical properties of natural polymer pullulan were improved by blending with PVA. Cross linker glutaraldehyde was introduced to improve miscibility between PVA and pullulan. Effecting of cross-linking reaction on the chemical structure, degree of swelling, film morphology thermal and mechanical properties to the different PVA/pullulan ratios at different time of reaction was studied

Materials and Methods

Pullulan was obtained by Shandong Freda Biotechnology, China. Poly (vinyl alcohol) (PVA) average MW $\approx 31.000-50.000$ with 98-99% hydrolyzed was achieved from Aldrich, Germany. Glycerol was acquired from Aldrich, Germany. 25% Glutaraldehyde (GA) aqueous solution was acquired from Aldrich, Germany.

Preparation of Pullulan /PVA Blend Films

Preparations of Pull/PVA blend films were done by mixing Pullulan and PVA in 100ml DW at various Pullulan/PVA 100/0, 85/15, 70/30, 55/45, 40/60, 25/75 and 0/100 (wt %). Polymer mixture was stirred at 80°C to be dissolved. Then glycerol 1.19 ml was added to the polymer solution as plasticizer. The Cross linking blend film were prepared by adding 10% (v/v) HCl and 0.0001% (v/v) GA to 20 mL form Pullulan /PVA blend solutions and stirred for 10, 30 and 60 min at room temperature. Pullulan/PVA blends before and after cross linking solution were poured on a petri dish and the films were cast by drying at 45°C for 72 hr.

Characterizations of the Blend Film

FTIR spectrum of KBr pellets for film was studied with Mattson Satellite 5000 spectrophotometer. The tensile strength, E-modulus, and % elongation at break of the polymer films with and without cross linker measured at room tem-

perature on a tensile test machine Jinqiao, China. The rectangular specimens with about (width 12.6, thickness 0.10 and length 60.0) mm mounted between the grips of the machine before applying the stress at a 40.599 N.

The polymer blend specimens were observed under a (Stereoscan 360, Cambridge) scanning electron microscope (SEM) in order to explore surface properties.

Water up take behavior of the pullulan/PVA with 75% PVA (Wt %) films only and with different cross-linking reaction time (10, 30 and 60 min) was studied at room temperature by immersing a bout (25X25x0.1 mm³) from weighed and dry samples of the films in distilled water. The strips were removed from water at different time intervals and weighed after blotting out the excess water from the surface of the films with filter paper. The percent water absorption was calculated using the following equation:

$$\% \text{ Water Absorptivity} = ((D_s - D_d) / D_d) \times 100.$$

Where D_d and D_s are the weight of the blend films in the dry and swollen states respectively. Differential Scanning Calorimetry (DSC) and Thermogravimetric Analysis ((TGA) have been done at university of Baghdad / college of education for pure sciences Ibn Al-haitham -Central service laboratory. Heating temperature was started from 0 to 300°C. With heating rate 10°s per minute. Study was done with 20 mg from PVA/Pull and crosslinking PVA/Pull with 75% PVA (Wt %).

Results and Discussion

Fourier Transform Infrared (FTIR)

Cross-linking reaction between pullulan /PVA blend film and the cross linker was investigate by using FTIR spectroscopy. Cross linking reaction was done when aldehyde groups of the glutaraldehyde reacted with the hydroxyl groups for both pullulan and PVA. The spectra of pure films for pullulan and PVA and cross linked blend pullulan /PVA were compared to study the effecting of cross linking reaction at different period of time on the pullulan/PVA miscibility. Figure 1 (a, b and c) present the FTIR spectra for pure pullulan, pure PVA and cross-linked blend pullulan/PVA films respectively. Figure 1 (a) shown abroad $-OH$ band at 3418cm⁻¹. Moreover, Characteristic polysaccharide band was found at 1423 cm⁻¹. Strong band was found at

1158 cm^{-1} related to C-O-C polysaccharide ring. While in Figure (c) - OH band for PVA film was found at 3437 cm^{-1} and Characteristic absorption peak for C-O stretching appears at 1044 cm^{-1} and 1444 cm^{-1} . However, in Figure (c) - OH stretching was shifted to lower intensity and appears at cm^{-1} by blending pullulan with PVA and cross linking with (GA). Thus it can be related to the formation of hydrogen bond between pullulan and PVA with (GA). Therefore, the FTIR spectroscopy results confirm the reaction between PVA and Pullulan.

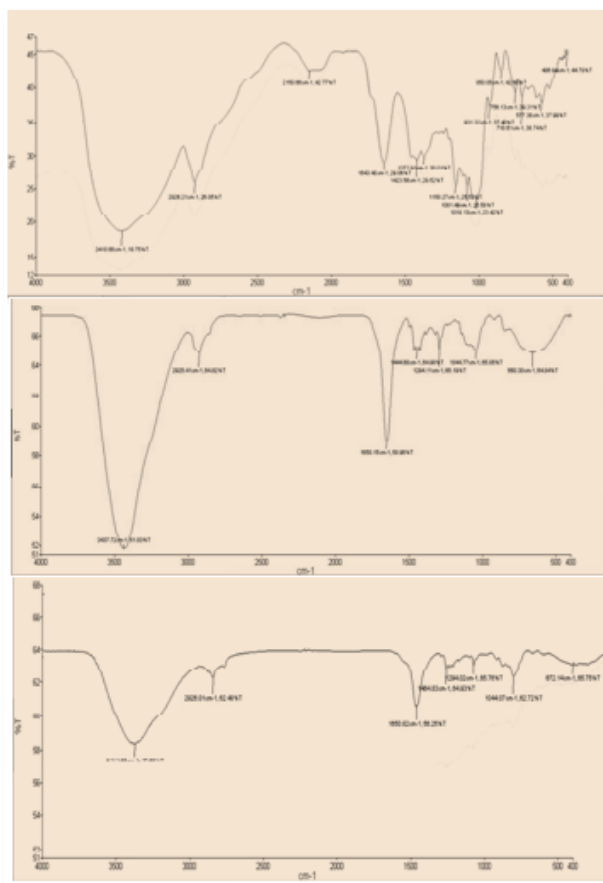


Figure 1: FTIR Spectroscopy for Pure Pullulan Film (a), Pure PVA Film (b) and Cross Linked Pullulan/PVA Film (c).

Mechanical properties

Studies of mechanical behaviors of polymer films are very essential for the reason that they show the film applications. The mechanical properties of pullulan/PVA blend films with (0, 15, 30, 45, 60, 75 and 100) PVA (Wt %) contents were study before and after cross linking with

(GA) at 10, 30 and 60 min. The tensile strength, tensile modulus and elongation (%) was shown in Figure 2 (a, b and c) respectively. Figure 2(a,b) show the lowest values of tensile strength and tensile modulus at lowest PVA contents of 15 and 30 wt%, respectively. The tensile strength and modulus of the blend films were increased at lower pullulan contents. Thus, it can be correlated to weakness mechanical properties of pure pullulan film such as other polysaccharide that form a slight brittleness polymer film. Lower mechanical properties for pullulan were confirmed to study done by [16] [17] As a result, by increasing the PVA contents in the blend film the (%) elongation at break decreasing as present in the Figure 2 (c). This can be attributed to the semi-crystalline structure of PVA [6]. Mechanical properties for pullulan/PVA blend film cross linked with (GA) at 10, 30 and 60 min in (a) tensile strength, (b) tensile modulus and (c) elongation (%) at break were shown in Figure 3. It was found after incorporating (GA) and increasing cross-linking reaction time from 10 min to 60 min both tensile strength and tensile modulus were increasing equivalent with increasing PVA content. Therefore, by addition of (GA) to the polymer blend miscibility was improved due to increase the hydrogen bond interaction among pullulan and PVA via (GA). As a result by increasing the cross linking reaction time the interaction was improved parallel with improved both tensile strength and tensile modulus. [19] While, (%) elongation at break decreased due to increase the interaction between these polymer reduce the brittleness of polymer film. Moreover, Figure 3 was shown by addition of (GA). The tensile properties of pullulan /PVA were improved comparing to the results of the tensile properties before cross-linking reaction as shown in Figure 2. It was found the maximum tensile strength and tensile modulus about 82 and 4000 MPa respectively at 75% PVA Wt% content. However, at same PVA content the maximum tensile strength was found about 86.89 and 89.9 MPa and tensile modulus start from 4020, 4100 to 4387 MPa at 10, 30 and 60 min respectively. Thus above results were supported with above FTIR results.

Scanning electron microscopy (SEM)

The surfaces micrographs of the pure pullulan film ,pure PVA film, PVA /Pullulan blend film with compositions of 75% PVA (Wt%) without cross linker and PVA /Pullulan blend film with compositions of 75% PVA (Wt%) and cross linked with (GA) at 30 min was shown in Figure.4 (a,b,c and d) respectively. The pure PVA and pullulan film shows a continuous phase as shown in Figure 1a and 1b respectively Figure 1c PVA /Pullulan film illustrate a co-continuous phase separation from PVA and pullulan particles. Moreover the presence of interfaces domain and empty spaces is apparent in the micrographs of the PVA /Pullulan film, which are due to the weak interactions between PVA and pullulan. In Figure (d) homogeneity was improved, as a result of cross linking reaction and continuous phase was found from PVA/pullulan film with (GA) as crosslinker.

Water up Take Behavior

The water up take of the dried PVA/ pullulan at 75% PVA (wt %) films only and with different cross-linking reaction time was shown in Figure 6 (a and b). As shown in these Figures, the swelling degree of the polymer decreased with the increase in cross-linking reaction time. As conferred previous, at increases time of cross-linking reaction the density of cross-linking produced increases while the intermolecular space is freely decreases. The latter is up taking within the polymer film matrix when it is in contact with water. Pure pullulan film is not showing any swelling behavior as a result of its water soluble polysaccharide [12]. Blending pullulan with PVA water resistance properties was improved, thus related to the crystallinity stature of PVA as shown in Figure 5. When (GA) was introduced with PVA /pullulan matrix, the swelling behavior was improved due to the presence of (GA) introduce cross-linking points between PVA and pullulan in film sample and therefore, less -OH groups which reduce the hydrophilicity are predictable. [18].

Thermal properties

DSC and TGA were achieved for the Pull/PVA and pull/PVA cross linked with GA, shown in Figures (5) and (6). Thermogram measurement was performed to find out the thermal stability of polymer film. First loss in mass of Pull/PVA and cross linked Pull/PVA was due the water loss at

127 °C and 230°C respectively TGA curves demonstrated that pull/ PVA cross linked with GA was stable up to 230°C with 36.2 % mass loss occur above 303°C. Thus, pull/ PVA showed 49.1% mass loss occur above 300°C. Cross linked Pull/PVA showed higher thermal stability model, it specifies that cross-linking between the PVA and pullulan increase the thermal stability of PVA. The DSC thermogram of pull/PVA shows endothermic peak at 86.1°C can be attributed as T_g of PVA followed by melting of the crystalline portion start at 195.6°C that is T_m melting temperature of PVA as shown in Figure 6. The values of T_m and T_g are in concurrence with those in previous report (19) above results indicating that this blend was phase-separated and that the interfacial adhesion between PVA and pullulan was poor. DSC thermograms of Pull/PVA cross linked formulations showed two major endothermic peaks. However peak at 101°C can be attributed as T_g for pull/PVA crosslinking with GA. Shifting in T_g to higher value 101 °C can be related to the intermolecular crosslinking modifies the stuffing of local molecular, ensuing decline in free volume, then increase in T_g. Moreover as a result of crosslinking reaction hindrance to the chain orientation can form elastic polymer having lower melting point. [20]

Conclusions

In this study PVA/pullulan films was prepared both mechanical and thermal properties, water solubility of pullulan were improved via blending with PVA. We found addition of (GA) to the polymers blend produce humongous polymer film rather than film PVA/pullulan without cross-linker. Above results indicate that cross-linking is effective way for improving physical properties of polymer blend film.

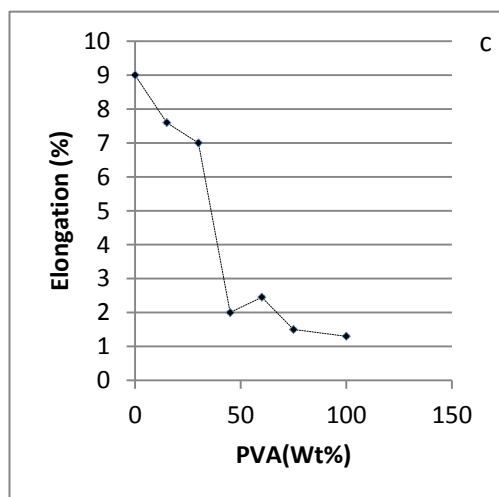
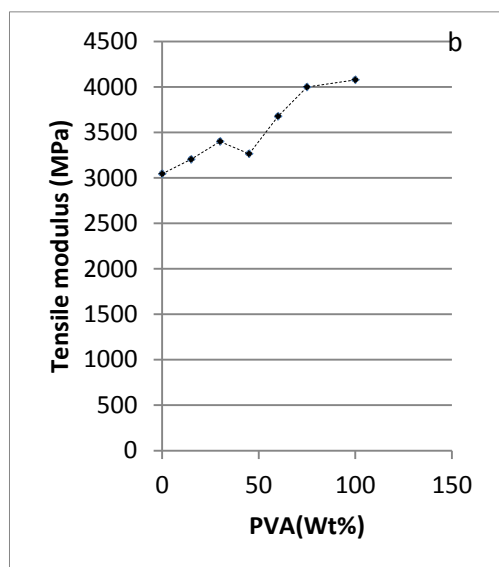
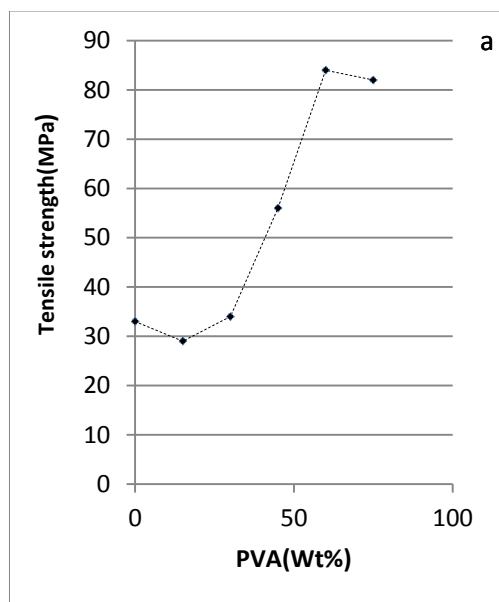


Figure 2: Mechanical Properties for Pullulan/PVA Blend Film in (a) Tensile Strength, (b) and (c) Elongation (%).

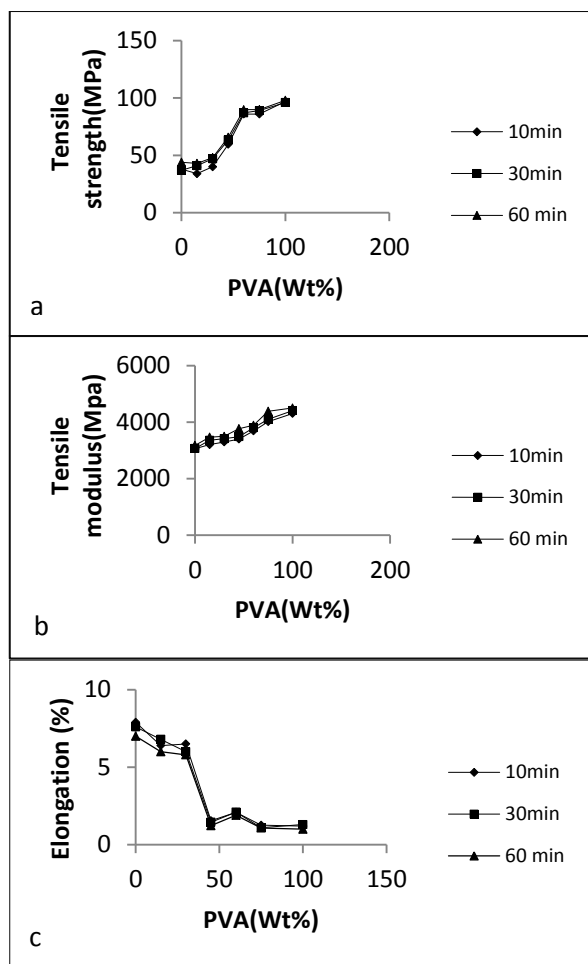


Figure 3: Mechanical Properties for Pullulan/PVA Blend Film cross linked with (GA) at 10, 30 and 60 min in (a) Tensile Strength, (b) Tensile Modulus and (c) Elongation (%).

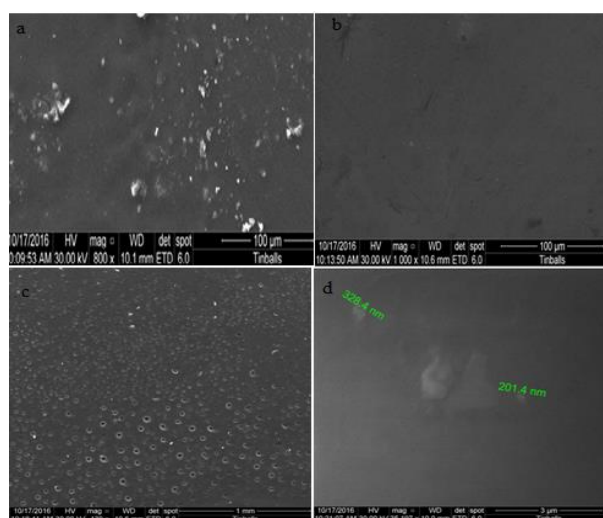


Figure 4: Scanning Electron Microscopy (SEM) of Pure Pullulan Film (a), Pure PVA film (b), Pullulan /PVA (c) and Cross-Linked Pullulan /PVA.

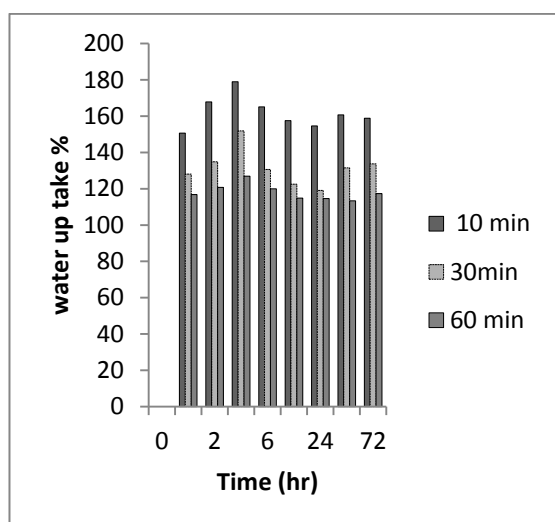
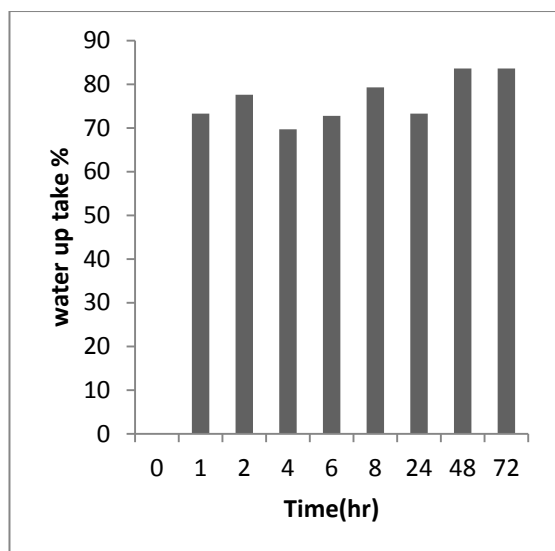


Figure 5: water up take behavior of PVA/Pullulan in (a) and cross –linked PVA /Pullulan film at different time of cross linking reaction.

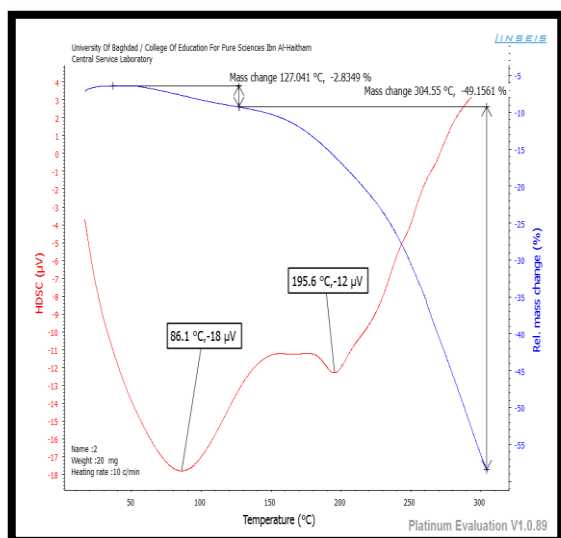


Figure: 6 DSC and TGA for the Pull/PVA.

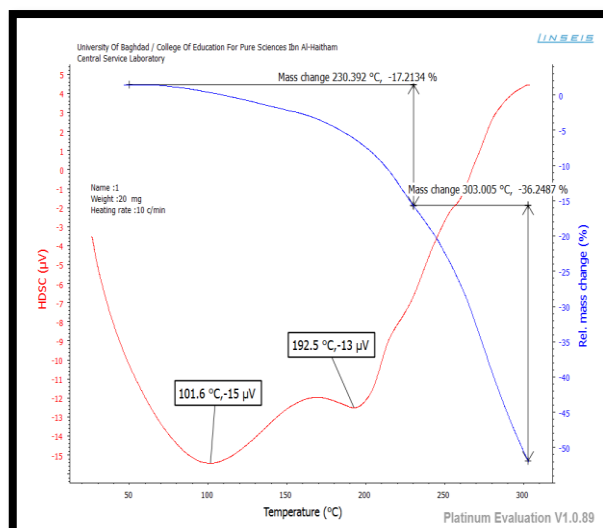


Figure 7: DSC and TGA for the pull/PVA cross linked with GA.

References

- [1] Silva, B. D, Ulhoa C. J, Batista A. K., Di Medeiros C. M, Da Silva Filho R. R, Yamashita F. and Fernandes K F., "Biodegradable and bioactive CGP/PVA film for fungal growth inhibition," *Carbohydrate Polymers* 89, p.964–970, 2012.
- [2] Krause S., Paul, D. R., and Newman S., *Polymer-Polymer Compatibility in polymer blend*, New York, USA: Academic press, 1978.
- [3] Coleman M. and Varnell D., "FT I. R. studies of polymer blends: V. Further observations on polyester-poly(vinyl chloride) blends," *Polymer*, vol.22, no.10, p.1324–1328, 1981.
- [4] Woo E. M., Barlow J. W, and Paul D, "Phase behavior of blends of aliphatic polyesters with a vinylidene chloride/vinyl chloride copolymer," *Applied Polymer Science*, pp. VOL 32, no.3, pp.3889–3897, 1986.
- [5] Varnell D. F., Runt J. P, and Coleman M. M., "FT I. R. and thermal analysis studies of blends of poly(ε-caprolactone) with homo- and copolymers of poly(vinylidene chloride)," *Polymer*, vol.24, no.1, p.37–42, 1983..
- [6] Tsukasa M, Yuuki T, Sachiko A, Takahiko I, Akie H, Keiko E, "Role of boric acid for a poly (vinyl alcohol) film as a cross-linking agent: Melting behaviors of the

- films with boric acid," *Polymer*, pp. Volume 51, Issue 23: Pages 5539–5549, 2010.
- [7] Zhu J, ". Bioactive modification of poly (ethylene glycol) hydrogels for tissue engineering," *Biomaterials*, p.31(17): 4639–4656, 2010.
- [8] Steinbuchel, A. and Rhee, S. K., In *Polysaccharides and Polyamides in the Food Industry: Properties, Production, and Patents*, Vol.1: Polysaccharides, Weinheim: Wiley-VCH, 2005Chapter 11.
- [9] Maitra J. and Shukla V., "Cross-linking in Hydrogels - A Review," *American Journal OF Polymer Science*, vol.4, no.2, pp.25-31, 2014.
- [10] Sawhney A. S, Pathak C. P, Rensburg J. J, Dunn R. C and Hubbell J. A, "Optimization of photopolymerized bioerodible hydrogel properties for adhesion prevention," *Biomed Mat Res*, vol.28, pp.831-838, 1994.
- [11] Kimoto T, Shibuya T and Shiobara S, ". Safety studies of a novel starch, pullulan: chronic toxicity in rats and bacterial mutagenicity," *Food Chem Toxicol*, vol.35, no.3-4, pp.323-9, 1997.
- [12] Nguyen KT and West JL, "Photopolymerizable hydrogels for tissue engineering applications. I," *Biomateria*, vol.23, pp.4307-4314, 2002.
- [13] Ramamurthi A and Vesely I, " Ultraviolet light-induced modification of crosslinked hyaluronan gels. ," *Biomed Mater Res A*, vol.66, no.2, pp.317–329,, 2003.
- [14] Abed A., Assoul N., Ba M., Mohamed D. S. and Portes P., "Influence of Polysaccharide Composition on the Biocompatibility of Pullulan/Dextran-Based Hydrogel," *Journal of Biomed Mater Res Part A*, vol.96A, p.535– 542, 2011.
- [15] Prasad, P., Guru, S. G., Shivakumar, R. H. and Rai, S. K., "Investigation on Miscibility of Sodium Alginate/Pullulan Blends," *Journal of Polym. Environ*, vol.20, pp.887-893, 2012.
- [16] Prasad, P., Guru, G. S., Shivakumar, H. R. and Sheshappa, K., "Miscibility, Thermal, and Mechanical Studies of Hydroxypropyl Methylcellulose/Pullulan Blends," *Journal of Appl Polym Sci.*, vol.110, p.444–45, 2008.
- [17] Denizli BK, Can HK, Rzaev ZMO and Guner A, "Preparation conditions and swelling equilibria of dextran hydrogels prepared by some crosslinked agents., ." *Polymer*, vol.45, no.19, p.6431–6435, 2004.
- [18] Göksungu Y. r, Dağbağlı S., Uçan A., Güvenç U, ". Optimization of pullulan production from synthetic medium by *Aureobasidium pullulans* in a stirred tank reactor by response surface methodology," *Chem. Technol. Biotechnol*, pp.80, 819,, 2005.
- [19] ElSayedS., MahmoudA. A and Hassen A, "DSC,TGAanddielectricpropertiesofcarboxymethylcellulose/polyvinyl alcohol blends K. H. ," *Physica B*, vol.406, p.4068–4076, 2011.
- [20] Bernal, A,KURITKAI and SAHAP, "Poly(vinyl alcohol)-poly(vinyl pyrrolidone) blends: Preparation andcharacterization for a prospective medical application., "Mathematical Methods and Techniques in Engineering and Environmental Science., pp.431-434.

Research Article

Development of Dispersive Liquid-Liquid Microextraction method combined with UV spectrophotometry for the Determination of Malathion Pesticide

Wijdan S. Khayoon

Department of Chemistry, College of Science, University of Baghdad, IRAQ.

*Correspondent Author Email: wijdansh2012@gmail.com

Article Info

Received
19/10/2016

Accepted
18/01/2017

Abstract

A simple and novel method was developed by combination of dispersive liquid-liquid microextraction with UV spectrophotometry for the preconcentration and determination of trace amount of malathion. The presented method is based on using a small volume of ethylenechloride as the extraction solvent was dissolved in ethanol as the dispersive solvent, then the binary solution was rapidly injected by a syringe into the water sample containing malathion. The important parameters, such the type and volume of extraction solvent and disperser solvent, the effect of extraction time and rate, the effect of salt addition and reaction conditions were studied. At the optimum conditions, the calibration graph was linear in the range of 2-100 ng mL⁻¹ of malathion with a limit of detection of 0.8 ng L⁻¹. In addition, the enrichment factor was 30. The developed method was successfully applied for the determination of malathion pesticide in water samples.

Keywords: Malathion, Spectrophotometry, Pesticide, Microextraction, Sample preparation.

الخلاصة

يهدف البحث الى تطوير طريقه جديدة وبسيطة وذلك بأقتران طريقه تشتت سائل-سائل المايكرويه مع مطياف الاشعه فوق البنفسجية وذلك لتقدير تراكيز ضئيلة جدا من مبيد الملاثيون. تعتمد الطريقة على الحقن السريع لمزيج المذيبات الثنائي والمكون من حجوم صغيرة من مذيب كلوريد الميثيلين (كمذيب استخلاص) والممزج مع حجوم صغيره جدا من الايثانول المستخدم كمذيب تشتت الى محلول مائي يحتوي على الملاثيون. تمت دراسة الظروف المثلى للاستخلاص والمتضمنه ظروف التفاعل ونوع وحجم كل من المذيب المشتت والمذيب المستخلص وتأثير سرعة وزمن الاستخلاص وتأثير إضافة الملح. عند الظروف تم الحصول على خطيه جيدة تراوحت بين 2-100 نانو غرام لكل مل مع حد كشف قيمته 0,8 نانو غرام لكل مل. بالإضافة الى ذلك تم الحصول على عامل تركيز جيد قيمته 30. تم تطبيق الطريقة المطورة بنجاح على لتقدير مبيد الملاثيون في عينات مياه ملوثة.

Introduction

Pesticides are one of the most potentially harmful chemicals introduced into the environment. Worldwide using pesticides increased enormously since the 1960s. However, using pesticides helped to significantly reduce crop losses and to improve the yield of crops such as corn, maize, vegetables, potatoes, and cotton. Organophosphate pesticides are commonly used pesticides in the world and require more awareness because of their possible toxic effects on-target animals [1]. Malathion (*S*-1,2-bis(ethoxycarbonyl) ethyl-*O,O*-dimethyl-phosphorodithioate) Figure 1 is an organophosphorus pesticide that used in both agriculture and households to control insect pests affecting a number of crops, stored grains and livestock feed via ground and aerial sprays and aerosols. Malathion rapidly converts to its metabolism malaoxon either after absorption or in-

gestion into the human body or in untreated water during the chlorination phase of water treatment. Therefore, malathion should not be used in the drinking waters or any upstream waters. In addition, the toxic exposure effect to high level of malathion considers a source of body-wide symptoms such skin and eye irritation, cramps, nausea, diarrhea, excessive sweating, seizures and even death [2] [3] [4].

Various analytical methods have been reported for the determination of malathion such gas chromatography [3] [5] HPLC [6] [7] thin layer chromatography [8], capillary electrophoresis [9], spectrophotometry [2] [3], atomic absorption spectrometry [10], fourier transform infrared (FTIR) spectrometry [11] [12] [13] [14].

taining different concentrations of malathion was examined according to the recommended procedure of DLLME and corresponding spectra of sedimented phase were recorded in the range of 200-650 nm.

Figure 2 shows maximum absorbance wavelength at 226 nm. Therefore, this wavelength was selected for measuring the absorbance of the extracted phase throughout this work. In order to achieve a high recovery and enrichment factor, all the parameters that can probably influence the extraction performance such as; type and volume of extraction solvent, kind and volume of disperser solvent, extraction time and salt concentration that were investigated and optimized.

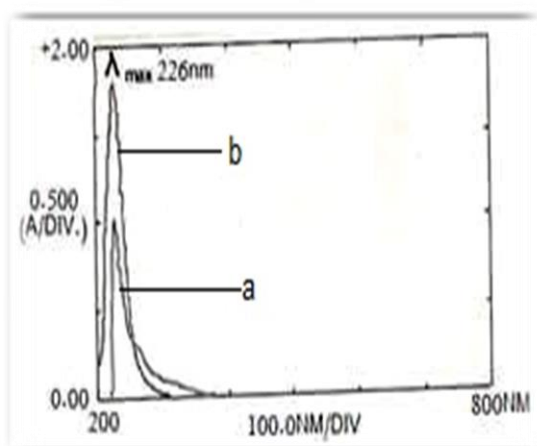


Figure 2: UV-Spectrum of malathion a) 500 ng mL⁻¹ before DLLME and b) 50 ng mL⁻¹ after DLLME.

Effect of type and volume of the extraction solvent

In DLLME, the type of extraction solvent is an important factor for efficient extraction and should meet three requirements. The solvent should be denser than water, low solubility in water and it capable to extract the interested compounds [26]. Due to high density of halogenated hydrocarbons, usually they are examined as an extraction solvent. Thus, chloroform (CHCl₃), carbon tetrachloride (CCl₄), 1,2-dichloroethane (C₂H₄Cl₂), dichloromethane (CH₂Cl₂), and ethylene chloride were examined for this purpose. In spite of a cloudy solution and two-phase system was formed using the selected solvents but ethylene chloride shows higher signal than others. Therefore, ethylene chloride was selected as extraction solvent. The effect of the extraction solvent volume was performed using 1.5 mL of ethanol different volumes of ethylene chloride in the range of 200–800 μL. According to Figure 3,

the absorbance increased by increasing the volume of ethylene chloride to 300 μL and then remained approximately constant with further increasing of its volume. Therefore, 300 μL was selected as optimum volume in other experiments.

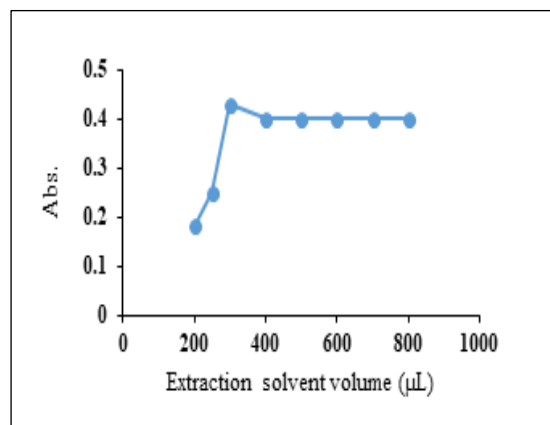


Figure 3: Effect of the extraction solvent (ethylene chloride) volume on the analytical responses after DLLME

Effect of type and volume of the disperser solvent

Selection of the disperser solvent is based on its miscibility in the extraction solvent and aqueous solution, which enables the extraction solvent to be dispersed as fine droplets in the aqueous phase to form a cloudy solution. Therefore, it is limited to some solvents such as methanol, ethanol, acetonitrile, and acetone. A series of sample solutions were studied using 1.5 mL of each disperser solvent with 400 μL of ethylene chloride as the extraction solvent. The results show that high enrichment factors were obtained with ethanol. The effect of different volume of ethanol ranged from 1000–3000 μL using 400 μL of chloroform on the extraction recovery was examined. As it is shown in Figure 4 the absorbance reached its maximum value at 1500 μL of ethanol to disperser solvent volume and after that, the absorbance decreases slowly. Thus, 1500 μL of ethanol was chosen as the proper amount.

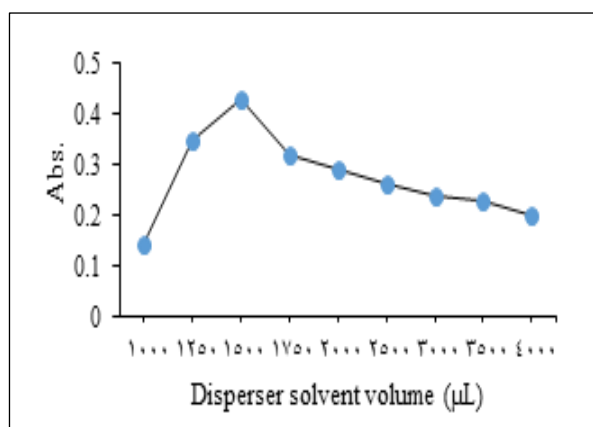


Figure 4: Effect of the disperser solvent (ethanol) volume on the analytical responses after DLLME.

Effect of extraction time and extraction rate

Extraction time is the important factor in most extraction techniques. It defined as the interval time between the injection of the solvents mixture and starting to centrifuge. The effect of extraction time was studied over the range of 1 to 15 min under the constant experimental conditions. Due to the infinitely large surface area between extraction solvent and aqueous phase after the formation of cloudy solution, malathion diffuses quickly into the extraction solvent. Therefore, equilibrium state is achieved quickly and the extraction time is very short about 3 min. Extraction rate (centrifuge rate) was also examined in the range of 1000-5000 rpm for 5 min. Higher absorbance value was obtained at 4000 rpm. Subsequently, it was selected as the best centrifuge rate.

Effect of salt addition

In general, addition of salt decreases the solubility of analytes in the sample solution by increasing the ionic strength (salting out effect) and enhances their partitioning into the organic phase. The influence of ionic strength on the performance of DLLME, was investigated by adding 0, 2.5, 5 and 10% (w/v) sodium chloride, respectively to sample that was spiked with malathion. However, it was found that salt addition did not result in an increase in extraction efficiency while addition of large amounts of salt to the aqueous phase increases its viscosity. Therefore, the velocity of the mass transfer processes of the analytes from the aqueous layer to the organic layer is diminished. Thus, no salt was added in further experiments.

Analytical features of the proposed method

After optimization all the experimental conditions, analytical parameters of the proposed method such regression equation, linear range, limit of detection, reproducibility, preconcentration, and improvement factors were investigated and the obtained data were summarized in Table 1. The calibration graph was linear in the range of 2-100 ng/mL⁻¹ with a correlation coefficient (*r*) of 0.9996 while, the limit of detection (LOD) was calculated based on $LOD = 3S_b/m$ and limit of quantification (LOQ) based on $10S_b/m$ (where *S_b*, and *m* are standard deviation of the blank, and slope of the calibration equation, respectively). However, LOD and LOQ values were 0.8 ng/mL⁻¹ and 2.56 ng/mL⁻¹, respectively. The preconcentration factor for the proposed DLLME method is calculated by the ratio of the highest sample volume (10 mL) and the final volume of nearly 300 µL. Therefore, the solution is concentrated by a factor of 33.3. The enrichment improvement factor was obtained from the slope ratio of the calibration graph after and before the extraction. According to this concept, enrichment improvement factor of 29 was obtained.

Table 1: Analytical parameters of the proposed method.

Parameters	Data
Regression equation using DLLME	$A = 0.0088C + 0.012$, $R^2 = 0.9996$
Regression equation before DLLME	$A = 0.0003C + 0.02$, $R^2 = 0.9993$
Linear range (ng mL ⁻¹)	2-100 (200-5000) ^a
Limit of detection (ng mL ⁻¹)	0.8 (6) ^a
Repeatability (RSD%) (n=5)	1.74 (1.34) ^a
Preconcentration factor	33.3
Enrichment factor	29

^a The results before DLLME

Application to real samples

To evaluate the performance and validation of the suggested method, it was applied to determine the malathion in two water samples, which were selected from Tap and river water (Baghdad, Iraq). The tested water samples were found to be free from malathion according to the optimized procedure. The results are presented in Table 2. The recoveries for the addition of different concentrations of malathion to samples are in the range of 98.8–102.1% and indicate that the proposed method is suitable for determination of trace amounts of malathion in the real samples.

Table 2: Determination of malathion in river and tap waters samples by proposed method..

Sample	Added (ng mL ⁻¹)	Found ^a (ng mL ⁻¹)	Recovery %
River water	0	ND ^b	-
	10	10.21	102.10
	50	50.80	101.60
	80	79.99	99.98
Tap water	0	ND ^b	-
	10	9.98	99.8
	50	49.40	98.8
	80	80.12	100.12

^a Standard deviation (n= 5); ^b Not detected

Conclusions

Spectrophotometric method by using DLLME technique for the extraction, preconcentration and determination of trace amount of malathion in water was developed. Besides employment of usual laboratory equipment, the proposed DLLME method provides advantages such as simplicity of operation, low sample volume, low cost and high preconcentration factor.

Moreover, due to the large surface area between the organic droplets and the aqueous sample solution, it is much shorter since the extraction equilibrium is reached quickly. Finally, in comparison to solvent extraction methods, it is much safer, since only a small amount of the solvent is used.

References

- [1] W. Aktar, D. Sengupta and A. Chowdhury, "Impact of pesticides use in agriculture: their benefits and hazards," *Interdisciplinary toxicology*, vol.2, no.1, pp.1-12, 2009.
- [2] B. Sumalatha and N. V. S. Venugopal, "Spectrophotometric determination of Malathion (an organo phosphorous insecticide) with Potassium bromate," *Eurasian Journal of Analytical Chemistry*, vol.8, pp.131-135, 2013.
- [3] N. V. S. Venugopal,, B. Sumalatha and S. Bonthula, "Spectrophotometric determination of Malathion (an organo phosphorous insecticide) with Potassium bromate," *Eurasian Journal of Analytical Chemistry*, vol.8, pp.131-135, 2013.
- [4] A. Rauf, "Acute toxicity and effects of malathion exposure on behavior and hematological indices in Indian carp, *Cirrhinus mrigala* (Hamilton)," *International Journal of Aquatic Biology*, vol.3, no.4, pp.199-207, 2015.
- [5] H. M. Lofty, A. E. -A. A. Abd El-Aleem and H. H. Monir, "Determination of insecticides malathion and lambda-cyhalothrin residues in zucchini by gas chromatography," *Bulletin of Faculty of Pharmacy, Cairo University*, vol.51, pp.255-260, 2013.
- [6] M. Khuhawar, A. Channar and S. Lanjwani, "Indirect liquid chromatographic determination of malathion based on Copper (II) dimethyldithiophosphate complex formation," *Chromatographia*, vol.42, pp.680-682, 1996.
- [7] A. W. Abu-Qare and M. B. Abou-Donia, "Simultaneous determination of malathion, permethrin, DEET (N,N-diethyl-m-toluamide), and their metabolites in rat plasma and urine using high performance liquid chromatography," *Journal of Pharmaceutical and Biomedical Analysis*, vol.26, pp.291-299, 2001.
- [8] . K. Futagami, C. Narazaki, Y. Kataoka, H. Shuto and R. Oishi, "Application of high-performance thin-layer chromatography for the detection of organophosphorus

- insecticides in human serum after acute poisoning," *Journal of Chromatography B: Biomedical Sciences and Applications*, vol.704, pp.369-373, 1997.
- [9] . C. García-Ruiz, G. Alvarez-Llamas, Á. Puerta, E. Blanco, A. Sanz-Medel and M. L. Marina, "Enantiomeric separation of organophosphorus pesticides by capillary electrophoresis: Application to the determination of malathion in water samples after preconcentration by off-line solid-phase extraction," *Analytica chimica acta*, vol.543, pp.77-83, 2005.
- [10] J. H. Méndez, O. J. De Bias, V. R. Martín and E. S. López, "Indirect Determination of the Pesticide Malathion by Atomic Absorption Spectrophotometry," *Analytical Letters*, vol.18, pp.2069-2081, 1985.
- [11] M. Khanmohammadi, M. A. Karimi, K. Ghasemi, M. Jabbari and A. B. Garmarudi, "Quantitative determination of Malathion in pesticide by modified attenuated total reflectance-Fourier transform infrared spectrometry applying genetic algorithm wavelength selection method," *Talanta*, vol.72, pp.620-625, 2007.
- [12] A. K. Sharma, U. Tiwari, M. S. Gaur and R. K. Tiwari, "Assessment of malathion and its effects on leukocytes in human blood samples," *Journal of biomedical research*, vol.30, pp.52-59, 2015.
- [13] G. Quintás, S. Garrigues and M. de la Guardia, "FT-Raman spectrometry determination of Malathion in pesticide formulations," *Talanta*, vol.63, pp.345-350, 2004.
- [14] G. Quintás, A. Morales-Noé, S. Armenta, S. Garrigues and de la Guardia, Miguel, "Fourier transform infrared spectrometric determination of Malathion in pesticide formulations," *Analytica Chimica Acta*, vol.502, pp.213-220, 2004.
- [15] S. Magdic and J. B. Pawliszyn, "Analysis of organochlorine pesticides using solid-phase microextraction," *Journal of Chromatography A*, vol.723, pp.111-122, 1996.
- [16] J. Beltran, F. J. López and F. Hernández, "Solid-phase microextraction in pesticide residue analysis," *Journal of chromatography A*, vol.885, pp.389-404, 2000.
- [17] M. Andraščíková, E. Matisová and S. Hrouzková, "Liquid phase microextraction techniques as a sample preparation step for analysis of pesticide residues in food," *Separation & Purification Reviews*, vol.44, pp.1-18, 2015.
- [18] M. A. Farajzadeh, S. M. Sorouraddin and M. R. A. Mogaddam, "Liquid phase microextraction of pesticides: a review on current methods," *Microchimica Acta*, vol.181, pp.829-851, 2014.
- [19] W. Liu, Y. Hu, J. Zhao, Y. Xu and Y. Guan, "Determination of organophosphorus pesticides in cucumber and potato by stir bar sorptive extraction," *Journal of Chromatography A*, vol.1095, pp.1-7, 2005.
- [20] A. Juan-García, Y. Picó and G. Font, "Capillary electrophoresis for analyzing pesticides in fruits and vegetables using solid-phase extraction and stir-bar sorptive extraction," *Journal of Chromatography A*, Vols.229-236, p.1073, 2005.
- [21] M. Pastor-Belda, I. Garrido, N. Campillo, P. Vinas, P. Hellín, P. Flores and J. Fenoll, "Dispersive liquid-liquid microextraction for the determination of new generation pesticides in soils by liquid chromatography and tandem mass spectrometry," *Journal of Chromatography A*, vol.1394, pp.1-8, 2015.
- [22] C. Basheer, A. A. Alnedhary, B. S. M. Rao and H. K. Lee, "Determination of carbamate pesticides using micro-solid-phase extraction combined with high-performance liquid chromatography," *Journal of Chromatography A*, vol.1216, pp.211-216, 2009.
- [23] Basheer, Chanbasha, A. A. Alnedhary, B. M. Rao, S. Valliyaveetil and H. K. Lee, "Development and application of porous membrane-protected carbon nanotube micro-solid-phase extraction combined with gas chromatography/mass spectrometry," *Analytical Chemistry*, vol.78, pp.2853-2858, 2006.
- [24] M. Rezaee, Y. Assadi, M. -R. Milani Hosseini, E. Aghaee, F. Ahmadi and S. Berijani, "Determination of organic compounds in water using dispersive

liquid–liquid microextraction," *Journal of Chromatography A*, vol.1116, pp.1-9, 2006.

- [25] . H. Ebrahimzadeh,. Y. Yamini and F. Kamarei, "Optimization of dispersive liquid–liquid microextraction combined with gas chromatography for the analysis of nitroaromatic compounds in water," *Talanta*, vol.79, pp.1472-1477, 2009.
- [26] A. R. Zarei and F. Gholamian, "Development of a dispersive liquid–liquid microextraction method for spectrophotometric determination of barbituric acid in pharmaceutical formulation and biological samples," *Analytical biochemistry*, vol.412, pp.224-228, 2011.

Research Article

Preparation and Characterization of TiO₂ Nanostructure by TiCl₄ Hydrolysis with Additive NaOH

Rashed Taleb Rasheed

Department of Applied Sciences, Chemistry Division, University of Technology, IRAQ

*Correspondent Author Email: r_awsy@yahoo.com

Article Info

Received
08/09/2016

Accepted
21/05/2017

Abstract

Titanium dioxide (TiO₂) nanostructures were synthesized via the hydrolysis of TiCl₄ in alcohol / water solution/with sodium hydroxide solution in the ice-bath (0-5 °C). The particles were characterized by using X-ray diffraction technique (XRD), spectroscopy of Ultra Violet-Visible (UV / Visible) and infrared (FT-IR), atomic force microscope (AFM) and scanning electron microscope (SEM) analysis were used in order to gain information about the material, morphology, size and the shape of the particles.

Keywords: TiO₂ nanostructures, TiCl₄, hydrolysis.

الخلاصة

تم تحضير ثنائي اوكسيد التيتانيوم (TiO₂) بواسطة التحلل لرابع كلوريد التيتانيوم (TiCl₄) في محلول مائي/كحولي مع محلول هيدروكسيد الصوديوم في حمام ثلجي (0-5 °C). تم تشخيص الراسب المتكون باستخدام تقنية حيود الاشعة السينية (XRD)، مطيافية الاشعة فوق البنفسجية / المرئية (Uv/Visible) والاشعة تحت الحمراء (FT-IR)، ومجهر القوى الذرية (AFM) لدراسة الاطوار والحجم الحبيبي للجسيمات النانوية وتم دراسة طوبوغرافية السطح باستخدام المجهر الالكتروني الماسح (SEM).

Introduction

Titanium dioxide (TiO₂) or titania, is one of the most attracted materials in nanotechnology and nanoscience because of a very useful semiconducting transition and exhibits unique characteristics such as non-toxicity, easy handling and low cost [1]. Interests towards the nanostructures titanium dioxide (TiO₂) was grown in the past decades, due to its interesting physical and chemical properties [2] [3].

These advantages make TiO₂ a material in solar cells, fuel cell, environmental purification applications, a pigment, selfcleaning, surfaces, resistance to photochemical, chemical erosion and chemical sensors for hydrogen gas evolution [1] [4] [5]. Titania has three different crystalline phases: brookite (orthorhombic), anatase [6] and rutile [7]. Rutile is the most stable phase at sizes greater than 35 nm, while brookite is more stable than anatase for crystal sizes greater than 11 nm. Among these phases, the TiO₂ exists mostly as anatase and rutile which have the tetragonal structures while brookite has orthorhombic structure [8].

However, the high-temperature stable phase is rutile [9].

Several methods have been reported in the literature to prepare TiO₂, including the hydrolysis of titanium alkoxides, acidic solutions of Ti (IV) salts, oxidations of TiCl₄ on gaseous phase [10], sputtering, chemical vapor deposition and sol-gel process [11]. Among them, one of the most used methods is the sol-gel technique due to its excellent chemical homogeneity and possibility of deriving unique metastable structure at low reaction temperatures [12]. The different routes were usually found produced different results. Even for the same route, the obtained powder size is different when using a different amount of the starting materials [13]. Many methods have been employed to prepare TiO₂ films, including sol-gel process, chemical vapor deposition, e-beam evaporation and sputtering.

The sol-gel conventional method uses the hydrolytic route, which involves the initial hydrolysis of the chloride or alkoxide precursor followed by continual condensations between the hydrolyzed particles forming the gel [14]. In this work, we

have prepared TiO₂ nanostructures using TiCl₄ as a precursor.

Materials and Methods

Titanium tetrachloride (TiCl₄), sodium hydroxide (NaOH) and ethanol (EtOH) absolute grade, all these chemicals have purity 99.9%, where obtained from Fluka Company in high purity and no further purification was done before use.

Synthesis of TiO₂ nanostructures

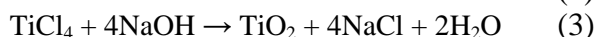
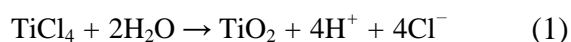
TiO₂ nanostructures were prepared by sol-gel technique using titanium tetrachloride (TiCl₄), absolute ethanol (EtOH), distilled water, and sodium hydroxide (NaOH) as the starting materials. TiCl₄ is added to a mixture of water/ alcohol (50:50) in an ice bath.

The receiving water is maintained at 0°C while TiCl₄ is added dropwise under vigorous stirring. The resulting precursor solution has a TiCl₄:H₂O volume ratio of 1:40 and pH ≈ 1. Subsequent condensation of the hydrolysis product results in gel formation.

In order to obtain a more stable suspension, the Cl⁻ concentration was reduced and pH increased to around 2.5 by added dropwise of sodium hydroxide solution under vigorous stirring and the gel is precipitated from the suspension. The resulting material is then subjected to repeated cycles of centrifugation, washing, and resuspension until the final product, usually in powder form, is considered free from impurities.

Results and Discussion

We prepared crystalline titanium dioxide by sol-gel precipitation method using titanium tetrachloride in aqueous solution and subsequently annealed at 300°C and 500 °C. As soon as TiCl₄ hydrolyses TiO₂ particles, H⁺ and Cl⁻ ions were generated, the process of reaction can be described by the following steps [15]:



The general process for preparing TiO₂ by sol-gel process, at low temperature, anatase is the primary structure phase formed observed which transforms only upon annealing to rutile phase which is thermodynamically more condense and most stable [16]. As annealing treatment prolonged the

rutile XRD peaks became sharper indicating the formation of larger r-TiO₂.

Calcinations temperature

Characterization of Nanostructures

The XRD is employed for the identification and understanding the crystalline growth nature of titanium dioxide structures prepared by sol-gel method. Calcination is a common treatment used to improve the crystallinity of TiO₂ powders [12]. Two phase structures of titanium dioxide powders were characterized at (300 and 500 °C) for (4-hours), by X-ray diffraction (XRD) at room temperature.

Major peaks corresponding to the tetragonal TiO₂ were observed.

The diffraction peak at 2θ with 27.5°, 36.2°, 39.2°, 41.3°, 44.1°, 54.4°, 56.6°, 62.6°, 64.1°, 68.8°, and 70.0° corresponds to the (110), (101), (200), (111), (210), (211), (220), (002), (310), (301) and (112) planes of rutile TiO₂ (JCPDS Card No.21-1276), respectively, except the peaks (2θ = 64.1° and 70.0°) corresponds to the crystal planes of (310) and (112) respectively, were undistinguished at 300 °C calcination, indicating the formation of rutile phase of TiO₂. Our FT-IR peaks are in good agreement with the literature report [17]. The presence of titanium dioxide particles was confirmed by the location of the peaks which compared to literature values [18]. As a result of annealing, the nanostructures are found to have increased intensity and a slight reduction of the full width at half maximum (FWHM). The crystalline size of the titanium dioxide calculated by the equation of Debye-Scherrer's which is given by:

$$D = K\lambda / (\beta \cos\theta) \quad (4)$$

Where *D* is the crystal size; *K* is usually taken as 0.89, β is the line width at half-maximum height (FWHM) and λ is the wavelength of the X-ray radiation (λ=0.15406 nm) for CuKα [19]. The representative XRD charts, Figure 1, samples as-prepared and calcined at (300 and 500 °C).

Miller indices provided in the Figure 1 and all peaks determine the transformation of calcined powder to TiO₂ crystallites with tetragonal rutile crystal structure. In addition, the increasing of the calcination temperature causes increases the number of reflection. We can calculate the lattice

constant of the titanium dioxide particles by using the formula:

$$1/d^2 = ((h^2 + k^2)/a^2) + (l^2/c^2) \quad (5)$$

Where (d) is the interplanar distance, (a) and (c) are the lattice constant for the tetragonal structure and ($h k l$) are the Miller indices. The calculated crystalline size (D) and lattice constant (a and c) of TiO_2 are tabulated in Table 2.

It is observed that the TiO_2 crystallinity improves with increasing substrate temperature (300 °C to 500 °C) for study peaks (110, 101 and 211) evident from XRD pattern. The crystallite size of TiO_2 obtained using Debye-Scherrer's equation and the XRD parameters of nanostructures at various crystalline orientations at 300 °C and 500 °C respectively were shown in Table 1.

Scanning Electron Microscope (SEM) Analysis

SEM was used to further examine the morphology, crystallinity, and shape and particle size of the sample. A SEM image of TiO_2 nanostructures in rutile phase are shown in Figure 2. It is clearly seen that the TiO_2 consist of shapes like porous hollow.

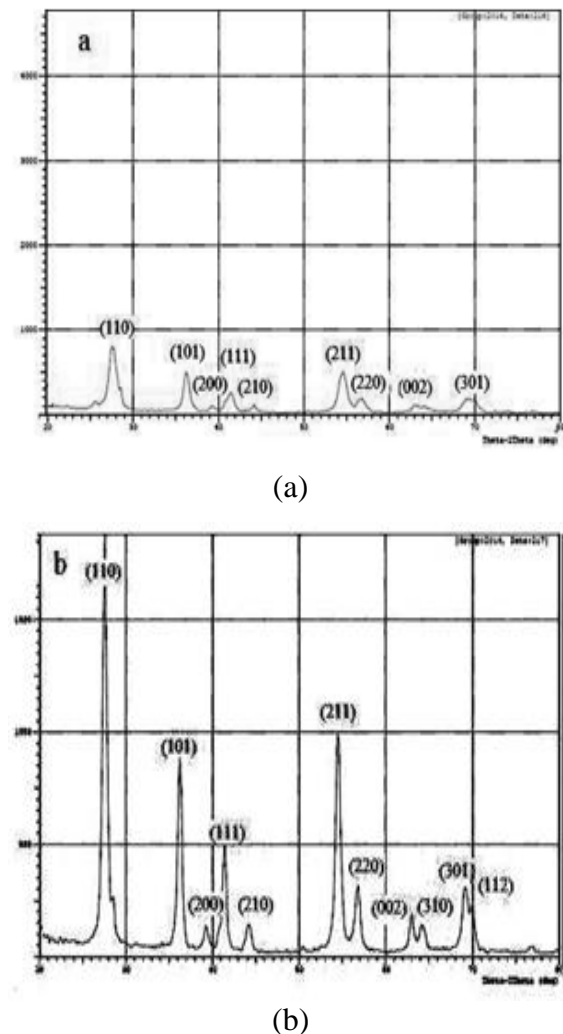


Figure 1: XRD peaks for the prepared TiO_2 nanostructures after annealing at (a) 300 °C and (b) 500°C for (4 hours).

Table 2: The crystallite size and lattice parameters of TiO_2 nanostructures.

Substrate temperature	hkl	$d(\text{Å})$	2θ	θ	FWHM (β)	$D(\text{Å})$	$a(\text{Å})$	$c(\text{Å})$
300 °C	110	3.226	27.560	13.833	1.029	7.955	4.562	4.271
	101	3.118	28.600	14.300	0.500	16.390	-	-
	211	1.682	54.502	27.250	1.140	7.835	-	-
500 °C	110	3.233	27.560	13.780	0.670	12.206	4.572	4.263
	101	3.118	28.600	14.300	0.431	19.014	-	-
	211	1.683	54.446	27.223	0.677	13.194	-	-

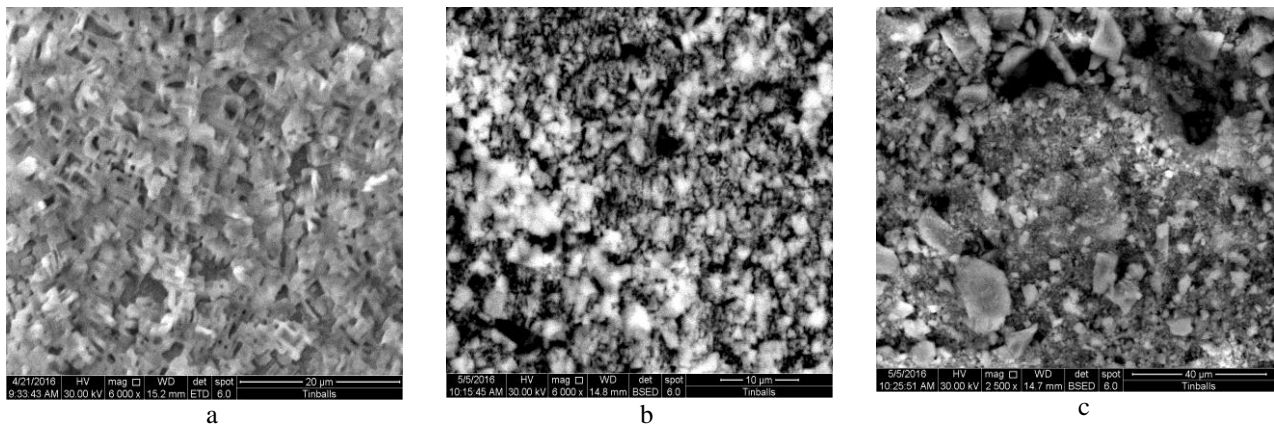


Figure 2: A top-view SEM image of TiO₂ nanostructures annealing at (a) 100 °C (b) 300 °C and (c) 500 °C for (4- hours).

FT-IR Spectroscopy

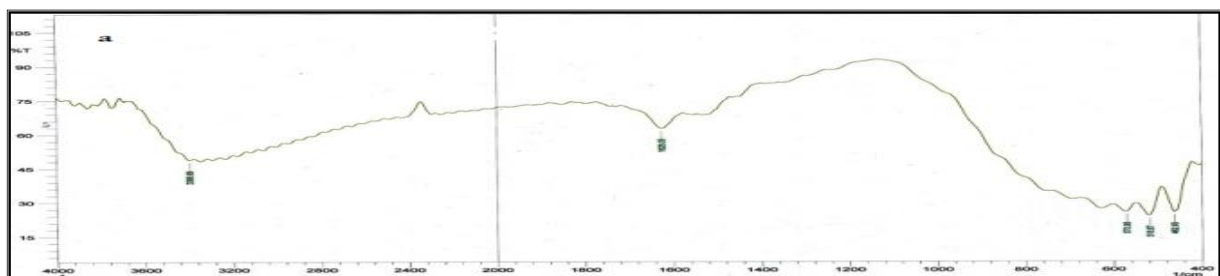
It is well known that the vibrational spectroscopy is a very useful technique for the determination of the functional groups of titanium dioxide nanostructures. The FT-IR spectrum of TiO₂ nanostructures shows in Figure 3. The peaks, in the spectra around, to 3400 and 1630 cm⁻¹ are due to stretching and bending vibration of the –OH group respectively. In the FT-IR spectra, all the peaks observed were around 560-460 cm⁻¹ represent to both stretching and bending of Ti-O-Ti group [4]. When annealing at (300 °C and 500 °C) the broad peaks of O-H stretching vibration become smaller with increase temperature and the Ti-O stretching become broad and more significant.

Atomic force microscope (AFM)

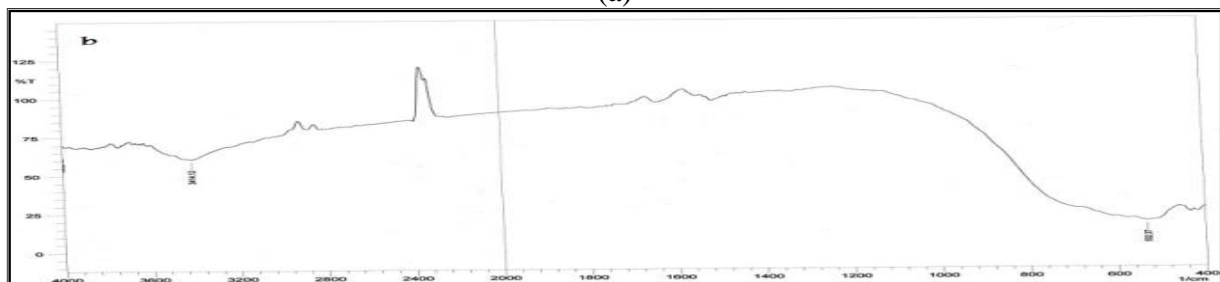
Figure 3 shows a typical three-dimensional atomic force microscope (AFM) images and the cor-

responding size distributions of the titanium dioxide nanostructures as prepared, annealing at 300 °C and 500 °C. As shown in the Figure the better surface quality and crystallographic structure are obtained.

It's clear from the Figure 4 that TiO₂ nanostructures are porous in shape, having an average diameter of 64.56 nm, 94.29 nm and 100.48 nm for as-prepared, annealing at 300 °C and 500 °C respectively. The 3-dimensional (3D) AFM image of material nanostructures in which the regularly distributed TiO₂ nanostructures pillars and voids over the entire surface can be seen with a maximum value and morphology with a root-mean-square (RMS) roughness and average diameter as shown in Table 2.



(a)



(b)

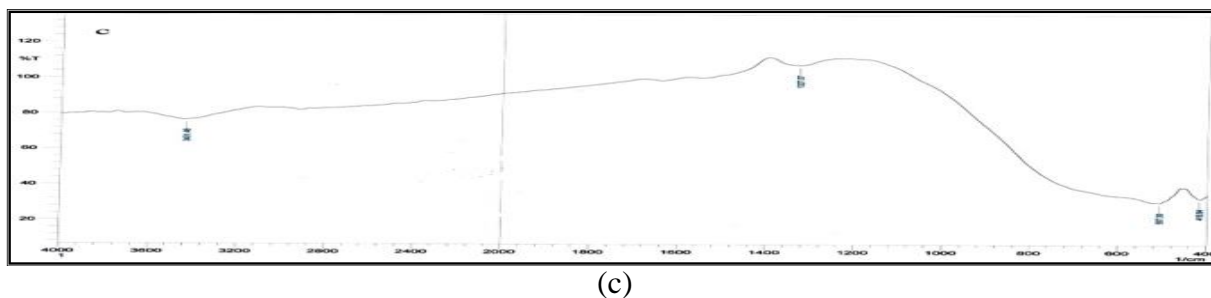


Figure 3: FT-IR spectra of TiO₂ annealing at (a) 100 °C (b) 300 °C and (c) 500 °C for (4 hours).

Table 2: Roughness average, root-mean-square (nm) roughness and the average diameter of TiO₂ annealing at 100 °C, 300 °C and 500 °C in nm units.

Samples	Roughness average	root-mean-square (RMS) roughness	Average Diameter
100 °C	0.612	0.712	64.56
300 °C	0.335	0390	94.29
500 °C	0.637	0.746	100.48

ured by using UV-Vis spectrophotometer. The UV- Vis optical properties in the range (250–1000) nm at various temperatures (as-prepared (100), 300 and 500 °C) showed temperature dependent transmittance and absorbance, as shown in Figure 5. Both samples (300 and 500 °C) showed a slight decrease in optical transmittance at higher temperatures. This is probably due to the increased particle size and surface roughness, and also to the phase transformation from anatase to rutile which results in band gap decrease and led to higher surface scattering [20].

Optical Properties

The optical transmittance and absorbance of the TiO₂ solution (0.001 M) in ethanol, was meas-

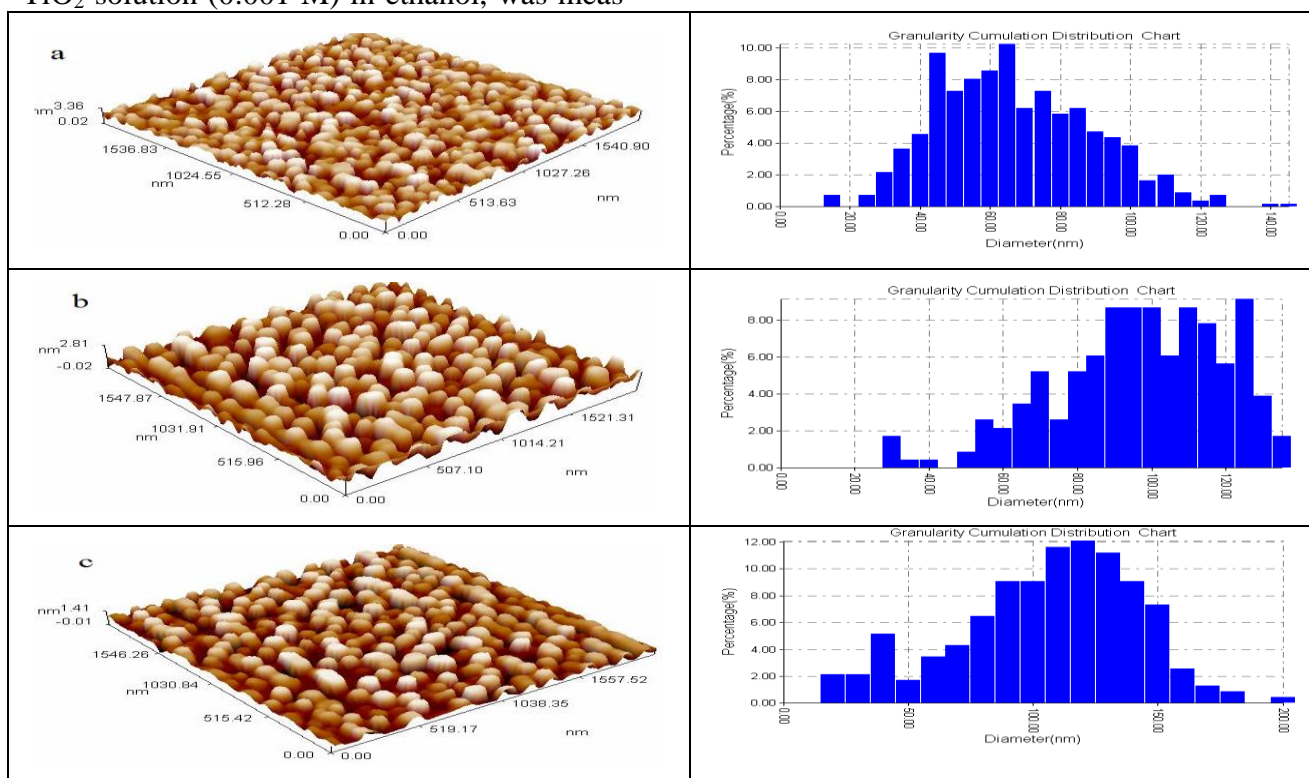


Figure 4: AFM image of TiO₂ nanostructures annealing at (a) 100 °C (b) 300 °C and (c) 500 °C.

The optical band gaps were measured by plotting $(\alpha h\nu)^2$ versus $h\nu$ for TiO₂ thin films prepared by dip coating technique are illustrated in Figure 6. The band gap values: (3.24, 3.19 and 3.21 eV) are corresponding to the (as-prepared, 300 and 500) °C. The optical band gaps were measured by plotting $(\alpha h\nu)^2$ versus $h\nu$ for TiO₂ films and are illustrated in Figure 6. The band gap energy (E_g) of as-prepared TiO₂ nanoparticles (3.31 eV), which is larger than that values of (3.25 and 3.20 eV) for the bulk TiO₂, corresponding to the (300 and 500) °C temperatures respectively.

This can be explained because the band gap of the semiconductors has been found to be particle size dependent [21]. The band gap decreases with increasing particle size and the absorption edge is shifted to a lower energy (red shift) with increasing particle size.

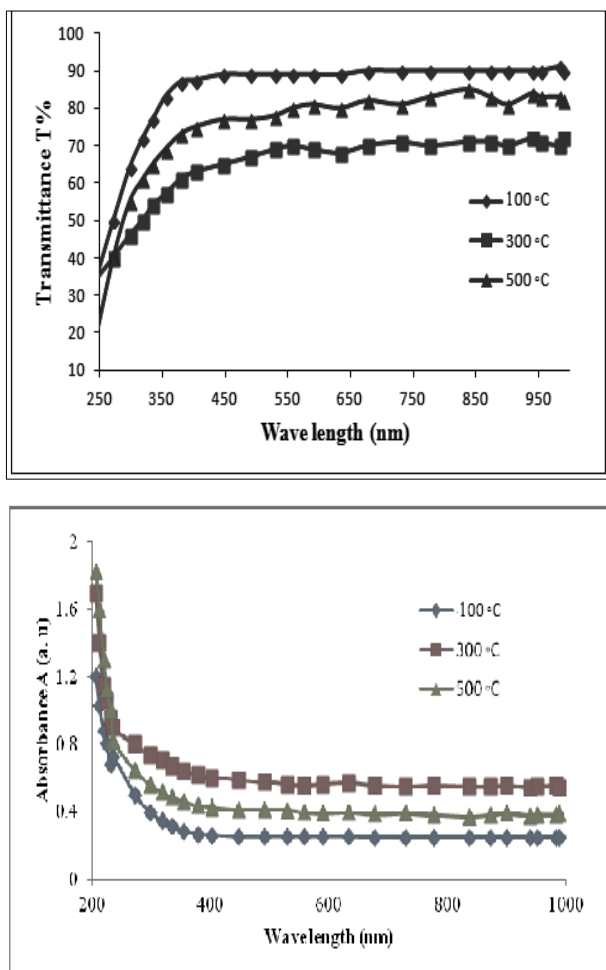


Figure 5: Optical Transmission (upper) and Absorption (lower) as a function of wavelength for TiO₂ at different temperatures (100, 300 and 500 °C).

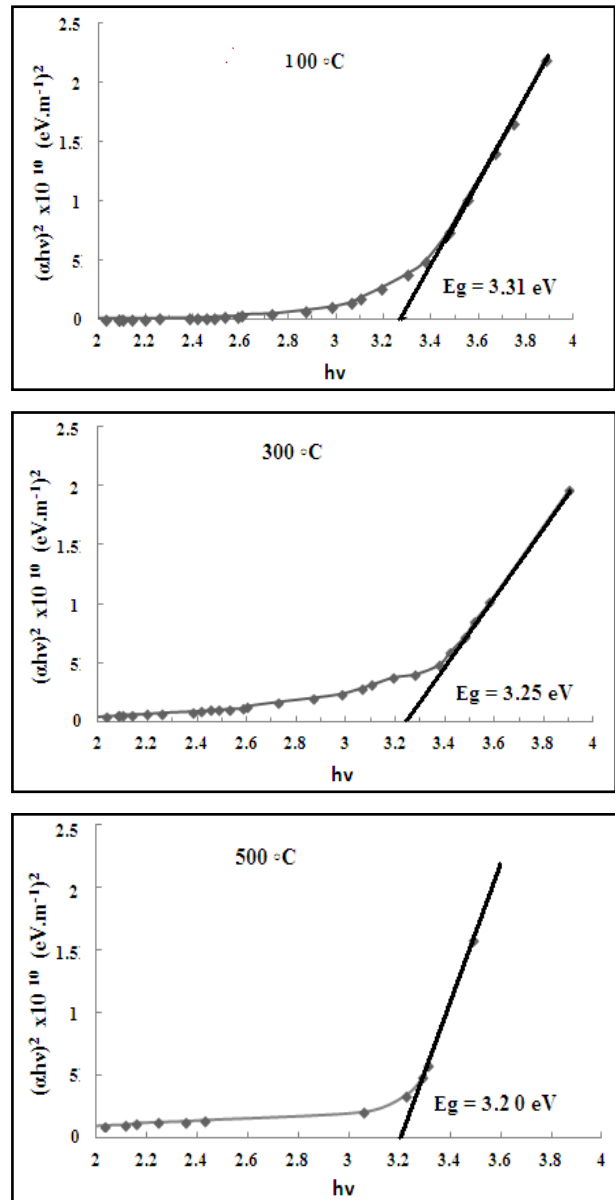


Figure 6: A plots of $(\alpha h\nu)^2$ versus photon energy ($h\nu$) of TiO₂ thin films with different temperature: 100 °C, 300 °C and 500 °C.

Conclusions

TiO₂ nanoparticles have been prepared from titanium tetrachloride (TiCl₄) with sodium hydroxide solution. We confirmed the nanoparticles by X-ray diffraction (XRD) and subsequently annealed at 300 and 500 °C. The studies of surface morphological obtain from SEM micrograph showed that the particles with the shapes like porous hollow are rutile in nature. Based on the XRD, SEM and AFM analyses, the current study shows that the size range of the nanoparticles is (64.56, 94.29 and 100.48 nm) at a temperature (As-prepared (100 °C), 300 °C and 500 °C) respectively.

Acknowledgements

The author would like to thank the University of Technology, Applied Sciences Department for technical assistance to complete this work.

References

- [1] S. M. W. C. a. D. B. M. R. Hoffmann, "Environmental Applications of Semiconductor Photocatalysis," *Chem. Rev.*, vol.95, no.1, pp.69-96, 1995.
- [2] A. P. K. Z. J. P. a. P. Y. S. A. Sher Shah, "Green synthesis of biphasic TiO₂-reduced graphene oxide nanocomposites with highly enhanced photocatalytic activity," *ACS Appl. Mater. Interfaces*, vol.4, pp.3893-3901, 2012.
- [3] R. B. Z. a. L. Gao., "Synthesis of nanosized TiO₂ by hydrolysis of alkoxide titanium in micelles.," *Eng. Mate*, vol.573, pp.224-226, 2002.
- [4] R. V. a. R. S. R. Sharmila Devi, "Synthesis of Titanium Dioxide Nanoparticles by Sol-Gel Technique," *I. J. I. R. S. E. T.*, vol.3, no.8, pp.15206-15211, 2014.
- [5] D. O. A. C. -. G. a. S. J. -. S. N. Castillo, "Structural and morphological properties of TiO₂ thin films prepared by spray pyrolysis.," *Revista Mexicana De Fisica*, vol.50, no.4, p.382, 2004.
- [6] B. L. B. a. M. A. Anderson., "Peptization Process in the Sol-Gel Preparation of Porous Anatase (TiO₂).," *Chem. Mater.*, vol.7, pp.1772-1778, 1995.
- [7] T. I. a. X. S. J. -G Li., "Anatase, brookite, and rutile nanocrystals via redox reactions conditions: phase-selective synthesis and physicochemical properties.," *J. Phys. Chem. C*, vol.111, pp.4969-4976, 2007.
- [8] M. -S. Z. J. -M. H. a. Z. Y. K. -R. Zhu, "Size effect on phase transition sequence of TiO₂ nanocrystal.," *Mater. Sci. Eng.*, vol.403, pp.87-93, 2003.
- [9] G. Brady, *Materials Handbook*, New York: McGraw-Hill., 1971.
- [10] C. L. A. C. Y. Z. a. D. F. L. Shi, "Morphology, and structure of nanosized TiO₂ particles synthesized by gas-phase reaction.," *Materials Chemistry and Physics*, vol.66, no.51(1), pp.51-57, 2000.
- [11] K. S. Mazdiyasi., "Powder synthesis from metal-organic precursors," *Ceram Int.*, vol.8, no.2, pp.42-45, 1982.
- [12] X. X. a. J. N. J. Zhang, "Hydrothermal hydrolysis synthesis and photocatalytic properties of nano-TiO₂ with an adju table crystalline structure.," *Journal of Hazardous Materials*, vol.176, pp.617-622, 2010.
- [13] B. X. W. M. Y. a. L. L. Li, "Preparation and characterization of nano-TiO₂ Powder," *Mater. Chem. Phys*, vol.78, pp.184-188, 2002.
- [14] E. I. T. D. S. S. D. M. C. R. V. P. G. P. a. H. I. N. R C Suci., "TiO₂ thin films prepared by sol - gel method.," *Journal of Physics: Conference Series*, vol.182, pp.1-4, 2009.
- [15] D. W. B. a. M. R. H. C. Kormann, "Preparation and Characterization of Quantum-Size Titanium Dioxide.," *Journal of Physical Chemistry*, vol.92, pp.5196-5201, 1988.
- [16] B. -Y. H. a. C. -M. T. C. Su, "Sol-gel preparation and photocatalysis of titanium dioxide.," *Catalysis Today*, vol.96, no.3, pp.119-126, 2004.
- [17] P. L. a. B. N. K. Thamaphat, "Phase Characterization of TiO₂ Powder by XRD and TEM.," *Nat. Sci.*, vol.42, pp.357-361, 2008.
- [18] M. U. f. N. K. a. E. h. M. Akarsu, "A Novel Approach to the Hydrothermal Synthesis of anatase titania Nanoparticles and the Photocatalytic Degradation of Rhodamine B," *Turk J Chem*, vol.30, no.3, pp.333-343, 2006.
- [19] B. D. Cullity, *Elements of X-Ray Diffraction*, Addison-Wesley, 1978.
- [20] Y. A. A. H. A. J. a. Y. K. Z. K. Sarmad S, "Annealing Effect on the Growth of Nanostructured TiO₂ Thin Films by Pulsed Laser Deposition (PLD)," *Eng. and Tech.*



Journal, vol.31B, no.4, pp.460-470, 2013.

- [21] S. M. A. R. R. K. Madhusudan Reddy, "Bandgap studies on anatase titanium dioxide nanoparticles. ," *Materials Chemistry and Physics.*, vol.78, pp.239-245, 2002.

Research Article

Synthesis and Identification of Heterocyclic Compounds (Oxazepine, Tetrazole) Derived from Benzidine as Photostabilizing for Poly vinyl chloride

Olfat A. Nief, Hamid G. Lawfah

Department of chemistry, Mustansiriyah University, IRAQ

*Correspondent author Email: Olfat_nife@yahoo.com

Article Info

Received

Accepted

Abstract

This research describes preparation of new four compounds (A2-A5) having 1,3-oxazepine and Tetrazole rings. The first step involves reaction of benzidine (A1) with aromatic aldehyde (cinnamaldehyde) in ethanol as a solvent in the presence of acid as catalyst to yield the Schiff base (A2), Schiff base (A2) was condensed with maleic anhydride and phthalic anhydride in dry benzene to give a seven-membered heterocyclic ring derivative (A3, A4), In addition, we synthesis novel tetrazole derivative (A5) from the reaction of Schiff base (A2) with sodium azide in tetrahydrofuran. The structure of synthesized compounds was identified by spectral methods [FTIR, $^1\text{H-NMR}$, and $^{13}\text{C-NMR}$] and measurement physical properties. The photo stabilization of poly (vinyl chloride) films by compounds (A1-A5) was studied. The Photo stabilization activities of these compounds were determined by monitoring the carbonyl and hydroxyl indexes values with irradiation time. The changes in viscosity average molecular weight of PVC with irradiation time were studied by using tetrahydrofuran as a solvent. The influence of concentrations additives (range 0.1-0.5wt) on the rate of photo degradation and Photo stabilization course was studied. Therefore, we found that was an increase Photo stabilization rates with increasing concentrations of additives. In addition, Studying the effect of film thickness and the results showed that an increase in film thickness would reduce the rate of photolysis. The results indicated that Photo stabilization proportion of plastic in the presence of additives follow the trend: (PVC blank) > PVC+A1 > PVC+A2 > PVC+A5 > PVC+A4 > PVC+A3. According to the results obtained, it proposed mechanisms depending on the structure of the additive.

Keywords: 1,3-Oxazepine, Photochemistry, PVC, Photo stabilizer, UV absorber, Tetrazole.

الخلاصة

يصف هذا البحث تحضير أربعة مركبات جديدة (A2-A5) تحتوي على 1,3-oxazepine و Tetrazole والخطوة الأولى تتضمن تفاعل البنزدين (A1) مع ألديهيد اروماتي (سينمألدهيد) في الإيثانول كمذيب بوجود حامض كعامل مساعد لتنتج قاعدة شيف (A2)، وعند تكثيف قاعدة شيف (A2) مع الانهيدريدات (أنهيدريد المالك وأنهيدريد الفثاليك) في البنزين الجاف لإعطاء حلقة سبعة غير متجانسة (A3, A4) الى جانب ذلك، حضرنا مشتق جديدة (A5) من تفاعل قاعدة شيف (A2) مع أزيد الصوديوم في نترأهيدروفيوران كمذيب.

وقد تم التعرف على تركيب المركبات المحضرة بالطرق الطيفية [FTIR، $^1\text{HNMR}$ ، $^{13}\text{CNMR}$] وقياس الخواص الفيزيائية. وقد درس التثبيت الضوئي لافلام بولي (كلوريد الفينيل) بوجود المركبات (A1-A5).

تم تحديد فعالية التثبيت الضوئي لهذه المركبات من خلال رصد مؤشرات قيم معاملات الكربونيل والهيدروكسيل مع وقت التشعيع. تم دراسة التغيرات في اللزوجة وأيجاد متوسط الوزن الجزيئي للبولي كلوريد الفينيل مع وقت التشعيع باستخدام رباعي هيدرو الفوران كمذيب. كذلك تمت دراسة تأثير تركيز المضافات (0.1-0.5wt) على معدل التحلل الضوئي وعملية التثبيت الضوئي. ولذلك، وجدنا أن سرعه التثبيت الضوئي تزداد مع زيادة تركيزات المواد المضافة. الى جانب ذلك، تم دراسة تأثير سمك الفيلم وأظهرت النتائج أن بزيادة سمك الفيلم يقل معدل التحلل الضوئي. أشارت النتائج إلى أن نسبة التثبيت الضوئي لبولي كلوريد الفينيل بوجود المضافات تتبع الترتب التالي:

(PVC blank) > PVC+A1 > PVC+A2 > PVC+A5 > PVC+A4 > PVC+A3

ووفقا للنتائج التي تم الحصول عليها اقترحت ميكانيكية عمل تلك المضافات اعتمادا على تركيبها.

Introduction

The chemistry of carbon-nitrogen double bonds has played a basic role in March of chemical sciences. Because there is a lone pair of electrons

on the nitrogen atom and general electron donating character of the double bond, it has found these compounds is very large applications in the field of chemistry . It is known that the com-



pounds containing $>C=N$ group as imines or azomethines or anils or ligands, but in general, which is known as "Schiff bases" in honors of Schiff who synthesized these compounds for the very first time [1] [2]. Oxazepine derived was presented in 1965 for use in mental ease characterized by anxiety and stress [3]. Oxazepine is an unsaturated, seven membered containing heteroatoms and oxygen in the position (1) and nitrogen in position 3 in addition to five carbon atoms. It is prepared by the pericyclic cycloaddition of Schiff bases with anhydrides [4]. Oxazepine and derivatives have medical and biological importance and they have medicinal and pharmaceutical application [5], [6] based on its spectrum therefore many of industrial and medical applications like photo stabilizer, pigments, and dyes take place in these fields [7], [8]. Tetrazole ring is unsaturated five-membered heterocyclic containing four nitrogen atoms and one carbon atom in position (5). Tetrazoles also serve as precursors for the synthesis of further interesting heterocyclic. Tetrazole derivatives were prepared by the reaction of Schiff bases derivatives with sodium azide

There is considerable importance at present in the photo-oxidative degradation of polymeric compounds as large molecules have ever more rife merchant applications. When exposed to synthetic polymer, semi-synthetic and natural environment [9].

All commercial organic polymers destroy in air when exposed to rays, as energy from sunlight is sufficient to cause the collapse of the C-C bonds because of polymer degradation. Synthetic polymers require almost all the stability against the negative impact with the improvement of synthetic resin has become essential that looking at ways and means for the prevention, or at least a limit, the damage due to ecological light, air and heat factors. This can be accomplished by adding the chemicals and optical stabilizers special or stabilizers, UV, which must be adjusted to the specific nature of the resin and the application in mind. Photostabilization polymers has achieved in many ways. It has been developed following the stability of systems. That rely on the work of stabilizer: - (1) Screeners light, (2) the excited state quenchers, (3) UV absorption, (4) analyzers peroxide, and (5) scavengers free radical, this is generally believed that the types 2 and 4 and 5 is the most effective [10].

In our research we were studied Photostabilization of PVC using four compounds derived from benzidine and contain 1,3-Oxazepine and Tetrazole rings.

Materials and Methods

Preparation methods of organic compounds

Melting points were determined on Gallen Kamp Melting Points apparatus MFB-600-Olof, and Stuart Scientific Co. LTD melting point SMP1 in the University of Mustansiriyah, College of Science.

FT-IR spectra were recorded using Shimadzu FT-IR 8000 series Fourier Transform, Infrared Spectrophotometer in the University of Mustansiriyah, College of Science.

1H -NMR spectra were recorded on a Fourier transform spectrometry [11], company Bruker, model, ultra-shield 300 MHz, and origin: Switzerland, in DMSO- d_6 solution with the TMS as internal standard, measurements were made at the Chemistry Department, AL-Albait University, Jordan.

Intrinsic viscosities were determined with viscometer.

Preparation of Schiff base (A2)

1mmole (0.184 gm) of Benzidine was dissolved in 20ml absolute ethanol with 2 mmole (0.264gm) of Cinnamaldehyde in presence (2-3) drops of glacial acetic acid and the mixture was stirred and refluxed for 7 hours. The precipitate was filtered to give (A2). The product was washed with cold water and recrystallized from ethanol to give the pale yellow color solid.

N4-Allylidene-N4'-(3-phenyl-allylidene)-biphenyl-4, 4'-diamine (A2)

Yield: 82%; M.p: 200°C; FTIR (ν, cm^{-1}): 3057.3032 (CH aromatic), 2947.2874 (CH aliphatic), 1627 (CH=N), 1602, 1581 (C=C), 833, 746.692 (CH out of plane) Figure 18; 1H -NMR (300 MHz, DMSO- d_6 , δ , ppm): 8.6-7.2 (m, Ar-H), 9.1 (signal, 1H), 5.6 (d, 2H, CH=CH) Figure 19; ^{13}C -NMR (DMSO- d_6): 163 (CH=N), 148 (C aromatic), 138 (Caro-CH=), 137 (Caro-Caro), CH aromatic (129-110) Figure 20

Preparation of Oxazepine compound (A3, A4):

A mixture of (A2) (0.0012mole) and (phthalic anhydrides) (A3), maleic anhydrides (A4) (0.0025mole) was melted in (20mL) solvent (dry benzene). The mixture was stirred and refluxed at 9-10 hours. Excess solvent was distilled; the precipitate was filtered and recrystallized from ethanol to give the Orang color solid for (A3) and the Deep Orange color solid for (A4).

4,4-biphenyl-diyl)bis(3(cinnymyl)-3,4-dihydrobenzo[e]1,3-oxazapine-1,5dione)(A3)

Yield:68%;M.p:230°C(Dec);FTIR(ν, cm^{-1}):3055-3194(CH aromatic),2994,2872(CHaliphatic), 1600,1555(C=C),825,813,746.69(CH out of plane) ,1697 (C=O lactam) , 1723 (C=O lacton) Figure 21; $^1\text{H-NMR}$ (300 MHz, DMSO- d_6 , δ , ppm): N-CH, (d,1H7.12 N)-HC-CH, =tri,1H (6.17-576)= .CH H1(d, 7.20), Ar CH (m, ,8.59.-67.7) Figure 22 $^{13}\text{C-NMR}$ DMSO- d_6):125, 129, 78 (CH=CH-CH-N), 150 (C aro-N), 139 (Caro-CH=),140-148(Cphtha), CH aro. (129 -110) 165 (C=O ester), 164 (C=O amid) Figure 23.

3,3--biphenyl-4,4--diyl)bis(2-(phenyl-3,4-dihydro-[1,3]oxazapine-4,7-dione)(A4)

Yield:72%;M.p:235°C;FTIR(ν, cm^{-1}):3045.3138(CHaro-matic),2992,2854(CHaliphatic),1535(C=C) ,817,850,755.613(CH out of plane) ,1639 (C=O lactam) , 1722 (C=O lacton) Figure 24 ; $^1\text{H-NMR}$ (300 MHz, DMSO- d_6 , δ , ppm): Maleic + CH=CHN-7 (d,1H, CH,N) -CH-(tri,1H, =CH 656.-76) ,6. =CH (d, 1H .28), 7Ar (m, CH 6.7-76 7)Figure 25; $^{13}\text{C-NMR}$ DMSO- d_6) : 129,128,79(C=C-C-N), 135 (C aro-N) ,134 (Caro-CH=) , 156-158(C =C oxa) , CH aro.(123 - 114) 169 (C=O ester), 164 (C=O amid) Figure 26

Preparation of Tetrazole compound (A5):

Compound (A2) 0.001 mole (0.412gm) was melted in (20mL) solvent (tetrahydrofuran) and mixed with 0.002mole (0.134gm) sodium azide. This mixture was stirred and refluxed for 12hours. Excess solvent was distilled; the precipitate

was filtered and recrystallized from Methanol to give the Pale Yellow color solid.

Bis (4, 4-(5-styryl-2, 5-dihydro-tetrazol-1-yl)-biphenyl (A5)

Yield:60%;M.p:260°C;FTIR(ν, cm^{-1}):3045.3138(CHaro-matic),2922,2885(CHaliphatic),1600,1581(C=C) ,833,812,746,692(CH out of plane) ,1453 (N=N ring) , 3174 (NH) Figure 27; $^1\text{H-NMR}$ (300 MHz, DMSO- d_6 , δ , ppm):) .aro H8(m , -7]a11 9.3(singlet, NH) [reference =CH),CH-,1H(CH tri(35.,)CHCH=-(CHH1(d, 6, 5. CH=)-CH-1H (N, d (3.7) Figure 28; $^{13}\text{C-NMR}$ DMSO- d_6):81[reference, 121,124(N-CH-CH=CH), 149 (C aro-N), 139 (Caro-CH=), (138,129,118,107) CH aro Figure 29.

Process of preparing the films:

Poly (vinyl chloride) (PVC) [supplied from Batteries factory in (Iraq) (the origin of the United States)] was re-precipitated from THF solution by methanol several times and lastly dried under vacuum at room temperature for (24) hours. Fixed concentrations of PVC solution (4 gm in 100 ml) in THF were used to get thickness (measured through a micrometer type 2610A, Germany). The prepared compounds (0.4% concentrations) were added to the films starting at 0 concentrations (control). It was essential to control the dimension of humidity and the rate of solvent vaporization during casting to maintain good visual quality is very narrow.

The films were get ready by vaporization method at room temperature for 24h. for removing the solvent. Films prepared were fixed on stands specially used for irradiation. The stand is provided with an aluminum plate (0.6 mm in thickness) by Q-panel Company.

Method for the accelerated test:

Weather accelerator meters QUV test (panel Q, Inc., USA), and was used for the irradiation of polymer films. Accelerated weathering test panel include stainless steel, which has two of the holes on the front side, and other behind. Each side contains side a lamp (type fluorescent UV lights) 40W each. These lamps are the type of UV-B 313 tender spectrum range between 290

and 360 nm with a maximum wavelength of 313 nm. Polymer film samples were fixed vertically parallel to the lamps to make sure that ultraviolet radiation is incident perpendicular to the samples. Irradiated samples have been rotated from time to time to make sure that the incident light intensity on all samples is same.

Measuring photolysis rate of polymer films using infrared spectroscopy:

This was followed by the degree of photolysis of samples of polymer film by monitoring FTIR spectra in the range of 4000- 400 cm^{-1} using 8400S Shimadzu FTIR spectrum. It is determined by the position of the hydroxyl and carbonyl absorption (3430.1720) cm^{-1} respectively. The provide photo deteriorating at different times of irradiation followed by monitoring changes in hydroxyl and carbonyl peaks. Then calculated hydroxyl (I_{OH}) and carbonyl (I_{CO}) comparing the absorption peak in the FTIR (3430.1720) cm^{-1} with a peak signal at 1332 cm^{-1} , respectively. This method is called the band the way the index, which contain

$$I_s [CO \text{ or } OH] = \frac{A_s}{A_r} \quad (1)$$

Where (A_s) represents the absorbance of peak below study. (A_r) represents absorbance of reference peak. (I_s) is the index of carbonyl or hydroxyl group below study. The actual absorbance difference between the absorbance of the highest peak and the baseline (A Top beak-base line) is calculated using the baseline method [12] [13].

Determining the average molecular weight by using the method of measuring the viscosity:

Determining the viscosity average molecular weight of the polymer property was used using the relationship Mark Houwink [14] [15].

$$[\eta] = K (\overline{M}_v)^{\alpha'} \quad (2)$$

Where " $[\eta]$ " is the intrinsic viscosity, K and α' constants based on polymer- solvent system at a given temperature". It was measured viscosity of the polymer solution with the U-tube measure viscosity Ostwald. The solutions provided by dissolving the polymer in a solvent (g / 100 ml), and the times the flow of the polymer solution and the solvent is pure (t) and (t_0) respectively. The specific viscosity account η_{sp} as follows:

$$\eta_{re} \text{ (relative viscosity)} = t/t_0 \quad (3)$$

$$\eta_{sp} \text{ (specific viscosity)} = \eta_{re} - 1 \quad (4)$$

Intrinsic viscosities by the relation (5) which is then converted to the average viscosity molecular weight by using

$$[\eta] = K (\overline{M}_v)^{\alpha'} \quad (2)$$

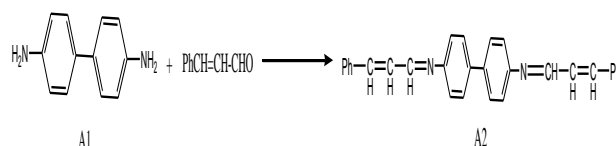
:

$$[\eta] = \left[\left(\sqrt{2} / C \right) (\eta_{sp} - \ln \eta_{rel}) \right]^{1/\alpha'} \quad (5)$$

Where C is the concentration of polymer solution (g/100 ml).

Results and Discussion

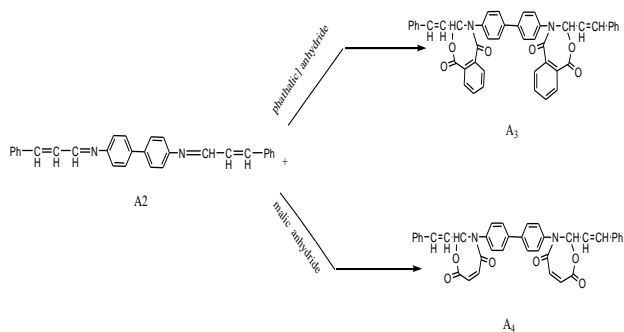
One new Schiff base (A2) have been synthesized from the condensation of Cinnamaldehyde with amino compound (A1)



The formation of compound (A2) was indicated by presence in their IR spectra of (CH=N) stretching bands at 1627 cm^{-1} combined with the disappearance doublet bands of NH_2 stretching bands. ^1H - NMR of compound (A2): 9.1 (s, 1H, CH=N), 6.6-5.6 (d, 2H, CH= CH), 8.6-7.2 ppm which belonged to aromatic protons [16].

The ^{13}C - NMR spectra provide further support for the structural characterization of the Schiff base: 163ppm due to (CH=N) group and signals at (110 -148) ppm due to aromatic carbons.

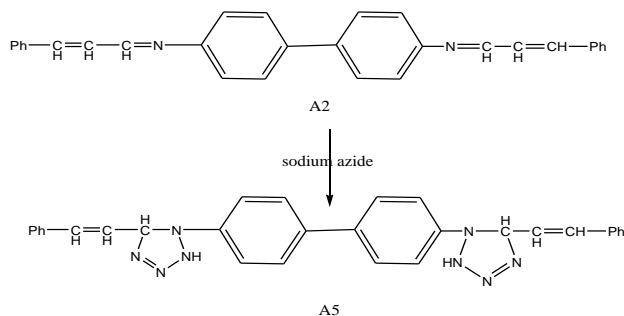
In addition, in the present work two new Oxazepine compounds (A3, A4) were prepared by reaction compound (A2) with (phthalic anhydride (A3) and maleic anhydride (A4) in good yields.



The structures of prepared compounds were identified by FTIR spectral and Magnetic resonance (^{13}C , ^1H -NMR, the FTIR-spectra of these compounds shows the appearance of the absorption bands at $(1722-1639)\text{cm}^{-1}$ characteristic to $(\text{C}=\text{O})$ of (lacton – lactam) and the disappearing of the two absorption bands at $(1750-1800)\text{cm}^{-1}$ of pure anhydrides. The ^1H -NMR spectrum of compound (A3) showed the following characteristic signals at: $(7.67-8.59)$ multiplet signal due to aromatic protons, 7.20 (d, 1H CH=), $6.57-6.17$ (tri, 1H, =CH-CH-N) 7.12 (d, 1H, CH-N) while ^{13}C -NMR spectrum of the same compound showed signal at $:125, 129, 78$ (CH=CH-CH-N), signal $(107-150)$ due to carbon aromatic and signals at 165 ppm due to $(\text{C}=\text{O}$ ester) signal at 164 ppm due to $(\text{C}=\text{O}$ amide).

The ^1H -NMR spectrum of compound (A4) showed the following characteristic signals ^1H -NMR (300 MHz, DMSO- d_6 , δ , ppm): $7.2, 7.7$ (m, Ar-H) $6.6, 5.67, 6.17$ (d, 2H, tri, 1H CH=CH-CH), ^{13}C -NMR DMSO- d_6 : $129, 128, 79$ (C=C-C-N), 135 (C aro-N), 134 (Caro-CH=), $156-158$ (C = C oxa), CH aro. ($123-114$) 169 (C=O ester), 164 (C=O amid)

Tetrazole derivatives (A5) was prepared by the reaction of Schiff base derivative (A2) with sodium azide in tetrahydrofuran as solvent.



The structure of synthesized compound was shown in Scheme 4. The synthesized compound was characterized by its melting point, FT-IR,

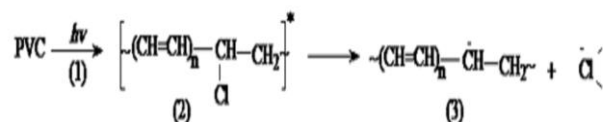
^1H -NMR. and ^{13}C -NMR, FT-IR spectrum of compound (A5) Figure 27 showed absorption bands at $1453\text{cm}^{-1}, 3174\text{cm}^{-1}$ due to $\nu(\text{N}=\text{N}, \text{NH})$. The ^1H -NMR spectrum of compound (A5) Figure 28 showed singlet signal at 9.3 ppm due to NH group, multiplet signals at $(7-8)$ due to aromatic protons.

^{13}C -NMR spectrum of compound (A5) Figure 29 showed signals at $(138-107)$ ppm due to aromatic carbon and at $121, 124$ ppm due to $(\text{N}-\text{CH}-\text{CH}=\text{CH})$ and 139 ppm due to Carbon arom-CH=.

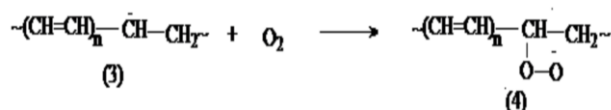
Mechanism of photodegradation of PVC:

It may be outlined steps photochemical degradation of PVC as follows:-

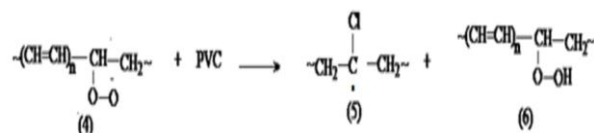
1. Free radicals (P1) and (Cl) were Formed by homolytic cleavage of $(\text{C}-\text{Cl})$ bond in (2).



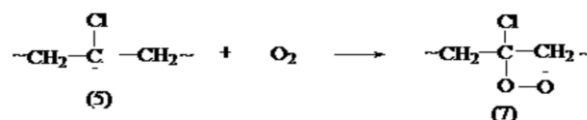
2. Peroxy radical (4) was produce by reaction of free radical (3) with oxygen.



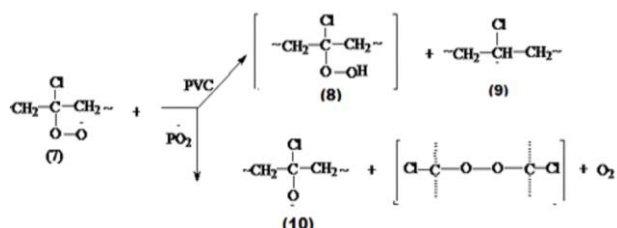
3. Hydro peroxide polymers (5,6) were produced by abstraction of hydrogen atom in polymer chain by peroxy radicals (4).



4. The free radical polymers (5) react with O_2 to give chloro alkyl peroxy radical (7).



5. The radical (7) abstraction from PVC with the formation of hydroperoxide (8) and (9) or it reaction with PO_2 leads to formation of Peroxide bridge and alkoxy radicals (10).



6. Alkoxy radical (10) suffered some interactions such as:

- i) Abstraction of hydrogen atom from polymer chain to give polymeric alcohols (11).
- ii) β -scission reaction to produce ketonic polymers.

Forming a keto group in the polymer chain plays an important role in increasing the oxidative degradation of the polymer chain through the defecation of a key chain for the production of acyl radical mechanism. The Oxazepine–tetrazole compounds usage as additives for the polymeric films. In order to studying the optical activity of these additives for Photostabilisation of plastic films, Led, irradiation of plastic films using light of wavelength $\lambda=313\text{nm}$ new changes in their FTIR spectrum. Appearance of bands at range ν ($1770-1720$) cm^{-1} , and (ν 3430) cm^{-1} , attributable respectively to form a carbonyl and hydroxyl groups. These absorptions account as carbonyl and hydroxyl index. It is reasonable to assume that the growth indicators carbonyl and hydroxyl is a measure of the extent of polymers degradation.

Nevertheless, in the Figure 30, Figure 31 the I_{CO} and I_{OH} of (A3), (A4), (A5), (A2), (A1) and (PVC control) showed fewer growth rate with irradiation time with respect to the (PVC control) film without additives. Since the growth of carbonyl and hydroxyl index with irradiation time is lower than PVC blank, as seen in the Figure 30, Figure 31 it is suitable to conclude that these additions can be considered photo stabilizers of PVC polymer.

Photo stabilizer shows the efficiency of the induction period is longer. Therefore, the (A3) studies such as photo stabilizer more active, followed by of (A4), (A5), (A2) and (A1), which is the least active.

In this work the Photostabilization of PVC films of $40\ \mu\text{m}$ thickness was examined with changed additive concentration, Figure 32, Figure 33 shows the relationship between carbonyl index and hydroxyl index with irradiation time for ad-

ditive (3) concentrations Figure 34, Figure 35 shows the relationship between the (3) additive concentrations and carbonyl or hydroxyl index for PVC film at fixed irradiation time (150) hours and fixed thickness $40\ \mu\text{m}$.

In addition, in this work studying the relationship between the carbonyl and hydroxyl indexes with various different thicknesses for PVC samples Figure 36, Figure 37 could be explained considering the relatively important permeability of polymer to oxygen, which results in the core zone of the selected films thickness being rich in oxidation product in addition to the superficial. However, Figure 36, Figure 37 presented decrease of photodegradation with increasing of thickness of the film.

Variation of PVC molecular weight during photolysis in the presence 1,3-Oxazepine-Tetrazole:

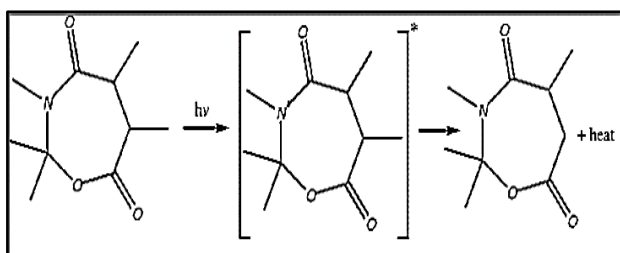
Viscosity of PVC solution depends on concentration and size of the dissolved polymer. Measuring the solution viscosity and idea about molecular weight [17] Figure 38 show the plot of M_v versus irradiation time for (PVC) film with and without 0.4% (wt/wt) of the additives selected. M_v is measured using Equation 2 with tetrahydrofuran as a solvent at 25°C . It is worth mentioning that hints of the films with additives are not soluble in tetrahydrofuran representing that cross-linking or branching in the (PVC) chain does occur during the course of photolysis. To provide the best support from this point of view, the number of average chain scission (average number cut per single chain) (S) [18] was calculated using the relation:

$$S = \frac{M_{v,0}}{M_{v,t}} - 1 \quad (6)$$

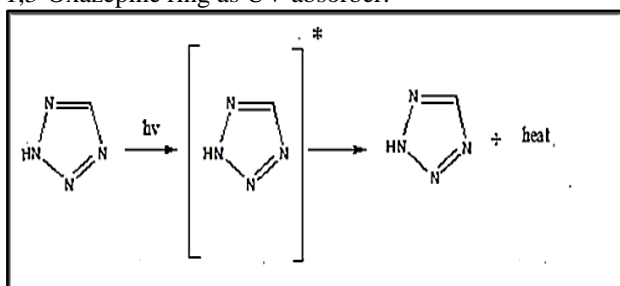
Where: " $M_{v,0}$ and $M_{v,t}$ are viscosity average molecular weight at initial (0) and (t) irradiation time" respectively. It shows a plot of the (S) versus time Figure 39. In addition, it indicates an increase in the degree of branching that may arise, such as the occurrence of cross-linking curve. It was observed that the material is soluble formed during irradiation, which provided additional evidence on the idea that cross-linking occurs. For randomly distributed weak bond links [19], which break down quickly in the early stages of photolysis, and given the degree of deterioration (α) as follows:

$$\alpha = \frac{m}{Mv,0} S \quad (7)$$

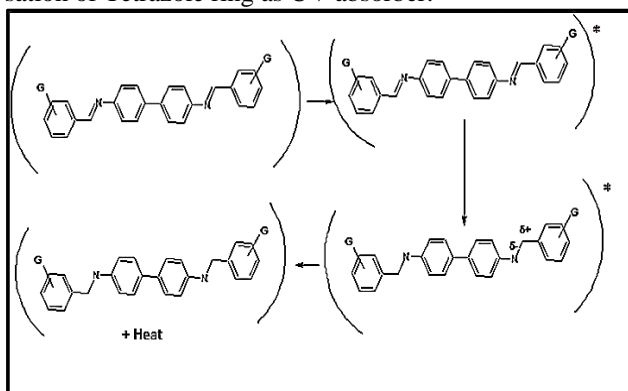
Where m is the initial molecular weight. The scheme of α as a function of irradiation time in the Figure 40. In addition, the values of samples irradiated higher when absent and lower additions in the presence of additives compared to the corresponding values of PVC free additive [20]. In the early stages of the photolysis of PVC, and the value of (α) increases rapidly with time, these indicators point to a random breaking of bonds in the polymer chain.



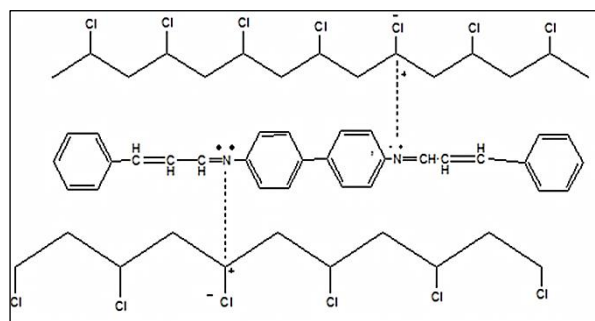
Scheme 2: Suggested mechanism of Photostabilisation of 1,3-Oxazepine ring as UV absorber.



Scheme 3: Suggested general mechanism of Photostabilisation of Tetrazole ring as UV absorber.



Scheme 4: Suggested mechanism of Photostabilisation of PVC by Schiff base as UV absorber.



Scheme 5: Suggested mechanism of Photostabilisation of PVC by compound (A2) through the interaction between PVC and Schiff base.

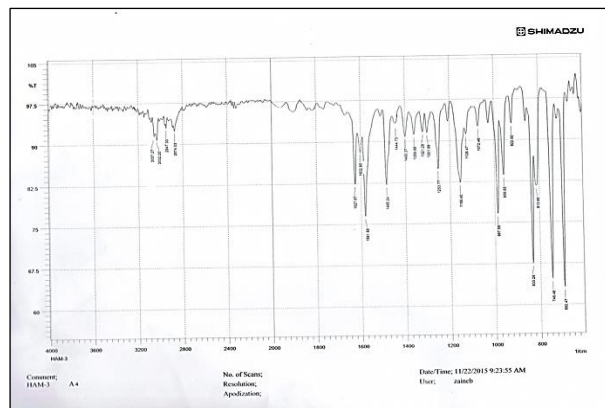


Figure 18: The FT-IR spectrum of compound (A2).

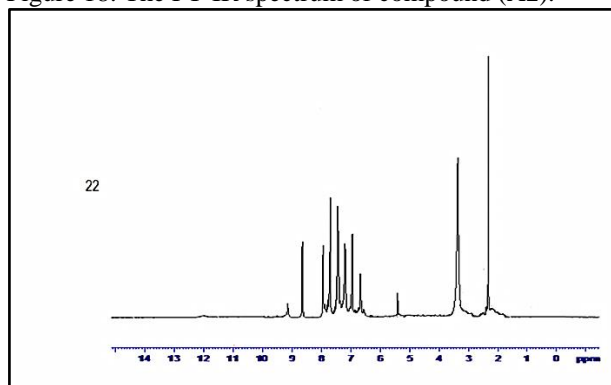


Figure 19: ¹H NMR spectrum of (A2).

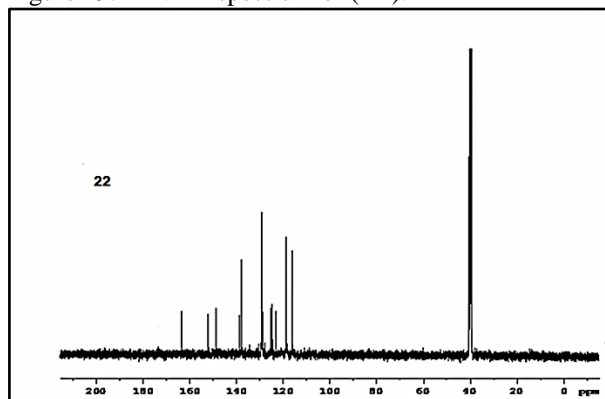


Figure 20: ¹³C NMR spectrum of compound (A2).

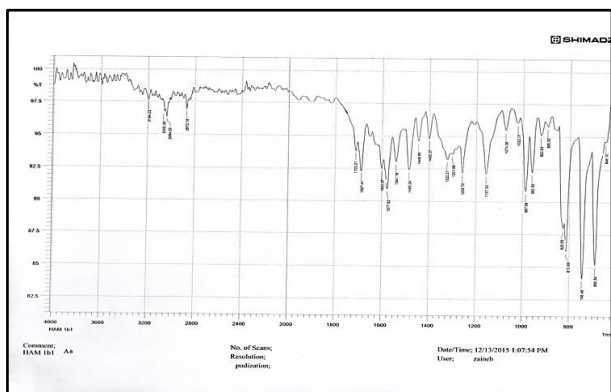


Figure 21: The FT-IR spectrum of compound (A3).

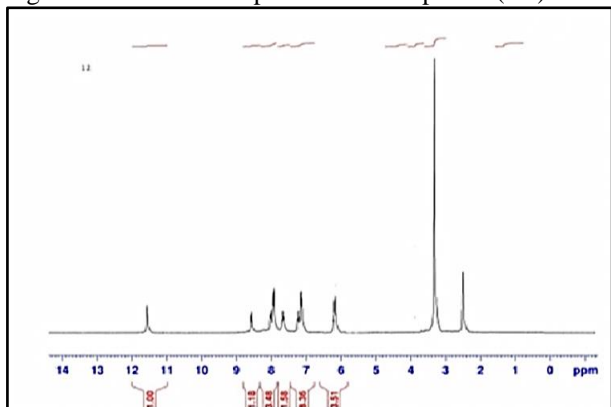
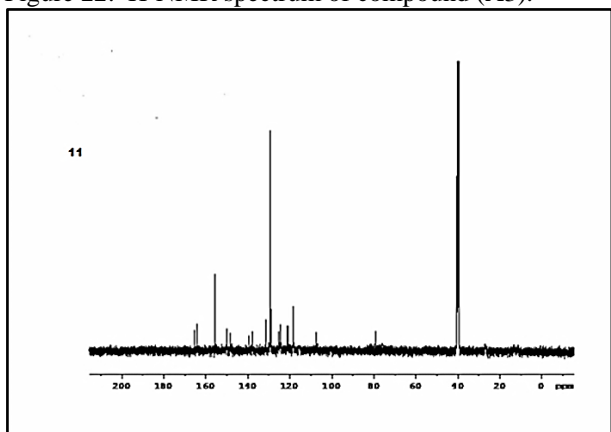
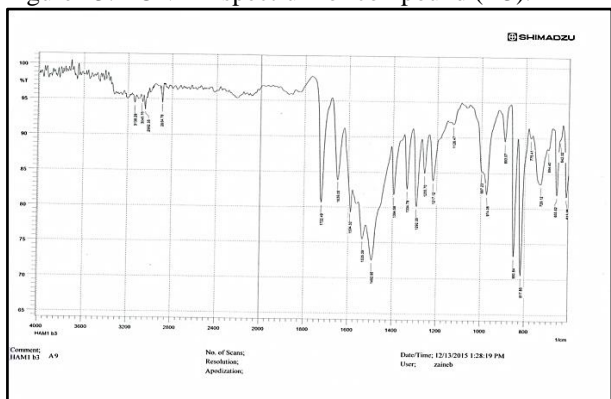
Figure 22: ¹H-NMR spectrum of compound (A3).Figure 23: ¹³C-NMR spectrum of compound (A3).

Figure 24: The FT-IR spectrum of compound (A4).

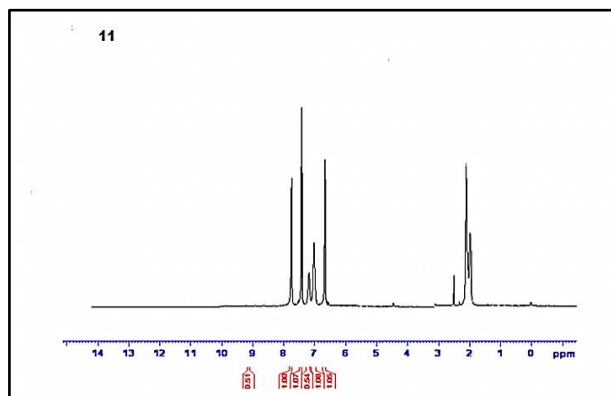
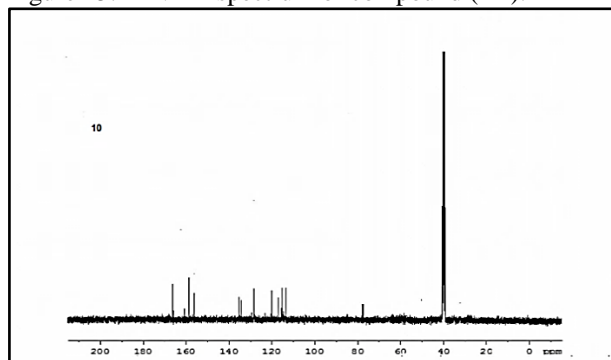
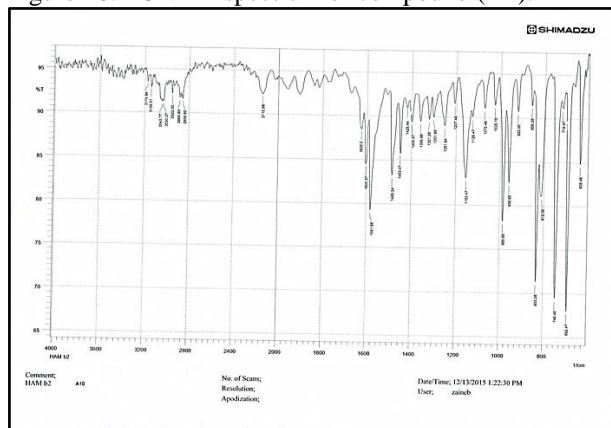
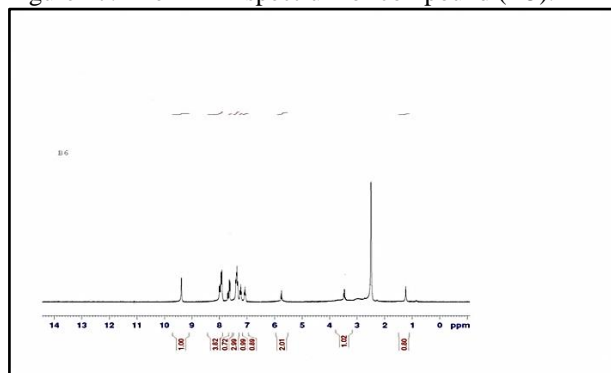
Figure 25: ¹H-NMR spectrum of compound (A4).Figure 26: ¹³C-NMR spectrum of compound (A4).

Figure 27: The FT-IR spectrum of compound (A5).

Figure 28: ¹H-NMR spectrum of compound (A5).

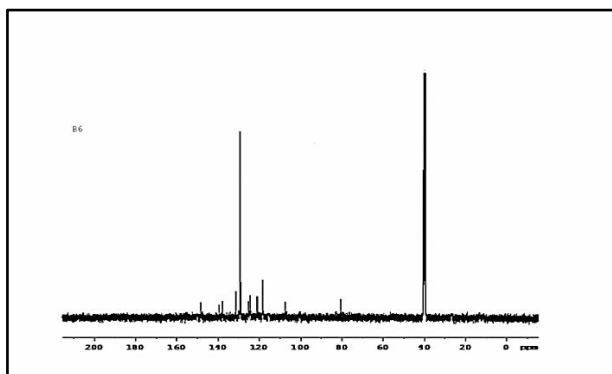


Figure 29: ¹³C NMR spectrum of compound (A5).

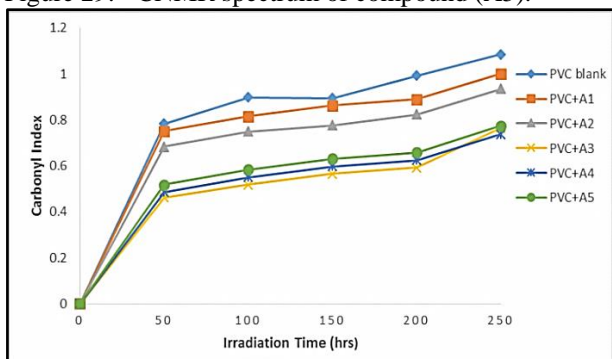


Figure 30: The relationship between the (I_{CO}) and irradiation time for PVC films ($40 \mu\text{m}$) thickness containing 0.4% additive.

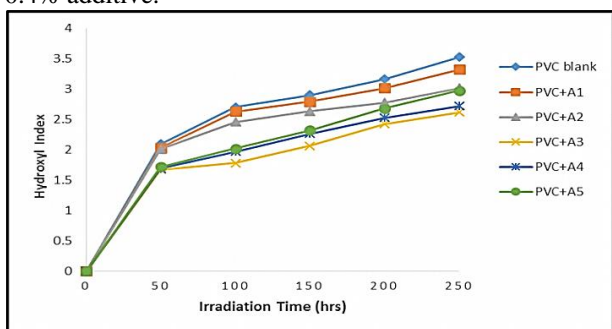


Figure 31: The relationship between (I_{OH}) and irradiation time of PVC films ($40 \mu\text{m}$) Thickness containing 0.4% additives.

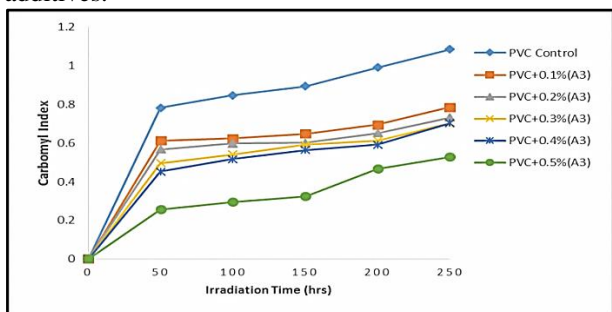


Figure 32: The relationship between the (I_{CO}) and irradiation time for PVC films ($40 \mu\text{m}$) thickness containing different concentrations of compound (A3).

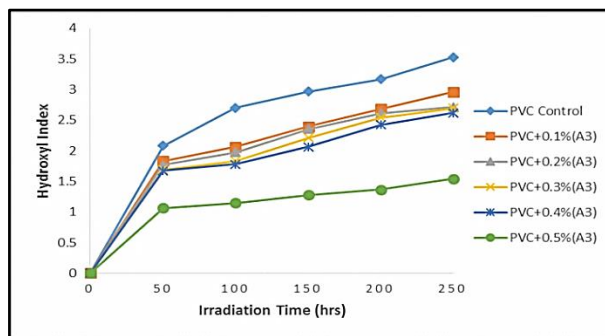


Figure 33: The relationship between the (I_{OH}) and irradiation time for PVC films ($40 \mu\text{m}$) thickness containing different concentrations of additive (A3).

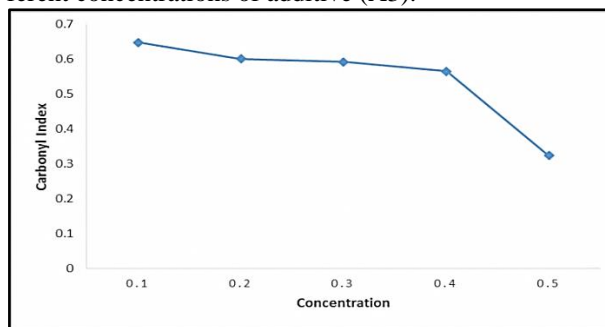


Figure 34: The relationship between the (I_{CO}) and irradiation time at (150hrs) for PVC films ($40 \mu\text{m}$) thickness containing different concentrations of compound (A3).

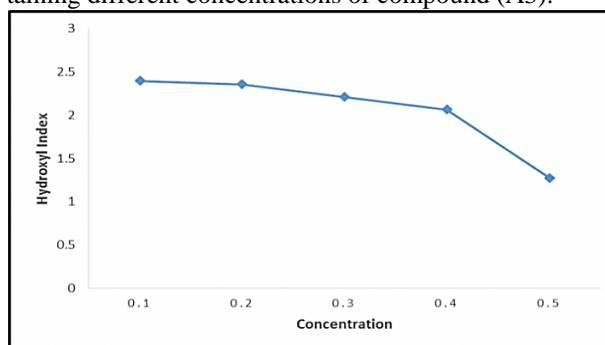


Figure 35: The relationship between the (I_{OH}) and irradiation time at (150hrs) for PVC films ($40 \mu\text{m}$) thickness containing different concentrations of compound (A3).

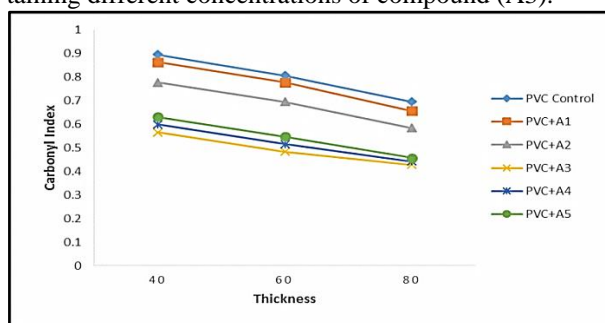


Figure 36: The relations ship between the carbonyl indexes with different thicknesses (μm) at (150hrs) irradiation time containing (0.4%) Wt. of additives.

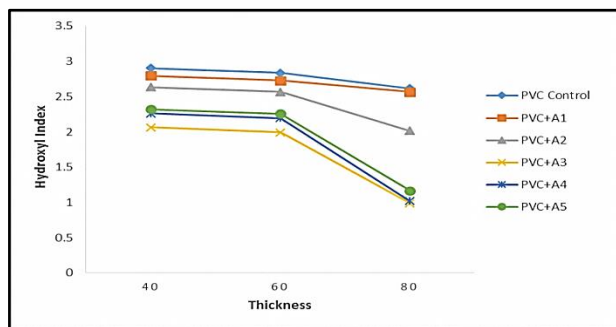


Figure 37: The relationship between the Hydroxyl indexes with different thicknesses (μm) at (150hrs) irradiation time containing (0.4%) Wt. of additives.

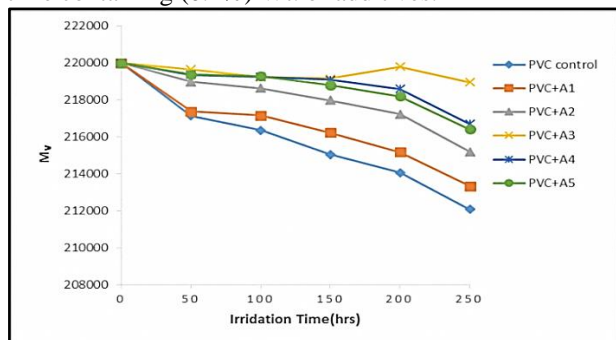


Figure 38: Variation of the viscosity-average molecular weight with irradiation time of PVC films ($40\mu\text{m}$) (control) and 0.4% wt. of additives.

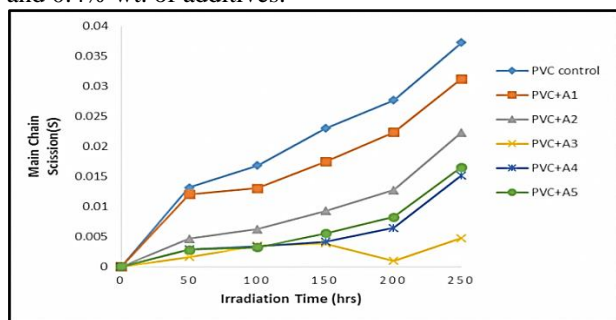


Figure 39: Changes the average number cut per single chain (s) during irradiation of PVC films ($40\mu\text{m}$) (control) and with 0.4% wt. of additives.

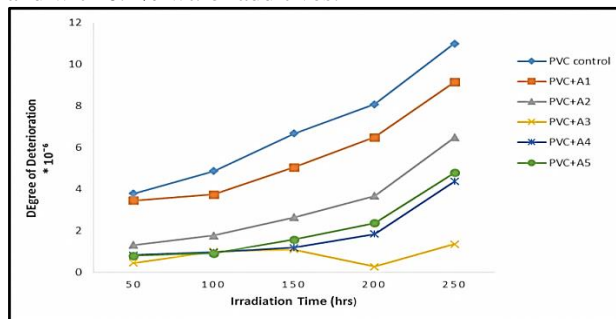


Figure 40: Changes in the degree of deterioration during irradiation of PVC films ($40\mu\text{m}$) (control) and with 0.4% wt. of additives.

Conclusions

References

- [1] H. Schiff, *Ann. Chem.*, vol. 131, p. 118, 1864.
- [2] P. Saul, "The chemistry of the carbon nitrogen double bond," *Ltd., London*, (1970).
- [3] Ahmed, A., Sarah, M., Anwar, H., Ayad, H. and Emad, Y, "Antibacterial Study of Some Oxazepine Derivatives," *Journal of Al -Nahrain University*, vol. 18, pp. 22-26, 2015.
- [4] Dhanya Sunil 1, Ranjitha C1, Rama M 1, "Oxazepine Derivative as an Antitumor Agent and Snail1 Inhibitor against Human Colorectal Adenocarcinoma," *international Journal of Innovative Research in Science*, vol. 3, pp. 15357-15363, 2014.
- [5] Matsuzaki, H., Takuchi, I., Hamad, Y. and Hatano, K, "Studies on the 1, 4-oxazepine ring formation reaction using the molecular orbital method," *Chemical and Pharmaceutical Bulletin*, vol. 48, pp. 755 - 756, 2000.
- [6] Hamak, K. F., Eissa, H. H, "Synthesis, Characterization, and Biological Evaluation and Anti Corrosion Activity of Some Heterocyclic Compounds Oxazepine Derivatives from Schiff Bases," *Organic Chemistry Current Research*, vol. 2, no. 3, pp. 1-7, 2013.
- [7] H. Ayad, "Microwave Synthesis of Some New 1, 3 -Oxazepine Compounds as Photostabilizing Additives for Pmma Films," *Journal of Al -Nahrain University*, vol. 15, pp. 47-59, 2012.
- [8] T. A. A. -. Khitam, "Synthesis, Identification and Evaluation the Biological Activity for Some New Heterocyclic Compounds Derived from Schiff Bases," *Journal of Applied Chemistry*, vol. 9, no. 5, pp. 1-11, 2016.
- [9] Andrady, A., Hamid, S., Hu, X. and Torikai, A, "Effects of increased solar ultraviolet radiation on materials in Environmental

- Effects of Ozone Depletion," *J. Photochem. Photobiol*, vol. 46, p. 96–103, 1988.
- [10] Grassie N., Scott, G, "Polymer Degradation and Stabilization," *Cambridge University Press, London*, 1985.
- [11] Diana C. G. A. Pinto., Clementina, M. M. Santos. and Artur, M. S. Silva, "Advanced NMR techniques for structural characterization of heterocyclic structures," *Recent Research Developments in Heterocyclic Chemistry*, vol. 81, pp. 397-475, 2007.
- [12] Arct J., Dul, M., Rabek, J.F. and Ranby, B, "Studies on modified benzotriazoles as photostabilizers for poly (vinyl chloride)," *Eurp. Polym.J*, vol. 17, pp. 1041-1048, 1981.
- [13] Ranby B.G., Rabek, J.F, "Photodegradation, Photooxidation and Photostabilization of Polymers," *London: John Wiley & Sons*, 1975.
- [14] J. Mark, "Physical Properties of Polymers Handbook," *Springer, New York*, 1988.
- [15] Mori, F., Koyama, M. and Oki, Y, "Studies on photodegradation of poly (vinyl chloride)," *Die Angewandte Mak-omolekulare Chemie*, vol. 64, no. 1, p. 89–99, 2007.
- [16] Silverstein, R.M., Basslar, G.C, "Spectroscopic identification of organic compound," 2005.
- [17] Fisher, P.E., Lawrence, W, "Selection of Engineering Materials and Adhesives," *CRC Press*, 2005.
- [18] Shyichuk A., White, J, "Analysis of chain – scission and crosslinking rates in the photo –oxidation of polystyrene," *Appl. Poly. Sci*, vol. 77, no. 13, pp. 3015-3023, 2000.
- [19] F. Gugumus, "Mechanism of Polymer Degradation and Stabilization," 1990.
- [20] A. N. Olfat, "Photostabilization of polyvinyl chloride by some new thiadiazole derivatives," *Eur. J. Chem*, vol. 3, no. 6, p. 242-247, 2015.

Research Article

Fractal Image Compression Based on High Entropy Values Technique

Douaa Younis Abbaas¹, Jamila H. Saud¹, Shatha J. Mohammed²
¹Departement of Computer Science, College of Science, Mustansiriyah University, IRAQ.
²College of Science, Mustansiriyah University, IRAQ.
*Correspondent Author Email: douaayounis89@gmail.com

Article Info

Received
19/02/2015

Accepted
14/04/2015

Abstract

There are many attempts tried to improve the encoding stage of FIC because it consumed time. These attempts worked by reducing size of the search pool for pair range-domain matching but most of them led to get a bad quality, or a lower compression ratio of reconstructed image. This paper aims to present a method to improve performance of the full search algorithm by combining FIC (lossy compression) and another lossless technique (in this case entropy coding is used). The entropy technique will reduce size of the domain pool (i. e., number of domain blocks) based on the entropy value of each range block and domain block and then comparing the results of full search algorithm and proposed algorithm based on entropy technique to see each of which give best results (such as reduced the encoding time with acceptable values in both compression quality parameters which are C. R (Compression Ratio) and PSNR (Image Quality)). The experimental results of the proposed algorithm proven that using the proposed entropy technique reduces the encoding time while keeping compression rates and reconstruction image quality good as soon as possible.

Keywords: Fractal Image Compression, Entropy, Image Quality, Domain Pool, Similarity, Encoding.

الخلاصة

هناك عدة محاولات أجريت لتحسين وقت الترميز في خوارزمية ضغط الصور الكسورية بسبب انها مستهلكة للوقت. هناك محاولات عدة تم عملها لتقليل حجم مستودع البحث لكل عملية مطابقة بين المدى والمجال لكن اغلب هذه المحاولات أدت الى كفاءة رديئة او نسبة ضغط قليلة للصورة المسترجعة. هذا البحث يهدف الى تقديم طريقة لتحسين أداء خوارزمية البحث الكلي من خلال دمج و تركيب خوارزمية البحث الكلي التقليدية التي هي من نوع Lossy Compression Algorithm مع خوارزمية الانتروبي المقترحة التي هي من نوع Lossless Compression Algorithm. تقنية الانتروبي المقترحة تقلل من حجم مستودع المجال Domain Pool (عدد بلوكات المجال) و بالتالي تقلل عدد المقارنات بين بلوكات المدى و المجال بالاعتماد على قيمة الانتروبي لكل من بلوكات المدى و المجال و من ثم حساب نتائج الخوارزمية البحث الكلي التقليدية و مقارنتها مع نتائج تقنية المقترحة لرؤية أي خوارزمية تعطي نتائج افضل (تقلل من وقت البحث المستغرق مع تحقيق نسب مقبولة في كفاءة الصورة المسترجعة PSNR و نسبة الضغط). النتائج التجريبية للخوارزمية المقترحة اثبتت ان استخدام تقنية الانتروبي المقترحة يقلل من وقت الترميز و يحافظ على نسبة الضغط و كفاءة الصورة المسترجعة على قدر الإمكان.

Introduction

The goal of image compression is to reduce the amount of data required to represent a digital image [1]. Fractal compression is a lossy compression method for digital images, based on fractals [2]. The idea of fractal image compression (FIC) also named full search algorithm was originally introduced by Barnsley in 1988 and the first practical FIC scheme was realized by Jacquin in 1992 [3] since each natural image has sub sections and the pixels of each subsection have great self-similarity to each other that is called Partitioned Iterated Function System or PIFS [4]. FIC

is best suited for textures and natural images, relying on the fact that parts of an image often resemble other parts of the same image [2] which can be regarded as possessing fractal nature [5]. In full search algorithm, fixed block size partitioning will be used to generate the range and domain blocks. The main drawback of FIC is larger computational time in encoding stage because 8- symmetry mappings that must be tried to each domain block and then select the symmetry case of the domain block that led to least square error (lesser difference) and optimum matching when comparing this domain block

with range block this caused that the number of comparisons between range and domain block is $8n_r n_d$. Number of the range blocks can be calculated using $(N/n)^2$ while number of the domain blocks can be calculated using $(N - 2n + 1)^2$ where N is image dimension while n is block dimension.

In order to reduce the computation time, different optimization techniques have been proposed. The main objective of this paper is to develop an efficient optimization technique for FIC which is called “entropy technique” that involves performing the search in part of domain pool rather than over the whole domain pool by reducing the domain pool size based on entropy value of both range and domain blocks this make the domain pool more productive. Using proposed FIC based on entropy technique has two fundamental targets which are speeding up the encoding time by check the entropy value of all domain blocks in the domain pool, the domain blocks having high value of entropy threshold (ϵ) will be excluding while the domain blocks having low value of ϵ only will be selected. This technique will reduce size of the domain pool, therefore the matching stage pair of range and domain blocks will be achieved in faster time. Also the other target is keeping on quality of the reconstructed image good after their construction as well as increasing compression ratio. The balance of the paper is organized as follows: introduction to fundamentals of FIC scheme is given in section 1. The proposed encoding and decoding stages of the proposed algorithm based on entropy technique are described in sections 2 and 3. The experimental results of our proposed entropy technique and comparing this technique with full search algorithm are illustrated in sections 4-A and 4-B. Finally, some concluding remarks are given in section 5.

1. The Encoding Stage in Proposed FIC Based on Entropy Technique

As said before that full search algorithm is time consuming so that a new approach must be proposed to overcome this problem. In this paper, entropy technique will be used; it is information theory that provides the basic tools needed to deal with image representation directly and quantitatively. The proposed FIC based on entropy technique is similar to the full search algorithm expect few differences. See Figure 1 that ex-

plains the main steps of the proposed FIC based on entropy technique. The proposed entropy technique can be illustrated in the following points:

a. Generating Range and Domain Pools

Generating range and domain pools starting with loading the original image into its buffer to create the range image and generating the domain image from the range image by down sampling process using averaging method then the range and domain blocks must be formed to need them in the remaining steps in the encoding stage by partitioning the range and domain images using quad tree technique since the range blocks are non-overlapped to make the decoder capable of reconstruction the image while the domain blocks are allowed to be overlapped depend on the step size values where allowing the domain blocks to be overlapped improving quality of the reconstructed image. In proposed FIC we will use quad tree partitioning technique to generate these range and domain blocks since the reasons that make us use this partitioning technique is by using quad tree technique more acceptable quality of reconstructed images will be obtained as well as because each range block will be compared only with four domain blocks so the encoding time for FIC systems that use this technique will be less than these FIC systems that use fixed block size partitioning technique which this most important reason. Mean absolute error (MAE) which can be calculated using equation 1 is used to decide whether range and domain blocks partitioned or not since MAE of range and domain blocks are computed then comparing MAE of range block with MAE of domain block must be occurred if MAE difference of them within specific threshold then range and domain blocks are not partitioned (they are similar):

$$MAE = \frac{1}{MN} \sum_{i=1}^M \sum_{j=1}^N (|x(i, j) - y(i, j)|) \dots (1)$$

Otherwise this means that these blocks are not similar then partitioning of these blocks will be applied. The specific threshold that used to decide whether MAE values of range and domain blocks are approximate or non is minimum block error (MBE) which its tested values in our work are (0.1, 0.01, 0.001, 0.0001 and 0.00001). If the difference between MAE values of range and domain blocks lesser than MBE then these

blocks are partitioned otherwise no partitioning process is implemented. The matching computation will be reduced in the proposed algorithm where the entropy values of the range and domain pools will be computed and used these values to find the best matching between pairs range-domain locks in an encoding stage.

b. Entropy Values Determination

After completing the partitioning process, the domain pool size is resulted very large, this size will be consume time in the encoding stage when searching in the domain pool to find the best matched domain block that satisfied least error for each pair range-domain blocks. In the best matched domain block that satisfied least error for each pair range-domain blocks. In the proposed algorithm, the entropy values will be computed from equation 2 to each range and domain blocks separately. In the encoding stage, the best matching between the entropy values of range with the entropy values of domain block can be found if these blocks satisfied the condition in equation 3:

$$entropy = -\sum_{i=1}^n p_i \log p_i \dots (2)$$

$$|entropy(R_i) - entropy(\tilde{D}_j)| \leq \epsilon \dots (3)$$

Where: p is the probability value, \tilde{D}_j is the average of domain block, and ϵ is the entropy threshold. Before searching and matching processes, the entropy values of range and domain blocks must be tested to show whether the domain block satisfy this condition or not.

In this paper entropy threshold (ϵ) determined to be in values from 0.1 to 0.9 where according to ϵ a decision will be made to determine if the domain block belong to the domain pool or not.

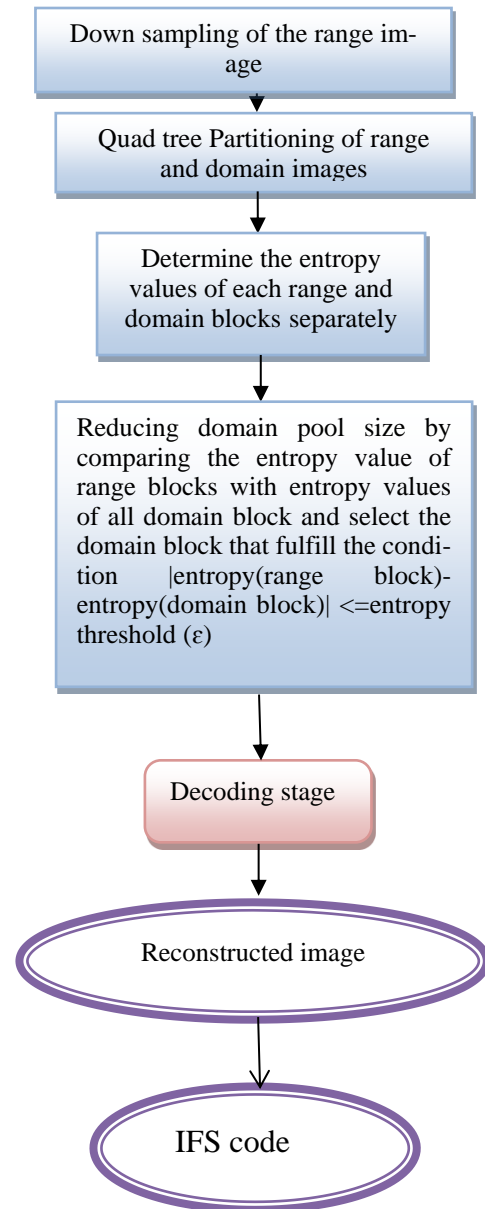
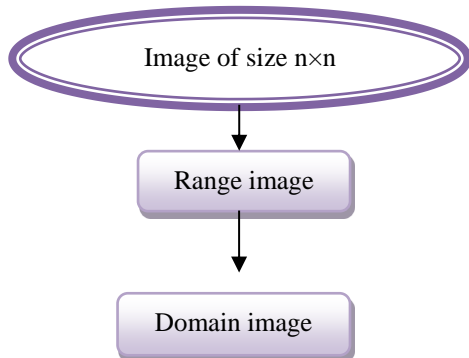


Figure1: The schematic diagram of proposed FIC based on entropy technique.

According to equation 3 the new reduced domain pool will be formed since if the difference of entropy values between range and domain blocks lesser than or equal to ϵ then this domain block will join to the domain pool. Otherwise the domain block will be discarded and excluded from the domain pool so the new domain pool consists of only the domain blocks that have low entropy value instead of all domain blocks this will lead to reducing number of the comparisons for finding the best matched domain block for each range block and then speeding up the encoding time. ϵ value will be controlled parameter in the

encoding stage, if ε value is high this mean that the encoding stage need long time to be done (large domain pool). But if ε value is small the encoding process need short time to compare the domain block in domain pool with suitable range block (small domain pool). This process will reduce the encoding time with acceptable quality of the reconstructed image.

c. Searching and Matching Processes

After computing the entropy values of all range and domain blocks, the searching and matching process among each range block and all overlapped domain blocks in the reduced domain pool size must be done but may be noticed that range and domain blocks must be at the same size since must not comparing range and domain blocks of different sizes.

In general, the best matched domain block must be found for each range block so that the error between each range block and all domain block will be computed based on their entropy values but before calculating the error the scale coefficient s_i must be calculated and quantized as well as index of the quantized scale coefficient must be computed. If the computed error lesser than minimum block error (MBE) then this domain block will consider the best matched block and information of the best matched domain block such as the position (x_d, y_d) and index of quantized scale I_s will be stored in the compressed file (Frac) but the quantized offset coefficient doesn't be saved in the compressed file because the offset coefficient doesn't change the entropy value of the block. After that the searching process will continued for another range block.

Otherwise, if the computed error greater than minimum block error (MBE) then newly searching process in the reduced domain pool for the range block will be done until finding the best matched domain block with minimum error. The proposed encoding stage diagram can be shown in Figure 2. In this work, index of quantized scale coefficient will be stored in IFS code instead of quantized values of it to reduce the size of compressed file (to increase the compression ratio C. R) and to access to the quantized scale coefficient. Also, to increase the compression ratio, the values of x_d and y_d must be minimized.

At the end, result of the encoding stage is compressed file (code book file or IFS code) where the compressed files of both full search and pro-

posed algorithms contain the similar information expect compressed file of the proposed algorithms doesn't contain index of the quantized offset I_o . The compression information must be saved in header of the compressed IFS file before starting the encoding stage such image width (W), image high (H), block length, step size, no. of bit used to quantize scale coefficient, maximum and minimum scale coefficient, entropy threshold ε and MBE to make the decoder capable of reconstruction the original image from the compressed file. The decoder needs this information to reconstruct the original image.

2. The Decoding Stage

The decoding stage in proposed FIC based on entropy is similar to the decoding stage in full search algorithm since this process very fast when compared with encoding stage which considers the first advantage of decoding stage because no searching step for finding the best matched domain block for each range block which spent a lot of time. Any initial image can be taken such as zero images and then reconstructed the compressed image from it. To reconstruct the compressed image, the range image must be created by loading the initial image into a buffer and then domain image must be created by down sampling range image.

The same as to the decoding stage in full search algorithm, range and domain images must be partitioned using quad tree partitioning that used in encoding stage. Before starting the decoding stage, content of the header in IFS code must be extracted because they are necessary to integrate other parameters that the decoder need them also the quantized values of scale coefficient (s_q) must be de-quantized to their original values since we can arrive to these quantized scale coefficient by using quantized scale indexes as well as coordinate of the best matched domain block (x, y) also must be reconstructed to their original value. Now, all data of IFS code become prepared to be using them in reconstruction operation since content of each domain block multiplied by de-quantized scale value to reconstruct the range blocks, these steps will continue until small or no change appear in quality of the reconstructed image. compression ratio (C. R), PSNR, bit rate (B. R) and mean square error (MSE) are calculated using the following equation to need them in section 4:

$$\begin{aligned} & \text{compression} - \text{ratio} (CR) \\ &= \frac{\text{Original} - \text{image} - \text{size}}{\text{Compressed} - \text{image} - \text{size}} \dots (4) \end{aligned}$$

$$PSNR(db) = 10 \log_{10} \frac{(L-1)^2}{MSE} \dots (5)$$

$$MSE = \frac{1}{MN} \sum_{i=1}^M \sum_{j=1}^N (x(i, j) - y(i, j))^2 \dots (6)$$

$$\begin{aligned} \text{Bit Rate} &= \frac{\text{number of bits}}{\text{number of pixels}} = \\ & \frac{(8) \text{ number of bytes}}{N \times N} = \frac{8 \times N \times N}{N \times N} \dots (7) \end{aligned}$$

Where : L is number of the grey levels in the image M, N is image dimensions, x(i, j) is the original image, y(i,j) is the reconstructed image, N is high or width of an image.

Experimental Results

Experimental results were implemented using Visual Basic (Ver.6.0). It is tested on laptop Acer, 2 GHz processor. Entropy technique had been tested specially on bitmap grey scale images of size $n \times n$ since in this thesis we will use lenna, golden hill, girl, train and plane images of size (256 x 256 pixel, 8-bits) as a test images as well as other color images of size (256 x 256 pixel, 24-bits) are also used in experimental tests.

Results of the Decoding (Reconstruction) Stage Based on Entropy Technique

The sample images are compressed using MBE, block length ,step size, scale bits ,maximum scale and entropy threshold (ϵ) parameters since these parameters are set to be (0.0001, 4, 2, 11, 0.9, 0.8) respectively, Figure 3 can be shown to observe results of applying the proposed algorithm on these sample images. Newly, the encoding parameters will be set again to be (0.001, 8, 2, 12, 0.8, and 0.7) respectively to show the new effects on these sample images in Figure 4. Because in the proposed entropy technique, the offset coefficient doesn't be used in compression process since as said in section 2 the offset coefficient don't change the entropy value of the block so the memory of offset coefficient will be exploited to enlarge the number of bits that used

to store scale coefficient to arrive to the 12-bit this give chance for obtaining on best results of the reconstructed images using proposed technique.

Comparing Results of Full search algorithm and Proposed FIC Based on Entropy Technique

To verifying from any proposed algorithm give the required results the comparing between this proposed algorithm and traditional algorithm must be done so that results of the proposed algorithm that use quad tree partitioning will be compared with results of full search algorithm that use fixed block partitioning and sure from does that proposed algorithm speed the encoding time and reconstruct the images with acceptable C. R and PSNR or not, see Tables 1, 2 and 3. See Figures 5, 6 and 7 that show the reconstructed images in both full search algorithm and proposed algorithm according to the encoding parameter values which determined in Tables 1, 2 and 3.

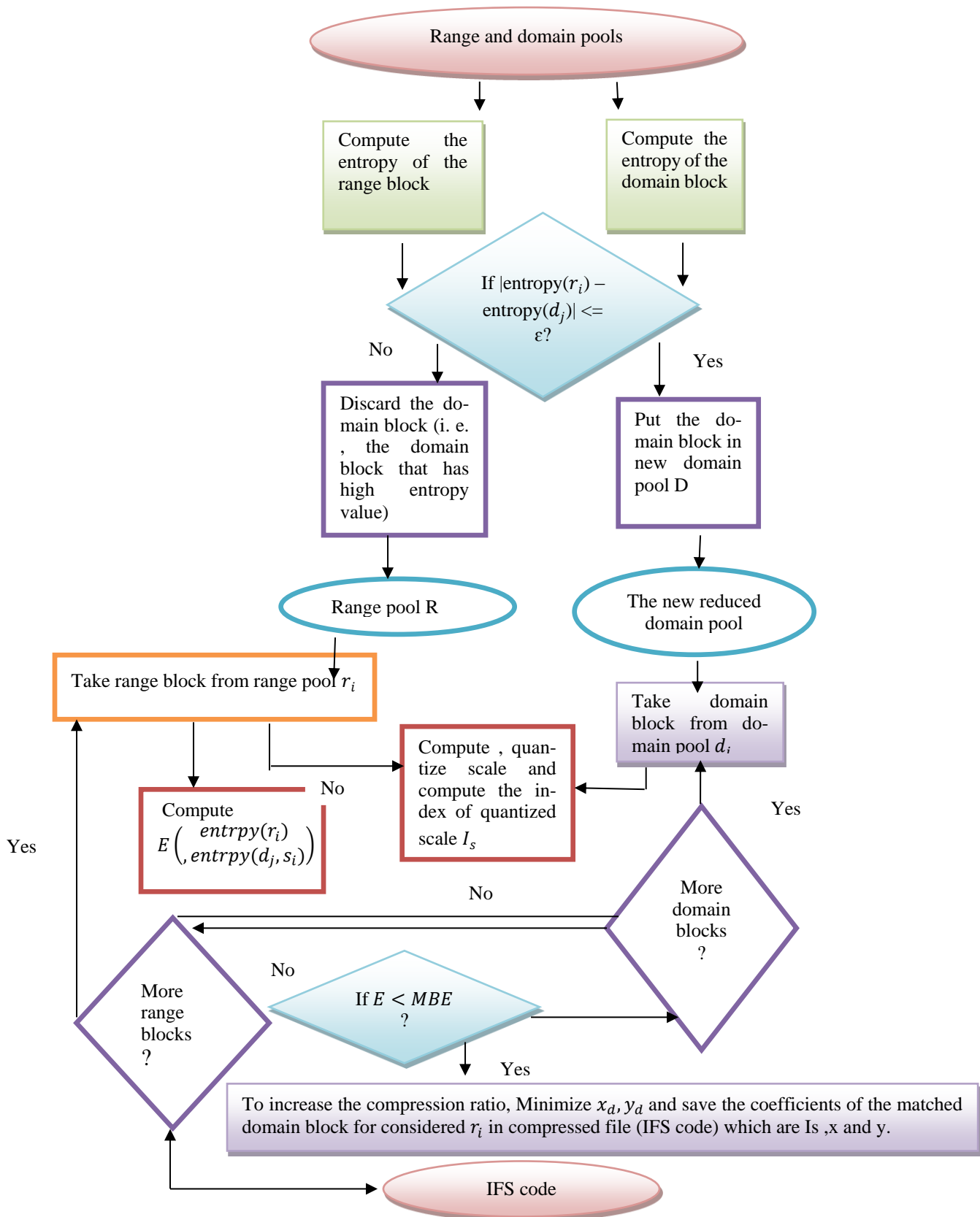


Figure 2: The proposed encoding stage diagram.



**Original Image:
Lenna Image (24-bit)**



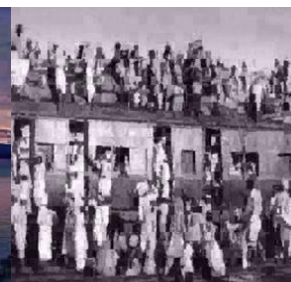
The Reconstructed Image

E. T=120.230 sec
C. R=52.63
PSNR=21.230 dB
MSE=489.76
MAE=38.390
B. R=16.313 bpp



The Reconstructed Image

E. T=79.56 sec
C. R=177.604
PSNR=19.959 dB
MSE=656.33
MAE=35.235
B. R= 3.378 bpp



The Reconstructed Image

E. T=80.36 sec
C. R=168.099
PSNR=18.282 dB
MSE=965.74
MAE=46.436
B. R= 3.569 bpp



**Original Image:
Lenna Image (8-bit)**

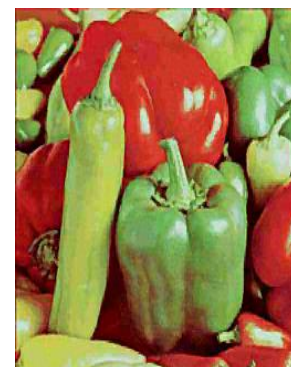


The Reconstructed Image

E. T=109.51 sec
C. R=69.066
PSNR=27.155 dB
MSE=125.17
MAE=8.241
B. R=12.510 bpp



**Original Image:
Fruits Image**



The Reconstructed Image

E. T=120.95 sec
C. R=35.366
PSNR=19.586 dB
MSE=715.17
MAE=43.920
B. R=10.858 bpp



**Original Image:
Rose Image**

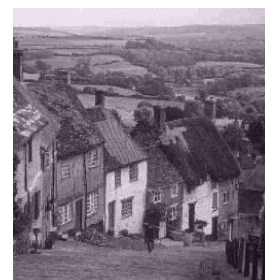


The Reconstructed Image

E. T=124.74 sec
C. R=46.241
PSNR=27.254 dB
MSE=122.35
MAE=16.675
B. R=12.975 bpp



**Original Image:
Golden Hill Image**



The Reconstructed Image

E. T=109.14 sec
C. R=23.583
PSNR=22.863 dB
MSE=336.32
MAE=24.784
B. R=4.071 bpp

Figure 3: Reconstructed images with its values

Figure 3: Reconstructed images with its values



**Original Image:
Girl Image**

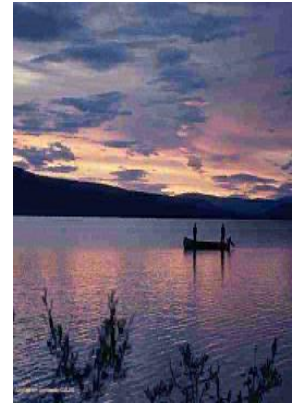


**The Reconstructed
Image**

E. T=109.18 sec
C. R=70.323
PSNR=22.070 dB
MSE=403.69
MAE=40.547
B. R=12.28 bpp

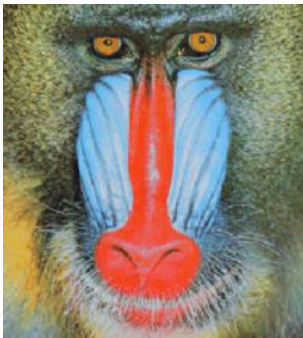


**Original Image:
Lake Image**

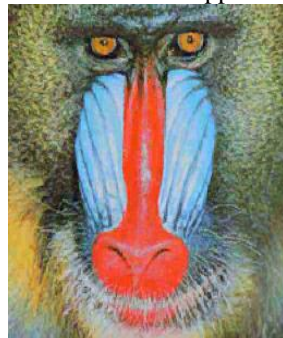


The Reconstructed Image

E. T=121.45 sec
C. R=18.552
PSNR=29.270 dB
MSE=76.919
MAE=6.319
B. R=5.174 bpp



**Original Image:
Mandrill Image**



The Reconstructed Image

E. T=123.26 sec
C. R=53.633
PSNR=24.363 dB
MSE=238.10
MAE=16.219
B. R=15.110 bpp



**The Reconstructed
Image**

E. T=79.80 sec
C. R=169.023
PSNR=25.640 dB
MSE=177.44
MAE=9.016
B. R=3.550 bpp



**The Reconstructed
Image**

E. T=70.81 sec
C. R=177.284
PSNR=17.787 dB
MSE=1082.3
MAE=51.341
B. R=2.166 bpp

Figure 4(a): Reconstructed images with its values



**Original Image:
Train Image**



**The Reconstructed
Image**

E. T=112.20 sec
C. R=56.393
PSNR=14.258 dB
MSE=2124.5
MAE=80.430
B. R=10.640 bpp

Figure 4 (b): Reconstructed images with its values



The Reconstructed Image

E. T=79.08 sec
C. R=171.53
PSNR=20.132 dB
MSE=630.71
MAE=32.438
B. R= 3.508 bpp



The Reconstructed Image

E. T=74.02 sec
C. R=45.343
PSNR=18.551 dB
MSE=907.66
MAE=44.684
B. R=0.529 bpp



The Reconstructed Image

E. T=80.36 sec
C. R=168.099
PSNR=18.282 dB
MSE=965.74
MAE=46.436
B. R=3.569 bpp



The Reconstructed Image

E. T=79.67 sec
C. R=140.084
PSNR=30.807 dB
MSE=53.991
MAE=5.157
B. R=2.741 bpp

Newly, the encoding parameters will be set again to be (0.001, 8, 2, 12, 0.8, 0.7) respectively to show the new effects on these sample images in Figure 4 (a and b).

Because in the proposed entropy technique, the offset coefficient doesn't be used in compression

process since as said in section 2 the offset coefficient don't change the entropy value of the block so the memory of offset coefficient will be exploited to enlarge the number of bits that used to store scale coefficient to arrive to the 12-bit this give chance for obtaining on best results of the reconstructed images using proposed technique.

Comparing Results of Full search algorithm and Proposed FIC Based on Entropy Technique

To verifying from any proposed algorithm give the required results the comparing between this proposed algorithm and traditional algorithm must be done so that results of the proposed algorithm that use quad tree partitioning will be compared with results of full search algorithm that use fixed block partitioning and sure from does that proposed algorithm speed the encoding time and reconstruct the images with acceptable C. R and PSNR or not, see Tables 1, 2 and 3. See Figures 5, 6 and 7 that show the reconstructed images in both full search algorithm and proposed algorithm according to the encoding parameter values which determined in Tables 1, 2 and 3. Finally, the main important reasons that make the proposed encoding stage faster than the encoding stage in full search algorithm will be explained in the following points:

1-Using quad tree partitioning technique which reducing the encoding time of proposed FIC technique since every range block will compared with only 4- domain block in every search process of finding best matched pair of range – domain blocks while in the full search algorithm fixed block partitioning is used which slowing the encoding time since every range block will compared with all domain blocks in every comparing time.

2-Reducing size of the domain pool according to the entropy threshold (ϵ) participate in decreasing size of the searching space that led to reducing the number of comparing for finding the best matched domain block for each range block.

Table 1: Comparing results of full search and proposed algorithms
 The encoding parameters of both algorithms are block
 length=4, MBE=0.00001, step size=2, scale bits=7,
 offset bits=10 (only for full search algorithm), MaxScale =1, $\epsilon=0.6$

Experimental Results of Full search algorithm

Image Name	E. T	C. R	PSNR	MSE	MAE	B. R
Lenna (24-bit)	821.16	8.476	33.873	26.651	3.222	2.831
Lenna (8-bit)	803.26	11.088	31.320	147.970	9.184	2.164
Fruits	834.68	8.387	31.094	50.538	4.234	2.861
Golden Hill	796.41	11.291	36.747	13.751	1.418	2.126
Mandrill	901.70	8.534	30.622	56.352	5.302	2.812
Girl	788.07	11.192	40.898	5.287	1.288	2.144
Rose	436.83	8.957	42.917	3.321	1.757	2.680
Train	732.58	10.956	25.230	195.01	8.924	2.191
Lake	233.28	8.073	33.413	29.631	3.350	2.675
Plane	805.64	11.637	36.031	16.215	1.909	2.062

**Experimental Results of Proposed FIC
 Based on entropy technique**

Image Name	E. T	C. R	PSNR	MSE	MAE	B. R
Lenna (24-bit)	121.11	25.429	26.396	149.11	16.912	8.494
Lenna (8-bit)	105.41	11.088	24.611	224.89	17.937	2.164
Fruits	120.65	41.937	25.931	165.94	13.232	14.307
Golden Hill	107.03	11.291	24.449	233.43	22.593	2.126
Mandrill	120.11	34.132	25.453	185.25	16.674	11.249
Girl	110.29	33.576	35.451	18.531	4.172	6.433
Rose	121.54	53.426	35.826	16.997	5.653	16.172
Train	111.59	32.867	24.503	230.54	9.644	6.572
Lake	123.46	8.973	29.851	67.293	2.095	2.675
Plane	106.56	58.185	29.144	79.182	8.345	10.312

The reconstructed images using full search algorithm



The reconstructed images using proposed algorithm



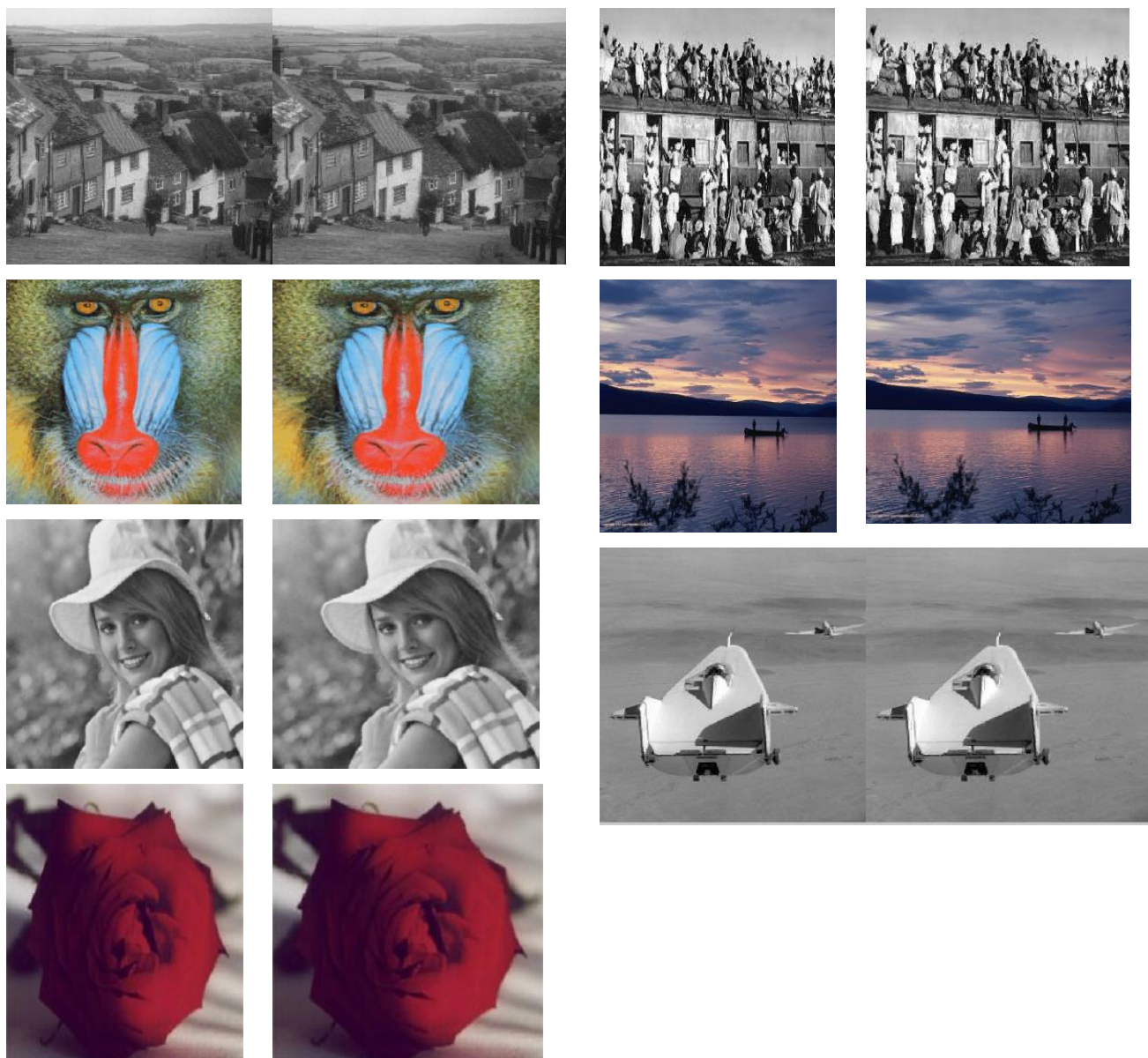


Figure 5: Comparing in reconstructed images between full search algorithm and proposed algorithm based on entropy technique (using parameter values in Table 1).

Table 2: Comparison results between full search and proposed algorithms

The encoding parameters of both algorithms are block length=4, MBE=0.00001, step size=2, scale bits=9, offset bits=6 (only for full search algorithm), MaxScale =0.8, $\epsilon=0.7$

Experimental Results of Full search algorithm						
Image Name	E. T	C. R	PSNR	MSE	MAE	B. R
Lenna (24-bit)	903.94	9.151	32.758	34.457	3.953	2.623
Lenna (8-bit)	802.67	11.849	29.860	67.140	5.455	2.026
Fruits	899.85	9.120	30.363	59.799	4.920	2.632

Golden Hill	796.91	11.291	36.747	13.751	1.418	2.126
Mandrill	913.49	9.255	30.005	64.937	5.783	2.593
Girl	789.49	12.057	35.748	17.306	3.388	1.990
Rose	722.172	9.640	38.611	8.952	2.249	2.490
Train	806.14	11.619	24.120	251.83	10.568	2.066
Lake	881.05	9.674	32.326	38.054	4.094	2.481
Plane	785.52	12.619	32.977	32.765	3.894	1.918

Experimental Results of Proposed FIC Based on Entropy Technique

Image Name	E. T	C. R	PSNR	MSE	MAE	B. R
Lenna (24-bit)	119.34	45.757	25.402	187.41	15.482	13.113
Lenna (8-bit)	109.50	35.547	22.040	406.425	33.302	6.071
Fruits	124.63	45.600	24.223	245.88	19.944	13.158
Golden Hill	114.41	60.695	22.687	350.20	33.173	9.886
Mandrill	120.69	18.510	26.784	136.32	11.901	5.187
Girl	110.16	72.344	35.659	17.666	3.416	11.943
Rose	115.91	38.560	30.690	55.972	13.740	9.958
Train	109.39	46.477	19.523	725.60	31.307	8.262
Lake	121.80	9.674	32.117	39.931	4.216	14.886
Plane	108.88	62.578	25.835	169.64	17.276	9.588

The reconstructed images using full search algorithm

The reconstructed images using proposed algorithm



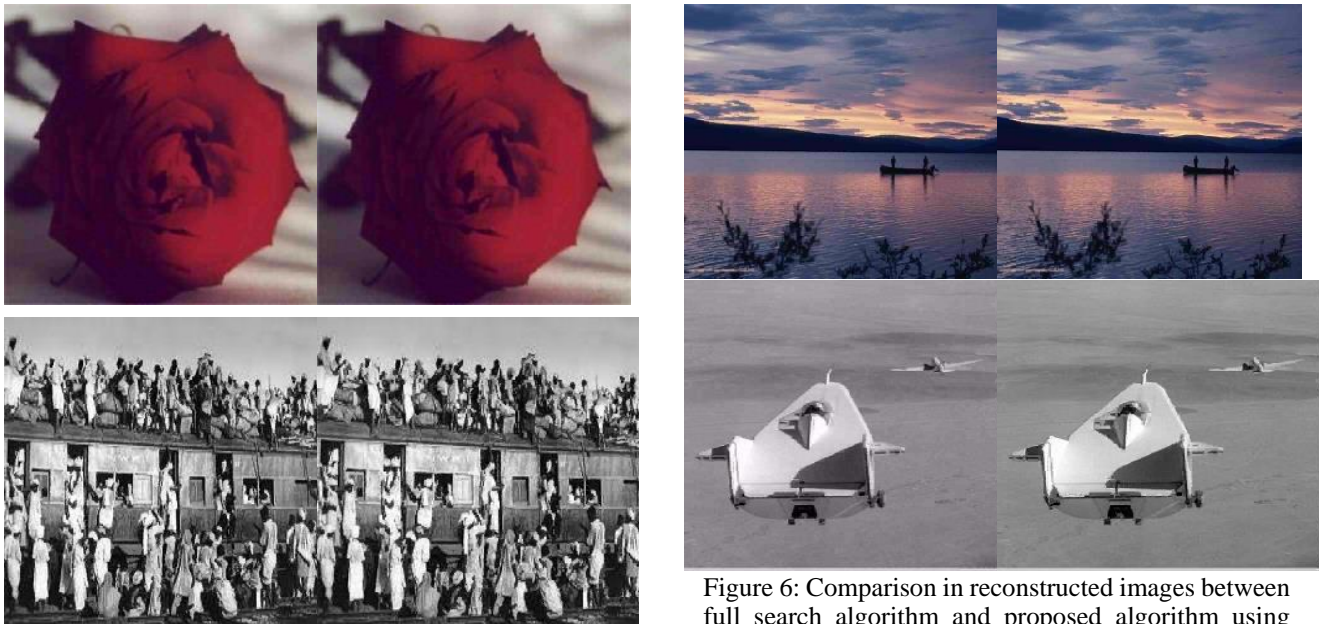


Figure 6: Comparison in reconstructed images between full search algorithm and proposed algorithm using based on entropy technique (using parameter values in Table 2).

Table 3: Comparison results between full search and proposed algorithms.

The encoding parameters of both algorithms are block Length=4, MBE=0.001, step size=3, scale bits=10, offset bits=10 (only for full search algorithm), MaxScale =0.9, $\epsilon=0.9$

Experimental Results of Full search algorithm

Image Name	E. T	C. R	PSNR	MSE	MAE	B. R
Lenna (24-bit)	324.53	7.950	33.269	30.630	3.441	3.019
Lenna (8-bit)	362.28	10.483	30.482	58.191	4.520	2.894
Fruits	403.75	7.872	30.623	56.326	4.480	3.049
Golden Hill	377.602	10.664	36.048	16.151	1.536	2.251
Mandrill	416.15	8	30.140	62.960	5.623	2.999
Girl	279.52	10.575	39.931	6.605	1.480	2.269
Rose	102.85	8.610	41.655	4.441	1.391	2.787
Train	308.44	10.364	24.322	240.32	9.879	2.316
Lake	341.77	8.404	32.743	34.572	3.619	2.856
Plane	393.93	10.972	34.821	21.428	2.169	2.187

Experimental Results of Proposed FIC Based on entropy technique

Image Name	E. T	C. R	PSNR	MSE	MAE	B. R
Lenna (24-bit)	54.48	31.799	27.332	120.174	11.592	12.076
Lenna (8-bit)	47.45	31.449	29.799	68.168	4.927	6.868
Fruits	54.55	7.872	30.346	60.04	4.602	3.049
Golden Hill	48.14	53.319	26.155	157.59	14.487	11.253
Mandrill	54.82	8	22.782	342.63	29.341	2.100

Girl	47.73	10.575	31.586	45.127	4.140	2.269
Rose	53.26	49.951	42.166	3.949	1.202	17.297
Train	49.16	41.457	17.851	1066.5	41.579	9.263
Lake	55.32	8.385	29.272	76.886	7.535	2.862
Plane	48.02	43.888	29.399	74.662	6.928	8.750

The reconstructed images using full search algorithm

The reconstructed images using proposed algorithm

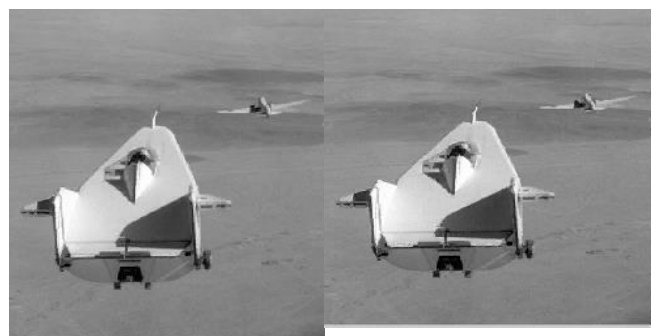
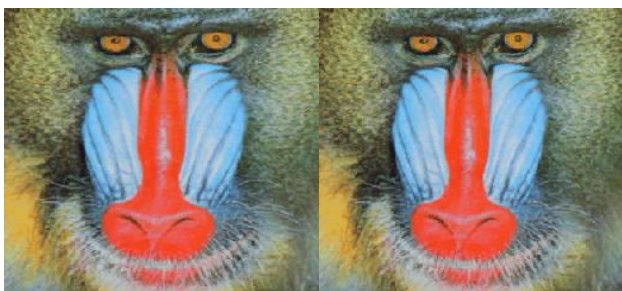


Figure 7: Comparison in reconstructed images between full search algorithm and proposed algorithm based on entropy technique (using parameter values in Table 3).

Conclusions

The experimental results in Tables 1, 2 and 3 which include 10 grey scale and color images of size 256×256 indicate that the proposed FIC algorithm based on entropy technique reconstructed the images with faster E. T and acceptable C. R as well as good quality of the reconstructed image.

The resulted C. R by proposed algorithm within the values that ranged from 7.872 to 72.344 which consider acceptable values when compared with C. R values of full search algorithm that ranged from 7.950 to 12.619 this means that the proposed algorithm reconstruct the images with C. R values better than C. R values of full search algorithm also the proposed algorithm reconstruct the images with good PSNR values which ranged from 17.851 dB to 42.166 dB that close to PSNR values of full search algorithm which included in values from 24.120 dB to 42.917 dB.

Relatively E. T, must be noticed from the mentioned tables that the highest E. T value of full search algorithm (for step size is 2 of Mandrill image) was 913.49 sec while the highest E. T value of the proposed algorithm (for the same step size of Mandrill image) was 120.69 sec this means that E. T of full search algorithm decreased about 792.8 sec where the main target from the proposed algorithm is breaking the slowing encoding time problem after then the secondary targets is to reconstruct the images with acceptable C. R and good PSNR that also invoked by the proposed algorithm as shown from results of the previous Tables.

References

- [1] JyotiBholaand SimarpreetKaur, "Encoding Time Reduction Method For The Wavelet Based Fractal Image Compression", International Journal of Computer Engineering Science (IJCES), Vol.2, Issue 5, May 2012.
- [2] S. Michael Vanitha and K. Kuppusamy, "Survey On Fractal Image Compression", International Journal of Computer Trends and Technology (IJCTT), Vol.4, May 2013.
- [3] Yih-Lonlin and Wen-Linchen, "Fast Search Strategies For Fractal Image Compression", Department of Information Engineering ,I-Shou University Kaohsiung, 840 Taiwan, Journal Of Information Science and Engineering 28, 2012.
- [4] Mahdi Jampour, Mahdi Yaghoobi and Maryam Ashourzadeh, "Fractal Images Compressing By Estimating The Closest Neighborhood With Using Of Schema Theory", Journal of Computer Science 6 (5): 591-596, 2010.
- [5] K. Revathy and M. Jayamohan, "Dynamic Domain Classification For Fractal Image Compression", International Journal of Computer Science & Information Technology (IJCSIT), Vol.4, No 2, April 2012.

Research Article

Network Intrusion Detection System (NIDS) in Cloud Environment based on Hidden Naïve Bayes Multiclass Classifier

Hafza A. Mahmood, Soukaena H. Hashem

Department of Computer Science, University of Technology, IRAQ.

*Correspondent Author Email: h_adel_89@yahoo.com

Article Info

Received
02/06/2016

Accepted
05/10/2016

Abstract

Cloud Environment is next generation internet based computing system that supplies customizable services to the end user to work or access to the various cloud applications. In order to provide security and decrease the damage of information system, network and computer system it is important to provide intrusion detection system (IDS). Now Cloud environment are under threads from network intrusions, as one of most prevalent and offensive means Denial of Service (DoS) attacks that cause dangerous impact on cloud computing systems. This paper propose Hidden naïve Bayes (HNB) Classifier to handle DoS attacks which is a data mining (DM) model used to relaxes the conditional independence assumption of Naïve Bayes classifier (NB), proposed system used HNB Classifier supported with discretization and feature selection where select the best feature enhance the performance of the system and reduce consuming time. To evaluate the performance of proposal system, KDD 99 CUP and NSL KDD Datasets has been used. The experimental results show that the HNB classifier improves the performance of NIDS in terms of accuracy and detecting DoS attacks, where the accuracy of detect DoS is 100% in three test KDD cup 99 dataset by used only 12 feature that selected by use gain ratio while in NSL KDD Dataset the accuracy of detect DoS attack is 90 % in three Experimental NSL KDD dataset by select 10 feature only.

Keywords: Cloud Environment, IDS, NSL KDD Dataset, KDD CUP 99 Dataset, Multiclass Classification, Hidden Naïve Bayes (HNB), and Dos.

الخلاصة

ان بيئة الغيمة هي الجيل الجديد الذي يعتمد على نظام الحوسبة والذي يجهز مختلف الخدمات الى المستخدمين للوصول والعمل على تطبيقات الغيمة المتعددة. لكي يتم توفير الامن وتقليل الاضرار التي تحصل لنظام المعلومات والشبكات ونظام الحاسبة فان من الضروري توفير نظام كشف التطفل في بيئة الغيمة. لقد اصبحت بيئة الغيمة حاليا تحت تاثير المتطفلين على الشبكة ويعد DoS من اكثر الانواع انتشارا وهجومية هو الذي يسبب تاثير خطير على بيئة الغيمة. في هذا البحث تم اقتراح المصنف HNB ليتم اكتشاف DoS والتي تعتبر احدى طرق DM التي تستخدم للتخلص من افتراضية الاستقلالية المشروطة الموجودة في NB, النظام المقترح يستخدم HNB مع discretization و feature selection حيث يتم اختيار افضل حقول لتحسين اداء النظام وتقليل وقت التنفيذ. لتقييم النظام المقترح تم استخدام KDD Dataset, NSL KDD Dataset. حيث اظهرت النتائج ان استخدام HNB يحسن من اداء نظام كشف التطفل من ناحية اكتشاف Dos حيث اصبحت نسبة اكتشافه 100% في ثلاث مجاميع من KDD Cup 99 استخدمت لفحص النتائج باستخدام اثني عشر صفة فقط تم اختيارها باستخدام GR بينما في NSL KDD كانت نسبة اكتشاف DoS 90% في ثلاث مجاميع مختلفة اخرى باستخدام عشرة صفات فقط.

Introduction

Cloud computing enables the customers to access and use resources that are distributed in the internet to make processing or computations without installing in their own computer and they must to pay just for the service they consumed, it is a modern technology that provide immediately access to resources as per the needs of the users [1]. Cloud environment started in the mid of 2007 and it is developed rapidly to satisfy infu-

sion and diffusion of IT in systems, it's important to provide IDS in cloud environment because of the Distributed model of cloud that makes it susceptible and prone to sophisticated attacks like DoS, ID is process of examining the events happen in a network resources or computer system and analyzing them to determine the presence of intrusion and possible accident that can cause threats to security measures [2]. While the IDS are defined as the hardware or software product

that detecting attacks over network, computer systems or against information systems [3]. ID methods can be classified into misuse detection and anomaly detection, in misuse detection that is also called rule-based detection or signature-based the user's activities are compared with known behaviors of attackers, its gathered information, analyzed and compared with huge databases for attack signatures [4]. While in anomaly detection is used to identify abnormal behavior on a network or host, where assume that intrusions are different from legitimate events and therefore can be detected by the systems that identify these differences [5]. Data mining (DM) is used for extracting relevant information from huge database; DM techniques are used to analyze and monitor large network data and classify these data into anomalous and normal data. DM commonly involves four classes of task. Clustering, Classification, Regression and Association rule learning [6]. A classification is process of taking each instance in dataset and determines it to a specific class attack or normal, that means known structure will be used for new instances [7]. In last two decades, there are several studies focused on reducing the independence assumption of NB classifier, one of these studies introduced HNB classifier, this new model depends on build additional layer, this layer represents a hidden parent for every feature as shown in Figure 1. The benefit of using hidden parent (A_{hpi}) is to gather the weighted influences from all other features (A_j), where $i, j = 1, 2, \dots, n$ and i is not equal to j , and $P(C)$ is the probability of class. Joint distribution is defined as Equation 1, while the hidden parent defined as Equation 2, and HNB classifier is defined as Equation 3 [8].

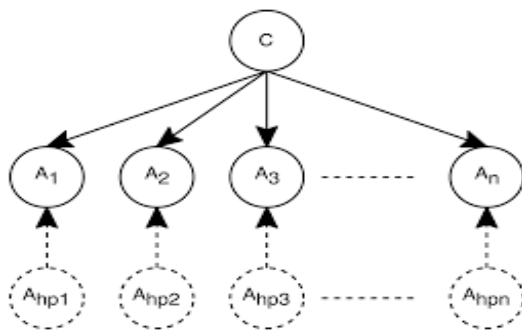


Figure 1: HNB Structure.

$$P(A_1, \dots, A_n | C) = P(C) \prod_{i=1}^n P(A_i | A_{hpi}, C) \quad (1)$$

$$P(A_i | A_{hpi}, C) = \sum_{j=1, j \neq i}^n W_{ij} * P(A_i | A_j, C) \quad (2)$$

$$c(E) = \arg \max_{c \in C} P(c) \prod_{i=1}^n P(a_i | a_{hpi}, c) \quad (3)$$

The method to calculate the weights W_{ij} , is by using conditional mutual information (CMI) between every two features A_i and A_j as shown in Equation 4, The CMI is defined as Equation 5 [8]:

$$W_{ij} = \frac{I_p(A_i; A_j | C)}{\sum_{j=1, j \neq i}^n I_p(A_i; A_j | C)} \quad (4)$$

$$I_p(A_i; A_j | C) = \sum_{a_i, a_j, c} P(a_i, a_j, c) \log \frac{P(a_i, a_j | c)}{P(a_i | c)P(a_j | c)} \quad (5)$$

Feature selection is an essential data processing step prior to applying a learning algorithm. Feature selection is a process of finding a subset of significant features from the original set of features and reduces the number of irrelevant redundant features from dataset to improve the performance of the classification and also decreases storing of memory space, one of the most common methods in feature selection is Information Gain that measures the amount of information in bits about the class prediction. It measures the expected reduction in entropy. Entropy measure is considered as a measure of systems unpredictability which is usually used in information theory measure.

The Expected information (Entropy) of a feature A is defined as Equation 6, where a is a value of feature, and $a = 1, 2, \dots, n$. The Information needed to classify D after using A for divide D into n partitions is mention in Equation 7. Information gained by branching an attribute A as in Equation 8 [9]:

$$Info D = H(A) = - \sum_{a=1}^n P(a) \log_2 P(a) \quad (6)$$

$$Info_A(D) = \sum_{j=1}^v \frac{|D_j|}{|D|} * I(D_j) \quad (7)$$

$$\text{Gain (A)} = \text{Info D} - \text{Info}_A(D) \quad (8)$$

Gain ratio (GR) is an enhancement of the information gain to solve the matter of bias towards features with big set of values that appeared in Information Gain. GR should be small when all data belong to one branch attribute and large when data is equally spread. GR selecting an attribute by takes size and number of values into account.

It's correct IG by taking the substantial information of a split into account (i. e. How much information is needed to determine which branch the instance belongs to?) Where substantial information is the entropy of distribution of instances into branches based on Equation 9. This value generated by splitting the training data set as in Equation 10 where represents the substantial information [10]:

$$\text{Split Info}_A(D) = - \sum_{j=1}^v \frac{|D_j|}{|D|} \log_2 \frac{|D_j|}{|D|} \quad (9)$$

$$\text{Gain Ratio (A)} = \frac{\text{Gain (A)}}{\text{Split Info (A)}} \quad (10)$$

Related Work

Mukherjee S. et al., 2012, discussed the importance of reduce features to build effective and efficient IDS. They checked performance of (Information Gain, Gain Ratio and Correlation-based Feature Selection methods, they propose Feature Vitality Based Reduction Method to identify the importance of reduce feature. They applied NB classifier on NSL KDD dataset for ID. Experimental results showed that select Features enhance performance to design effective and efficient NIDS [11].

Koc L. et al., 2012, introduced HNB model as a solution of ID problem. To decrease the resource requirements and enhance the accuracy, they used NB and structurally extended Naïve Bayes methods augmented with feature selection and discretization. They compared the performance of the NB classifier and leading extended Naïve Bayes approaches with the HNB classifier as an IDS, they uses KDD99 dataset, The results proved that HNB model enhance the accuracy of

detecting DOS attacks, where the accuracy of detect Dos is 0.99 [12].

Padmakumari P. et al., 2014 presented IDS in a cloud environment, to detect most occurring attacks in several network environments by applying the Apriori algorithm using k-means clustering and combine it with a frequent attacks generation module.

Experimental results showed that applying a clustering algorithm separately for different attributes enhance the accuracy of detection. The frequent attack detection module increases the reliability and achieve low false alarm rate, they used KDD 99 CUP dataset to evaluate their system [13].

Koc L. et al., 2015, they discussed that the HNB binary classifier model can be applied to ID problem. They used KDD Cup 99 dataset to prove that the HNB binary classification model with CONS feature selection method and EMD discretization enhance performance of system in terms of accuracy and error rate than the traditional NB model, where the accuracy of detect normal and attack events is 0.93 [8].

Datasets and Attacks in Cloud Environment

The KDD Cup 99 dataset is widely used in IDS which consist of 10% of the original dataset that containing 494,020 records each record consist of 41 features and class feature labeled either normal or attack. It has 80.31% attack and 19.69% normal. The NSL KDD data set solve some of the ingrained problems of the KDD CUP 99 dataset, which selected records of the complete KDD data set that contain the same features as KDD cup 99. The class feature contains 21 kinds of attacks within four types: DOS, Probe, R2L attacks and U2R attacks as mention in Table 3 [13].

Table 3: description of attacks in KDD Cup 99 and NSL KDD Datasets.

Attack type	Description	Types
DOS	Denial of services attacks	Pod, Land, smurf, back etc.
Probe	Surveillance and probing	Satan, ipssweep, nmap etc.
R2L	Unauthorized access from remote machine to local machine	Guess_passwd, ftp_write, imap, phf etc.
U2R	Unauthorized access to local superuser privileges by a local unprivilege user	Rootkit, buffer overflow, load-module etc.

The benefit of using NSL KDD over the original KDD data set, that it doesn't contain redundant records in the train and test dataset and from every difficulty level set, the number of records that selected is inversely commensurate to the percentage of records in KDD 99 dataset [14]. Since large size of data translates between cloud environments, the intrusions are eager to exploit the vulnerabilities in cloud and by this way they can gain the important data. DoS attacks are the dangers attack among numerous threats in cloud computing, even the Cloud Security Alliance has been indicated as one of the nine major attacks. DoS make the system cannot respond to any requests by overloads the system with requests and that leads to make the resources unavailable to its users [1].

Proposal Network Intrusion Detection System

The proposed system is multiclass NIDS in Cloud environment based on HNB classifier, as we mention above the attackers in cloud environment is different from traditional network, where is usually from DOS attack which is the most dangerous attack that effect the availability of resource, the reason of used NIDS instead of host intrusion detection system HIDS is that the HIDS can be detected by use antivirus, to evaluate the system we used the well-known dataset KDD Cup 99 and NSL KDD Dataset. Figure 2 describes the general structure of the proposed NIDS, for more understanding see Algorithm 1. The proposed NIDS consists of the following steps:

1. Normalization.
2. Discretization.
3. Feature Selection method.
4. Training and testing

Algorithm 1: General structure of the proposed system.

Input: training dataset

Output: evaluation for three test dataset

Begin

1. Normalization process

For each Attribute in Dataset

 select Maximum value (Max)

 select Minimum value (Min)

 For each value v in Attribute

 Combine the new value by use Equation 11

$$\text{New } v = \frac{\text{Old } v - \text{Min}}{\text{Max} - \text{Min}} \quad (11)$$

 End For

End For

2. For each continues feature in dataset

 Discrete the values into specific range

 End for

3. Feature selection

 Find the size of training dataset D

 Find the Probability of each class

 compute the entropy of five class (c) to find info D by use Equation 6

$$\text{Info } D = H(A) = - \sum_{a=1}^n P(a) \log_2 P(a) \quad (6)$$

 For each Feature F in training dataset

 For each value j in Feature F

 compute the frequency of value in all training dataset Ft

 compute the frequency of value with each class Fn

 compute the entropy for each value with five class by using Equation 6

$$I(D_j) = - \sum \frac{F_n}{F_t} \log_2 \frac{F_n}{F_t}$$

 End For

 compute info A by used Equation 7:

$$\text{Info}_A(D) = \sum_{j=1}^v \frac{|D_j|}{|D|} * I(D_j) \quad (7)$$

 compute gain for each Feature as in Equation 8

$$\text{Gain (A)} = \text{Info D} - \text{Info}_A(\text{D}) \quad (8)$$

compute Split Info by use Equation 9
Split Info_A(D)

$$= - \sum_{j=1}^v \frac{|F_{t_j}|}{|D|} \log_2 \frac{|F_{t_j}|}{|D|} \quad (9)$$

compute the Gain ratio by use Equation 10

$$\text{Gain Ratio (A)} = \frac{\text{Gain (A)}}{\text{Split Info (A)}} \quad (10)$$

End For

4. Select set of features that have the highest gain ratio.
5. Applied HNB classifier in training dataset to build the NIDS by use Algorithm 2.
6. Evaluation the proposed system by use three experimental test dataset

For each test dataset

Compute accuracy (acc) by use Equation 12

$$\text{acc} = \frac{\text{TP} + \text{TN}}{\text{TP} + \text{TN} + \text{FP} + \text{FN}} \quad (12)$$

Compute the detection rate (DR) by use Equation 13

$$\text{DR} = \frac{\text{TP}}{\text{TP} + \text{FN}} \quad (13)$$

Compute error rate(ER) by use Equation 14

$$\text{ER} = \frac{\text{FP} + \text{FN}}{\text{TP} + \text{TN} + \text{FP} + \text{FN}} \quad (14)$$

Find the confusion matrix

End for

End

when test dataset which it is not appeared in training dataset.

Feature Selection

Feature selection is one of the most important preprocessing of DM methods that used to remove the unrelated and redundant features in large dataset, and to improve the performance of the system by use the correct feature and reduce the consuming time. In our study, we used gain ratio as a feature selection method.

Training and Testing

The system used HNB Classifier (see Algorithm 2) by select 4000 records in learning phase by select 2169 DOS, 388 probes, 173 R2L, 35 U2R and 1235 normal in both datasets (KDD cup 99 and NSL KDD), while in test phase it will be used 1200 samples to evaluate the work and two other datasets (600,900) samples to validate the performance of the system in KDD Cup 99 Dataset, the selection samples of attack mention in Table 4. While in NSL KDD Dataset the test samples that have been used is 1028 and two other dataset to validate the performance of system with (795 and 566), as mention in Table 5. It is important to note that, the NSL KDD Dataset different from the original KDD Cup 99 Dataset where the samples of attack is less than the KDD Cup 99 Dataset as a result of remove the redundant samples and there is some kind of attack is not mention in NSL KDD Dataset like (warezclient and spy) Which is R2L attack, for that reason the selected test dataset in NSL KDD is different from the selected test in KDD Cup 99.

Normalization dataset

The first step in the proposed system is applied normalization process to continue feature in dataset to enhance the performance and effectiveness of the system by making the values of attribute within specific range from 0 to 1, in our system will be used Min-max normalization method.

Discretization dataset

As a result of contains continues and discrete feature in KDD Cup 99 and NSL KDD Datasets it is important to convert the continuous attribute to discrete to ensure the efficiency of the system and to solve the problem of appear new value

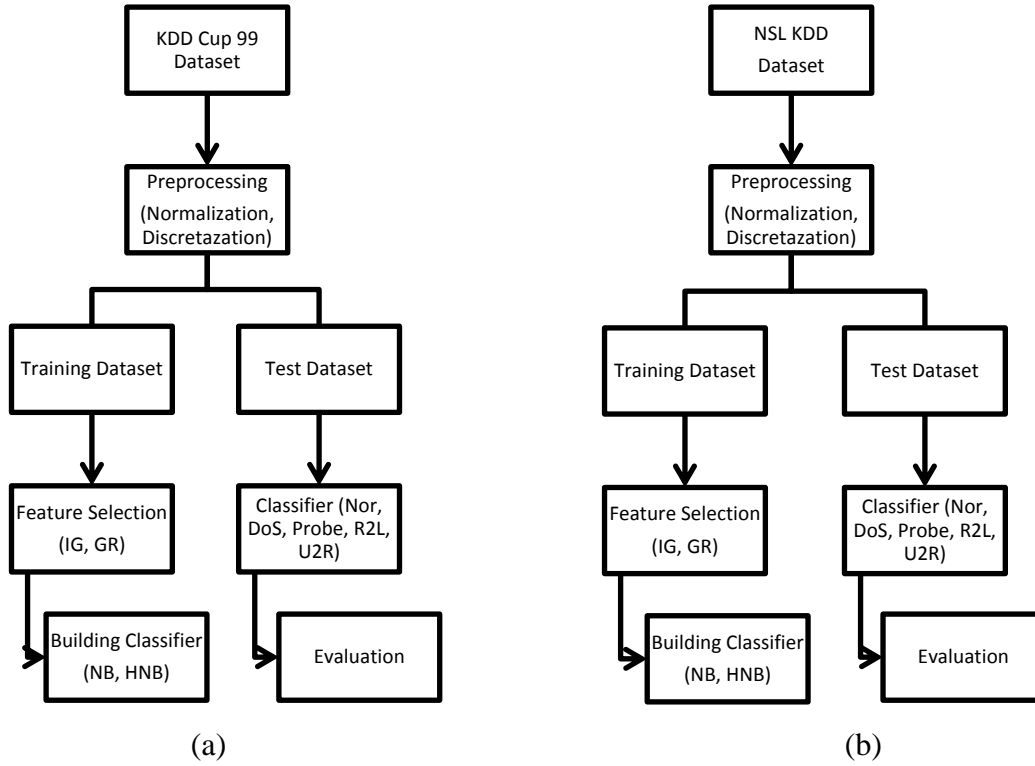


Figure 2: (a) Block Diagram of KDD Cup 99 Dataset. (b) Block Diagram of NSL KDD Dataset.

Algorithm 2: Hidden Naïve Bayes Classifier

Input: training and testing dataset after normalization and discrete processes (KDD Cup 99 10% or NSL KDD Dataset)

Output: classification the test dataset

Begin

Step1: Training phase

- 1) Compute the size of training dataset D
- 2) For each class c in training dataset
 - Compute P(c) from training dataset
 - End for
- 3) For each class c
 - For each Feature a_i, a_j in training dataset
 - Compute $P(a_i, a_j, c)$ by divide FrEquation of appeared (a_i, a_j, c) on training D
 - Compute $P(a_i, a_j|c)$ by divide FrEquation of appeared $(a_i, a_j|c)$ on FrEquation of class
 - Compute $P(a_i|c)$ by divide FrEquation of appeared $(a_i|c)$ on FrEquation of class
 - Compute $P(a_j|c)$ by divide FrEquation of appeared $(a_j|c)$ on FrEquation of class
 - Apply Equation 5 to find the CMI between two feature:

$$I_p(A_i; A_j|C) = \sum_{a_i, a_j, c} P(a_i, a_j, c) \log \frac{P(a_i, a_j|c)}{P(a_i|c) * P(a_j|c)} \quad (5)$$

End for
 For each feature
 compute $W_i = \sum_{j=1, j <> i}^n I_p(A_i, A_j|C)$
 compute $W_{ij} = \frac{I_p(A_i, A_j|C)}{w_i}$
 End for

End for
Step 2: Testing phase
 4) For each record in test dataset
 For each value in test dataset
 find probability of v_i with c in training dataset
 End for
 Multiply the probability of each record as Equation 2

$$P(E|c) = P(a_1, a_2, \dots, a_n|c) = \prod_{i=1}^n P(a_i|c) \quad (2)$$
 Classify the record by Multiply the result of Equation 2 with probability of class and choose the maximum value to classify the record as Equation 1:

$$c(E) = \arg \max_{c \in C} P(c)P(a_1, a_2, \dots, a_n|c) \quad (1)$$
 End For
End

Table 4: Test KDD Cup 99 Dataset selected.

Dataset	DOS	Probe	R2L	U2R	normal
600	342	74	23	4	157
900	515	111	36	5	233
1200	680	133	53	8	326

Table 5: Test NSL KDD Dataset selected.

Dataset	DOS	Probe	R2L	U2R	normal
566	326	68	10	6	156
795	434	100	17	11	233
1028	539	122	24	13	330

Experimental Work and Results

The proposed network intrusion detection system is used three test dataset (KDD cup 99 and NSL KDD) to evaluate the system where the records selected randomly and then build the classifier proposed system by use HNB classifier supported by discretization and feature selection method, to evaluate the detection effectiveness of the proposed system we used confusion matrix, accuracy, detection rate and error rate, the confusion matrix is a quality measurement of classifier.

KDD CUP 99 Dataset Evaluations

Table 6 shows the evaluation of classification in three KDD cup 99 test datasets with used 12 best features selected by gain ratio method. The evaluation consists of (Accuracy binary) which is the accuracy of detecting normal and attack, the accuracy of multiclass is the accuracy of detecting normal, DoS, probe, R2L and U2R, detection rate (DR), error rate (ER) and Precision. The accuracy for each class show in Table 7 that demonstrates the accuracy of detecting DoS attack is 100%.

Table 6: Performance measure of KDD cup 99 Dataset.

DS	Acc. multiclass	Acc. binary	DR	ER	Precision
Test1	0.94	0.97	0.96	0.02	100
Test2	0.92	0.97	0.97	0.02	0.98
Test3	0.93	0.96	0.95	0.03	0.99

Table 7: Accuracy for each class in KDD Cup 99 Dataset.

DS	DOS	Probe	R2L	U2R	Normal
Test1	100	0.89	0	0	100
Test2	100	0.83	0	0	0.96
Test3	100	0.87	0	0	0.99

Tables (8, 9, and 10) show the confusion matrix for Tests (1, 2 and 3) of KDD Cup 99 dataset based on select 12 feature by gain ratio which achieve best result in detecting DoS attack.

Table 8: Confusion matrix for test1.

	Normal	DOS	Probe	R2L	U2R
Normal	157	0	0	0	0
DOS	0	342	0	0	0
probe	0	8	66	0	0
R2L	11	12	0	0	0
U2R	3	1	0	0	0

Table 9: Confusion matrix for test2.

	Normal	DOS	Probe	R2L	U2R
Normal	226	7	0	0	0
DOS	0	515	0	0	0
probe	0	18	93	0	0
R2L	17	13	6	0	0
U2R	0	5	0	0	0

Table 10: Confusion matrix for test3.

	Normal	DOS	Probe	R2L	U2R
Normal	324	2	0	0	0
DOS	0	680	0	0	0
probe	0	16	117	0	0
R2L	28	25	0	0	0

As shown in the Table 7 the rate of detect R2L as R2L attack and U2R as U2R attack is low, but actually when you look at Tables (Table 8, Table 9, and

Table 10) you can observe that it's detected but another kind of attack.

NSL KDD Dataset Evaluations

The evaluation of classification in three NSL KDD test datasets viewed in Table 11 (accuracy binary, accuracy of multiclass, detection rate (DR) and error rate (ER), Precision), while the accuracy for each class show in Table 12 that demonstrate the accuracy of detecting DoS attack is best when select 10 feature based on gain ratio method.

Table 11: Performance measure of NSL KDD Dataset.

DS	Acc. multiclass	Acc. binary	DR	ER	Precision
Test1	0.83	0.92	0.90	0.07	100
Test2	0.82	0.92	0.90	0.06	100
Test3	0.83	0.93	0.90	0.06	100

Table 12: the accuracy for each class in NSL KDD.

DS	DOS	Probe	R2L	U2R	Normal
Test1	0.90	0.29	0	0	100
Test2	0.90	0.29	0	0	100
Test3	0.90	0.28	0	0	100

In Tables (13, 14, and 15), show the confusion matrix for Test (1, 2 and 3) of NSL KDD dataset based on select 10 features by using gain ratio method which achieves best result in detecting DoS attack.

Table 13: Confusion matrix for test1.

	Normal	DOS	Probe	R2L	U2R
Normal	157	0	0	0	0
DOS	30	296	0	0	0
probe	0	48	20	0	0
R2L	0	10	0	0	0
U2R	3	3	0	0	0

Table 14: Confusion matrix for test2.

	Normal	DOS	Probe	R2L	U2R
Normal	233	0	0	0	0
DOS	40	394	0	0	0
probe	0	71	29	0	0
R2L	1	16	0	0	0
U2R	6	5	0	0	0

Table 165: Comparison between proposed system and previous studies.

Dataset	parameters	Pre1 2012	Pre2 2015	Proposed system		
				Test1	Test2	Test3
KDD Cup 99	Accuracy binary	–	0.9340	0.97	0.97	0.96
	Accuracy of DoS	0.99	–	100	100	100
	Accuracy multiclass	0.9372	–	0.94	0.92	0.93
	Precision	–	–	100	0.98	0.99
	Error_rate	0.06	0.0660	0.02	0.02	0.03
	Detection rate	–	–	0.96	0.97	0.95

Table 15: Confusion matrix for test3.

	Normal	DOS	Probe	R2L	U2R
Normal	330	0	0	0	0
DOS	50	489	0	0	0
probe	0	87	35	0	0
R2L	3	21	0	0	0
U2R	7	6	0	0	0

As shown in Table 12 the accuracy of detect normal events is 100% and the accuracy of detect DOS is 90 %, while the accuracy of detect probe as probe attack, R2L as R2L attack and U2R as U2R attack is low rate, but its detect it as a DoS attack and this is the important is to detect attack as any kind of attacks, look at Tables (13, 14, and 15).

Table 16 shows comparison the experimental results between the proposed system and the previous studies [12] [8].

Conclusions

Our research indicates the important to use NIDS in cloud environment to detect the most harmful attack in network which is DoS attack that effect the availability of the resource, The experimental results have revealed that when working with gain ratio and select only 12 features from 41 features in KDD Cup 99 dataset our detection system achieves high accuracy rate, reduce the computation time and reduce the error rate as mention in Table 7, while in NSL KDD it is best to select only 10 feature by used gain ratio method as shown in Table 11. The proposed system show that use KDD Cup 99 dataset in cloud environment is best than NSL KDD in detecting DOS attacks.

NSL KDD	Accuracy binary	-	-	0.92	0.92	0.93
	Accuracy of DoS	-	-	0.90	0.90	0.90
	Accuracy multiclass	-	-	0.83	0.82	0.83
	Precision	-	-	100	100	100
	Error_rate	-	-	0.07	0.06	0.06
	Detection rate	-	-	0.90	0.90	0.90

References

- [1] Vidhya. V, "A Review of DOS Attacks in Cloud Computing," *IOSR Journal of Computer Engineering*, vol.16, no.5, 2014.
- [2] Singh S. and Srivastava R, "Intrusion Detection Using Data Mining Technique," *International Journal of Innovative Technology and Exploring Engineering (IJITEE)*, vol.2, no.4, 2013..
- [3] Bandgar M., dhurve K., Jadhav S., Kayastha V. and Parvat T. J., "Intrusion Detection System using Hidden Markov Model (HMM)," *OSR Journal of Computer Engineering (IOSR-JCE)*, vol.10, no.3, 2013.
- [4] Madni H. A., Javed M. and M. J. Arshad, "An Overview of Intrusion Detection System (IDS) along with its Commonly Used Techniques and Classifications," *International Journal of Computer Science and Telecommunications*, vol.5, no.2, 2014.
- [5] Arora S. and Bawa R. K., "A Review on Intrusion Detection System to Protect Cloud Data," *International Journal of Innovations & Advancement in Computer Science*, vol.3, no.5, 2014.
- [6] Abhaya, Kumar K., Jha R. and Afroz S., "Data Mining Techniques for Intrusion Detection: A Review," *International Journal of Advanced Research in Computer and Communication Engineering*, vol.3, no.6, 2014.
- [7] Kanagalakshmi. R and Raj N. V., "Network Intrusion Detection Using Hidden Naive Bayes Multiclass Classifier Model," *International Journal of Science, Technology & Management*, vol.3, no.12, 2014.
- [8] Koc L. and Carswell A. D., "Network Intrusion Detection Using a HNB Binary Classifier," in *UKSIM-AMSS International Conference on Modelling and Simulation*, 2015.
- [9] Ghosh P., Debnath C., Metia D. and Dr. Dutta R., "An Efficient Hybrid Multilevel Intrusion Detection System in Cloud Environment," *IOSR Journal of Computer Engineering*, vol.6, no.4, 2014.
- [10] Ibrahim H. E., Badr S. M. and Shaheen M. A., "Adaptive Layered Approach using Machine Learning Techniques with Gain Ratio for Intrusion Detection Systems," *International Journal of Computer Applications*, vol.56, no.7, 2012.
- [11] Mukherjee S., Sharma N., "Intrusion Detection using Naive Bayes Classifier with Feature Reduction," *Elsevier Ltd.*, 2012.
- [12] Koc L., Thomas A. Mazzuchi and Sarkani S., "A network intrusion detection system based on a Hidden Naive Bayes multiclass classifier," *Elsevier Ltd.*, 2012.
- [13] Padmakumari P., Surendra K., Sowmya M. and Sravya M., "Effective Intrusion Detection System for Cloud Architecture," *ARPJ Journal of Engineering and Applied Sciences*, vol.9, no.11, 2014.
- [14] Ibrahim L. M., Basheer D. T. and Mahmud M. S., "A Comparison Study For Intrusion Database (KDD99, NSL-KDD) Based On Self Organization Map (SOM) Artificial Neural Network," *Journal of Engineering Science and Technology*, vol.8, no.1, 2013.

Research Article

Best Approximate of Vector Space Model by Using SVD

Raghad M. Hadi, Soukaena H. Hashem, Abeer T. Maalood

Departement of Computer Science, College of Science, Mustansiriyah University, IRAQ.

*Correspondent Author Email: {Raghad_alrudieny, soukaena. hassen, abeer282003}@yahoo.com

Article Info

Received
10/11/2016

Accepted
21/05/2017

Abstract

A quick growth of internet technology makes it easy to assemble a huge volume of data as text document; e. g., journals, blogs, network pages, articles, email letters. In text mining application, increasing text space of datasets represent excessive task which makes it hard to pre-processing documents in efficient way to prepare it for text mining application like document clustering. The proposed system focuses on pre-processing document and reduction document space technique to prepare it for clustering technique. The mutual method for text mining problematic is vector space model (VSM), each term represent a features. Thus the proposed system create vector-space model by using pre-processing method to reduce of trivial data from dataset. While the hug dimensionality of VSM is resolved by using low-rank SVD. Experiment results show that the proposed system give better document representation results about 10% from previous approach to prepare it for document clustering.

Keywords: High Dimensional Datasets, Dimensionality reduction, SVD, Vector Space Model.

الخلاصة

ان النمو السريع لأجهزة الكمبيوتر والإنترنت يجعل من السهولة تجميع وتوريد كمية كبيرة من المعلومات على شكل النص؛ على سبيل المثال، استعراض، المدونات الالكترونية، وصفحات الويب، مقالات، رسائل البريد الإلكتروني. وغيرها ، ان زيادة نطاق قواعد البيانات النص والأبعاد العالية غير مهمة مما يجعل من الصعب تصنيف الوثائق في مختلف الفئات. لذلك فان النظام المقترح ركز في معالجة هذه البيانات الكبيرة وتقليص من ابعادها ليتم تهيئتها الى عملية تصنيف البيانات. وذلك من خلال تجهيز تقنية VSM هو نموذج فضاء المتجه ، حيث تعتبر الكلمات هي الخصائص المهمة فيها. وهكذا يهدف النظام المقترح إلى استخدام نموذج فضاء المتجه والتي تعتمد على طريقة المعالجة المسبقة للحد من الخسائر من المعلومات التافهة. يتم حل مشكلة الأبعاد العالية مع تقنية اختبار ميزة من خلال تطبيق رتبة منخفضة لل SVD على القيم VSM. وتشير النتائج أن النظام المقترح اعطى نتائج أفضل بتمثيل البيانات الكبيرة مع تقليص ابعادها بنسبة 10% ليتم ادخالها الى عملية تصنيف البيانات.

Introduction

In the latest years, there has been a growing attention in English Language pre-processing research. English is the intuitive language of residents of more than 380 million. So the big documents datasets convert to term-document matrices which called a Vector Space Model which the term-specific weights in the document vectors are products of local and global parameters. The model is known as term frequency-inverse document frequency model of information (TF-IDF) [1]. In the VSM, a vector is castoff to characterize all piece or paper in a gathering. All section of the direction mirrors key word, or word related through the known paper. The cost given near that module replicates the status of the word in signifying the document. Typically, the cost is a role of the occurrence by the word ensues in the paper or in the paper gathering as a total. To

create term-document matrix the collection of document must preprocessing first [2].

Preprocessing phase

The preprocessing holds a practice for increase the set of words to categorize meeting. The drive for pre-processing stage is to clip all words from the datasets that have cheap material that container perhaps touch an excellence of the collection reports. While Singular value decomposing skilled the commerce by loud information, the popular of open immaterial ideas would be connected to empty common relations [3].

The chief procedure of preprocessing phase exists through eliminating stop words. The stop words are common words that transmit not at all evidence then empty after castoff as a hunt relations (i. e., pronouns, prepositions, conjunctions etc) [4].

The additional procedure is to stem a term. Morphological variations of arguments typically need related imports. Unknown these arguments are conflated into only word, the presentation of document reclamation can be enhanced. By consuming the procedure of stemming in a method that verses are stemmed hooked on a root formula through eliminating their affixes [5].

Dimension Reduction techniques

• **Singular Value Decomposition (SVD)**

Is built by deduction since linear algebra which states a four-sided m-by-n matrix. A container by damaged into the creation of three array - an orthogonal matrix U, a diagonal matrix S, and the transpose of an orthogonal matrix V. SVD of an n x n matrix A is defined by the operation:

$$A=U*S*V^T$$

$$= \begin{bmatrix} U_{1,1} & \dots & U_{1,n} \\ U_{2,1} & \dots & U_{2,n} \\ \dots & \dots & \dots \\ U_{n,1} & \dots & U_{n,n} \end{bmatrix} \cdot \begin{bmatrix} S_{1,1} & 0 & 0 \\ 0 & S_{2,1} & 0 \\ \dots & \dots & \dots \\ 0 & 0 & S_{n,n} \end{bmatrix} \cdot \begin{bmatrix} V_{1,1} & \dots & V_{1,n} \\ V_{2,1} & \dots & V_{2,n} \\ \dots & \dots & \dots \\ V_{n,1} & \dots & V_{n,n} \end{bmatrix}^T \dots (1)$$

The matrix is formerly rotten via singular value decomposition into: word path matrix involving in the left singular vectors, the document vector matrix involving in the right singular vectors and the diagonal matrix involving of singular values [117].

The following steps show how SVD applied on a matrix A: [117]

$$A = \begin{bmatrix} 3 & 1 & 1 \\ -1 & 3 & 1 \end{bmatrix} \rightarrow A^T = \begin{bmatrix} 3 & -1 \\ 1 & 3 \\ 1 & 1 \end{bmatrix}$$

$$AA^T = \begin{bmatrix} 3 & 1 & 1 \\ -1 & 3 & 1 \end{bmatrix} \begin{bmatrix} 3 & -1 \\ 1 & 3 \\ 1 & 1 \end{bmatrix} = \begin{bmatrix} 11 & 1 \\ 1 & 11 \end{bmatrix}$$

$$\begin{bmatrix} 11 & 1 \\ 1 & 11 \end{bmatrix} \begin{bmatrix} x_1 \\ x_2 \end{bmatrix} = \lambda \begin{bmatrix} x_1 \\ x_2 \end{bmatrix}$$

$$11x_1 + x_2 = \lambda x_1$$

$$x_1 + 11x_2 = \lambda x_2$$

$$(11-\lambda)x_1 + x_2 = 0$$

$$x_1 + (11-\lambda)x_2 = 0$$

$$\begin{vmatrix} (11-\lambda) & 1 \\ 1 & (11-\lambda) \end{vmatrix} = 0$$

$$(11-\lambda)(11-\lambda) - 1 = 0$$

$$(\lambda-10)(\lambda-12) = 0$$

$$\lambda = 10, \lambda = 12$$

$$(11-10)x_1 + x_2 = 0$$

$$x_1 = -x_2$$

$$(11-12)x_1 + x_2 = 0$$

$$x_1 = x_2$$

$$U = \begin{bmatrix} 1 & 1 \\ 1 & -1 \end{bmatrix}$$

$$U = \begin{bmatrix} \frac{1}{\sqrt{2}} & \frac{1}{\sqrt{2}} \\ \frac{1}{\sqrt{2}} & -\frac{1}{\sqrt{2}} \end{bmatrix}$$

$$A^T A = \begin{bmatrix} 3 & -1 \\ 1 & 3 \\ 1 & 1 \end{bmatrix} \begin{bmatrix} 3 & 1 & 1 \\ -1 & 3 & 1 \end{bmatrix} = \begin{bmatrix} 10 & 0 & 2 \\ 0 & 10 & 4 \\ 2 & 4 & 2 \end{bmatrix}$$

$$\begin{bmatrix} 10 & 0 & 2 \\ 0 & 10 & 4 \\ 2 & 4 & 2 \end{bmatrix} \begin{bmatrix} x_1 \\ x_2 \\ x_3 \end{bmatrix} = \lambda \begin{bmatrix} x_1 \\ x_2 \\ x_3 \end{bmatrix}$$

$$10x_1 + 2x_3 = \lambda x_1$$

$$10x_2 + 4x_3 = \lambda x_2$$

$$2x_1 + 4x_2 + 2x_3 = \lambda x_2$$

$$V = \begin{bmatrix} \frac{1}{\sqrt{6}} & \frac{2}{\sqrt{5}} & \frac{1}{\sqrt{30}} \\ \frac{2}{\sqrt{6}} & \frac{-1}{\sqrt{5}} & \frac{1}{\sqrt{30}} \\ \frac{1}{\sqrt{6}} & 0 & \frac{-5}{\sqrt{30}} \end{bmatrix}$$

$$V^T = \begin{bmatrix} \frac{1}{\sqrt{6}} & \frac{2}{\sqrt{5}} & \frac{1}{\sqrt{30}} \\ \frac{2}{\sqrt{6}} & \frac{-1}{\sqrt{5}} & 0 \\ \frac{1}{\sqrt{6}} & 0 & \frac{-5}{\sqrt{30}} \end{bmatrix}$$

$$S = \begin{bmatrix} \sqrt{12} & 0 & 0 \\ 0 & \sqrt{10} & 0 \end{bmatrix}$$

$$A = U * S * V^T$$

$$= \begin{bmatrix} \frac{1}{\sqrt{2}} & \frac{1}{\sqrt{2}} \\ \frac{1}{\sqrt{2}} & -\frac{1}{\sqrt{2}} \end{bmatrix} \begin{bmatrix} \sqrt{12} & 0 & 0 \\ 0 & \sqrt{10} & 0 \end{bmatrix} \begin{bmatrix} \frac{1}{\sqrt{6}} & \frac{2}{\sqrt{5}} & \frac{1}{\sqrt{30}} \\ \frac{2}{\sqrt{6}} & \frac{-1}{\sqrt{5}} & 0 \\ \frac{1}{\sqrt{6}} & 0 & \frac{-5}{\sqrt{30}} \end{bmatrix} = \begin{bmatrix} 3 & 1 & 1 \\ -1 & 3 & 1 \end{bmatrix}$$

Related works

The approach presented in [7] is to find the damage to the use of electronic documents over databases. The solution is by text illustration which critical stage for writing pre-treating. Text (article) is a pool of arguments, in [7] Research was recognized in numerous steps. Text assembly, Format cancelling, Data pre-processing on numerous levels, with subsection serial identification. With a stretch sequence identification. By stop words subtraction and section order documentation with stop words elimination then a judgment order identification. In [8] the paper discussed about the text mining and its preprocessing techniques, discuss the three key steps of preprocessing namely, stop words removal, stemming and TF/IDF algorithms. In [9] their methodology to use an actual Preprocessing stages to protect both galaxy then while supplies through consuming developed stemming algorithm. Stemming algorithms are castoff near alter the arguments in editions into their correct origin formula. In [10] Mining text document from a preprocessed stage is calm as relate to natural languages documents. So, preprocessing phase it is a significant process in text mining application. This paper talk about shrink the dimensionally of the words space, different procedures such as cleaning (filtering) and stemming are practical. Filtering methods eliminate those words from the regular of wholly words, which do not offer related evidence; stop word filtering is a typical filtering manner.

Proposal of Preprocessing and reduction techniques

• Module1: Preprocessing

The proposed system selects a domain from Reuters 21578 datasets. collect whole documents from datasets by using Body based feature: All body-based features existing in the body of Reuter's document that includes: (body-keyword), (<body >), (body-java script), and etc. after these body the content of document begin, each body document in datasets was represented using the bag-of-words approach, also these representation known as Vector space model (VSM): it includes the words as column and the documents as rows in VSM matrix. The proposed system tokenize

the file content into individual word as shows in the Figure 1, then removed stop words. In order reduces the dimensionality of TF-IDF matrix (VSM representation). In the stop words removal function the proposal system use the classic method which it is traditional and simple method based on removing stop words by compared the words of the text with in the words store in list so if there are any match the word is remove from text, then the proposed system apply porter stemming algorithm with enhancement on its rules, at each step, a certain suffix is deleted by uses of set rules to decrease amount of verses, to must accurately similar stems, and to protect recollection space and period. The proposed system used Porters algorithm and table look up approach by having two dictionaries, one for various irregular English words, and another for various suffixes. To applied the following:

Root = past simple or past participle.

Suffixed = root + suffix.

As the result of preprocessing phase which it produce the TF-IDF matrix with hug dimension, so the second phase is dimensionality reduction techniques by using SVD.

• Module2 :Dimensionality Reduction Techniques using SVD

The proposed system decomposition the Term Frequency-Inverse Document Frequency matrix (TF-IDF) matrix by using Singular Value Decomposition (SVD) in to three matrixes USV^T , then find k greatest chief scopes (through the top singular values in S matrix) is nominated.completely additional features stay absent. The summary matrix perfectly denotes the significant and dependable patterns underlying the data in TF-IDF matrix. The proposed system dropping the rank of the TF-IDF matrix is incomes of eliminating unimportant info or clatter from the datasets it embodies.

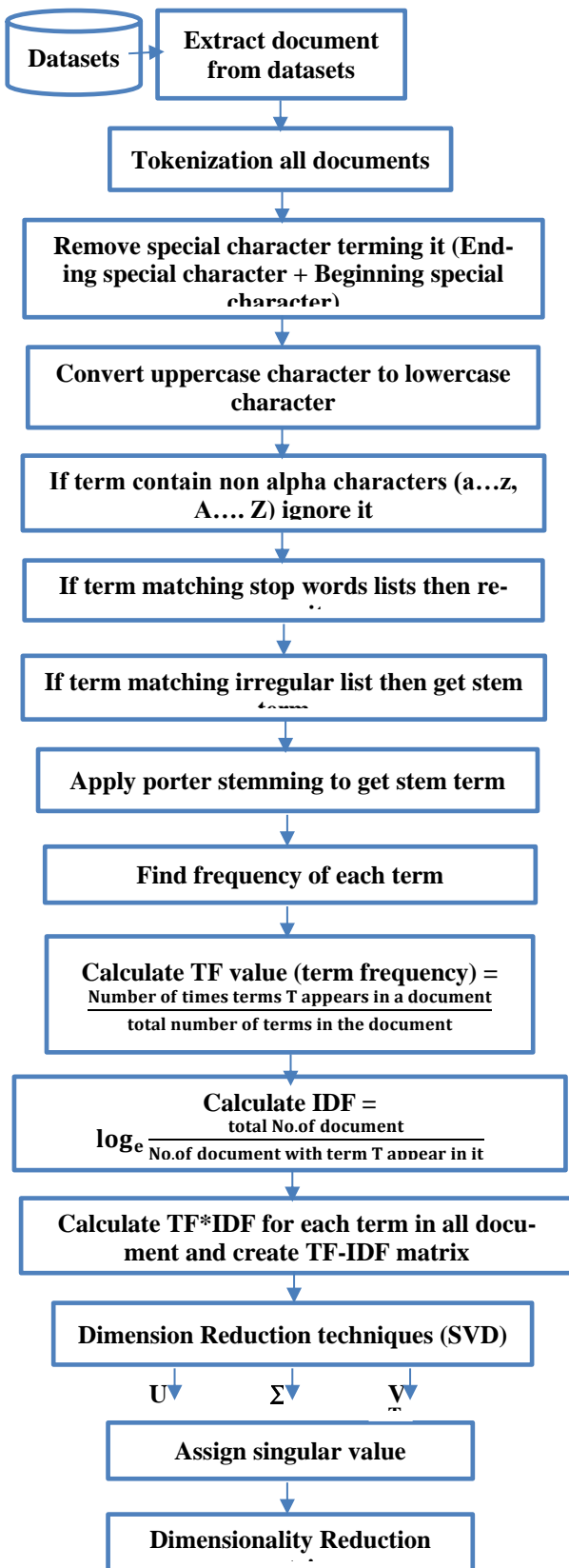


Figure 1: The system Architecture

The proposed system is summarized using the following algorithm:

Algorithm 1: Best approximate vector space model algorithm

Input: The documents datasets

Step1: Input datasets, a document by term matrix is created using only term counts. The proposed system set the following:

- The stop words list and the ignore characters are specified.
- The short words are also declared (the proposed system propose to exclude words less than 4 characters).
- Apply porter stemming enhancement and finally, create TF*IDF matrix.

Step 2: Execute the Singular value decomposing on the TF-IDF matrix to get matrix Σ , the right matrix V^T , and matrix U.

Step 3: Select the K-th rank approximation through save the chief k singular values from matrix Σ and set the residual singular values to null, The proposed system propose to investigate different k values around $k > 30$.

Step 4: Choice the top k'th from matrix VT: set V_k^T equal to the first k rows of V^T (TF - IDF_{k+n}) matrix.

Step 5: Select only the top k singular values: set Σ_k equal to the first k rows and columns of Σ , (TF - IDF_{k+k}) matrix, corresponding to the selected k singular values of TF-IDF matrix.

Step 6: Select only the top k left singular vectors: set U_k equal to the first k columns of U (TF - IDF_{m+k}) matrix.

Step 7: proposed system computed low- rank approximation is then $TF - IDF_k = U_k * \Sigma_k * V_k^T$

Step 8: If k ranges the required number then end the process; else, addition k value by one, go to Step 4. **End.**

The Experimental Results

The proposed system presents the experimental results. The stop words list is specified as: {a, an, the, all, am, able, and, after, also, anybody, among, yet, yes..... ect}. The ignore non alpha characters list is: {~, ` , !, @, \$, %, , &, *, (,), -, _, +, =, ,, {, }, [,], |, \, /, :, ;, 0,1,2,3,4,5,6,7,8,9}. All words that are less than 4 characters in lengths are ignored. The results are shown by applied tokenization with vectors (with pre-processing) on given input documents. The results created by testing the proposed system on

925 input documents, and whole number of tokens made in all effort documents after treating are (13195). Lacking tokenization treating to huge number of tokens, which is hard to supply, and time expended in complete tokenization procedure is right relative to show degree of an information retrieval system, as it acutely moves the indexing and storing features. The proposed system extraction the documents from Reuters 21578 datasets as shown Table 1, and finally the proposal system calculates TF-IDF value for each term in datasets, a small example from huge TF-IDF matrix shown in Table 2.

Table 1: Datasets Extraction

<u>Do. Id</u>	<u>Document contents</u>
1	Showers continued throughout the week in behind coca zone alleviating drought since early January improving prospects coming tempora
2	Standard oil co and bp north America said they plan form venture manage borrowing investment activities both companies north
3	Texa commerce Bancshares incs texa commerce bank Houston said filed application with comptroller currency
4	Bankamerice corp is not under pressure quickly proposed equity offering would well delay because stocks recent poor
5	The u. s. agriculture department reported farmer-owned reserve national five day average price through February follows dlrs/ bu
6	Argentine grain board figures show crop registrations grains oilseeds their products February thousands tonnes showing
7	Lion inns limited partnership said filed registration statement with securities exchange commission covering proposed

The role of the preprocessing is to prepare the datasets as shown in table1 for next proposed system stage. This is basically to reduce the noise from the dataset and keep only the desired information represent by document body.

Table 2: Sample of TF-IDF value calculation

<u>Term</u>	<u>TF val- ue</u>	<u>IDF val- ue</u>	<u>TF-IDF value</u>
week	0.0108	4.3027	0.0464
behia	0.0144	8.0163	0.1153

cocoa	0.0216	7.3232	0.1581
come	0.0072	6.9177	0.0498
tempora	0.0072	8.0163	0.0577
have	0.0072	3.7536	0.0270
commissari	0.0180	8.0163	0.1442
said	0.0180	1.7174	0.0309
Period	0.0072	5.9369	0.0427
year	0.0072	2.9226	0.0210
arrive	0.0072	8.0163	0.0577
februari	0.0108	4.8383	0.0522
bag	0.0180	6.9177	0.1244
kilo	0.0072	6.9177	0.0498
total	0.0108	4.7582	0.0513
against	0.0108	5.1831	0.0559
consign	0.0072	8.0163	0.0577
still	0.0108	6.4069	0.0691
crop	0.0180	6.6300	0.1192
export	0.0072	4.3528	0.0313
dlr	0.0504	2.5191	0.1269
port	0.0108	6.4069	0.0691
open	0.0072	6.2246	0.0448
north	0.0476	6.6300	0.3157

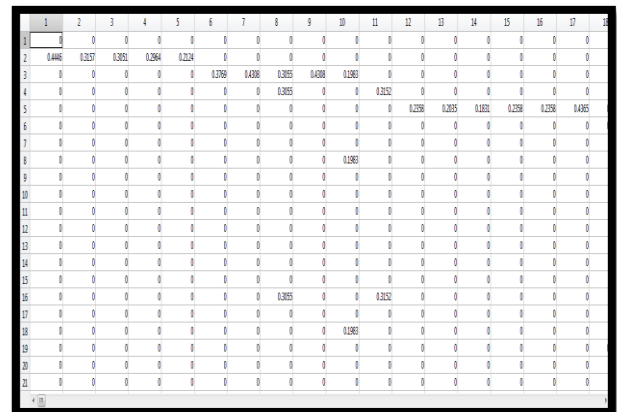


Figure 2: sample of TF-IDF matrix

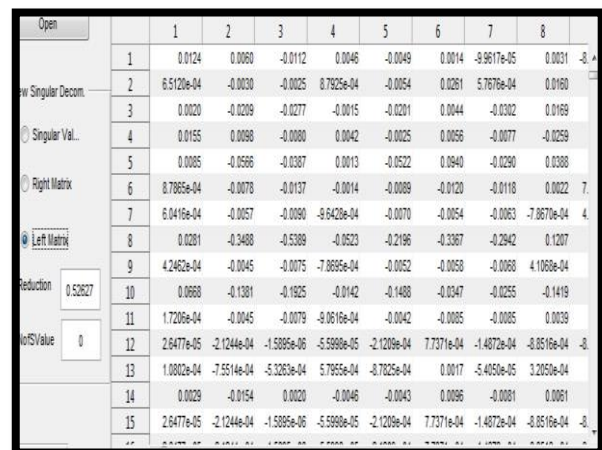


Figure 3: sample of left matrix U after applying SVD (TF-IDF matrix)

The first sample of calculate TF-IDF value, these coefficients give the best energy to reconstruct the original TF-IDF value as shows in table 2. In the proposed system, by testing the TF-IDF value it is found that the best value it have large number of TF-IDF coefficients to represent the subword as feature vector. In order to get these features and passed it to next stage in proposed system.

Figures 2 and 3 show the sample matrix of TF-IDF matrix in the proposed system and Figure 4,5,6,7 explain the procedure of the proposed system through applying r-rank SVD.

Figure 6: Final dimension reduction matrix ($U_K \Sigma_K V_K^T$) after input threshold value = 0.52627

Figure 4: Sample of Right matrix V^T after applying SVD (TF-IDF matrix)

Figure 5: Sample of singular value matrix Σ after applying SVD (TF-IDF matrix)

Results Discussion

The results obtained from applying the proposed algorithms and the effect of the proposed algorithm of the system are presented in tables. The test setup and the experimental results obtained for the preprocessing the datasets to obtain features represented by TF-IDF value. The proposed system is implemented in Visual Studio 2013 programming languages.

The experiments were performed on an Intel Core i7, 64 bit Operating System, 2.50 GHz processor and 6GB RAM. In order to evaluate the proposed system, number of metrics is obtained by applying singular value decomposition.

The results of applying the proposed system are shown in Figure 7. The proposed preprocessing algorithm is applied for document sets from the Reuters 21578 datasets.

Figure 7: The proposed system

Conclusions

The proposed system introduces an enhancement to the pre-processing information retrieval system by using an existing open source Reuters 21578 datasets; this step affects the outcomes of any IR system. The lack of standard porter stemming algorithm and preprocessing steps such as, stop-word removal and stemming also motivates us to bring out these instruments.

The proposed system GUI has many options including reading dataset files, display output in tables, and produce statistics about preprocessing steps. And it is careful as a chief step through a Standard English language preprocessing systems and then applies low-rank SVD, Singular Value Decomposition (SVD) is a dimensionality technique that can be used to create lower-dimensional embedding from a full term-document matrix. The compared of porter algorithm enhancement in the proposed system with the popular porter stemming algorithms that failed with 22 English words and we understood that the proposed enhanced stemming algorithm output the best result that consider English words, this also should be regarded as a standard feature for any upcoming English stemming algorithm.

References

- [1] H. Froud, A. Lachkar and S. A. Ouatik, "Arabic text summarization based on latent semantic analysis to enhance arabic documents clustering," *Journal of university sidi mohamed ben abdellah, Morocco*, 2012.
- [2] N. S. Pathak, P. P. Rajurkar and A. G. Bhor, "effective approach towards exporter IR system through comparison of various preprocessing techniques," *International conference on advances in engineering science and management*, vol.8, 2015.
- [3] N. A. Samat, M. A. Azmi and M. T. Abdullah, "Malay documents clustering algorithm based on singular value decomposition," *Faculty of computer science and information technology, university of Putra Malaysia*, vol.3, 2016.
- [4] M. W. Berry, Z. Drma and E. R. Jessuo, "Matrices vector spaces and information retrieval," *website www.amazon.com*, 2012.
- [5] S. Lappin and C. Fox, "Vector space models of lexical meaning," *Stephen clark university of cambridge computer laboratory*, vol.25th, 2014.
- [6] S. Shama and L. Padmalatha, "Performance comarison of image fusion using singular value decomposition," *International journal of innovative research in science, Engineering and technology*, vol.4, no.9, 2015.
- [7] D. Munkova, M. Munk and M. Vozar, "Data pre processing evaluation for text mining: Transaction/Sequence Model," *international conference on computational Science*, 2013.
- [8] S. Vijayarani and J. Ilamathi, "Preprocessing Techniques for text mining an overview," *International journal of computer science and communication networks*, vol.5, 2015.
- [9] C. Ramasubramanian, R. Ramya and V. Tamilnadu, "Effective preprocessing activities in text mining using improved porters stemming algorithm," *international journal of adanced research in computer and communication engineering*, vol.2, no.12, 2013.
- [10] N. P. Katariya, S. Chaudhari and N. P. Katariya, "Text preprocessing for text mining using side information," *international journal of computer science and mobile application*, vol.3, no.1, 2015.

Research Article

Hybrid Lossless Image Compression Using Wavelet Transform and Hierarchical non Linear Prediction

Rana T. Al-Timimi

Department of Banking and Financial Sciences, College of Management and economic,
Mustansiriyah University, IRAQ.

*Email: altemimi2016@yahoo.com.

Article Info

Received
04/09/2016

Accepted
21/12/2016

Abstract

This paper introduces a promising hybrid lossless image compression method by combining the wavelet transform along with a hierarchal non-linear polynomial approximation model to compress natural and medical images.

The test results showed good performance in which the compression ratio is improved about three times or more on average in compered with the results of a non-linear coding system that does not adopt the techniques used in this research.

Keywords: Wavelet Transform, Non-linear Polynomial..

الخلاصة

في هذا البحث تم تقديم طريقة هجينة واعدة جمعت بين طريقة التحويل المويجي و طريقة التنبوء الهرمي اللالخطي متعدد الحدود لضغط الصور الاعتيادية والطبية بدون خسارة. اظهرت النتائج اداء جيد حيث تم تحقيق نسبة ضغط بما يعادل 3 مرات او اكثر كمعدل مقارنة مع نتائج نظام التشفير اللاخطي والذي لايتبنى فكرة الدمج بين الطرق المقترحة في هذا البحث.

Introduction

Image compression is very important in the present world for efficient archiving and transmission. Lossless image compression is characterized by preserving image quality; where the image can be reconstructed exactly as the original image with error free [1]. Unfortunately, there is a limitation in the compression performance (i. e., small compression ratio from 2 to 10) because of exploiting the statistical redundancy only (i. e., exploits the coding redundancy and/or inter pixel redundancy) [2] [3] [4].

The performance of a lossless compression system can be improved either by combining different techniques such as wavelet and prediction or by exploiting a technique that selects significant blocks and exclude others [5] [6] [7].

Recently, many researchers, such as [8] [9] [10] [11] [12], focused on using the Discrete Wavelet Transforms (DWT) in image compression. In contrast to the discrete cosine transform (DCT); the advantage of DWT is that; it does not require the image to be divided into blocks, but it analyses the image as whole.

In one-dimensional wavelet transform (1D) the image is decomposed into high and low sub-images, more details about 1D transform can be listed in [13], while in two dimensions (2D) DWT, the decomposition is achieved by applying (1D) transform in horizontal and vertical directions; so this will result into four sub bands images; low sub band image (LL), high sub band image (HL), low sub band image (LH), and high sub band image (HH). This process can be repeated with the (LL) image several times. Generally, the approximation sub band (LL) considered the most significantly important part since it contains all image information, while other sub bands considered to be less significant, since they contain very small image information and they can be set to zero without significantly changing the image [13].

In this paper, an efficient, simple and fast hybrid lossless method was suggested to compress images; based on exploiting a two dimensional wavelet transform along with polynomial representation of non-linear base which utilized hierarchically in order to maximize the compression ratio.

Materials and Methodologies

The main taken concerns in the suggested hybrid system are:

First, the polynomial coding of non-linear approximation model is exploited to compress image efficiently using six coefficients ($a_0, a_1, a_2, a_3, a_4, a_5$) [14].

Second, the hierarchal scheme was adopted to improve the compression ratio and preserve image quality [15]. The Hierarchical technique worked reversely from subsequent layers to construct up layers, this means, the coefficients ($a_{00}, a_{01}, a_{02}, a_{03}, a_{04}, a_{05}$) of layer2 are used to construct layer1 coefficient ($a^{\hat{0}}$); then layer1 coefficients ($a^{\hat{0}}, a_1, a_2, a_3, a_4, a_5$) are used to reconstruct the approximated image LL.

The following steps illustrate the system implantation in more details. Figure (1) shows the basic steps clearly:

The following steps were adopted in this study:

- 1- Input grayscale image (I) of size $N \times N$.
- 2- Apply the wavelet transform which is characterized by simplicity and high compression ratio. The transform based on decomposing image (I) into four quadrants sub band namely (LL and detail sub bands LH, HL and HH) each of size $(N/2 \times N/2)$.
- 3- For the approximation sub band (LL), the polynomial prediction of non-linear based model is utilized hierarchically to remove the redundancy embedded within image pixel values, using the following steps:
 - a- Construct layer1 of hierarchal representation, first partition the approximation sub band (LL), (LL considered here as the original image), into non overlapped blocks of fixed size $n \times n$. Then, the polynomial coefficients a_0, a_1, a_2, a_3, a_4 and a_5 was calculated using the following equations [14]:

$$a_1 = \frac{\sum_{i=0}^{n-1} \sum_{j=0}^{n-1} I(i, j) \times (j - x_c)}{\sum_{i=0}^{n-1} \sum_{j=0}^{n-1} (j - x_c)^2} \quad (1)$$

$$a_2 = \frac{\sum_{i=0}^{n-1} \sum_{j=0}^{n-1} I(i, j) \times (i - y_c)}{\sum_{i=0}^{n-1} \sum_{j=0}^{n-1} (i - y_c)^2} \quad (2)$$

$$a_5 = \frac{\sum_{i=0}^{n-1} \sum_{j=0}^{n-1} I(i, j)(j - x_c)(i - y_c)}{\sum_{i=0}^{n-1} \sum_{j=0}^{n-1} (j - x_c)^2 (i - y_c)^2} \quad (3)$$

Where a_1, a_2 and a_5 coefficients corresponds to the ratio of sum pixel multiplied by the distance from the center divided by the squared distance in i, j .

$$x_c = y_c = \frac{n - 1}{2} \quad (4)$$

Where $(j-x_c)$ and $(i-y_c)$ measure the distance from a pixel coordinates to the block center (x_c, y_c) .

Other coefficients, namely the a_0, a_3 and a_4 can be founded by applying the Crammers rule, where:

$$a_0 = \frac{\begin{vmatrix} V_1 & W_2 & W_2 \\ V_2 & W_3 & W_4 \\ V_3 & W_4 & W_3 \end{vmatrix}}{\begin{vmatrix} W_1 & W_2 & W_2 \\ W_2 & W_3 & W_4 \\ W_2 & W_4 & W_3 \end{vmatrix}} \quad (5)$$

$$a_3 = \frac{\begin{vmatrix} W_1 & V_1 & W_2 \\ W_2 & V_2 & W_4 \\ W_2 & V_3 & W_3 \end{vmatrix}}{\begin{vmatrix} W_1 & W_2 & W_2 \\ W_2 & W_3 & W_4 \\ W_2 & W_4 & W_3 \end{vmatrix}} \quad (6)$$

$$a_4 = \frac{\begin{vmatrix} W_1 & W_2 & V_1 \\ W_2 & W_3 & V_2 \\ W_2 & W_4 & V_3 \end{vmatrix}}{\begin{vmatrix} W_1 & W_2 & W_2 \\ W_2 & W_3 & W_4 \\ W_2 & W_4 & W_3 \end{vmatrix}} \quad (7)$$

Where:

$$V_1 = a_0 W_1 + a_3 W_2 + a_4 W_2 \quad (8)$$

$$V_2 = a_0 W_2 + a_3 W_3 + a_4 W_4 \quad (9)$$

$$V_3 = a_0 W_2 + a_3 W_4 + a_4 W_3 \quad (10)$$

$$W_1 = n \times n \quad (11)$$

$$W_2 = \sum_{j=0}^{n-1} (j - x_c)^2 = \sum_{i=0}^{n-1} (i - y_c)^2 \quad (12)$$

$$W_3 = \sum_{j=0}^{n-1} (j - x_c)^4 = \sum_{i=0}^{n-1} (i - y_c)^4 \quad (13)$$

$$W_4 = \sum_{i=0}^{n-1} \sum_{j=0}^{n-1} (j-xc)^2 (i-yc)^2 \quad (14)$$

4- Construct layer 2 of the hierarchal representation from layer1 a_0 coefficient. The non-linear polynomial coding technique will be utilized again in this layer using Equations (1-14) to construct coefficients $a_{00}, a_{01}, a_{02}, a_{03}, a_{04}$ and a_{05} (in this layer a_0 coefficient from layer1 will be considered here as original image).

5- For Layer 2:

a- Determine the deterministic part (function formula) $a\tilde{0}$.

$$a\tilde{0} = a_{00}W_1 + a_{01}(j-xc) + a_{02}(i-yc) + a_{03}(j-xc)^2 + a_{04}(i-yc)^2 + a_{05}(j-xc).(i-yc)$$

b- Find residual image using the following equation [16]:

$$a0 \text{ Re } sd = a0 - a\tilde{0}$$

c- Build the modeled approximated $a\hat{0}$

$$a\hat{0} = a\tilde{0} + a0 \text{ Re } sd$$

6- Reconstruct layer1 from layer2 hierarchically as follows:

a- Determine the deterministic part $L\tilde{L}$.

$$L\tilde{L} = \hat{a}0W_1 + a1(j-xc) + a2(i-yc) + a3(j-xc)^2 + a4(i-yc)^2 + a5(j-xc).(i-yc)$$

b- Find the error (residual)

$$LL \text{ Re } sd = L - L\tilde{L}$$

7- Use Run Length and LZW and Huffman coding techniques to encode:

a- Layer 2 information of coefficients ($a_{00}, a_{01}, a_{02}, a_{03}, a_{04},$ and a_{05}) and the error ($a0Resd$) along with the layer1 information of coefficients (a_1, a_2, a_3, a_4, a_5) and the error ($LLResd$).

b- The sub bands LH, HL and HH.

8- Reconstruct the compressed image (that identical to the original one I) using the following steps:

a- For the approximation sub band LL, the residual along with the coefficients used to rebuild the LL quadrant

$$LL = L\tilde{L} + LL \text{ Re } sd$$

b- Apply the inverse wavelet transform to reconstruct image I.

Results and Discussion

To evaluate the performance of the suggested hybrid method; two sets of image natural and medical were tested (as illustrated in Figure 2) all images in size of 256×256 . Figure 3 shows the reconstructed image after the compression process.

In this paper, the compression ratio was adopted as a guide to the performance of the suggested system; because in lossless image compression system there is no degradation needed to be evaluated; i. e., the compressed image will be identical to the original one.

Table 1, summarizes the results of the suggested method; it shows the size of the compressed information and the compression ratio against the utilized block sizes for the tested images.

Table 2, illustrates the results obtained from a non-linear compression system without using the suggested techniques in this paper; these results are used to illustrate the effectiveness of the suggested method.

The results show the high compression ratio is achieved for a lossless compression system characterizes this technique compared to other technique, in which the compression ratio is improved about three times or more on average.

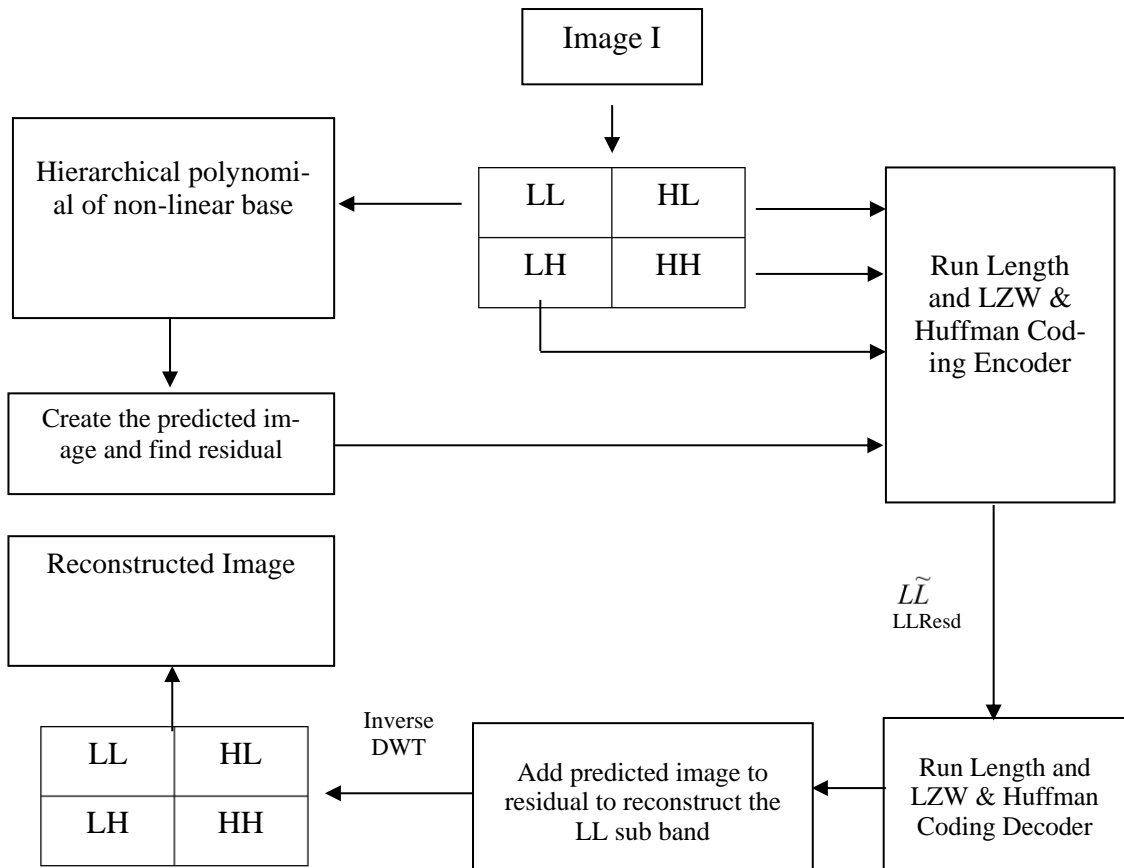


Figure 1: The suggested Compression System Structure.



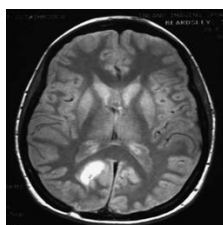
(a) Camera



(b) Pepper



(c) Rose



(d) MR



(e) Brain



(f) Knee

Figure 2: The Tested Grayscale Images.

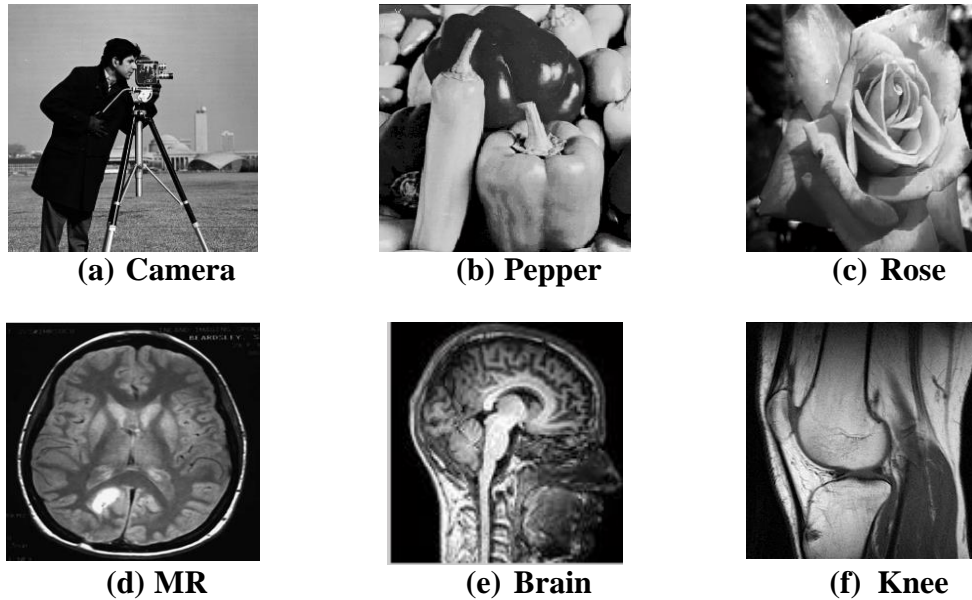


Figure 3: The Reconstructed Images using block size of 8*8.

Table 1: Performance of the Suggested Method.

Test im- age	Size of original image (in bytes)	Block size of 4		Block size of 8	
		Size of com- pressed image (in bytes)	Compression Ra- tio	Size of com- pressed image (in bytes)	Compression Ratio
Camera	65536	1400	46.8114	1388	47.2161
Pepper	65536	1216	53.8947	1204	54.4319
Rose	65536	932	70.3176	920	71.2348
Mr	65536	988	66.3320	976	67.1475
Brain	65536	1126	58.2025	1116	58.7240
knee	65536	1084	60.4576	1072	61.1343

Table 2: The Performance of non linear prediction compression system.

Test im- age	original image size (in bytes)	Block size of 4		Block size of 8	
		Size of com- pressed image (in bytes)	Compression Ra- tio	Size of com- pressed image (in bytes)	Compression Ratio
Camera	65536	12470	5.2555	8320	7.8769
Pepper	65536	12852	5.0993	8533	7.6803
Rose	65536	12251	5.3494	7512	8.7242
Mr	65536	11764	5.5709	7981	8.2115
Brain	65536	12482	5.2504	8659	7.5685
knee	65536	12672	5.1717	6989	9.3770

Conclusions

The results in this paper are promising in terms of the higher compression gain achieved compared to the current standard technique. The compression ratio is affected by two factors; *the first one is the image nature*, natural images contain more details than the medical one, which implicitly means; decreasing in the compression rate compared to the medical. The *block size of the approximation sub band LL was the second factor*; whereas the block size gets bigger, less coefficient are needed (i. e., 6 coefficients for larger block sizes); and this will implicitly improve the compression ratio. On the other hand; exploiting the wavelet transform along with a hierarchical polynomial approximation of non-linear base effectively improved the compression ratio about three times or more on average.

References

- [1] Gonzalez, R. C. and Woods, R. E., Digital Image Processing, 2nd edn. ed., Prentice Hall, 2003.
- [2] Jones, G. A. and Jones, J. M., Information and Coding Theory, London: Springer, 2000.
- [3] M. Baer, "A General Framework for Codes Involving Redundancy Minimization," *IEEE Transactions on Information Theory*, vol.52, p.344–349, 2006.
- [4] Ghadah Al-Kafagi, Hazeem Al-K., "Medical Image Compression using Wavelet Quadrants of Polynomial Prediction Coding & Bit Plane Slicing," *Medical Image Compression*, vol.4, no.6, 2014.
- [5] Ghadah, Al-Kafagi. and Haider, Al-M., " Lossless Compression of Medical Images using Multiresolution Polynomial Approximation Model," *International Journal of Computer Applications*, vol.76, no.3, pp.38-42, 2013.
- [6] A. -K. Ghadah, "Wavelet Transform and Polynomial Approximation Model for Lossless Medical Image Compression," *International Journal of Advanced Research Computer Science and Software Engineering*, vol.4, no.3, pp.584-587, 2014.
- [7] Ghadah, Al-Kafagi. and George, L. E., "Fast Lossless Compression of Medical Images based on Polynomial," *International Journal of Computer Applications*, vol.70, no.15, pp.28-32, 2013.
- [8] George, L. E. and Sultan B., "Image Compression Based on Wavelet, Polynomial and Quadtree," *Journal of Applied Computer Science & Mathematics*, vol.11, no.5, pp.15-20, 2011.
- [9] Ghadah Al-Kafagi, Salah Al-I, Maha Abd R., " A Hybrid Lossy Image Compression based on Wavelet Transform, Polynomial Approximation Model, Bit Plane Slicing and Absolute Moment Block Truncation," *International Journal of Computer Science and Mobile Computing IJCSMC*, vol.4, no.6, pp.954-961, 2015.
- [10] V. Yap, "Wavelet-Based Image Compression For Mobile Applications," Doctor of Philosophy thesis, Middlesex University, 2005.
- [11] F. G. M., "Color Image Compression Based on DWT. ," PhD thesis of Philosophy in Astronomy Science, University of Baghdad, 2006.
- [12] Tasi, M. and Hung H., "DCT and DWT based Image Watermarking using Sub sampling," in *Fourth Int.2005 IEEE Conf. on Machine Learning and Cybernetics*, China, 2005.
- [13] Yap, V. V., Comley, R. A., "A Segmentation-based Wavelet Compression Scheme for Still Images," in *IASTED International Conference on Signal and Image Processing (SIP2004)*, Honolulu, 2004.
- [14] George, L. E, Ghadah, Al-K., "Image Compression based on Non-Linear Polynomial Prediction Model," *International Journal of Computer Science and Mobile Computing (IJCSMC)*, vol.4, no.8, pp.91-97, 2015.
- [15] Rasha Al-T., Ghadah Al-Kafagi, "Image Compression Using Hierarchical Linear Polynomial Coding," *International Journal of Computer Science and Mobile Computing (IJCSMC)*, vol.4, no.1, p.112 – 119, 2015.
- [16] G. Al-Kafagi, "Hierarchical Autoregressive for Image Compression," *Journal of College of Education for Pure Sciences*, vol.4, no.1, pp.236-241, 2014.

Research Article

Encryption of Stereo Images after Compression by Advanced Encryption Standard (AES)

Marwah K. Hussien, Alyaa J. Jalil

Department of Information Systems, College of Computer Sciences and Information Technology,
University of Basrah, IRAQ

*Correspondent Author Email: Lava85K@gmail.com, aliaa.jaber@yahoo.com

Article Info

Received
06/09/2016

Accepted
17/04/2017

Abstract

New partial encryption schemes are proposed, in which a secure encryption algorithm is used to encrypt only part of the compressed data. Partial encryption applied after application of image compression algorithm. Only 0.0244%-25% of the original data is encrypted for two pairs of different grayscale images with the size (256 × 256) pixels. As a result, we see a significant reduction of time in the stage of encryption and decryption.

In the compression step, the Orthogonal Search Algorithm (OSA) for motion estimation (the different between stereo images) is used. The resulting disparity vector and the remaining image were compressed by Discrete Cosine Transform (DCT), Quantization and arithmetic encoding. The image compressed was encrypted by Advanced Encryption Standard (AES). The images were then decoded and were compared with the original images.

Experimental results showed good results in terms of Peak Signal-to-Noise Ratio (PSNR), Compression Ratio (CR) and processing time. The proposed partial encryption schemes are fast, secure and do not reduce the compression performance of the underlying selected compression methods.

Keywords: Stereoimaging, Stereoimage compression, Image encryption, cryptography.

الخلاصة

تم اقتراح طرق جديدة للتشفير الجزئي، والذي يستخدم خوارزمية التشفير آمنة لتشفير فقط جزء من البيانات المضغوطة. وشفر يحدود (0.0244%-25%) من البيانات الأصلية لزوجين من الصور الرمادية المختلفة بأبعاد (256*256) عنصر صورة للحصول على تقليل مهم في زمن التشفير وفك الشفرة. استخدمت في مرحلة الضغط خوارزمية البحث المتعامد (OSA) لتقدير الحركة (الفرق بين الصورتين). متجه الحركة الناتج والجزء المتبقي تتم عملية ضغطه بالتحويل الجيبي المنقطع، التكميم الرقمي والترميز الحسابي. ثم تشفر بعد ذلك الصورة المضغوطة باستخدام طرق تشفير متقدمة مثلًا لتشفير القياسي المتقدم (AES) والصور المشفرة يعاد استرجاعها ثم فك ضغطها واسترجاعها و تقارن مع الصور الأصلية. أنظمة التشفير الجزئي المقترحة كانت سريعة وذات سرية عالية كما ان انجازية الضغط لا تقل ضمن طرق الضغط المختارة. النتائج التجريبية بينت نتائج جيدة عند حساب نسبة قمة الإشارة إلى الضوضاء (PSNR) ونسبة الضغط (CR) ووقت المعالجة.

Introduction

As a result of the increase in the use of images in recent years, it must be to have to deal with it (move) safely through the so-called pressure and encryption. For this, the researchers combined compression and encryption together to reduce the overall processing time.

In this research, has been selected a pair of stereo images which are very similar to each other are taken from two different angles (and this is why the pressure of each of the images independently, which means in the efficiency of the stereo im-

age compression). We can get the sequence of these images by film cameras or generated by demand sequentially. compress these pictures is the foundation necessary to reduce this data through the difference between the two images Account (matching), also known as disparity estimation, then squeeze one image independently. This is known as image as a reference, and can either is the right image or the left image, then use the reference image and vector disparity to rebuild the second image [2]. Figure 1 shows flowchart of encryption a pair of stereo image-

safter compressed.

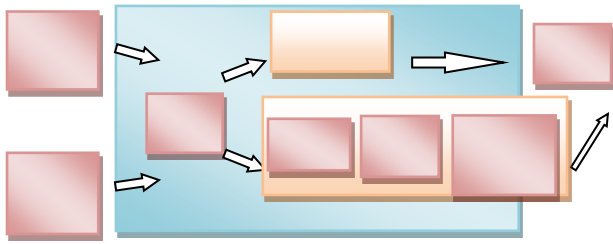


Figure 1: Encryption a pair of stereo images after Compressed.

The work aims to propose an efficient technique for stereo images compression by estimated the disparity vectors between them (The left and right image) using Orthogonal Search Algorithm (OSA). The remaining image is transformed using Discrete Cosine Transform (DCT). The resulting image is quantized using the scalar quantization and then compressed using arithmetic coding; we show that in Section 2. The two images are very similar to each other; disparity vectors between the two images are estimated. The resulting disparity vector and image compressed are encryption by Advanced Encryption Standard (AES), We show that in Section 3. Section 4 gives the experimental results. Finally, the paper has been concluded in Section 5.

Motion Estimation

Motion Estimation (ME) is the process of analyzing successive frames in any image sequence to identify objects motion. In this paper, motion estimation used to process of analyzing two stereo images by using OSA.

The motion of an object is usually described by a two-dimensional motion vector, which is the placement of the co-ordinate of the best similar block in previous frame for the block in current frame. This placement is represented by the length and direction of motion [3] [4].

Disparity Estimation Using Orthogonal Search Algorithm (OSA)

OSA was introduced by Puri. It has a vertical stage followed by a horizontal stage for the search for the optimal block. The algorithm may be described as follows:

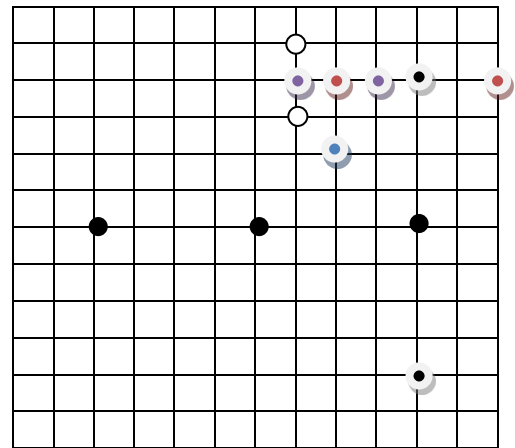
Step1- Pick a step size (usually half the maximum displacement in the search window). Take two points at a distance of step size in the horizontal direction from the center of the search window and locate (among these) the point of

minimum distortion. Move the center to this point.

Step 2- Take two points at a distance step size from the center in the vertical direction and find the point with the minimum distortion.

Step 3- Halve the step size, if it is greater than one, else halt.

A particular path for the convergence of the algorithm may be shown in the following Figure 2 [5]:



- Points for first stage
- Second stage points
- Third stage points
- Fourth stage points
- Fifth stage points
- Sixth stage points

Figure 2: Example of Orthogonal Search Algorithm.

Image Transform

Divide the source image into blocks and apply the transformations to the blocks [6].

Parameter quantization

Quantization is irreversible operation because of its lossy property. The data generated by the transformation are quantized to reduce the amount of information. This step represents the information within the new domain by reducing the amount of data [7] [8].

Arithmetic Encoding

Arithmetic encoding and its derivative technique, Q-coding, is used to overcome some of the limitations of Huffman codes. It is a non-block code, in that a single code word is used to represent an entire sequence of input symbols, in contrast to Huffman coding where a source symbol block corresponds to a code word block. Instead, it uses the real numbers to represent a sequence of symbols by recursively subdividing the interval

between 0 and 1 to specify each successive symbol. The limitation of this technique is the precision required in performing the calculations and arriving at the code word which will represent the entire sequence correctly [9].

Partial Encryption

Partial encryption (also called *selective encryption* or *soft encryption*) is a secure encryption algorithm which is used to encrypt only part of the data. It is used to reduce encryption and decryption time. During our work, only part of the compressed data is encrypted. Some compression algorithms have *important parts* that provide a significant amount of information about the original data, whereas the remaining parts may not provide much information without the important parts. For simplicity, we consider all the important parts as one unit, and the remaining parts are grouped into one unimportant part. Since it is difficult to obtain information from the unimportant part alone, partial encryption approach encrypts only the important part. A significant reduction in encryption and decryption time is achieved when the relative size of the important part is small.

In some cases, partial encryption allows the important part to be encrypted while the unimportant part is transmitted in parallel so that the encryption time becomes negligible [10]. A secure encryption algorithm is used to encrypt the important part.

Advanced Encryption Standard (AES) Cipher

The AES cipher described by Rijndael (called also *Rijndael encryption algorithm*). It was chosen in 1977 by the International Institute of Technological Standards As an international standard for encryption, And on the basis development in the types of encryption that are of class as Symmetric Encryption.

This algorithm is a widely accepted in the world; it is considered a safe method of encryption, and because of the length of the encryption key [10]. Encryption algorithm blocks which supports keys lengths and lengths of multiple texts. Encryption k key is a matrix with dimensions $N_k \times 4$ (any key length is $N_k \times 4$):

$$\underline{k} = \begin{pmatrix} k_{0,0} & k_{0,1} & \cdots & k_{0,N_k-1} \\ k_{1,0} & k_{1,1} & \cdots & k_{1,N_k-1} \\ k_{2,0} & k_{2,1} & \cdots & k_{2,N_k-1} \\ k_{3,0} & k_{3,1} & \cdots & k_{3,N_k-1} \end{pmatrix}$$

Where each $k_{i,j}$ can be considered:

- 8-bit or 1 byte that any number in the group $Z_{2,8}$
- Integer in the group Z_{256}
 the key length of the AES algorithm can be $N_k = 4, 6, 8$ (128, 192, 256) bytes. Read the encryption key from the matrix be according to each column from left to right any:

$$\underline{k} = (k_{0,0}, k_{1,0}, k_{2,0}, k_{3,0}, \dots, k_{0,N_k-1}, k_{1,N_k-1}, k_{2,N_k-1}, k_{3,N_k-1})$$

Block or text that you want to encrypt x is a matrix with lengths of $N_b \times 4$ (any key length is $N_b \times 4$ bytes):

$$\underline{x} = \begin{pmatrix} x_{0,0} & x_{0,1} & \cdots & x_{0,N_b-1} \\ x_{1,0} & x_{1,1} & \cdots & x_{1,N_b-1} \\ x_{2,0} & x_{2,1} & \cdots & x_{2,N_b-1} \\ x_{3,0} & x_{3,1} & \cdots & x_{3,N_b-1} \end{pmatrix}$$

Where each $x_{i,j}$ can be considered:

- 8-bit or 1 byte that any number in the group $Z_{2,8}$
- Integer in the group Z_{256}
 Block in Raendaul algorithm can be $N_b = 4, 6, 8$ (128, 192, 256) bytes. Read the block of the matrix be according to each column from left to right any:

$$\underline{x} = (x_{0,0}, x_{1,0}, x_{2,0}, x_{3,0}, \dots, x_{0,N_b-1}, x_{1,N_b-1}, x_{2,N_b-1}, x_{3,N_b-1})$$

Status Raendall ω is the matrix:

$$\underline{\omega} = \begin{pmatrix} \omega_{0,0} & \omega_{0,1} & \cdots & \omega_{0,N_b-1} \\ \omega_{1,0} & \omega_{1,1} & \cdots & \omega_{1,N_b-1} \\ \omega_{2,0} & \omega_{2,1} & \cdots & \omega_{2,N_b-1} \\ \omega_{3,0} & \omega_{3,1} & \cdots & \omega_{3,N_b-1} \end{pmatrix}$$

Where each $\omega_{i,j}$ is an integer in the Z_{256} Raendaul is installing transfers (Transformation), The positions Raendaul These transfers called cycles (iterations) ie:

$$R I J (\underline{x}) = \underline{y} = (T_{N_r} \circ T_{N_r-1} \circ \dots \circ T_{N_1} \circ T_{N_0})$$



Each $T_i: \omega \rightarrow \omega$ is the field and is long positions Raendaul, the number of cycles (N_r respect to the key length (N_k) and the length of the text (N_b): Raendaul number (N_r) courses

First Session of T_0 is XOR between the text (the first position) and any encryption key:

$$T_0(x) = \begin{pmatrix} k_{0,0} & k_{0,1} & \dots & k_{0,N_k-1} \\ k_{1,0} & k_{1,1} & \dots & k_{1,N_k-1} \\ k_{2,0} & k_{2,1} & \dots & k_{2,N_k-1} \\ k_{3,0} & k_{3,1} & \dots & k_{3,N_k-1} \end{pmatrix} \oplus \begin{pmatrix} x_{0,0} & x_{0,1} & \dots & x_{0,N_k-1} \\ x_{1,0} & x_{1,1} & \dots & x_{1,N_k-1} \\ x_{2,0} & x_{2,1} & \dots & x_{2,N_k-1} \\ x_{3,0} & x_{3,1} & \dots & x_{3,N_k-1} \end{pmatrix}$$

Courses that come after this will mean transforming the current situation, but this algorithm are doing this in stages:

1. confused linear - Remittances are **ShiftRow** and **MixColumn**;
2. non-linear - a crossover **ByteSub**;
3. Add the key - Shunt **AddRoundKey**. So blinded show is enough to turn the transfers, namely:

$$RIJ^{-1}(\underline{y}) = \underline{x} = (T_{N_0}^{-1} \circ T_{N_1}^{-1} \circ \dots \circ T_{N_{r-1}}^{-1} \circ T_{N_r}^{-1})$$

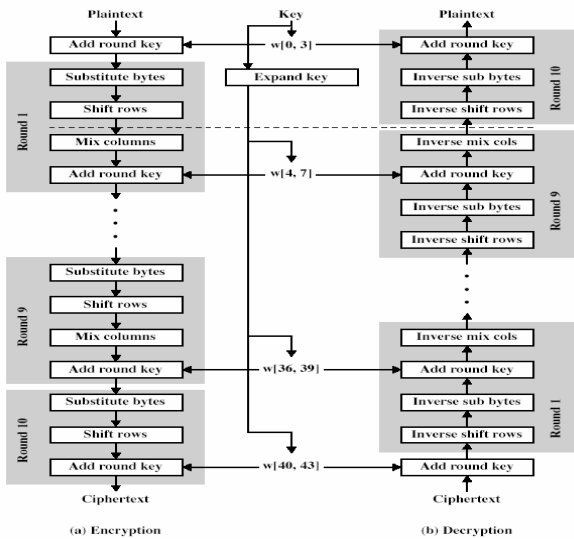


Figure 3: AES Encryption and Decryption Steps

PSNR and CR

Peak signal-to-noise ratio (PSNR) is the standard method for quantitatively comparing a compressed image with the original. For an 8-bit grayscale image, the peak signal value is 255. Hence, the PSNR of an $M \times N$ 8-bit grayscale image C_{ij} and its reconstruction R_{ij} is calculated as [11] [12]:

$$PSNR = 10 \log_{10} \frac{255^2}{MSE} \quad (1)$$

Where the Mean Square Error (MSE) is defined as [11]:

$$MSE = \frac{1}{N^2} \sum_{i=0}^{N-1} \sum_{j=0}^{N-1} [C_{ij}(m,n) - R_{ij}(m,n)]^2 \quad (2)$$

PSNR is measured in decibels (dB), M: height of the image, N: width of the image.

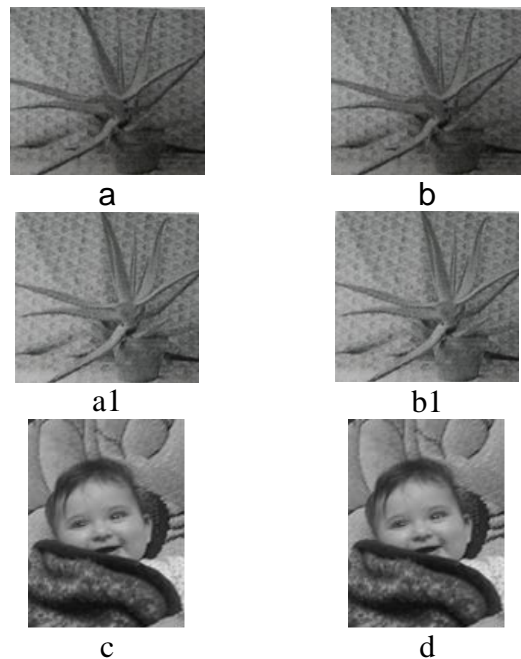
Experimental Results

This section explains the experiments which have been implemented on two stereo images, Aloe and child image from personal camera as test images, each one of them is in size of 256*256 and of JPEG format. MATLAB version 7.4.0.287 (R2012a) was used as a work environment to carry out these experiments. The decoded left and right images were compared with the original left and right images. The Mean Square Error (MSE) between the original and decoded left and right images was referred in Equation 2. The MSE of the image is the average of the MSE of the left image and the MSE of the right image.

$$MSE = (MSE_L + MSE_R) / 2 \quad (3)$$

The MSE was converted into Peak-Signal to Noise Ratio according in the Equation (1)

Results for Aloe and Child Images



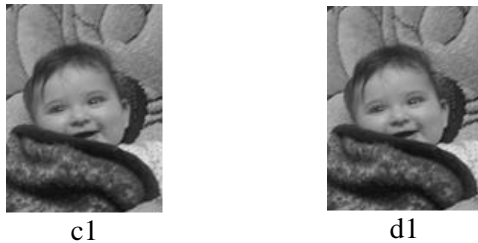


Figure 4: (a), (b), (c) and (d) Original Left and Right Images. (a1), (b1), (c1) and (d1) Reconstructed Left and Right Images.

Table1: Results for Stereo Images.

Images	PSNR (db)	CR	Time (sec)
Aloe	45.32	0.566	50.32
Child	47.45	0.6.98	59.44

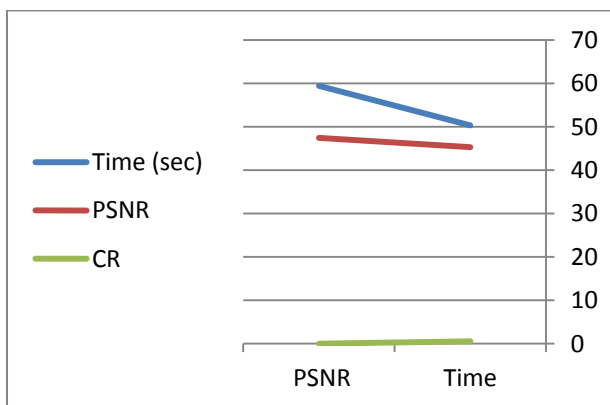


Figure 5: PSNR vs Bitrate for Stereo Images.

Conclusions

Pair stereo images in this research through phases are, DCT, quantization, arithmetic encoding and OSA was proposed in this paper with advanced encryption standard in the encryption step. The two images are very similar to each other; disparity vectors between the two images are estimated in OSA. The resulting disparity vector and image compressed are encryption by Advanced Encryption Standard (AES). Two pairs of images were encrypted after being compressed them and then reconstructed by reversing the steps followed to encrypt and compress the images.

The proposed partial encryption schemes are fast, secure and do not reduce the compression performance of the underlying compression selected methods. The proposed algorithms contain high level of security due to the size of the keyspace. A good image encryption algorithm

should be sensitive to the cipher key and PSNR which are good as shown in Table 1.

The reconstructed images were then compared with the original images.

References

- [1] Karthik A., Chandra S. and Das S. ,“3D Tool Wear Measurement and Visualization Using Stereo Imaging” in International Journal of Machine Tools and Manufacture, pp 1531-1522, 2005.
- [2] Beil W. and Carlsen I., “Surface reconstruction from stereoscopy and “shape from shading” in SEM images in Machine Vision and Applications, pp281-295, 2010.
- [3] Shi Q. and Sun H., “Image and Video Compression for Multimedia Engineering”, 2000.
- [4] Turaga D., Alkanhal M. ,” Search of Block Matching Algorithms in Motion Estimation”, International Journal of advanced Science and Technology, Vol.32, July, 2011.
- [5] Wang Y., OstermannJ. ,”Video Processing and Communications”, Prentice Hall, Upper Saddle River, 2001.
- [6] Fisch M. M., Stogner H., Uhl A., “Layered Encryption Techniques for DCT-Coded Visual Data”, In Proceedings (CD-ROM) of the European Signal Processing Conference, EUSIPCO '04, Vienna, Austria, September 2004.
- [7] SahaS. ,“Image Compression-From DCT to Wavelet: A Review”, ACM Crossroads Student Magazine, The ACM’s First Electronic Publication, 2001.
- [8] Salomon D., “Data Compression” second edition, 2002.
- [9] Watson J., “Image Compression Using Discrete Cosine Transform” Mathematic journal, 2007.
- [10] Hameed A. Y., “New Techniques for Partial Encryptionof Wavelet-based Compressed, May 2012.
- [11] Beegan A. P., “Wavelet-based Image Compression Using Human Visual System Models” M. Sc. Thesis, Electrical Engineering Department, Virginia Polytechnic

Institute and State University, Blacksburg, Virginia, May 2001.

- [12] Marwa K., “Video Compression by Wavelet Technique”, M. Sc. Thesis, *Department of Information Systems, College of Computer Sciences and Information Technology, University of Basrah, IRAQ*, April 2013.

Research Article

Comparison of Bayes Estimators for Parameter and Reliability Function for Inverse Rayleigh Distribution by Using Generalized Square Error Loss Function

Huda A. Rasheed, Raghda K. Aref

Department of Mathematics, College of Science, Mustansiriyah University, IRAQ.

*Correspondent Author Email: raghda291992@yahoo.com

Article Info

Received
18/08/2016

Accepted
13/04/2017

Abstract

In the current study, we have been derived some Bayesian estimators for the parameter and reliability function of the inverse Rayleigh distribution under Generalized squared error loss function. In order to get the best understanding of the behavior of Bayesian analysis, we consider non-informative prior for the scale parameter using Jefferys prior Information as well as informative prior density represented by Gamma distribution. Monte-Carlo simulation have been employed to compare the behavior of different estimates for the scale parameter and reliability function of inverse Rayleigh distribution based on mean squared errors and Integrated mean squared errors, respectively. In the current study, we observed that more occurrence of Bayesian estimate using Generalized squared error loss function using Gamma prior is better than other estimates for all cases.

Keywords: Inverse Rayleigh distribution, Bayesian estimator, Generalized Squared error loss Function, Jefferys prior and Gamma prior.

الخلاصة

في الدراسة الحالية، تم اشتقاق على بعض المقدرات البيزية لدالة المعولية لتوزيع معكوس رايلي تحت تعميم دالة خساره الخطأ التريبيعية. بغية الحصول على اكثر فهما للتحليل البيزي فقد افترضنا عدم وجود معلومات مسبقة عن معلمة الشكل باستخدام دالة جيفري للمعلومات كذلك وجود معلومات مسبقة متمثلة بتوزيع كاما. تم توظيف مونت-كارلو للمحاكاة لمقارنة سلوك مختلف تقديرات معلمة القياس ودالة المعولية لتوزيع معكوس رايلي على اساس متوسط مربعات الخطا ومتوسط مربعات الخطا التكاملي على التوالي. في الدراسة الحالية، لاحظنا ان اداء التقدير البيزي باستخدام تعميم دالة خساره الخطا التريبيعية باستخدام توزيع كاما اكثر دقة من التقديرات الأخرى في جميع الحالات.

Introduction

The inverse Rayleigh distribution is one of important distributions. The distribution originally derived by Voda since (1972). In (1993) Gharrafi derived five measures of location for the inverse Rayleigh distribution [1]. Soliman et al. (2010) studied the estimation and prediction from inverse Rayleigh distribution based on lower record values, Bayes estimator have been developed under squared error and zero one-loss functions [2]. In (2012) Dey discuss the Bayesian estimation of the Parameter and Reliability Function of an Inverse Rayleigh Distribution use different loss function which is Square error, LINEX loss function [3]. In (2013) Sindhu and other researchers studied the Bayes estimation of the parameters of the inverse Rayleigh distribution for left censored data under different loss functions (Symmetric and asymmetric) [4]. Also,

In (2013) Prakash discuss the Bayes estimation in the inverse Rayleigh model under two different loss functions (Square error, LINEX loss function) [5]. In (2014) Khan obtained, the Modified inverse Rayleigh distribution is special case of inverse Weibull, which is extension to it [6]. In (2015) the Fan discuss Bayes Estimation for Inverse Rayleigh model under different loss functions squared error loss, LINEX loss and entropy loss functions [7]. In (2015) Rasheed discussed the Comparison of the classical estimators with the Bayes estimators of one Parameter inverse Rayleigh distribution under generalized squared error loss function [8]. In (2016) Rasheed and Aref discussed the Bayesian approach for estimating the scale parameter of Inverse Rayleigh distribution under different loss function [9]. Finally, in (2016) Rasheed and Aref obtained Reliability estimation in inverse Rayleigh distribu-



tion using Precautionary loss function [10]. The current study will obtain some Base estimators for Reliability estimation of inverse Rayleigh distribution using generalized square error loss function.

One Parameter Inverse Rayleigh Distribution

The probability density function (pdf) of the inverse Rayleigh distribution with scale parameter θ is defined as follows [11]:

$$f(x; \theta) = \frac{2\theta}{x^3} e^{-\frac{\theta}{x^2}} \quad x > 0, \theta > 0 \quad (1)$$

The cumulative distribution function is:

$$F(x; \theta) = e^{-\frac{\theta}{x^2}}; \quad x > 0, \theta > 0 \quad (2)$$

The Reliability, failure rate and the Cumulative failure rate (Hazard Rate) functions of this distribution are given, respectively, by:

$$R(t; \theta) = 1 - F(t; \theta) = 1 - e^{-\frac{\theta}{t^2}} \quad (3)$$

$$h(t; \theta) = \frac{f(t; \theta)}{R(t; \theta)} \quad (4)$$

We can say, the function $h(t)$ is a failure function if and only if [12]

$$1. \quad h(t) \geq 0 \quad 2. \int_0^\infty h(t) dt = \infty$$

The relationship between $R(t)$ and $h(t)$ can be defined as

$$h(t) = \frac{f(t)}{R(t)} = -\frac{d}{dt} \ln R(t)$$

By integrating and using $\ln R(0) = \ln(1) = 0$, yields

$$\ln R(t) = -\int_0^t h(u) du$$

$$R(t) = \exp \left[-\int_0^t h(u) du \right]$$

$$R(t) = \exp[-H(t)]$$

$$H(t; \theta) = -\ln R(t) = -\ln \left(1 - e^{-\frac{\theta}{t^2}} \right) \quad (5)$$

Where $H(t)$ is cumulative hazard function.

Bayesian estimators under generalized square error loss function

Al-Nasser and Saleh (2006) introduced a new loss function in estimating the scale parameter and reliability function for Weibull distribution, which is called Generalized squared error loss function, that is defined as follows[13]:

$$L(\hat{\theta}, \theta) = \left(\sum_{j=0}^k a_j \theta^j \right) (\hat{\theta} - \theta)^2, \quad k = 0, 1, 2, 3, \dots$$

$$L(\hat{\theta}, \theta) = (a_0 + a_1\theta + \dots + a_k\theta^k) (\hat{\theta} - \theta)^2$$

So, the risk function under Generalized squared error loss function which is denoted by

$R_{GS}(\hat{\theta}, \theta)$, will be:

$$R(\hat{\theta}, \theta) = E[L(\hat{\theta}, \theta)] = \int_0^\infty L(\hat{\theta}, \theta) h(\theta | \underline{x}) d\theta$$

The risk can be minimized simply, by setting the first derivative to zero [8]

Hence, $\hat{\theta}$ based on generalized squared error loss function will be:

$$\hat{\theta} = \frac{a_0 E(\theta | \underline{x}) + a_1 E(\theta^2 | \underline{x}) + \dots + a_k E(\theta^{k+1} | \underline{x})}{a_0 + a_1 E(\theta | \underline{x}) + \dots + a_k E(\theta^k | \underline{x})} \quad (6)$$

Prior and Posterior Distribution

In the current study, we consider informative as well as non-informative prior density for θ as follows:

(i) Posterior Distribution Using Jeffreys Prior Information

Assume that (θ) has non-informative prior density defined as using Jefferys prior information $g(\theta)$, which is given by[14]:

$$g_1 \propto \sqrt{I(\theta)}$$

Where, $I(\theta) = -nE \left[\frac{\partial^2 \ln f(x; \theta)}{\partial \theta^2} \right]$ is the Fisher information.

Hence,

$$g_1(\theta) = b \sqrt{-nE \left(\frac{\partial^2 \ln f(x; \theta)}{\partial \theta^2} \right)}, \text{ b is constant}$$

By taking the second derivative of $\log f(x; \theta)$ with respect to θ yields

$$\frac{\partial^2 \ln f(x_i; \theta)}{\partial \theta^2} = -\frac{1}{\theta^2}$$

Therefore,

$$E\left(\frac{\partial^2 \ln f(x_i; \theta)}{\partial \theta^2}\right) = -\frac{1}{\theta^2}$$

$$g_1(\theta) = \frac{b}{\theta} \sqrt{n}, \theta > 0$$

Now, the posterior density function, is defined as:

$$h(\theta|\underline{x}) = \frac{g(\theta)L(\theta; x_1x_2\dots x_n)}{\int_0^\infty g(\theta)L(\theta; x_1x_2\dots x_n)d\theta} \quad (7)$$

After simplification, the posterior density functions of (θ) based on Jefferys prior, will be:

$$h_1(\theta|\underline{x}) = \frac{T^n \theta^{n-1} e^{-\theta T}}{\Gamma n}, T = \sum_{i=1}^n \frac{1}{x_i^2} \quad (8)$$

It is clear that,

$\theta|\underline{x} \sim \text{Gamma}(n, T)$,

with $E(\theta) = \frac{n}{T}, Var(\theta) = \frac{n}{T^2}$

Now, based on Jeffreys prior, the m^{th} moment for θ is:

$$E(\theta^m|\underline{x}) = \int_0^\infty \theta^m h_1(\theta|\underline{x})d\theta$$

$$= \int_0^\infty \theta^m \frac{T^n \theta^{n-1} e^{-\theta T}}{\Gamma n} d\theta$$

$$E(\theta^m|\underline{x}) = \frac{\Gamma n + m}{\Gamma n T^m}$$

$$\hat{\theta}_{J_1} = \frac{a_0 \frac{n}{T} + a_1 \frac{(n+1)n}{T^2}}{a_0 + a_1 \frac{n}{T}} \quad (9)$$

$$\hat{\theta}_{G_2} = \frac{a_0 \frac{\alpha+n}{P} + a_1 \frac{(\alpha+n)(\alpha+n+1)}{P^2} + a_2 \left(\frac{(\alpha+n)(\alpha+n+1)(\alpha+n+2)}{P^3} \right)}{a_0 + a_1 \frac{\alpha+n}{P} + a_2 \frac{(\alpha+n)(\alpha+n+1)}{P^2}} \quad (13)$$

Reliability Function

In this subsection, we have derived the Bayesian estimates for reliability function of inverse Ray-

$$\hat{\theta}_{J_2} = \frac{a_0 \frac{n}{T} + a_1 \frac{(n+1)n}{T^2} + a_2 \left(\frac{(n+2)(n+1)n}{T^3} \right)}{a_0 + a_1 \frac{n}{T} + a_2 \frac{(n+1)n}{T^2}} \quad (10)$$

(ii) Posterior Distribution Using Gamma Prior

The prior predictive prior distribution using Gamma distribution prior is defined as follow:

$$g_2(\theta) = \frac{\beta^\alpha \theta^{\alpha-1} e^{-\theta\beta}}{\Gamma\alpha}; \theta > 0, \alpha > 0, \beta > 0$$

Where, β and α are the shape and the scale parameters respectively. Since, using Equation (9), the posterior distribution of (θ) will be as follows:

$$h_2(\theta|\underline{x}) = \frac{P^{\alpha+n} e^{-\theta P} \theta^{\alpha-1+n}}{\Gamma(\alpha+n)} \quad (11)$$

Where, $P = \sum_{i=1}^n \frac{1}{x_i^2} + \beta$

Notice that: $\theta|\underline{x} \sim \text{Gamma}(\alpha+n, P)$, with:

$$E(\theta) = \frac{\alpha+n}{P}, Var(\theta) = \frac{\alpha+n}{P^2}$$

$$E(\theta^m|\underline{x}) = \int_0^\infty \theta^m h_2(\theta|\underline{x})d\theta$$

$$= \int_0^\infty \theta^m \frac{P^{\alpha+n}}{\Gamma(\alpha+n)} \theta^{\alpha-1+n} e^{-\theta P} d\theta$$

$$E(\theta^m|\underline{x}) = \frac{\Gamma(\alpha+n+m)}{\Gamma(\alpha+n) P^m}$$

$$\hat{\theta}_{G_1} = \frac{a_0 \frac{(\alpha+n)}{P} + a_1 \frac{(\alpha+n)(\alpha+n+1)}{P^2}}{a_0 + a_1 \frac{\alpha+n}{P}} \quad (12)$$

leigh distribution under Generalized squared error loss function, where

$$\hat{R}(t) = \frac{a_0 E(R(t)|t) + a_0 E(R(t)^2|t) + \dots + a_k E(R(t)^{k+1}|t)}{a_0 + a_1 E(R(t)|t) + \dots + a_k E(R(t)^k|t)} \quad (14)$$

(i) Bayesian Estimator for Reliability function under Jeffreys prior

Since $R(t) = 1 - e^{-\frac{\theta}{t^2}}$ (15)

Now, according to Jeffreys prior,

$$E(R(t)|t) = \int_0^\infty R(t) h_1(\theta|t) d\theta$$

$$E(R(t)|t) = 1 - \left(\frac{Tt^2}{t^2T + 1}\right)^n \quad (16)$$

$$E((R(t))^2|t) = \int_0^\infty (R(t))^2 h_1(\theta|t) d\theta$$

$$E((R(t))^2|t) = 1 - 2\left(\frac{Tt^2}{t^2T + 1}\right)^n + \left(\frac{Tt^2}{t^2T + 2}\right)^n \quad (17)$$

$$\hat{R}(t)_{GSJ2} = \frac{a_0 \left(1 - \left(\frac{Tt^2}{t^2T + 1}\right)^n\right) + a_1 \left(1 - 2\left(\frac{Tt^2}{t^2T + 1}\right)^n + \left(\frac{Tt^2}{t^2T + 2}\right)^n\right) + a_2 \left(2 - 3\left(\frac{Tt^2}{t^2T + 1}\right)^n + \left(\frac{Tt^2}{t^2T + 2}\right)^n\right)}{a_0 + a_1 \left(1 - \left(\frac{Tt^2}{t^2T + 1}\right)^n\right) + a_2 \left(1 - 2\left(\frac{Tt^2}{t^2T + 1}\right)^n + \left(\frac{Tt^2}{t^2T + 2}\right)^n\right)} \quad (20)$$

(ii) Bayes Estimator for Reliability function under Gamma prior

According to Gamma prior, $E(R(t)|t)$ will be

$$E(R(t)|t) = \int_0^\infty R(t) h_2(\theta|t) d\theta$$

$$E(R(t)|t) = 1 - \left(\frac{Pt^2}{t^2P + 1}\right)^{\alpha+n} \quad (21)$$

$$E((R(t))^2|t) = \int_0^\infty (R(t))^2 h_2(\theta|t) d\theta$$

$$E((R(t))^2|t) = 1 - 2\left(\frac{Pt^2}{t^2P + 1}\right)^{\alpha+n} + \left(\frac{Pt^2}{t^2P + 2}\right)^{\alpha+n} \quad (22)$$

And

$$E((R(t))^3|t) = 2 - 3\left(\frac{Pt^2}{t^2P + 1}\right)^{\alpha+n} + \left(\frac{Pt^2}{t^2P + 2}\right)^{\alpha+n} \quad (23)$$

$$\hat{R}(t)_{GSG1} = \frac{a_0 \left(1 - \left(\frac{Pt^2}{t^2P + 1}\right)^{\alpha+n}\right) + a_1 \left(1 - 2\left(\frac{Pt^2}{t^2P + 1}\right)^{\alpha+n} + \left(\frac{Pt^2}{t^2P + 2}\right)^{\alpha+n}\right)}{a_0 + a_1 \left(1 - \left(\frac{Pt^2}{t^2P + 1}\right)^{\alpha+n}\right)} \quad (24)$$

$$\hat{R}(t)_{GSG2} = \frac{a_0 \left(1 - \left(\frac{Pt^2}{t^2P + 1}\right)^{\alpha+n}\right) + a_1 \left(1 - 2\left(\frac{Pt^2}{t^2P + 1}\right)^{\alpha+n} + \left(\frac{Pt^2}{t^2P + 2}\right)^{\alpha+n}\right) + a_2 \left(2 - 3\left(\frac{Pt^2}{t^2P + 1}\right)^{\alpha+n} + \left(\frac{Pt^2}{t^2P + 2}\right)^{\alpha+n}\right)}{a_0 + a_1 \left(1 - \left(\frac{Pt^2}{t^2P + 1}\right)^{\alpha+n}\right) + a_2 \left(1 - 2\left(\frac{Pt^2}{t^2P + 1}\right)^{\alpha+n} + \left(\frac{Pt^2}{t^2P + 2}\right)^{\alpha+n}\right)} \quad (25)$$

Simulation Results

In the current the simulation study, we generated samples of different sizes, $n = 10, 25, 50,$ and

And $E((R(t))^3|t) = \int_0^\infty (R(t))^3 h_1(\theta|t) d\theta$

$$E((R(t))^3|t) = 2 - 3\left(\frac{Tt^2}{t^2T + 1}\right)^n + \left(\frac{Tt^2}{t^2T + 2}\right)^n \quad (18)$$

Hence, the Bayesian estimators for the $R(t)$ based on Generalized squared error loss function using Jeffreys prior with the first and second order polynomials, which are denoted by $\hat{R}(t)_{GSJ1}, \hat{R}(t)_{GSJ2}$ respectively, are as follows

$$\hat{R}(t)_{GSJ1} = \frac{a_0 \left(1 - \left(\frac{Tt^2}{t^2T + 1}\right)^n\right) + a_1 \left(1 - 2\left(\frac{Tt^2}{t^2T + 1}\right)^n + \left(\frac{Tt^2}{t^2T + 2}\right)^n\right)}{a_0 + a_1 \left(1 - \left(\frac{Tt^2}{t^2T + 1}\right)^n\right)} \quad (19)$$

100 from one parameter inverse Rayleigh distribution with three different values of $(\theta = 0.5, 1.5$ and $3)$. The constants of Generalized squared error loss function are choose as $a_0 = 5000, a_1 = 10$ and $a_2 = 0.5$. The values of parameters of Gamma distribution prior are $(\alpha = 0.8, \beta = 1.2, 3)$. The processes have been repeated 5000 times. The expected values and mean squared errors (MSE's) for the Bayes estimates of the parameter θ are obtained, where

$$MSE(\theta) = \frac{\sum_{i=0}^R (\hat{\theta}_i - \theta)^2}{R}; i = 1, 2, 3, \dots, R$$

And integral mean squared error (IMSE) for all estimates of the reliability function of Inverse Rayleigh distribution are obtained which is defined as follows:

$$IMSE(\hat{R}(t)) = \frac{\sum_{j=0}^{n_t} MSE(\hat{R}_i(t_j))}{n_t}$$

Where, $i = 1, 2, \dots, L$; n_i is the random limits of t_i

In current paper, we use

$$t = 1.5, 1.8, 2.1, 2.4, 2.7, 3$$

The results of the simulation study for estimating the scale parameter (θ) were summarized and tabulated in tables (1), (2) and (3) which are contain the expected values and MSE's for different estimates of the scale parameter, while tables (4),

(5) and (6) are contain IMSE's for different estimate of the Reliability function. We have observed that:

1. Table (1), shows that, the Bayesian estimation based on Gamma prior under Generalized Squared error loss function (GSELF) with ($\beta=3$ and $\alpha=0.8$) is the most occurrence in comparing to the others.
2. Table (2), shows that, the Bayes estimator according to Gamma prior under Generalized Squared error loss function (GSELF) with ($\beta=3$ and $\alpha=0.8$) is the best estimator comparing to the other estimator for all sample size expect the sample (10) the performance under Gamma prior with ($\beta=1.2$ and $\alpha=0.8$) is the best estimator.
3. Table (3), shows that, the performance of Bayes estimator with Gamma prior under Generalized Squared error loss function (GSELF) with ($\beta=1.2$ and $\alpha=0.8$) is the best estimator comparing to the other estimator for all sample size.
4. Table (4), shows that, the performance of Bayes estimator with Gamma prior under Generalized Squared error loss function (GSELF) with ($\beta=1.2$ and $\alpha=0.8$) is the best estimator comparing to the other estimator for all sample size expect the sample (10) the performance under Gamma prior with ($\beta=3$ and $\alpha=0.8$) is the best estimator.
5. Table (5) and (6), shows that, the performance of Bayes estimator with Gamma prior under Generalized Squared error loss function (GSELF) with ($\beta=1.2$ and $\alpha=0.8$) is the best estimator comparing to the other estimator for all sample size.
6. Provided that chosen the value of β is inversely proportional to the value of θ in estimation the scale parameters
7. It is clear that, MSE's of all estimates of scale parameter is increasing with increase of the parameter value with all sample sizes.
8. In general, we conclude that, in situation involving estimation of parameter and Reliability of inverse Rayleigh distribution using Generalized squared error loss function using Gamma prior is most occurrence in comparing to the corresponding other estimates.

Table 1: Expected values and MSE's of the different estimators for the Inverse Rayleigh distribution with $\theta=0.5$, $A_0 = 5000$, $A_1 = 10$, $A_2 = 0.5$, $\alpha=0.8$

Estimator	n Criteria	10	25	50	100	
		θ_{j_1}	EXP.	0.553371 4	0.521807 5	0.5102229
	MSE	0.042094 8	0.012818 8	0.0056789	0.0026506	
θ_{j_2}	EXP.	0.553376 7	0.521809 0	0.5102234	0.5053626	
	MSE	0.042098 5	0.012819 0	0.0056790	0.0026507	
$\hat{\theta}_{G_1}$	$\beta=1.2$	EXP.	0.556374 4	0.524782 2	0.5119841	0.5063035
		MSE	0.036269 8	0.012420 0	0.0056124	0.0026389
	$\beta=3$	EXP.	0.505081 2	0.505511 2	0.5026784	0.5017222
		MSE	0.021696 6	0.010139 7	0.0050806 9	0.0025085 5
$\hat{\theta}_{G_2}$	$\beta=1.2$	EXP.	0.556378 8	0.524783 4	0.5119846	0.5063038
		MSE	0.036272 4	0.012420 2	0.0056124	0.0026389
	$\beta=3$	EXP.	0.505084 5	0.505512 3	0.5026789	0.5017225
		MSE	0.021697 6	0.010139 9	0.0050807 3	0.0025085 7

Table 2: Expected values and MSE's of the different estimators for the Inverse Rayleigh distribution with $\theta=1.5$, $A_0 = 5000$, $A_1 = 10$, $A_2 = 0.5$, $\alpha=0.8$

Estimator	n Criteria	10	25	50	100	
		θ_{j_1}	EXP.	1.660525 0	1.565559 00	1.5307320 0
	MSE	0.379388 6	0.115427 30	0.0511227 6	0.023858 65	
θ_{j_2}	EXP.	1.660670 0	1.565596 00	1.5307460 0	1.516125 00	
	MSE	0.379685 8	0.115448 50	0.0511268 3	0.023859 61	
$\hat{\theta}_{G_1}$	$\beta=1.2$	EXP.	1.470881 0	1.498353 00	1.4990200 0	1.500668 00
		MSE	0.172541 6	0.086561 78	0.0445572 0	0.022280 35
	$\beta=3$	EXP.	1.167163 00	1.352119 0	1.4220680 0	1.461137 00
		MSE	0.176139 10	0.078635 5	0.0420131 2	0.021517 09
$\hat{\theta}_{G_2}$	$\beta=1.2$	EXP.	1.470958 0	1.498383 00	1.4990340	1.500675 00
		MSE	0.172601 3	0.086572 83	0.0445598 9	0.022280 96
	$\beta=3$	EXP.	1.167200 0	1.352141 0	1.4220810 0	1.461143 00
		MSE	0.176127 0	0.078634 9	0.0420131 40	0.021517 14

Table 3: Expected values and MSE's of the different estimators for the Inverse Rayleigh distribution with $\theta=3$, $A_0 = 5000$, $A_1 = 10$, $A_2 = 0.5$, $\alpha=0.8$

Estimator	n Crite-	10	25	50	100
-----------	-------------	----	----	----	-----

		ria					
θ_{J_1}	EXP.	3.322277 0	3.131524 0	3.061658 0	3.032330 0		
	MSE	1.520739 0	0.462053 5	0.204564 6	0.095452 1		
θ_{J_2}	EXP.	3.323429 0	3.131816 0	3.061781 0	3.032390 0		
	MSE	1.525432 8	0.462396 8	0.204631 0	0.095466 7		
$\hat{\theta}_{G_1}$	$\beta=1.2$	EXP.	2.505774 0	2.795267 0	2.893783 0	2.948242 0	
		MSE	0.594360 8	0.301940 9	0.165540 5	0.085610 7	
	$\beta=3$	EXP.	1.747872 0	2.328637 0	2.620616 0	2.799525 0	
		MSE	1.648842 0	0.574375 0	0.247032 5	0.107516 2	
$\hat{\theta}_{G_2}$	$\beta=1.2$	EXP.	2.506136 0	2.795448 0	2.893888 0	2.948292 0	
		MSE	0.594324 6	0.301975 0	0.165552 7	0.085614 1	
	$\beta=3$	EXP.	1.747990 0	2.328746 0	2.620690 0	2.799572 0	
		MSE	1.648581 0	0.574265 2	0.246993 7	0.107504 7	

Table 4: IMSE's of the Different Estimators for the Inverse Rayleigh distribution $\theta=0.5$, $A_0 = 5000$, $A_1 = 10$, $A_2 = 0.5$ and $R(t) = 0.0540405$, $\alpha=0.8$

		n				
			10	25	50	100
Estimator						
θ_{J_1}			0.001679	0.000576	0.000265	0.0001266
θ_{J_2}			0.001692	0.000581	0.000266	0.0001264
$\hat{\theta}_{G_1}$	$\beta=1.2$		0.001472	0.000556	0.00026	0.0001254
	$\beta=3$		0.0009735	0.0004745	0.0002434	0.0001224
$\hat{\theta}_{G_2}$	$\beta=1.2$		0.001488	0.000562	0.000263	0.0001257
	$\beta=3$		0.0009653	0.0004712	0.0002407	0.0001202

Table 5: IMSE's of the Different Estimators for the Inverse Rayleigh distribution $\theta=1.5$, $A_0 = 5000$, $A_1 = 10$, $A_2 = 0.5$ and $R(t) = 0.0540405$, $\alpha=0.8$

		n				
			10	25	50	100
Estimator						
θ_{J_1}			0.0064909	0.002557	0.0012243	0.0005951
θ_{J_2}			0.0064888	0.0025566	0.0012235	0.0005945
$\hat{\theta}_{G_1}$	$\beta=1.2$		0.0040743	0.0021145	0.0011193	0.0005704
	$\beta=3$		0.0057931	0.0023291	0.0011799	0.0005884
$\hat{\theta}_{G_2}$	$\beta=1.2$		0.0040354	0.0020983	0.0011103	0.0005657
	$\beta=3$		0.0056619	0.0022716	0.0011494	0.0005727

Table 6: IMSE's of the Different Estimators for the Inverse Rayleigh distribution $\theta=3$, $A_0 = 5000$, $A_1 = 10$, $A_2 = 0.5$ and $R(t) = 0.0540405$, $\alpha=0.8$

		n				
			10	25	50	100
Estimator						
θ_{J_1}			0.0097372	0.0041687	0.0020556	0.0010152
θ_{J_2}			0.0097182	0.0041611	0.0020514	0.0010131
$\hat{\theta}_{G_1}$	$\beta=1.2$		0.00948	0.0039513	0.0020082	0.0010035
	$\beta=3$		0.0292004	0.0089456	0.0035154	0.0014181
$\hat{\theta}_{G_2}$	$\beta=1.2$		0.0093714	0.0039059	0.0019848	0.0009917
	$\beta=3$		0.0289152	0.0088241	0.0034536	0.0013872

References

- [1] Gharraph, M. K., 1993. "Comparison of estimators of location measures of an inverse Rayleigh distribution", The Egyptian statistical Journal, 37(2): 295-309.
- [2] Soliman, A., A. E. Amin and A. A. Aziz, 2010. "Estimation and prediction from inverse Rayleigh distribution based on lower record values", Applied Mathematical Sciences, 4(62): 3057-3066.
- [3] Khan, M. SH.2014. "Modified Inverse Rayleigh Distribution", International Journal of Computer Applications, 87(13): 0975-8887.
- [4] Dey, S., 2012. "Bayesian estimation of the parameter and reliability function of an inverse Rayleigh distribution", Malaysian Journal of Mathematical Sciences, 6(1): 113-124.
- [5] Sindhu, T. N., M. Aslam, N. Feroze, 2013. "Bayes estimation of the parameters of the inverse Rayleigh distribution for left censored data". ProbStat Forum, 6: 42-59.
- [6] Prakash, G., 2013. "Bayes estimation in the Inverse Rayleigh model", Electronic Journal of Applied Statistical Analysis, 6(1): 67-83.
- [7] Fan, G., 2015. "_ Bayes Estimation for Inverse Rayleigh Model under Different Loss Functions", Research Journal of Applied Sciences, Engineering and Technology 9(12): 1115-1118, 2015 ISSN: 2040-7459; e-ISSN: 2040-7467.
- [8] Rasheed, H. A., Ismail, S. Z. and Jabir, A. G.2015. "A Comparison of the Classi-

cal Estimators with the Bayes Estimators of One Parameter Inverse Rayleigh Distribution", International Journal of Advanced.

- [9] Rasheed, H. A. and Aref, R. kh.2016. "Bayesian Approach in Estimation of Scale Parameter of Inverse Rayleigh distribution", Mathematics and Statistics Journal, ISSN-2077-459, 2(1): 8-13.
- [10] Rasheed, H. A. and Aref, R. kh.2016. "Reliability Estimation in Inverse Rayleigh Distribution using Precautionary Loss Function", Mathematics and Statistics Journal, ISSN-2077-4591, 2(3): 9-15.
- [11] Shawky, A. I. and M. M. Badr, 2012. "Estimations and prediction from the inverse Rayleigh model based on lower record statistics", Life Science Journal, 9(2): 985-990.
- [12] Oliwi N. A., 2015, "Some Estimators of the Pareto Type I Distribution / A Comparison Study ", M. Sc. Thesis in Mathematics, College of Science, Al-Mustansiriyah University.
- [13] Rasheed, H. A. and Al-Gazi, N. A., 2014. "Bayesian Estimation for the Reliability Function of Pareto Type I Distribution under Generalized Square Error Loss Function", International Journal of Engineering and Innovative Technology, 4(6): 33-40.
- [14] Rasheed, H. A. and R. kh. Aref, 2016. "Reliability Estimation in Inverse Rayleigh Distribution using Precautionary Loss Function", Mathematics and Statistics Journal, ISSN-2077-4591, 2(3): 9-15.

Research Article

Studying the Effect of Titania Additions on some properties of Porcelain

Abbas K. Saadon, Kirem Ali J., Shatha H. Mahdi

Department of Physics, College of Education for Pure Science Ibn-ALHaitham,
University of Baghdad, IRAQ.

*Correspondent Author Email: Abbas.Karim@yahoo.com

Article Info

Received
15/01/2017

Accepted
21/05/2017

Abstract

The paper presents the production of porcelain for the ceramic by inexpensive natural raw materials, the principal raw materials of porcelain composition was selected consisting of 50% kaolin, 25% feldspar, 25% silica, the sample synthesized were characterize by X-ray diffraction (XRD) technique, than study the effect additives at different concentration form titanium oxide (TiO_2) at (2, 5, 10, 15, 20) wt% on some physical and dielectric properties of porcelain.

The samples are prepared by the conventional manufacturing method.

The physical and dielectric properties of porcelain show that change considerably with the substituent sample. It was found that the increase of the titanium oxide (TiO_2) additives of all our sample produce increasing in dielectric constant and bulk density, while decreasing with open porosity and dielectric loss tangent.

Keyword: porcelain, feldspar, TiO_2 , dielectric constant, dielectric loss tangent.

الخلاصة

في هذه الدراسة تم تحضير البورسلين باستخدام تركيبة مكونة من مواد اولية طبيعية و غير مكلفة (50% كاؤولين - 25% فلبسبار - 25% سيليكيا). اضافة الى ذلك تم دراسة تأثير نسب مختلفة من اضافات التيتانيا (2, 5, 10, 15, 20 wt% على بعض الخصائص الفيزيائية والعزلية للبورسلين المحضر. حضرت النماذج بطريقة التصنيع التقليدية, حيث لوحظ ان تغير ثابت العزل والكثافة مع تراكيز التيتانيا المضافة بأنها تزداد مع زيادة تراكيز التيتانيا, اما بالنسبة الى ظل زاوية الفقدان و المسامية حيث وجد بأنها تتناقص مع زيادة تراكيز التيتانيا المضافة.

Introduction

One of the product materials madding by heat treatment is the ceramic. It is treatment of substance or mixture of non-metallic substance and inorganic metal material [1]. The producer of ceramic hardness is the porcelain, the porcelain make the ceramic white, intensive impermeable, and semitransparent to liquid that means the porcelain is good mixture of composite materials composing mainly of feldspar, caoling and silica materials raw, porcelain have many good characteristic features that means loads, chemical influence and resistance to mechanical stresses which exposing then beside satiable electric resistance [2].

Oxide of metal titanium TiO_2 is occurring naturally in several types of many mineral sands and rocks The titanium was the ninth common element in the crust earth [3] [4] [5] [6] [7] [8].

Masrtennikove G. M etal [4] had been studied the effect of addition of TiO_2 on fired properties of porcelain material reparation, they founded that four classes of addition normally used for porcelain, however the first kinds is including ,addition that controlling the coagulation thixotroics structure of porcelain suspension on the other hand it control of transition to condensation structure.

The second kind refers that additives which enhancing the sintering process and helping the transformation condense structure to the crystalline structure and the crystalline pseudo coagulation structure, the other kinds is including additive which enhancement the crystal structure of the new forms, the advantage and possibility of using the waste glass as fluxing in poscelaintiles without deterioration in mechanical properties had been investigation by Baker [5], Baker find

that the addition of waste glass enhance consequently and vitrification some surface and mechanical properties.

Materials and Methods

In this paper, we can prepare the porcelain material using elementary material, low cost and foundation of nature freely (50% kaolin, 25% feldspar, 25% silica). These materials are maxing by this ratio and mixture stay at 24 hours. After mixing the sample of this material are presuing (7 ton) to result a bulk of materials.

Since, that bulk of material input furnace $5 \frac{^{\circ}\text{C}}{\text{min}}$ (electric furnace) at 1300°C for three hours and colling ($5 \frac{^{\circ}\text{C}}{\text{min}}$) this mixture to room temperature and made a powder to study the effect of X – Ray diffraction. The rangs of angle 2Θ are (5 – 80 degrees).

In this papere, we study and evaluated the inters atomic spacing (d), Millar indices (hkl).

However we added the Titania (2, 5, 10, 15, 20 wt%) to the porcelain and the material mixing with each other for 10 hours by circumference 1.5 cm and width 0.7 and sintering this sample in oven with 1300°C for 4 hours at air.

The density and porosity of sample have been studied by using Archimedes with water as the immersion medium and we measurement the dielectric constant using LCR meter range (50 HZ to 1 MHz).

Results and Discussion

X – Ray diffraction analysis Figure (1) show that the pattern of X- ray diffraction for porcelain that producing by traditional method from traditional materials.

Philips X-ray diffraction meter was using to tastig this samples. All six samples was transtation at rang angle 2Θ from (10-80) degrees with spectroscopic velocity (10 deg/min) estimation all modes that to fulfilment evaluation. the inter atomic spacing c and miller indices (hkl).

Bulk density and open porosity: data in Figure 2 and 3 show that, variation in open porosity and bulk density with amount of TiO_2 addition that's added at sintering (1300°C),

We can show the property improvement due to additive incorporation that view in the curve Figures 5 to 6.

Table 1: X-ray diffraction data of porcelain.

$2\theta(\text{dgrees})$	$d(\text{A}^{\circ})$	hkl
21.15	4.19	100
26.58	3.34	101
26.96	3.3	006
33.45	2.6	116
35.39	2.52	300
39.71	2.26	161
40.57	2.22	111
41.07	2.19	200
42.70	2.11	223
50.36	1.81	003
55.12	1.60	103
60.14	1.53	211
60.85	1.13	113

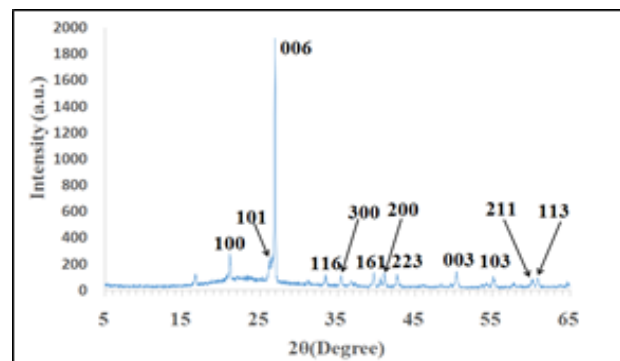


Figure 1: X-ray diffraction of composition (kaolin, feldspar, silica).

It was evident that high reduction in porosity founded when the porcelain sample which was due that the mass transport occurred as a results of glass phase formation.

The phase of glass formed enters in the pores presented in the compact and fills, due to these spherical pores were forming and also the compact gets dandified.

The two Figures (4, 5) show that the variation of dielectric constant and dielectric loss tangent as a function of TiO_2 that addition (Wt %) for porcelain.

Figures (4, 5) show that the dielectric constant value was increased when compared dielectric loss tangent with increasing TiO_2 additive (wt %). It may be due to the presence of some micrograms in the ceramic insulators when these cracks wave observing mainly near the quartz particles and those regions of the cry stalling phase was absent [6].

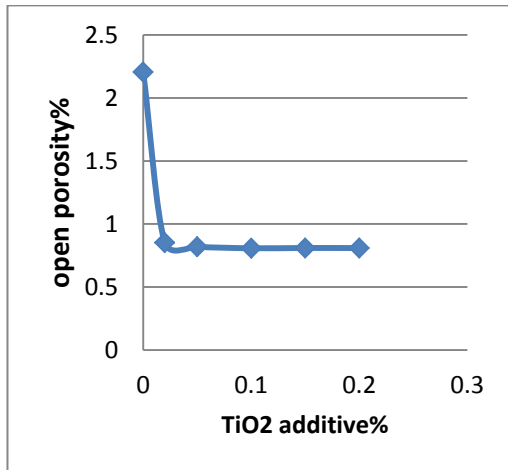


Figure 2: Porosity of porcelain with TiO_2 additives.

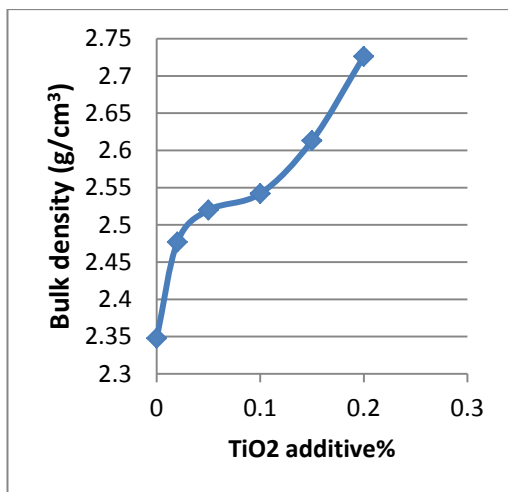


Figure 3: Density of porcelain with TiO_2 additives.

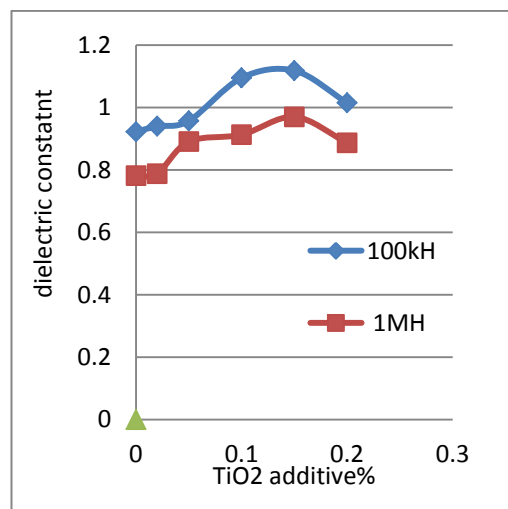


Figure 4: Dielectric constant of porcelain with TiO_2 additives at (1MHz) and (100 KHz).

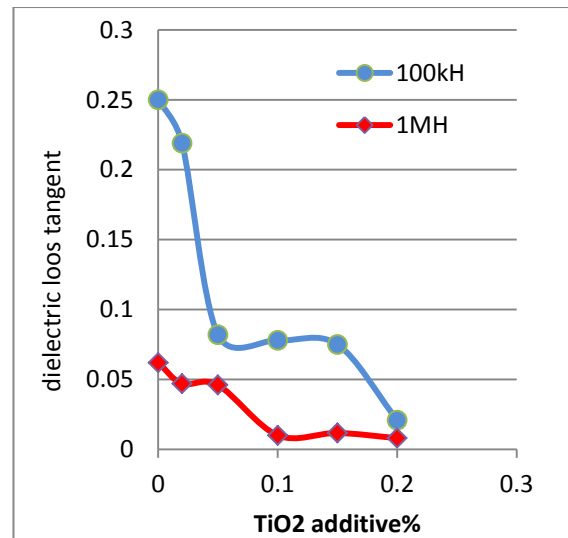


Figure 5: Dielectric loss tangent of porcelain with TiO_2 additives at (1MHz) and (100 KHz).

Conclusions

The experimental results obtained show that local raw materials are quite suitable for porcelain can be produced. The presence of TiO_2 additives (Wt %) in porcelain increased the bulk density and dielectric constant, while the open porosity and dielectric loss tangent to decreasing value.

References

- [1] Alshamri, A. K, 2007, the effect of mineralizes on ceramic body and studing some physical properties, thesis MCS, college of sciences for women, Baghdad university.
- [2] Al-Bermany, K. J, (2009), Enhancement mechanical and rheological properties and some is different industrial application, j. of collage of Education, No.2. Vol.2.
- [3] Boffetta P, Gaboriean V, Nadon L, Parent M – E, weirder pass E, siemiatycli J, (2001), Exposure to titanium dioxide and risk of lung cancer in a population – based study from Montreal, Scand, J. work Environ Health ,27(4), pp.227 – 232.
- [4] Maslennikavo. G. N, and Platov. Y. T,(2013), the process of porcelain formation in presence of additives (areview),glass and ceramic, vol .55,no.1-2.
- [5] Bark. I. M,2013, effect of waste glass and zircon on ceramic properties and microstructure of porcelain tiles, Advances in apple ce-

- ramic, vol.104, no.5, pp.243-248. ,
- [6] Verm a. A., Theakur. O. P., and Mendirate. R. A., 2005, study the physical and dielectric properties of ferrit-Sic compsite, material science and engineering, vol.116, no.1, pp.1-6.
- [7] Liebermann, J. Avoiding quartz in alumina porcelain for high-voltage nsulators. American Ceramic Society Bulletin, 2001, 80.6: 37-42.
- [8] De Sola, Esther Ruiz, et al. Solubility and microstructural development of TiO₂-containing 3Al₂ O₃· 2SiO₂ and 2Al₂ O₃· SiO₂ mullites obtained from single-phase gels. Journal of the European Ceramic Society, 2007, 27.7: 2647-2654.
- [9] fadhil,A. ch. Fadaa,Q. S; Innam. W. and Zahraa,F;2015, the influence of magnesia addition and sintering temp on the properties of synthesized electrical porcelain.; Eng. of tech Journal ,33,part A(2).

Research Article

Modification of Iraqi Asphalt 40/50 Properties Using Saw Dust (SD) and Natural Rubber Latex

Rusul M. Darwesh¹, Balqees M. Al-Dabbagh¹, Firas A. Mohammed²

¹ Department of Applied sciences, Materials science, University of Technology, IRAQ.

² Petroleum research and development center, Ministry of oil, IRAQ.

*Correspondent Author Email: rusulusul83@yahoo.com

Article Info

Received
20/01/2016

Accepted
17/04/2017

Abstract

The aim of this research is to enhance the fundamental properties for asphalt binder as those specifications relate to performance of asphalt mixtures. In this paper studied the effect of add (2, 4 %) SD in different sizes and (3, 5 and 7%) Natural rubber latex to the straight asphalt 40/50 produced from Al-Dura refinery at 160°C, it was added each additive separately and then added together to asphalt in same temperature, then tested physically and mechanically according to the American Society for Testing and Materials (ASTM), the result showed largely improvement.

Keyword: Asphalt binder, asphalt mixture, physical and chemical properties, sawdust, Natural rubber latex

الخلاصة

الهدف من هذا البحث هو تحسين خصائص الرابطة الاسفلتي وادائه خلال الخرسانة الاسفلتية، حيث تم دراسة تأثير اضافة (2,4 %) من نشارة الخشب وبعده ااحجام و(3,5 و7%) من المطاط الطبيعي اللاتكس الى الاسفلت نوع 50/40 المنتج من مصفى الدورة عند درجة حرارة 160°C. وتم اضافة كل مضاف الى الاسفلت على حدى ثم تم اضافة المضافين معا الى الاسفلت وبنفس الدرجة الحرارية. بعد ذلك تم اختبار النتائج فيزيائيا وميكانيكيا وفقا للمواصفات التابعة للجمعية الامريكية للاختبارات والمواد (ASTM) واطهرت النتائج تحسن كبيرا.

Introduction

Asphalt used in many applications especially in pavements [1] related to rheological properties where have a thermoplastic nature (making it solid in low temperature and soft in high temperature), adhesion, cohesion and water proofing properties [2].

Asphalts black or dark brown in color, amorphous and composed principally of high molecular weight hydrocarbons, soluble in carbon disulfide and in trichloroethylene with density 1g/cm³ and flows at high temperature.

Paving asphalt subjected to repeated loads and thermal loading, which make it lose the ability to maintain optimal performance and this leads to appearance defects on the asphalt pavement and structural degradation, therefore improving the quality of asphalt by additives is the target for researchers and engineers. [3].

In this research the additives was selected to enhance the quality of asphalt, blend and compatibility with it, to Produce a new better binder type

by increase viscosity, elasticity, softening point, stability and the strength of mixtures and improve the pavements, rutting resistance, thermal cracking, and fatigue resistance of blends after investigated by the physical and mechanical tests shown below.

Materials and Methodologies

Sawdust (SD) is a waste products obtained by cutting, grinding, drilling, sanding, or otherwise pulverizing wood with a saw or other tool. Wood consists of carbon about 50%, hydrogen, oxygen and ash. These elements share in to the formation cellulose which represents the chief constituent of plant cell wall and perhaps, characterized of fiber by durability and resistance to compression and hardness, which increases when the density is increase and increase the adhesion. In addition, it can reduce costs, and also environmental cost due to the recycling of waste sawdust [4].

The natural rubber latex(NRL) has a colloidal suspension collected from trees containing ~60%



rubber after stabilized with NH_3 with chemical formula $(\text{C}_5\text{H}_8)_n$, it has advantages such as elasticity, lower mixing temperature and faster mixing and has some disadvantages such as foaming, ammonia vapor and heat loss [5].

Penetration test: it is a measure of hardness of asphalt. Softening point is the temperature at which the asphalt becomes soft under the influence of steel ball and it affects the asphalt surface in bleeding. **Ductility Test:** It is the measure of cohesion strength and adhesion of bitumen. **Viscosity Test:** It is defined as the fluid characteristic of bitumen material at application temperature therefore it affects on the strength properties **Toughness and Tenacity:** Toughness is defined as the work required separating the tension

head from a sample of asphalt under a specified test conditions. **Tenacity** is defined as the work required stretching the material after the initial resistance is overcome. **Penetration Index (PI):** It is a consistency is an empirical measure of the resistance exhibited by a fluid to continuous deformation when it is subjected to shearing stress. **PVN:** is a function of Asphalt cement behavior at low temp performance.

Mechanical Tests (Marshall Test): has been carried out according to standard test method for resistance to plastic flow of bituminous paving mixture loaded on the lateral surface, it include tests (stability, flow, air voids%, bulk density and stiffness).

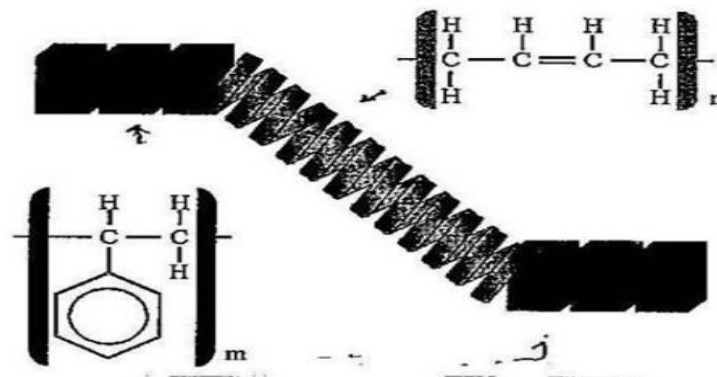
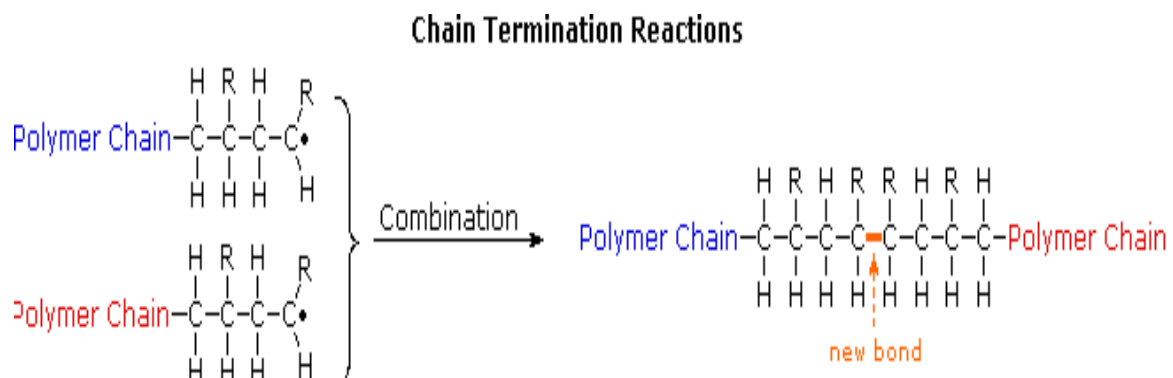


Figure 2: Structure of NRL [5].

The saw dusts with linear chain add to hot asphalt with homogeneous distribution of the components. There will be bonding across the interface and have inter-diffused into one another (Close in concept to the mechanical interlock theory). Consequently improvement of all asphalt properties except ductility test, there for natural rubber latex (NRL) was chosen for the purpose of increasing ductility value as elastomer polymer to enhance the elastic recovery of modified asphalt and reduces the thermal degradation problem. This is because the (NRL) polymer occupies a space of total mix and cause reduction in asphalt volume.

Results and Discussion

The addition of Sawdust (SD) and Natural rubber latex (NRL) to the asphalt with good mixing is the key to improving performance, all physical properties improved. The Figure (3) shows the penetration value generally will improve and decrease from 40 to 26 that is mean the additives improve the penetration value and makes the as-

phalt harder, softening point is increasing from 48.8 to 62 °C this indication to increase plasticity and decrease the temperature susceptibility, and for ductility values, it decrease from 100 to 31.5 with (4% SD), but when add NRL to SD keep value 100cm or more than it. Improving in viscosity values from 450 to with 1870 mean aggregates could absorb less asphalt and was able to be coated with thick film, thereby increasing adhesion among aggregates. Such results could be increasing the stability and reduce rate of stripping as shown in Figure (5). Toughness will enhance from 0.9 to 8.5 and tenacity increase from 0.3 to 6.7 with (2% SD + NRL5%), this enhance mean increase cohesive strength of asphalt and make it stiffen under loads as shown in Figure (6). Reducing the temperature susceptibility as shown in Figure(7), where have been improved the penetration index (PI) from -1.96 to -0.03 and the PVN from - 0.95 to 0.35, the mixture becomes more durable, all tests above shown mentioned with results in table (1).

Table 1: Physical and mechanical results.

Modifier content	test	penetration	Softening point	viscosity	ductility	toughnenacity	Penetration index	Penetration viscosity number	
AS		40	48.8	450	100	0.9	0.3	-1.96	- 0.95
As+ SD 2% (2-1mm)		37.4	51	558	100	1	0.3	-1.56	- 0.73
AS + SD4% (2-1mm)		24.8	52	590	40	1.1	0.5	-2.09	- 1.02
AS +SD4% (1-0.6mm)		23.5	54.8	900	90	1.4	0.4	-1.59	- 0.55
AS + SD4% (0.6-0.25mm)		31.5	52.3	577	31.5	1.4	0.5	-1.6	- 0.84
AS+3% NRL		38.5	53	876	100	3.8	2.4	-1.06	- 0.15
AS+5% NRL		37.5	55.8	1100	100	4.8	3.9	-0.49	0.1
AS+7% NRL		37	56.9	1200	100	5	4.1	-0.49	0.15
AS + NRL5% +SD 2%		31.4	56.5	1370	100	8.3	6.7	-0.71	0.18
AS + NRL5% +SD 4%		29	60.4	1542	100	8.4	5.4	-0.11	0.24
AS + NRL5% +SD 6%		28.3	62	1680	100	8.1	5.8	-0.13	0.31
AS + NRL5% +SD 8%		26	62	1870	68	8.5	5.6	-0.03	0.35

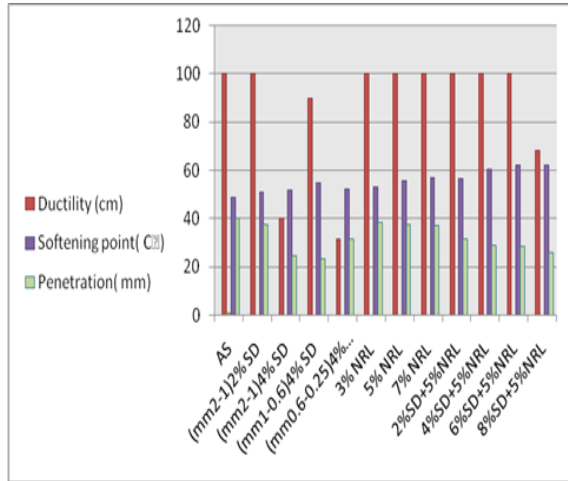


Figure 3: Influence of weight percentage and diameter of SD and NRL on Softening point, penetration and ductility tests.

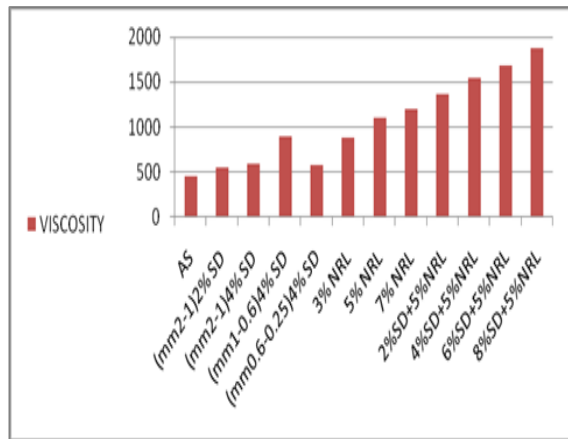


Figure 4: Influence of weight percentage and diameter of SD and NRL on Viscosity Test.

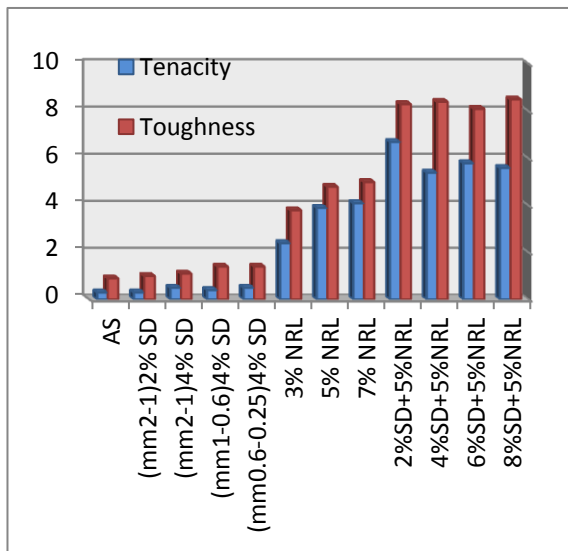


Figure 5: Influence of weight percentage and diameter of SD and NRL on Toughness and Tenacity.

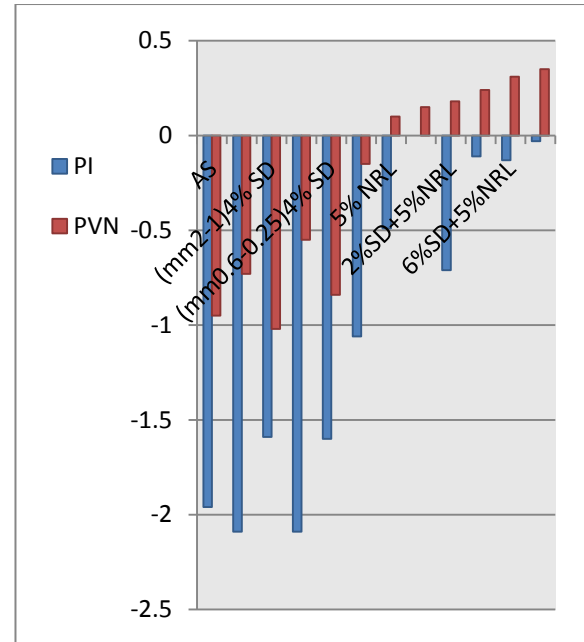


Figure 6: Influence of weight percentage and diameter of SD and NRL on Penetration index and PVN.

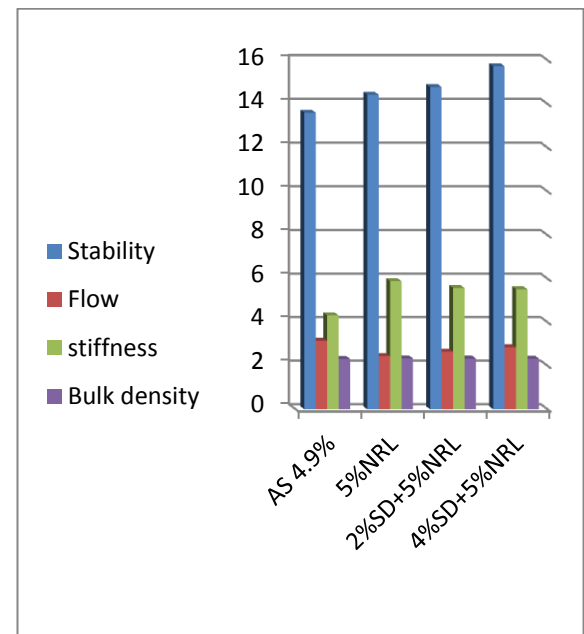


Figure 7: Influence of weight percentage and diameter of SD and NRL on stability, flow, stiffness and bulk density.

After determining the optimum asphalt binder by Marshall method (4.9), asphalt concrete mixture was done for three samples mentioned in Table 2 and investigated their properties.

The Figure (8) shown the stability value increase from 13.6 to 15.724 with (4% SD+5%NRL) this will be benefiting for the flexible pavement and so more resistance to both reflective and fatigue

cracking.

Further, the asphalt becomes more resistant to aging, the bulk density increase from 2.3181 to 2.3379 with (5%NRL), Stiffness from 4.317 to 5.886 this indicate to less strain through high stress and flow decrease from 3.15 to 2.4 mean no flow under load. The air voids content decrease from 4.2 to 3.533 with (5%NRL) (mixing with enough air voids improves stability and lessens bleeding when compacted), as shown in Figure (8), this improvement reflected in the performance of asphalt concrete.

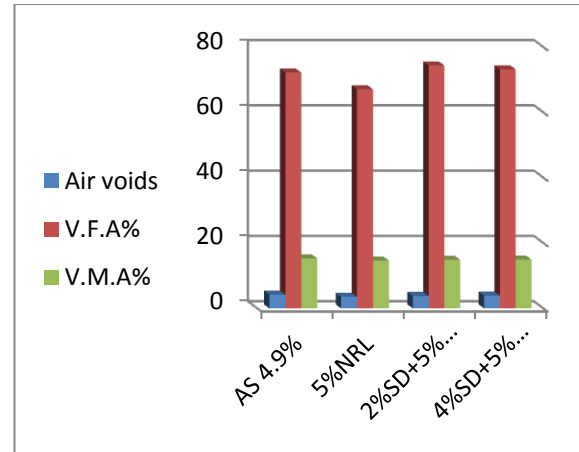


Figure 8: Influence of weight percentage and diameter of SD and NRL on air voids, V. F. A%, V. M. A% content.

Table 2: results of mechanical tests

	AS 4.9%	AS+5%NRL	As 4.9+NRL5%+SD2%	As 4.9+NRL5%+SD4%
Stability	13.6	14.4215	14.774	15.724
Flow	3.15	2.45	2.65	2.85
stiffness	4.3174	5.886	5.5750	5.5175
Bulk density	2.3181	2.3379	2.3313	2.3288
Air voids	4.2	3.533	3.807	3.907
V. F. A%	72.211	67.0849	74.3749	73.1950
V. M. A%	15.311	14.613	14.855	14.944

Conclusions

The well distribution of SD and cross-linking reactions of unsaturated carbon- carbon bonds of NRL with the hot asphalt enhance all physical properties, such as the increasing of softening point is indicates that will not bleed in pavement at high temperature, the increasing in viscosity mean more resist to flow, in addition to enhance the cohesion and adhesion properties. that's mean a greater force or tensile stress is required to break the molecular bonds of modified binders and cause failure and this reflected on the role of asphalt binder in asphalt concrete mixture and therefore improves the flexibility and the service life of the road and stability toward loads and environmental conditions and improvement the resistance to rutting at high temperatures and to cracking at low temperatures.

Acknowledgment

This work has been implemented in *petroleum*

research and development center / ministry of oil. Special thanks to all members in the department of the journal of science.

References

- [1] Dr joun Read, Dr david Whiteoak, "The shell bitumen hand book", Thomas telford fifth edition, London 2003.
- [2] Mang Tia, "bituminous materials", University of Florida, PH. D thesis, 2011.
- [3] "the bitumen industry", second edition, asphalt institute and eurobitume, USA 2011.
- [4] Hindustan petroleum corporation limited, "HP bitumen hand book", A Government of India Enterprise, India 2012.
- [5] Colin S Ruggles, " The Efficient Use of Environmentally-Friendly Natural Rubber Latex in Road Construction - Past, Present and the Future", Netherlands 2004.
- [6] Suleiman A. Y., Mohd. R. H., "Evaluation

- of Bitumen Properties Modified with Additive", *Journal of Research Review in Engineering Science and Technology*, volumes 13, NO.1-09, pp. (93-97), Malaysia 2012.
- [7] Meor O., babak G., "A Laboratory Investigation on the Rheological Properties of Asphalt Binder Containing Rediset", *Proceedings of the Eastern Asia Society for Transportation Studies*, Vol.9, pp. (1- 14), Malaysia 2013.
- [8] Khattak, M. J., Baladi, G. Y., "Fatigue and permanent deformation models for polymer-modified asphalt mixtures", *Journal of the Transportation Research Board* 1767, pp. (135-145), 2001.
- [9] Salah K., Riyadh K., "Polymers Effectiveness on Properties of Asphalt Concrete Mixtures", *Iraqi Journal of Science and Technology*, volume 3, No 2, pp. (33-39), 2012.
- [10] Nopparat V., jaratsri N., "Modification of Asphalt Cement by Natural Rubber for Pavement Construction", *rubber thai journal*, volume 1, pp. (33-39), Thailand 2012.

Research Article

Structural, Optical, and Morphological Properties of the Cadmium Oxide Thin Film

Taif S. Almaadhede

Al-Turath University College, Baghdad, IRAQ

*Email: stata86@yahoo.com

Article Info

Received
24/10/2017

Accepted

Abstract

Cadmium oxide nanoparticles CdO NPs has been prepared by laser ablation in ethanol at 600 pulses and 600 mJ as laser energy. The structural, optical, and morphological properties of the cadmium oxide CdO thin film deposited on a glass substrate have been studied. X-ray diffractometer (XRD 6000, Shimadzu, X-ray, diffractometer) with $CuK\alpha$ radiation at a wavelength of ($\lambda = 0.154056$ nm) was utilized to investigate the structural properties of CdO NPs. The optical absorption of colloidal CdO NPs was measured using a spectrophotometer (Cary, 100 cans plus, UV-Vis-NIR, Split Beam Optics, Dual detectors) in the range of (200–900) nm. The morphology of the CdO NPs was investigated by using AFM (AA 3000 Scanning Probe Microscope). The thickness of the films was measured using ellipsometer (Angstrom sun Technologies Ins).

Keywords: Nanoparticles, laser ablation, XRD, AFM, CdO.

الخلاصة

حضرت جسيمات أكسيد الكاديوم النانوية باستخدام تقنية السقواء الليزري في محلول الايثانول عند 600 نبضة و600J كطاقة ليزرية. درست الخصائص التركيبية والبصرية والتضاريسية التشكيلية لغشاء رقيق من جسيمات أكسيد الكاديوم النانوية المرسبة على قاعدة زجاجية. كانجهاز تداخل الأشعة السينية ذات $CuK\alpha$ عند طول موجي $\lambda = 0.1540$ nm = $\lambda_{\text{ملائم}}$ لتقصي الخصائص التركيبية للغشاء الرقيق لجسيمات أكسيد الكاديوم النانوي. قيس الأطنصاصية البصرية للمحلول الغروي لجسيمات أكسيد الكاديوم النانوي باستخدام مقياس الطيف (Cary, 100 cans plus, UV-Vis-NIR, Split Beam Optics, Dual detectors) في المدى 200-900 nm. أستقصى على تشكيل السطح للغشاء الرقيق لجسيمات أكسيد الكاديوم النانوية باستخدام مطياف القوى الذرية (AA 3000 Scanning Probe Microscope). قيس سمك الأغشية الرقيقة باستخدام مقياس السمك (Angstrom sun Technologies Ins).

Introduction

In general metal oxides can be possessed a transparent conducting property which is called transparent conducting oxides (TCO's). Andreas Stadler in his paper and Habubi with his coworkers as well as Khudheir *et al.* in 2012 said that the most of the studies of transparent conducting metal oxides are anion deficient (Oxygen deficient) and hence are always n-type conductors [1] [2] [3]. The transparent conducting metal oxides are also considered as oxide semiconductors. Metal oxide thin films (MOTF) are very important in the field of science and technology, it can be shown different properties of metals, semiconductors and insulators with enhanced electrical and optical properties. Some of MOTFs applications are referred in papers of Radi, Yu Yang, and also Radi as electrodes in optoelectronic devices, display devices and pho-

tovoltaic cells respectively [4], [5] and [6]. The n-type cadmium oxide CdO thin films exhibit rock salt structure (FCC) with band gap of 2.2eV. Ortega *et al.* in their paper emphasized that CdO thin film has a good optical conductivity and transmission in the visible region [7]. The main aim of this study is to create a simple, non-vacuum and economic deposition technique for efficient transparent conducting CdO thin films where there are many techniques exist to prepare the thin films such as spray pyrolysis[8], sputtering[9], sol-gel spin coating[10], activated reactive evaporation[11], metal Organic Chemical Vapor deposition [12], pulsed laser deposition[13]. In this study CdO films were synthesized using laser ablation in ethanol. Optical properties such as transmission, bandgap, refractive index, absorption coefficient, extinction coefficient, dielectric constant (imaginary and real)

and Urbach energy were studied for CdO NPs thin films deposited on FTO substrate.

Materials and Methods

The laser type Nd:YAG was selected for the ablation operating at 10 Hz repetition rate, with 7 ns pulse width and wavelength of 1064 nm. The laser pulses were focused by a 20 cm positive lens onto a cleaned 2 mm thick CdO bulk sample (99.99% purity provided by Porch Company) immersed in ethanol at laser energy (400 mJ) with an ablation time of 20 min. The energy of laser pulse was measured using calibrated Joule meter after taking into account the effect of ethanol transmittance. The CdO target was placed in the bottom of a quartz vessel filled with 10 ml of ethanol. Structural properties of CdO NPs deposited on a glass substrate was investigated by X-ray diffractometer (XRD 6000, Shimadzu, X-ray, diffractometer) with $CuK\alpha$ radiation at a wavelength of ($\lambda = 0.154056$ nm). Optical absorption of colloidal CdO NPs was measured using a spectrophotometer (Cary, 100 cans plus, UV-Vis-NIR, Split Beam Optics, Dual detectors) in the range of (200–900) nm. Morphological of the CdO NPs was emphasized by using AFM (AA 3000 Scanning Probe Microscope). The thickness of the films was determined using ellipsometer (Angstrom sun Technologies Ins). Measurements were carried out at room temperature at 200 nm thickness.

Results and Discussion

Figure 1 show XRD patterns of CdO thin films deposited on FTO substrate. X-ray diffraction patterns of CdO thin films revealed polycrystalline nature with a cubic structure. The observed diffraction patterns were indexed with standard values (JCPDS card no.78-0653). X-ray diffraction patterns also show that various diffraction peaks at 2θ values 26.42° , 33.62° , 37.67° , 55.52° and 69.44° , were identified to originate from (200) (110) (220) (222) and (111) planes, respectively, which corresponds to CdO face centered cubic structure. The large peak at 37.67° indicates that CdO thin film is preferentially oriented along the (200) crystallographic plane. The structural properties were calculated using expressions given by Abd [14]. Crystallite size was in the order of 20 nm to 76 nm. The microstrain,

number of crystallites and dislocation density of the CdO thin film is listed in Table 1.

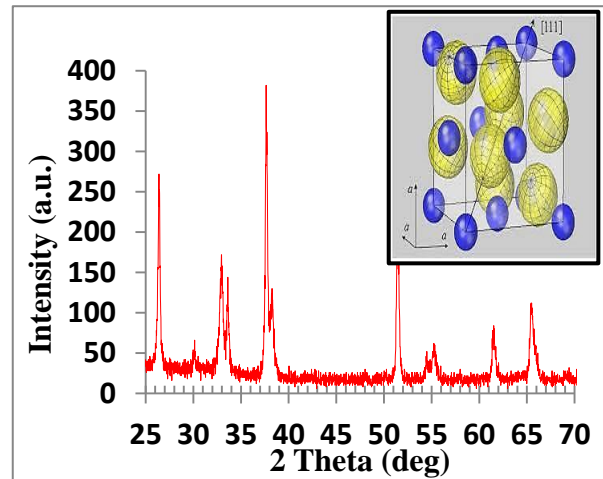


Figure 1: shows XRD patterns of the CdO thin films deposited on FTO substrate

Figure 2 shows the 2D-3D AFM images of CdO NPs thin film deposited on an FTO substrate by drop casing method. The surface of the thin film has vertically closely packed ball shaped, within the scanning area (2×2) μm . Using special software (4.62 imager), the estimated of the average grain was around 46 nm. Homogenous and a good roughness grain of CdO nanostructure were noticed. Figure 3 illustrates the UV-Vis spectra of ethanol solution containing CdO NPs prepared by laser ablation in liquid technique. The transmittance curve was subdivided into two regions at the visible and near IR regions. The transmittance curve decreases sharply from 400 nm up to 1100nm, so the CdO NPs has an acceptable transmittance in the visible range, which can be used in solar cell and a smart window and that is a good agreement with Aldwayyan *et al* [15]. Figure 4 shows the variation of $(\alpha h\nu)^2$ verses $h\nu$ for direct band gap which have been determined by the extrapolation of the linear portion versus the photon energy axis. It can be seen that the value of the energy gap was about 1.4 eV.

Table 1: Characterization of XRD patterns for CdO thin films deposited on FTO substrate.

2 Theta (deg)	FWHM (deg)	hkl planes	D (nm)	$\sigma \times 10^{14}$ lines. m ⁻²	$\eta \times 10^{-4}$ Lines ⁻² . m ⁻⁴	Nx 10 ¹⁸ 1/m ²
37.67	0.25	(200)	33.40818	8.95972	10.37171	80.9932
26.42	0.246	(110)	32.99681	9.184514	10.50102	84.06036
55.25	0.366	(220)	24.3946	16.8041	14.204	208.031
69.44	0.126	(222)	76.44941	1.711007	4.532409	6.759032
33.62	0.4	(111)	20.64165	23.4699	16.78645	343.3791

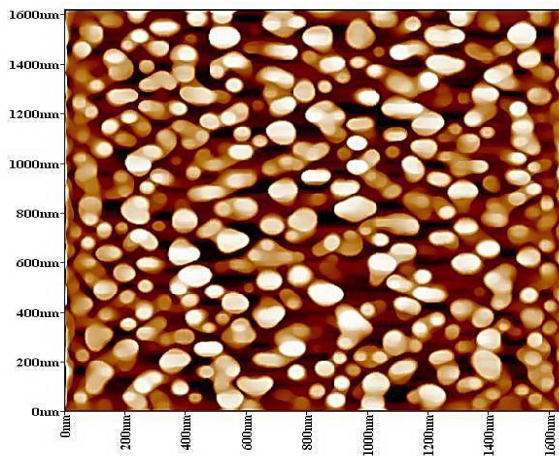
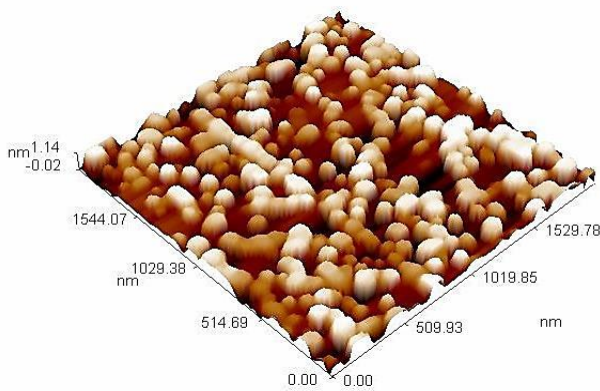


Fig.2: 2D and 3D AFM images of synthesized CdO nanoparticles.

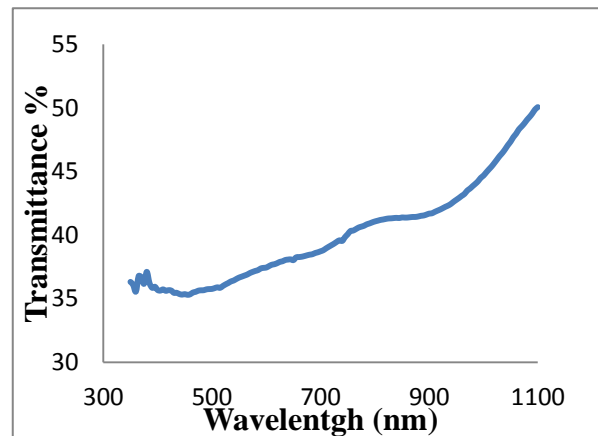


Figure 3: UV-Vis transmittance spectra of nanoparticles colloid fabricated at wavelength CdO ablated with 400 mg at 1064nm.

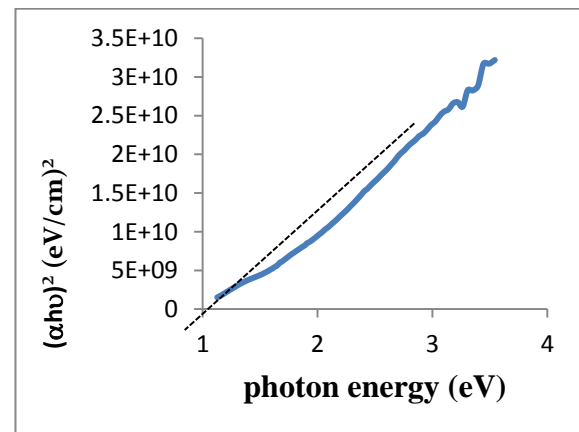


Figure.4: $(\alpha h\nu)^2$ versus photon energy plot for CdO NPs in ethanol.

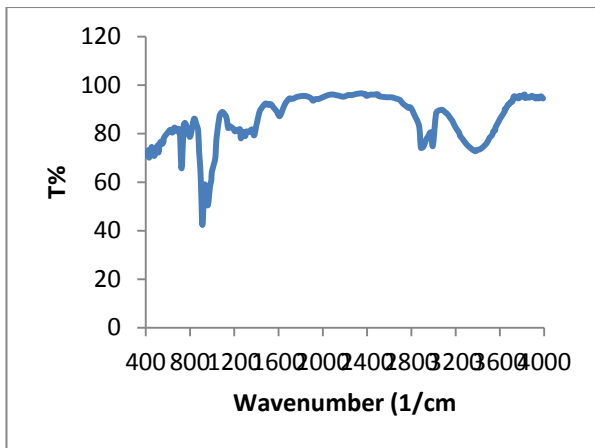


Figure 5: FTIR for CdO Nanoparticles.

Figure 6 shows the I-V dark characteristics in forward and reverse direction of Al/CdO/ p-Si/Al. The forward current of photodetector was very small at voltages less than 1 Volt. This current is known as *recombination current* which occurs at low voltages only. It is generated when each electron excited from valence band to conductive band. The second region at high voltage represented the diffusion or bending region, which depends on a series resistance. In this region; the bias voltage can deliver electrons with enough energy to penetrate the barrier between the two sides of the junction.

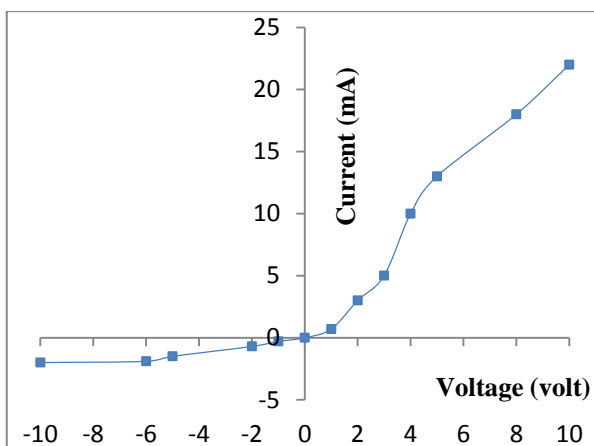


Figure 6 shows the I-V dark characteristics for CdO/Si heterojunction

Figure 7 shows that a linear relationship between $1/C^2$ and reverse bias voltage was obtained for the structure. This linear relationship represented the photodetector (CdO /Si) and (PSi/Si). The values of the built-in potential have been obtained and it had been found equal to 0.2 Volt.

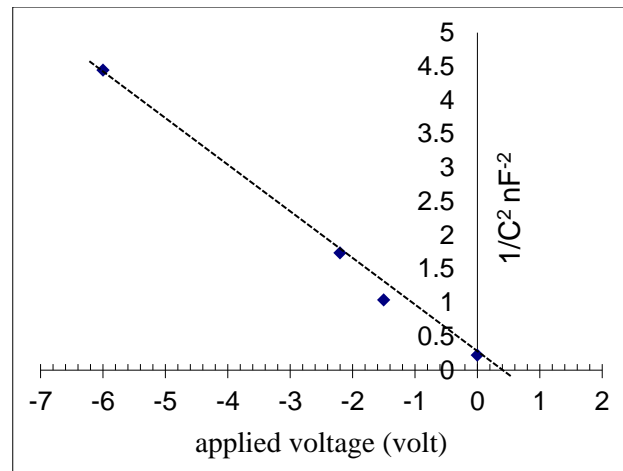
Figure 7: $1/C^2$ versus reverse voltage of CdO/PSi Photodetectors.

Figure 8 displays the responsivity as a function of wavelength for CdO/p-Si photodetector, the maximum responsivity is located in the visible region and the other at the NIR region, the spectral responsivity curve of CdO/p-Si consists of one peak of response; the peak was located at 575 to 850 nm due to the absorption edge of CdO NPs and Si nanoparticles.

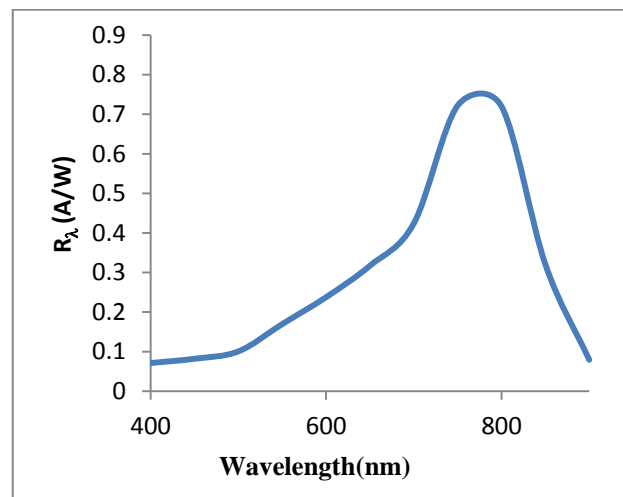


Figure 8: Spectral Responsivity plots for CdO/p-Si as a function of wavelength.

Conclusions

The synthesized CdO NPs were in nanosized of 46 nm prepared in ethanol by laser ablation in liquid method and the optical properties revealed that the direct band gap of CdO NPs indicated to the effect of quantum size. X-ray diffraction (XRD) measurement disclosed that the CdO NPs are polycrystalline and have FCC crystal structure and no other phases were noticed. Deposition of CdO NPs on silicon (Si) gave suspensions

photodetector characteristics enhanced the properties porous photodetectors. The spectral responsivity of Al/CdO /Si/Al photodetector was around 0.7 A/W at 790 nm.

References

- [1] Andreas Stadler, Transparent Conducting Oxides- An Up-To-Date Overview, *Materials* 2012, 5, 661-683.
- [2] A. A. Yousif, N. F. Habubi, A. A. Haidar, Nanostructure Zinc Oxide with Cobalt Dopant by PLD for Gas Sensor Applications, *JOURNAL OF NANO- AND ELECTRONIC PHYSICS*, Vol.4 No 2, 2007(6pp) (2012).
- [3] Khudheir A. Mishjil, Sami S. Chiad, Hazim L. Mansour, Nadir F. Habubi, INFLUENCE OF COPPER DOPING ON THE STRUCTURAL AND OPTICAL PROPERTIES OF SPRAYED SnO₂ THIN FILM, *Journal of Electron Devices*, Vol.14, 2012, pp.1170-1177.
- [4] P. A. Radi, A. G. Brito-Madurro, J. M. Madurro and N. O. DantasBraz, Characterization and properties of CdO nanocrystals incorporated in olyacrylamide, *J. Phys.*, 2006, 36, 412-414.
- [5] Yu Yang, Qinglan Huang, Andrew W. Metz, Shu Jin, Jun Ni, Lian Wang and Tobin J. Marks, Highly transparent and conductive CdO thin films as anodes for organic light-emitting diodes, *Film micro structure and morphology effects on performance*, *J Soc Inf Display*, 2005, 9, 383–387.
- [6] Raid A. Ismail and Omar A. Abdulrazaq, A new route for fabricating CdO/c-Si heterojunction solar cells, *Sol Energ Mat Sol C*, 2007, 91, 903–907.
- [7] M. Ortega, G. Santana, Morales and A. Acevedo, Optoelectronic Properties of CdO-Si Heterojunctions, *Superficies y Vacio*, 1999, 9, 294-295.
- [8] Dong Ju Seo, Structural and Optical Properties of CdO Films Deposited by Spray Pyrolysis, *J Korean Phys Soc*, 2004, 45,1575-1579.
- [9] T. K Subramanyam, S Uthanna and B Srinivasulu Naidu, Preparation and characterization of CdO films deposited by dc magnetron reactive sputtering, *Mater Lett*, 1998, 35, 214–220.
- [10] D. M Carballeda-Galicia, R Castanedo-Pérez, O Jiménez-SandovalS Jiménez-Sandoval, G Torres- Delgado and C. I Zúñiga-Romero, High transmittance CdO thin films obtained by the sol-gel method, *Thin Solid Films*, 2000, 371, 105–108.
- [11] X. R. Ye, C. Daraio, C. Wang, and J. B. Talbot, *J. Nanoscience and Nanotechnology*, 6 (2006)
- [12] Z. Guo-hua, L. Ming-fang, and L. Ming-Li *CEJC*, 5 (2007)
- [13] N. Ahmed Abd, A. Raid Ismail and F. Nadir Habubi, "Preparation of colloidal cadmium selenide nanoparticles by pulsed laser ablation in methanol and toluene", *journal of Materials Science: Materials in Electronics*, 25(2014)
- [14] N. Ahmed Abd, "Improved photoresponse of porous silicon photodetectors by embedding CdS nanoparticles", *World Scientific News (WSN)*, 13(2015) 23- 94.
- [15] A. S. Aldwayyan, F. M. Al-Jekhedab, M. Al-Noaimi, Synthesis and Characterization of CdO Nanoparticles Starting from Organometallic Dmphen-CdI complex, *Int. J. Electrochem. Sci.*, 8(2013) 10506 - 10514.

Research Article

Evaluating Cross Sections of Gallium Isotopes Production Using proton and deuteron Irradiation

Raghad S. Mohammed

Department of physics, College of Science, Mustansiriyah University, IRAQ.

*Email: raghad_almaliki@yahoo.com

Article Info

Received
19/10/2016

Accepted
17/04/2017

Abstract

In the present work, the production of the cross sections of three Gallium isotopes: $^{66}\text{Ga}_{35}$ ($t_{1/2} = 9.4\text{h}$, $\beta^+ = 4.2\text{MeV}$), $^{67}\text{Ga}_{36}$ ($t_{1/2} = 3.2617\text{d}$, $\text{EC} = 100\%$) and $^{68}\text{Ga}_{37}$ ($t_{1/2} = 68\text{min}$, $\beta^+ = 89\%$) have been discussed. The Gallium isotopes have important applications in nuclear medicine, particularly in Positron Emission Tomography (PET), Single Photon Emission Tomography (SPET) imaging technique and used in tumors diagnosing. The production of irradiant ^{66}Ga , ^{67}Ga and ^{68}Ga is made by irradiation of an enriched Zinc target using proton and deuteron charged particles. Utilizing high cyclotron yield and low radionuclide impurities, the optimum cyclotron energy range has been chosen for the production of Gallium isotopes. The cross sections of (p,xn), (p, γ) and (d,xn) reactions for the production of Gallium isotopes have been evaluated depending upon the empirical data taken from EXFOR library, which is belonging to the International Atomic Energy Agency (IAEA). Also the yield for each reaction has been evaluated.

Keywords: cross sections, Gallium Isotopes, optimized energy range

الخلاصة

في العمل الحالي، تم مناقشة إنتاج المقاطع العرضية لثلاث نظائر لعنصر الكالسيوم: ^{66}Ga ($t_{1/2} = 9.4\text{h}$, $\beta^+ = 4.2\text{MeV}$), ^{67}Ga ($t_{1/2} = 3.2617\text{d}$, $\text{EC} = 100\%$) و ^{68}Ga ($t_{1/2} = 68\text{min}$, $\beta^+ = 89\%$). والكاليوم لها تطبيقات مهمة في مجال الطب النووي وعلى وجه الخصوص استخدامها في تقنية التصوير المقطعي بالانبعاث البوزيتروني (PET) والتصوير المقطعي بأشعة فوتون منفرد (SPET)، واستخدامها في تشخيص الأورام. يتم إنتاج نظائر الكالسيوم المشعة بتشجيع هدف الزنك المخصب باستخدام الجسيمات المشحونة من البروتونات والديترونات باستخدام أعلى انتاجية للمعجل واقل نسبة شوائب للنظائر المشعة، تم تحديد أفضل مدى طاقة للمعجل لإنتاج نظائر الكالسيوم. تم تقييم المقاطع العرضية لتفاعلات (p, γ)، (p,xn) و (d,xn) لإنتاج نظائر الكالسيوم المشع اعتماداً على القيم العملية المتوفرة في مكتبة (EXFOR) التابعة لوكالة الطاقة الذرية الدولية (IAEA). كذلك تم حساب الانتاجية لكل تفاعل.

Introduction

The radioisotopes have a significant importance in the field of nuclear medicine, specifically in diagnostic imaging including Single Photon Emission Computed Tomography (SPECT) and Positron Emission Tomography (PET), and in the field of nuclear medical therapy. These radioisotopes are produced using reactors through nuclear reactions or accelerators through bombardment reactions using charged particle such as protons, deuterons and alpha particles [1]. The three radioisotopes of Gallium (^{66}Ga , ^{67}Ga and ^{68}Ga) have a great importance in nuclear medicine, especially in PET scan and in radiotherapy

by attaching them with monoclonal antibodies to detect tumors locations, and in investigation of different diseases [2]. Gallium-66 ($t_{1/2} = 9.49\text{h}$, $E_{\gamma} = 833.5, 1039.3\text{keV}$, β^+ : 56.5%, $E_{\text{max}\beta^+} = 4.153\text{MeV}$; $\text{EC}: 43.5\%$), has an intermediate half-life make it suitable for PET imaging of bioprocesses with intermediate to slow target tissue uptake [3]. The Gallium-67 ($t_{1/2} = 3.2617\text{d}$; $\text{EC} = 100\%$), is widely used in medical applications due to its ability to emit several Auger electrons with energies (7–8) keV. These electrons may reach the investigated cell nucleus from the cell surface or from cytoplasm; hence it is effective in single cell killing. Gallium-67 emits rays

with energies ranged from 91 to 394keV, which is suitable to be detected by gamma cameras [4]. for single photon imaging in PET scan [5]. Ga-68 ($t_{1/2} = 68\text{min}$, β^+ : 89.1%; EC: 10.9%) has distinctive characteristics that made it used in PET scan imaging and in tumor diagnosing[6]. The aim of the present work is to evaluate the experimental data of nuclear reactions induced by proton and deuteron particles on enriched Zn target and selected optimization energy range for the production of ^{66}Ga , ^{67}Ga and ^{68}Ga with small and/or medium-sized cyclotrons less than 30MeV and improve efforts in this field of production.

Materials and Methods

Cross Sections Calculations

The experimental data play an important role in the evaluation of nuclear reaction cross sections. Table (1), shows the experimental data that have been published in (EXFOR) library, which belongs to the International Atomic Energy Agency (IAEA) for proton and deuteron induced reactions specific for Zn target [7]. The empirical data that obtained by different authors listed in table (1) are not identical. In the present work the evaluations was made by including a careful analysis for these data by recalculating the energy in steps of the interval (0.01MeV) and the calculated cross sections were plotted using Matlab-8 programming language as shown in Figures (1→5).

Yield of Calculated Products

The yield of a nuclear reaction can be defined as the ratio of the number of the nucleus formed in a nuclear reaction to the number of the bombarding particles hitting the target. The yield production of nuclei for any energy, E can be expressed as a function of the cross section as [8]:

$$Yield = I(\phi n) H (1 - e^{-\lambda t}) \int_{E_{out}}^{E_{in}} \sigma(E) \left(-\frac{dE}{dx} \right)^{-1}$$

Where: Y is the activity in (Bq) of the product nuclei. I: current of projectile in (μA). ϕ : the flux is $\sim 10^{12}$ to $10^{14} \text{ n/cm}^2 \cdot \text{s}$. n: umber of atoms per unit volume (N/A).N: Avogadro's number. A: the mass number of the target in (amu). H: isotopic abundance (or enrichment) of the target. λ : The decay constant of the prod-

uct= $\left(\frac{0.693}{t_{1/2}} \right)$ in (h^{-1}). t: time of irradiation in
(h). $-\frac{dE}{dx}$: the stopping power, $\sigma(E)$: Cross section at energy E in (mb).

Results and Discussion

Gallium radioisotopes $^{66}\text{Ga}_{35}$ ($t_{1/2} = 9.4\text{h}$), $^{67}\text{Ga}_{36}$ ($t_{1/2} = 78\text{h}$) and $^{68}\text{Ga}_{37}$ ($t_{1/2} = 68\text{min}$) are commonly used for diagnostic studies using (PET) and (SPET), it can be produced via various reactions induced by charged particle as shown in Table 1.

There are three routes for the accelerator production of $^{66}\text{Ga}_{35}$ by proton projectile via $^{66}\text{Zn}_{36}(p,n)^{66}\text{Ga}_{35}$, and $^{67}\text{Zn}_{37}(p,2n)^{66}\text{Ga}_{35}$ reactions as shown in Figures (1-a), and (2-a) respectively; also by deuteron bombardment via $^{66}\text{Zn}_{36}(d,2n)^{66}\text{Ga}_{35}$ reaction as shown in (4-a).comparing the three reactions mentioned

above, the optimum reaction to produce ^{66}Ga is $^{66}\text{Zn}_{36}(p,n)^{66}\text{Ga}_{35}$ reaction with a production yield equals to $7.4\text{MBq (mCi)/}\mu\text{Ah}$ (Figure 6), high cross section (700mb), at area of optimum energy range $E_p = (8 \rightarrow 14)\text{MeV}$, and with no impurities. The obtained value is in a good agreement with the value obtained from ref. [2], with $E_p = (6 \rightarrow 15)\text{MeV}$ because of the highly

isotopic abundance (27.9%) [9] of ^{66}Zn in a natural Zinc matrix target. The yields of $^{67}\text{Zn}_{37}(p,2n)^{66}\text{Ga}_{35}$ and $^{66}\text{Zn}_{36}(d,2n)^{66}\text{Ga}_{35}$ reactions are $0.093\text{MBq mCi/}\mu\text{Ah}$ and $3.97\text{MBq(mCi)/}\mu\text{Ah}$ with optimum energy range $E_p = (5 \rightarrow 15)\text{MeV}$ and $E_p = (10 \rightarrow 15)\text{MeV}$ respectively.

The optimum production of ^{68}Ga is via $^{68}\text{Zn}_{38}(p,n)^{68}\text{Ga}_{37}$ reaction with a yield of $30.34\text{MBq (mCi)/}\mu\text{Ah}$ (Figure 8), high cross section (1060mb), optimum energy range $E_p = (8 \rightarrow 12)\text{MeV}$, and with a minimum impurity 0.002% of ^{67}Ga . This value is agree with value obtained from ref. [6] with

$E_p = (4 \rightarrow 13)MeV$ because of the highly isotopic abundance of ^{68}Zn (27.9%) compared with ^{67}Zn (4.1%) [9] in a natural Zinc matrix target. The results of the optimum energy range is less than 30MeV, hence the data obtained in the present work has a good agreement with some calculations made by researches. At which Gallium isotopes could conveniently yield at cyclotron energy for a medium *via* proton irradiation on natural Zinc target. However, calculations in the recent practical data of cross sections *via* deuteron irradiation on natural Zinc might be added a new production route for radio Gallium isotopes [4].

Conclusions

The accelerators production of Gallium radioisotopes has suitable physical properties, since it have intermediate or short half-life, so it is widely used in medical applications in imaging techniques and radiotherapy. In the present work, the evaluation of cross sections for the reactions induced by proton and deuteron particles give a good agreement with experimental calculations taken from IAEA which done by different authors. The high enrichment target is used to reduce the radio impurities due to the activation of impurities, but this radio impurity does not disappear. These impurities can be removed only by using enriched target and/or by a careful selection of the effectively charged particle energy range in the target. From the results, we concluded the optimum reactions to product ^{66}Ga , ^{67}Ga and ^{68}Ga from $^{66}Zn_{36}(p,n)^{66}Ga_{35}$, $^{68}Zn_{38}(p,2n)^{67}Ga_{36}$, $^{68}Zn_{38}(p,n)^{68}Ga_{37}$ and $^{68}Zn_{38}(d,2n)^{68}Ga_{37}$ reactions respectively. Another reactions are not desirable to product ^{66}Ga , ^{67}Ga and ^{68}Ga , because of minimum product yield and the production of isotopic impurities appear in reaction process. We found from the results that Gallium-68 is the best isotope to be used in medical application because it have a short half-life and high cross sections.

Acknowledgment: We wish to express our deep thanks and gratitude to the International Atomic Energy Agency (IAEA) to allow access to the experimental nuclear data libraries and made available.

References

- [1] International Atomic Energy Agency (IAEA), "Cyclotron Produced Radionuclides: Physical Characteristics and Production Methods", Technical Reports Series, No.468, P.2, Vienna (2009).
- [2] Rowshanfarzad P., Jalilian A. R., Sabet M., Akhlaghi M., "Production and quality control of ^{66}Ga as a PET radioisotope", Iran, Journal of Radiation Research, Vo.2, No.3, pp: 149-158, (2004).
- [3] Amir R. J., Pejman R., Mahsheed S., Ali R. K., Amir A. R. , " Development of ^{66}Ga oxine complex; a possible PET tracer", Nukleonika, Vol.51, No.3, pp: 155–159, (2006).
- [4] Khandaker M. U., Haba H. and Abu Kasim H., "Cyclotron produced ^{67}Ga , a potential radionuclide for diagnostic and therapeutic applications", AIP Conference Proceedings 1659, 030009; doi: 10.1063/1.4916857, (2015).
- [5] Ochab E., Petelenz B., Szałkowski M., Ruszel M., Sroka A., Bogdali P., "Upgrade of the equipment for production of gallium isotopes from proton-activated zinc targets", Institute of Nuclear Physics Polish Academy of Sciences, (2014).
- [6] Mukesh K. P., John F. B., Huailei J., Alan B. P., Timothy R., " Cyclotron production of ^{68}Ga via the $^{68}Zn(p,n)^{68}Ga$ reaction in aqueous solution", American Journal of Nuclear Medicine and Molecular Imaging, Vol.4, No.4, pp.303-310, (2014).
- [7] <https://www-nds.iaea.org/exfor/endl.htm>
- [8] Qaim S. M., "Nuclear data for medical applications: an overview, Radiochim Acta. Journal. Vol.89, PP.189-196, (2001).
- [9] Krane K. S., "Introductory Nuclear Physics", John Wiley and Sons, PP.378-379, (1988).
- [10] Szelecsenyi F., Suzuki K., Kovacs Z., Takei M. and Okada K., "Investigation of the $natZn(p,x)^{62}Zn$ nuclear process up to 70MeV: a new $^{62}Zn/^{62}Cu$ generator", Journal of Applied Radiation and Isotopes, Vol.58, p.377, UK (2003).
- [11] Hermanne A., "Evaluated cross section and thick target yield data of Zn+P processes for practical applications", Journal of ARI, Vol.49, No. 1005, (1998).

- [12] Hermanne A., Walravens N. and Cicchelli O., "Optimization of isotope production by cross section Determination", conference on Nuclear Data for Sciences and technology, Juelich, p.616, Germany (1991).
- [13] Levkovskij V. N., "Activation cross section nuclides of average masses ($A=40-100$) by protons and alpha-particles with average energies ($E=10-50$ MeV)", Book: Levkovskij, Act. Cs. By Protons and Alphas, Moscow, (1991).
- [14] Tarkanyi F., Szelecsenyi F., Kovacs Z. and Sudar S., "Excitation Functions of Proton Induced Nuclear Reactions on Enriched ^{66}Zn , ^{67}Zn and ^{68}Zn Production of ^{67}Ga and ^{66}Ga ", Journal of Radiochimica Acta, Vol.50, p.19 Germany, (1990).
- [15] Hille M., Hille P., Uhl M. and Weisz W., "Excitation Functions of (p,n) and (a,n) Reactions on Ni, Cu and Zn", Journal of Nuclear Physics, Section A, Vol.198, p.625, Netherlands (1972).
- [16] Howe H. A., "(P, N) Cross Sections of Copper and Zinc.", Journal of Physical Review, Vol.109, p.2083, USA, (1958).
- [17] Skakun E. A., Utenkov S. N., Bondarenko V. N., Goncharov A. V., Mishchenko V. M., Sukhostavets V. I. and Shebeko K. V., "Cross sections and rates of the thermonuclear reactions $^{64}\text{Zn}(p,g)^{65}\text{Ga}$ and $^{66}\text{Zn}(p,g)^{67}\text{Ga}$ ", Journal of Bulletin of Russian Academy of Sciences - Physics, Vol.72, p.376, USA (2008).
- [18] Zelecsenyi F., Boothe T. E., Takacs S., Tarkanyi F., Tavanoe., "Evaluated cross section and thick target yield data bases of Zn+p processes for practical applications", Journal of Applied Radiation and Isotopes, Vol.49, p.1005, UK (1998).
- [19] Little F. E. and Lagunas-Solar M. C., "Cyclotron Production of ^{67}Ga . Cross Sections and Thick-Target Yields for the $^{67}\text{Zn}(p,n)$ and $^{68}\text{Zn}(p,2n)$ Reactions", Journal of Radiochimica Acta, Vol.60, p.57, Germany (1993).
- [20] Hermanne A., "Evaluated cross section and thick target yield data of Zn+P processes for practical applications", Private communication Name. Hermanne (1997).
- [21] Krivonosov G. A., Ekchichev O. L., Nemashkalo B. A., Storizhko V. E. and Chirt V. K., "Radiative-Capture Cross Sections of Nuclides of Intermediate Atomic Weight for Low-Energy Protons", Journal of Izv. Rossiiskoi Akademii Nauk, Ser. Fiz., Vol.41, Issue.10, p.2196, Russia (1977).
- [22] Szelecsenyi F., Kovacs Z., Nagatsu K., Fukumura K., Suzuki K. and Mukai K., "Investigation of direct production of ^{68}Ga with low energy multiparticle accelerator", Radiochimica Acta, Vol.100, p.5, (2012).
- [23] Mcgee T., Rao C. L., Saha G. B. and Yaffe L., "Nuclear Interactions of Sc-45 and Zn-68 with Protons of Medium Energy", Journal of Nuclear Physics, Section A, Vol.150, p.11, Netherlands (1970).
- [24] Hille M., Hille P., Uhl M. and Weisz W., "Excitation Functions of (P,N) and (A,N) Reactions On Ni, Cu and Zn", Journal of Nuclear Physics, Section A Vol.198, p.625, Netherlands (1972).
- [25] Steyn J. and Meyer B. R., "Production of ^{67}Ga by deuteron bombardment of natural zinc", Journal of Applied Radiation and Isotopes, Vol.24, p.369, (1973).
- [26] Williams D. C. and Irvine J. W., "Nuclear excitation functions and thick-target yields: Zn+d and Ar-40(d, alpha)", Journal of Physical Review, Vol.130, No.1, p.265, USA (1963).
- [27] Vlasov N. A., Kalinin S. P., Ogloblin A. A., Pankratov V. M., Rudakov P., Serikov I. N. and Sidorov V. A., "Excitation functions for the reactions Mg-24(d,a)Na-22, Fe-54(d,a)Mn-52, Fe-54(d,n)Co-55, Zn-66(d,2n)Ga-66", Journal of Soviet Atomic Energy, Vol.2, p.189, USA (1957).
- [28] Nassiff S. J. and Munzel H., "Cross Sections for the Reactions $^{66}\text{Zn}(D,N)^{67}\text{Ga}$, $^{52}\text{Cr}(D,2N)^{52}\text{G}$ MN and $^{186}\text{W}(D,2N)^{186}\text{RE}$ ", Journal of Radiochimica Acta, Vol.19, Issue.3, p.97, Germany (1973).
- [29] Gilly J. L., Henriet G. A., Preciosa A. M. and Capron P. C., "Absolute cross sections and excitation functions for (d,p) and (d,2n) reactions on ^{55}Mn , ^{63}Cu , ^{65}Cu , ^{66}Zn , and ^{68}Zn between 3 and 11.6 MEV", Journal of Physical Review Vol.131, No.4, p.1727, (1963).

Research Article

Structural Properties of Nanoparticles TiO₂/PVA Polymeric Films

Samara A. Madhloom¹, Mahasin F. Al-Kadhemy¹, Jehan A. Salman²

¹Department of Physics, College of Science, Mustansiriyah University, IRAQ.

²Department of Biology, College of Science, Mustansiriyah University, IRAQ.

*Correspondent Author Email: samaraabbas1992@gmail.com, drmahasinf@yahoo.com, jehanmmd@yahoo.com

Article Info

Received
27/10/2016

Accepted
17/04/2017

Abstract

In this research, X-ray diffraction of the powder (PVA polymer, titanium dioxide with two particle sizes) and (TiO₂ (15.7 nm)/PVA and TiO₂ (45.7 nm)/PVA) films have been studied, the amount of polymer is (0.5) g and (0.01)g from each particle sizes of nanoparticles will be used. Casting method is used to prepare homogeneous films on glass petri dishes. All parameters accounted for the X-ray diffraction; full width half maximum (FWHM), Miller indices (hkl), size of crystalline (D), Specific Surface Area (S) and Dislocation Density (δ). The nature of the structural of materials and films will be investigated. The XRD pattern of PVA polymer has semi-crystalline nature and the titanium dioxide with two particle sizes have crystalline structure; anatase type. While the mixture between these materials led to appearing some crystalline peaks into XRD pattern of PVA polymer.

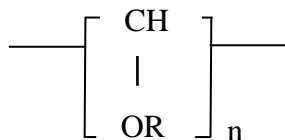
Keywords: Nanoparticle doped polymer, PolyVinyl Alcohol (PVA), Titanium dioxide (TiO₂), Structure Properties, X-ray diffraction (XRD) and Scanning Electron Microscopy (SEM).

الخلاصة

في هذا البحث، تم دراسة حيود الأشعة السينية لمساحيق (بوليمر PVA ، ثنائي أكسيد التيتانيوم ذو الحجمين الحبيبيين) و أغشية (TiO₂ (15.7 nm)/PVA and TiO₂ (45.7 nm)/PVA)، وقد استخدمت نسبة (0.5) غم من البوليمر و (0.01) غم من كلا الحجمين الحبيبيين للمادة النانوية. استخدمت طريقة الصب لتحضير أغشية متجانسة على أطباق زجاجية. تم حساب كل معاملات حيود الأشعة السينية ، أقصى منتصف لعرض الحزمة ، معاملات ميلر ، الحجم البلوري ، المساحة السطحية المحددة وكثافة الانخلاع. وتم بحث الطبيعة التركيبية للمواد والأغشية. وبينت النتائج أن حيود الأشعة السينية لبوليمر PVA هو ذو تركيب شبه بلوري وأن ثنائي أكسيد التيتانيوم ذو الحجمين الحبيبيين لها تراكيب بلورية: نوع (anatase). بينما المزيج بين هذه المواد أدى الى ظهور بعض الحزم البلورية في نموذج حيود الأشعة السينية لبوليمر PVA.

Introduction

The general chemical structure of PolyVinyl Alcohol (PVA) is shown in Fig. (1)[1].



Where R= H orCOCH₃

PVA is a polymer of great interest be-

Figure (1): Chemical structure of PVA polymer [1].

Biomedical applications [2]. It has been applied in the industrial, commercial, medical,

and food sectors and has been used to produce many end products, such as lacquers, resins, surgical threads, and food packaging materials that are often in contact with food [3]. PolyVinyl alcohol for food use is an odorless and tasteless, translucent, white or cream colored granular powder. It is most important soluble in water, Dimethyl Sulfoxide (DMSO), Ethylene Glycol (EG), and N-Methyl Pyrrolidone (NMP) [4]. Titanium dioxide belongs to the family of transition metal oxides. There are four commonly known polymorphs of TiO₂ found in nature: anatase (tetragonal), brookite (orthorhombic), rutile (tetragonal), and TiO₂ (B) (monoclinic). Besides these polymorphs,

two additional high-pressure forms have been synthesized from the rutile phase. These are TiO₂ (II) with the α -PbO₂ structure, TiO₂ (H) with hollandite, baddelleyite with ZrO₂, Co-tunnite with PdCl₂ [5]. Among these unique properties, nanosized organic and inorganic particles are being producing for use in medical properties. Titanium dioxide (TiO₂) also known as titanium oxide or titanium IV oxide or Titania, is the naturally occurring oxide of titanium. It is a versatile transition-metal oxide and a useful material in various present / future applications related to catalysis, electronics, photonics, sensing, medicine, and controlled drug release [6]. Used chemical spray pyrolysis technique to prepare thin films of titanium dioxide TiO₂ pure and TiO₂: PVA polymer on glass substrate preheated at (350 °C) for TiO₂ pure and at (160 °C) for TiO₂: PVA. With spray rate 3Sec. /1min, and thickness (250 nm). The investigation of (XRD) indicates that the structure of TiO₂ pure and TiO₂: PVA thin films are polycrystalline, and XRD investigation is anatase titanium dioxide. Where intensity of (101) is more than the intensity of (000), (200) and (105) for TiO₂ and TiO₂: PVA thin films. The optical properties measurement explains the effect of adding PVA on transmittance, absorbance, refractive index, absorption coefficient and electronic transitions of prepared thin films, their results observe that the filling of PVA generally increase optical properties [7]. Explained the effect of TiO₂ (5, 10 and 15 mg) nano-particles on optical, electrical and mechanical properties of poly (vinyl alcohol) (PVA) films. The un-doped (PVA) films show high transmittance in the visible region, and decrease with the increasing of TiO₂ [8]. Studied polyvinyl alcohol (PVA) doped with titanium dioxide nanoparticles at different weight percentage (1.25, 2.5, 5, 7.5, 10 TiO₂/PVA) are prepared using the sonification and casting techniques. The structural properties of those samples are examined by XRD, FTIR, and UV-Visible. The XRD pattern reveals that the amorphous domain in PVA polymer matrix increases with the raising of the TiO₂ content. The complexation of the dopant with the polymer is examined by FTIR studies. The absorption spectra of UV-Visible light shows irregular changes of the absorption for high doping samples in UV range (7.5, 10 TiO₂ /PVA). Ab-

sorbance, transmittance and reflectance spectra are used for the determination of the optical constants. The results indicate that the optical band gap is decreased with the increase of TiO₂ content, while the refractive index increases to high value for the composites of high dopant [9].

The aim of this work is to investigate the nature of the structural characteristics of PVA polymer, TiO₂ nanoparticles with two particle sizes (15.7 and 45.7) nm, TiO₂ (15.7 nm)/PVA and TiO₂ (45.7 nm)/PVA films that done by X-ray diffraction (XRD) and Scanning Electron Microscopy (SEM) measurement.

Materials and Methods

Pure PVA and TiO₂ nanoparticles doped PVA films have been prepared by employing solution casting method. Hot distilled water (~55°C) (10 ml) was used to dissolve (0.5 g) from PVA is a granular powder with molecular weight (M_w=14000 g/mole) obtained from (BHD Chemicals Ltd). This solution was magnetically stirred continuously for (3 hrs.) until mixture became homogeneous viscous solution. Then it poured into glass petri dish with diameter (8 cm) and keeps under room temperature (~30°C) for (7 days) to evaporate all solvent slowly. In order to prepare TiO₂ nanoparticles/PVA composite films with two particle sizes for TiO₂ nanoparticles; (15.7 and 45.7 nm) obtained from (Intelligent Materials Pvt. Ltd. United States) and (HIMEDIA), respectively. The amount of powder for each particle size as used (0.01 g) with (10 ml) hot distilled water. (6 ml) of this TiO₂ nanoparticles solution was added to PVA solution to get 15.7 nm TiO₂/PVA an and 45.7 nm TiO₂/PVA films. X-Ray Diffraction (XRD) instrument is from type (SHIMADZU XRD – 6000) made in Japan, with following specifications are Target is CuK_α, wavelength is 1.5406 Å, Current is 30 (mA) and Voltage is (40 KV) and Scanning Electron Microscopy (SEM) type (INSPECTS50) made in Holland. Mathematical definitions The particle size is calculating by equation (1). The average grain size of all the samples was estimated from X-ray line broadening analysis by Scherer's formula [10]:

$$D = \frac{K\lambda}{\beta \cos\theta} \quad (1)$$

Where (K) represents a Scherer's factor, normally taken as (0.94). λ is the X-ray wavelength, β is the value of the FWHM in degree unit and transform to radian by multiplying ($\pi/180$), θ is the Bragg's angle. Specific Surface Area (S) or (SSA) is the Surface Area (SA) per mass. Mathematically, SSA can be calculated using formula (2) [11]:

$$S = (6 \times 10^3) / (D_p \cdot \rho) \quad (2)$$

Where SSA & S are the specific surface area, D_p is the size (spherical shaped), and ρ is the density of TiO_2 (3.9 g/cm^3) and (4.23 g/cm^3) particle sizes (15.7 and 45.7) nm, respectively.

The dislocation density is the length of dislocation lines per unit volume of the crystal [12]. The dislocation density (δ) in the sample has been determined using equation (3) [13]:

$$\delta = 1/D^2 \quad (3)$$

Results and Discussion

The X-ray diffraction of pure PVA powder is shown in Figure (2). The observation of the maximum intensity diffraction peak (331) at $2\theta = 19.7167^\circ$ corresponding d-spacing 4.49908 \AA to the (110) reflection a plane which contains the extended planar zig-zag chain direction of the crystallites. That is indicate PVA has semi-crystalline nature [14]. Firstly; the peaks at 2θ less than (20°) are due to crystalline nature which may be attributed to intermolecular interaction of hydrogen bonding for PVA chains. Secondly; two small peaks at $2\theta = 23.2148^\circ$, 17.3494° corresponding d-spacing 3.82848 \AA 5.10727 \AA , with intensities (73) and (54), respectively. These re-

sults are matching with results obtained from [7] and [9]. The value of particle size is calculated by equation (1) nearly (3.0543 nm). Table (1) illustrated some structural properties for pure PVA powder.

Table 1: XRD Parameters for Pure PVA Powder.

2 θ (deg)	FWHM (deg)	Intensity (counts)	d (\AA)
11.5143	1.45000	19	7.67902
14.5363	0.52000	11	6.08869
15.8327	1.30660	28	5.59294
16.4911	0.0000	41	5.37110
17.3494	0.0000	54	5.10727
19.7167	1.954	331	4.49908
23.2146	1.4934	73	3.82848
40.6984	1.9900	42	2.21516
42.3323	1.1200	17	2.13336

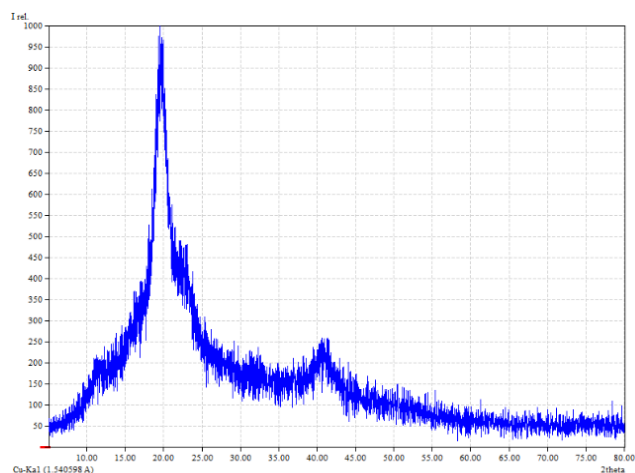


Figure (2): XRD pattern for pure PVA powder.

Table (2a): XRD Parameters for Pure TiO_2 (15.7 nm) Powder.

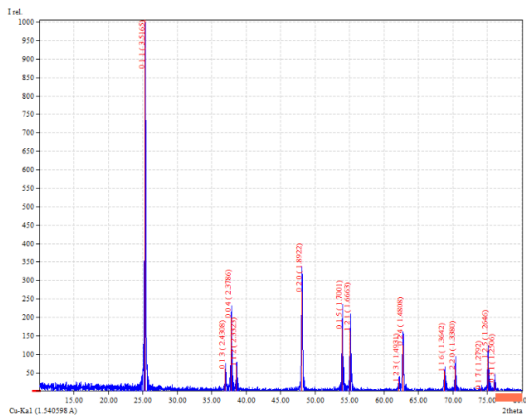
2 θ (deg)	FWHM (deg)	Intensity (counts)	d (\AA)	hkl	D(nm)	$S \times 10^6$ ($\text{m}^2 \cdot \text{g}^{-1}$)	$\square \times 10^6$ (m^2)
25.3424	0.54100	285	3.51165	011	15.1	0.1018	4.385
36.9362	0.28000	16	2.43168	013	30.4	0.0505	1.082
37.8804	0.67000	50	2.37321	004	12.6	0.1220	6.298
38.7148	0.50000	12	2.32396	112	16.9	0.0910	3.501
48.0716	0.59500	77	1.89120	020	14.7	0.1046	4.627
53.9815	0.75000	39	1.69727	015	11.9	0.1292	7.061
55.0311	0.73000	39	1.66735	121	12.2	0.1260	6.718



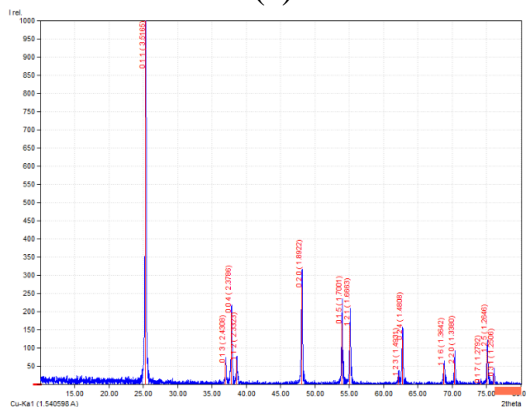
62.0836	0.40000	12	1.49380	123	23.4	0.0657	1.826
62.7034	0.76000	28	1.48052	024	12.3	0.1250	6.609
68.8616	0.76000	10	1.36237	116	12.7	0.1211	6.200
70.3212	0.64000	12	1.33763	220	15.2	0.1011	4.328
75.0799	0.84000	16	1.26421	125	11.9	0.1292	7.061

Table (2b): XRD Parameters for Pure TiO₂ (45.7 nm) Powder.

2θ(deg)	FWHM (deg)	Intensity (counts)	d (Å)	hkl	D(nm)	Sx10 ⁶ (m ² . g ⁻¹)	□x10 ⁵ (m ⁻²)
25.3712	0.21100	759	3.50773	011	39.5	0.0358	6.409
37.0077	0.19670	46	2.42715	013	43.0	0.0329	5.408
37.8515	0.2010 □ 0	172	2.37496	004	41.9	0.0338	5.696
38.6286	0.18750	48	2.32895	112	45.9	0.0308	4.746
48.0967	0.19930	253	1.89027	020	44.6	0.0317	5.0272
53.9434	0.20180	159	1.69838	015	44.4	0.0319	5.0726
55.1201	0.21570	147	1.66487	121	42.2	0.0336	5.6153
62.1691	0.17900	25	1.49196	123	52.2	0.0271	3.6699
62.7443	0.20810	119	1.47965	024	45.1	0.0314	4.9163
68.8009	0.21860	45	1.36343	116	44.2	0.0320	5.1186
70.3422	0.19800	55	1.33728	220	49.9	0.0284	4.0160
75.0910	0.214200	85	1.26405	125	47.3	0.0299	4.4696
76.0766	0.186000	25	1.25011	031	55.0	0.0257	3.3057



(a)



(b)

Figure (3): XRD Pattern for Pure TiO₂ nanoparticles powder with two particles sizes a-(15.7 nm) b-(45.7 nm).

The X-ray diffraction pattern of pure TiO₂ nanoparticles powder with two particles sizes are shown in Figure (3) (a) (b), respectively. Strong diffraction peaks at 25°, 48° and 37° indicating TiO₂ in the anatase phase, the intensities of XRD peaks of the sample reflects that the formed nanoparticles are crystalline [7,9]. The intensity is increased with decreasing the Particle size, the particle size is nearly (15.7 nm) for Figure 3a and (45.7 nm) for Figure 3-b. Table 2 (a) (b) illustrated some structural properties for pure TiO₂ nanoparticles with two particle sizes, respectively.

We conclude from table (2 A, B) the specific surface area (S) and dislocation density (□) are decreased with increasing the particle size of TiO₂ nanoparticles.

The X-ray diffraction pattern for (6 ml) TiO₂ (for two particles sizes (15.7 nm) and (45.7 nm))/PVA films are shown in Figure (4) (a)(b), respectively. From these figs., the effect of TiO₂ nanoparticles with two particles sizes on PVA structure still amorphous behavior with appear-

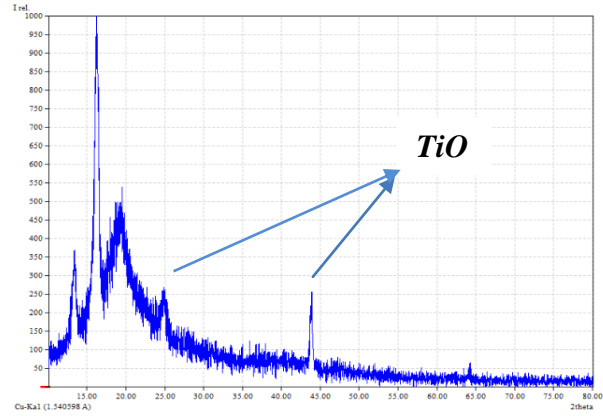
ing some crystalline peak with addition TiO₂ nanoparticles [7, 9]. The intensity is increase with increasing the particle size of TiO₂ nanoparticles and the particle size found by eq. (1) are nearly (17.0261, 79.4998) nm for TiO₂ (15.7, 45.7) nm/PVA, respectively. Table (4-5) (a) (b) which it emerged adding PVA polymer enhanced the structural properties of TiO₂ thin film.

Table (3a): XRD Parameters for TiO₂ (15.7 nm)/PVA Film.

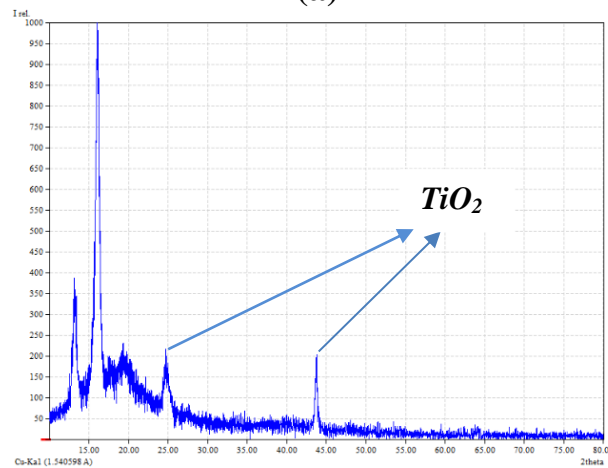
2θ (deg)	FWHM (deg)	Intensity (counts)	d (Å)	D (nm)
13.3140	0.62800	98	6.64479	12.838
14.5000	1.00000	15	6.10385	8.0610
16.1722	0.66200	396	5.47629	12.269
19.1800	2.00000	143	4.62374	39.758
24.8216	0.82330	48	3.58413	9.974
43.7905	0.44760	81	2.06564	19.257

Table (3b): XRD Parameters for TiO₂ (45.7 nm)/PVA Film.

2θ (deg)	FWHM (deg)	Intensity (counts)	d (Å)	D (nm)
13.2065	0.61890	172	6.69864	127.53
16.0854	0.61950	595	5.50564	127.81
19.7000	0.00000	53	4.50285	0.0000
20.4000	1.30000	28	4.34989	6.2286
24.8025	0.75500	71	3.58685	10.8405
43.7164	0.41290	85	2.06897	204.59



(a)



(b)

Figure (4): XRD Pattern for a- TiO₂ (15.7 nm)/PVA and b- TiO₂ (45.7 nm)/PVA Films.

The SEM images of TiO₂ at different magnification are shown in Figure (5) for TiO₂ (15.7 nm) and Figure (6) for TiO₂ (45.7 nm) which confirms that the TiO₂ nanoparticles are pseudo spherical in shape. It has been observed that TiO₂ nanoparticles are agglomerated to form clusters. The effect of increasing particle size of TiO₂ leads to form big agglomerated. This result is matching with [15].

Figures (7, 8) show micrographs of (6ml) TiO₂ nanoparticles with two particles sizes (15.7, 45.7) nm doped with PVA films, respectively. It can be seen that TiO₂ nanoparticles cover the surface of PVA films and emerge PVA particles to form white granule scattered randomly. The SEM image of TiO₂/PVA films shows the rough

surface with some gathering of TiO₂ nanoparticles in PVA, this result is matching with [8].

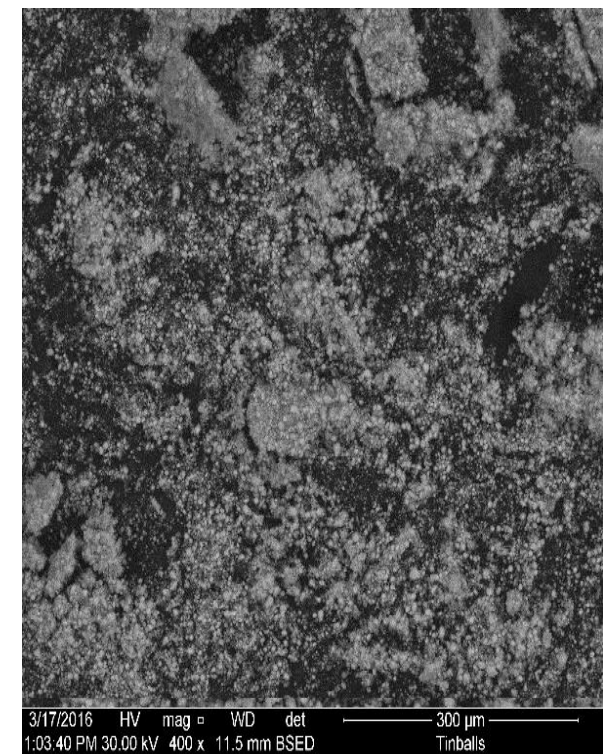
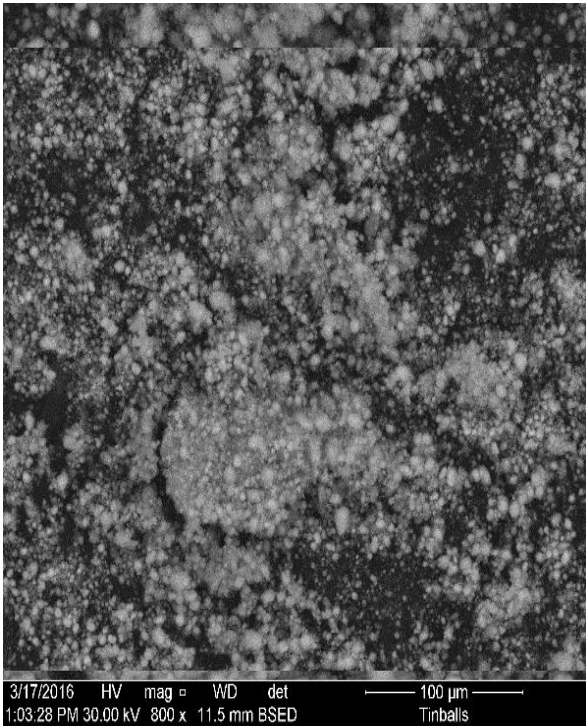


Figure (5): SEM micrographs for TiO₂ Powder with particle size (15.7 nm).

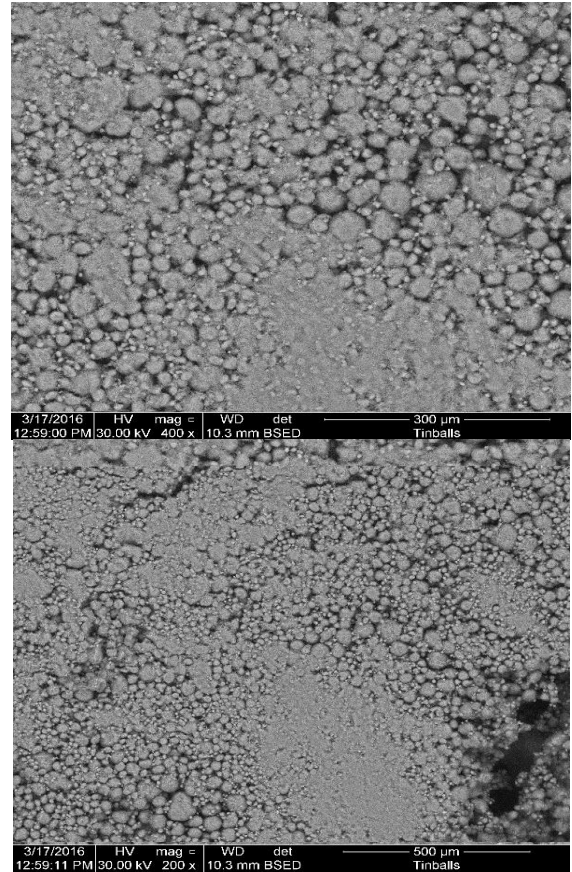


Figure (6): SEM micrographs for TiO₂ Powder with particle size (45.7 nm).

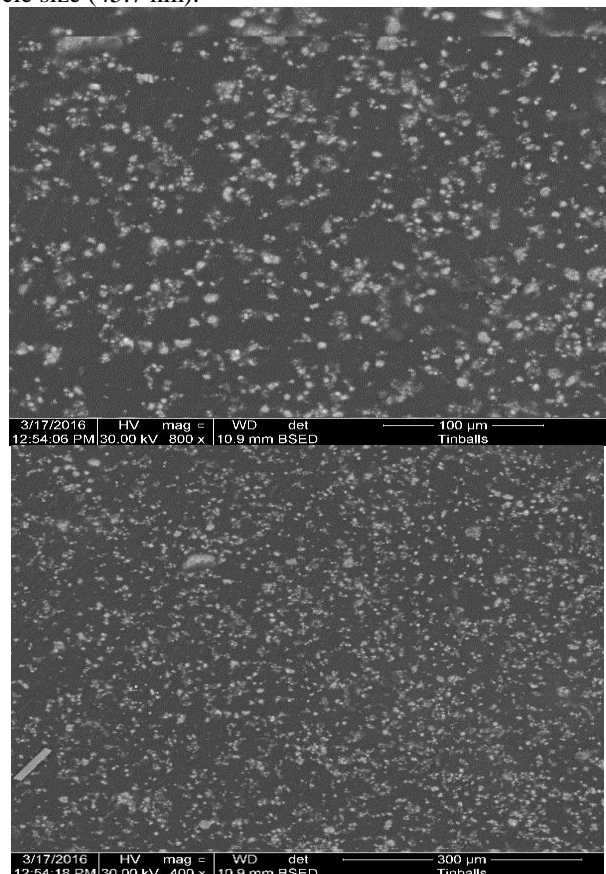


Figure (7): SEM micrographs for TiO₂ (15.7 nm)/PVA Films.

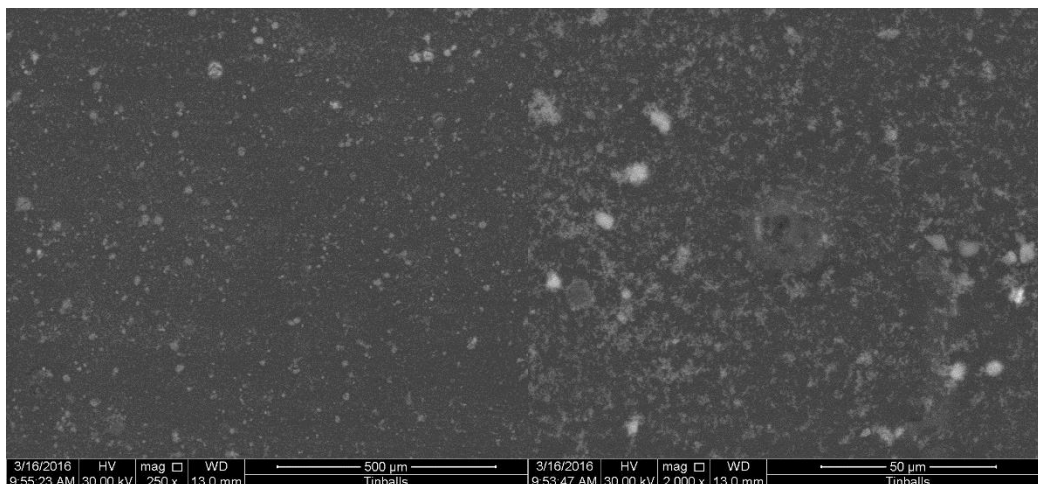


Figure (8): SEM micrographs for TiO₂ (45.7 nm)/PVA Films.

Conclusions

XRD parameters of materials and films calculated and have known the nature of the structural of materials and films. In spite of crystalline materials TiO₂ nanoparticles, the polymer still amorphous behavior with appearing some crystalline peak from these materials in it, the specific surface area (S) and dislocation density (D) are decreased with increasing the particle size of TiO₂ nanoparticles. The SEM showed crystalline structure of TiO₂ nanoparticles and matching with XRD results, The SEM image of TiO₂/PVA films showed rough surface with some gathering of PVA polymer.

References

- [1] S. K. Saxena, (2004), Polyvinyl Alcohol (PVA), Chemical and Technical Assessment 61st JECFA, 1-3.
- [2] C. M. Hassan, N. A. Peppas, (2000), Structure and Applications of Poly (vinyl alcohol) Hydrogels Produced by Conventional Crosslinking or by Freezing/Thawing Methods, *Adv. Polym. Sci.*, 153, 37-65.
- [3] C. C Demerlis, D. R. Schoneker, (2003), Review of the oral toxicity of polyvinyl alcohol (PVA), *Food Chem. Toxicol*, 41, 319–326.
- [4] J. C. J. F Tacx, H. M. Schoffeleers, A. G. M. Brands, L. Teuwen, (2000), Dissolution Behavior and Solution Properties of Polyvinylalcohol as Determined by Viscometry and Light Scattering in DMSO, Ethylene Glycol and Water, *Polymer*, 41, 947-957.
- [5] J. F. Banfield, A. Navrotsky, (2001), Nanoparticles and the Environment, Mineralogical Society of America, Washington, D. C.
- [6] A. Kumar, S. P. Hsun Lo and S. M Chen, (2008), Electrochemical synthesis and characterization of TiO₂ nanoparticles and their use as a platform for flavin adenine dinucleotide immobilization and efficient electrocatalysis, *Nanotechnology*, 19, 255501-255507.
- [7] A. F. Saleh, A. M. Jaffar, N. A. Samoom and M. W. Mahmmmod, (2014), Effect Adding PVA Polymer on Structural and Optical Properties of TiO₂ Thin Films, *Journal of Al-Nahrain University*, 17 (2), 116-121.
- [8] M. Vishwas, K. N. Rao, D. N. Priya, A. M. Raichur, R. P. S. Chakradhar and K. V. Warlu, (2014), Effect of TiO₂ nanoparticles on Optical, electrical and Mechanical Properties of Poly (vinyl Alcohol) Films, *Procedia Materials Science*, 5, 247-254.
- [9] A. M. Shehap and D. S. Akil, (2016), Structural and optical properties of TiO₂ nanoparticles/PVA for different composites thin films, *Int. J. Nanoelectronics and Materials*, 9, 17-36.

- [10] Jia-Guo Yu, Xiu-Jian Zhao, Huo-Gen Yu, Bei Cheng, Wing-Kei Ho, (2003), physical chemistry, The Effect of Calcination Temperature on the Surface Microstructure and Photocatalytic Activity of TiO₂ Thin Films Prepared by Liquid Phase Deposition, *B* 107 (50) ,13871-13879.
- [11] L. C. Nehru, V. Swaminathan, C. Sanjeeviraja, (2012), Photoluminescence Studies on Nanocrystalline Tin Oxide Powder for Optoelectronic Devices, *American. J. Mat. Sci.*, 2(2): 6-10.
- [12] D. B. Sirdeshmukh, L. Sirdeshmukh, K. G. Subhadra, (2006), *Micro- and Macro-Properties of solids: Thermal, Mechanical and Dielectric properties*, Springer, NewYork.
- [13] Y. P. V. Subbaiah, P. Prathap, K. T. R. Reddy, (2006), Structural, electrical and optical properties of ZnS films deposited by close-spaced evaporation. *Appl. Surf. Sci.*, 253(5): 2409-2415.
- [14] M. S. Jalil, (2015), *Physical Properties, Antibacterial and antibiofilm Activities of PVA Polymer with Safranin Dye and Biosurfactant*, Ph. D Thesis, College of Science, Al-Mustansiriyah University.
- [15] K. K. Senapati, Ch. Borgohain and P. Phukan, (2012), CoFe₂O₄-ZnS nanocomposite: a magnetically recyclable photocatalyst, *Electronic Supplementary Material (ESI) for Catalysis Science and Technology*.

Research Article

Study of Nuclear Structures for Nd 148,150,152 a Isotopes by Using IBM-1

Sallama S. Hummadi

Department of Physics, College of Science, AL-Mustansiriyah University, Iraq

*Correspondent Author Email: sallamasadiq@yahoo.com

Article Info

Received
16/01/2016

Accepted
17/04/2017

Abstract

The nuclear structures of even-even isotopes Nd (A=148,150,152) are studied by using the first Interacting Boson Model (IBM-1). The energy levels of ground state, beta and gamma bands ,energy ratios are calculated. The results showed dynamical symmetry of these isotopes SU(3)-SU(6), SU(5)-SU(6).

الخلاصة

في البحث الحالي استخدم نموذج البوزونات المتفاعلة الاول (IBM-1) لحساب مستويات الطاقة للنظير Nd ضمن الاعداد الكتليه (A= 148-150-154) وتم حساب مستويات الطاقة للحاله الارضية(ground band) وحزمة بيتا وكاما وكذلك تم حساب نسب الطاقة. وظهرت النتائج التناظرات الديناميكية للنظائر هي, SU(3)-SU(6) SU(5)-SU(6).

Introduction

The Interacting Boson Model version one (IBM-1) describes the low-lying nuclear spectra by assuming that an even-even nucleus, consists of inert core plus some valence particle ci. e particles outside the major closed shells at 2, 8, 20, 28, 50, 82, 126and 184. [1]

Many nuclei with N and Z values between magic numbers are constantly deformed in their shape, the deformation arises because of the way valence nucleons regulate themselves in an unfilled shell, in other words the deformation happens only when both proton and neutron shells are partially filled[1].

Furthermore, the valance particles tend to pair together to form bosons one with angular momentum 0 and 2. [1] The pairs with angular momentum I=2 called d-bosons, while the pairs with angular momentum I=0 called S-bosons.

[2]

Theoretical Bases

The Interacting Boson Model model (IBM) Hamiltonian operator function according to IBM-1 is written in terms of creation and annihilation operators as follows. [3,4]

$$\hat{H} = \varepsilon \hat{n}_d + a_0(\hat{P}^+ \cdot \hat{P}) + a_1(\hat{I} \cdot \hat{I}) + a_2(\hat{Q} \cdot \hat{Q}) + a_3(\hat{T}_3 \cdot \hat{T}_3) + a_4(\hat{T}_4 \cdot \hat{T}_4) \dots \dots (1)$$

Where ε , a_0 , a_1 , a_2 , a_3 and a_4 are parameters used in IBM-1 to determine the Hamiltonian function, and:

$$\mathcal{E} = \mathcal{E}_d - \mathcal{E}_s \quad (2)$$

Where \mathcal{E} = Boson's energy.

$$\mathcal{E}_d = d\text{-Boson's energy} \quad (3)$$

$$\mathcal{E}_s = s\text{-Boson's energy} \quad (4)$$

$$\hat{n}_d = (\hat{d}^+ \times \hat{d}) \equiv d\text{-bosons operator} \quad (5)$$

$$\hat{P} = \frac{1}{2}(\hat{d} \times \hat{d}) \frac{1}{2}(\hat{S} \times \hat{S}) \equiv \text{operator of pairing among bosons} \quad (6)$$

$$\hat{I} = \sqrt{10} \left[\hat{d}^+ \times \hat{d} \right]^{(1)} \equiv \text{Angular} \quad (7)$$



$$\hat{Q} = \left[\hat{d}^+ \times \hat{s}^- + \hat{s}^+ \times \hat{d}^- \right] - \frac{\sqrt{7}}{2} \left[\hat{d}^+ \times \hat{d}^- \right]^{(2)} \equiv \text{momentum operator} \quad (8)$$

$$\hat{T}_3 = \left[\hat{d}^+ \times \hat{d}^- \right]^{(3)} \equiv \text{Quadrupole operator} \quad (9)$$

$$\hat{T}_4 = \left[\hat{d}^+ \times \hat{d}^- \right]^{(4)} \equiv \text{Hexadecapole operator} \quad (10)$$

Where the operators of creation $\left(\hat{s}^+, \hat{d}^+ \right)$ and operators of annihilation $\left(\hat{s}^-, \hat{d}^- \right)$ are used in fulfilling the following commutatio relations. [5-7].

Results and Discussion

This is done to study the structure of deformed nuclei. These deformed nuclei are; Nd 148–152, Nd – 148 lying in the limit SU (5) – O (6) while the Nd – 150,154 in the limit SU (3) – O (6) dynamical symmetry. The dynamical symmetry of each isotope was determined according to the following:

1. Energy ratios shown in Table 3.
2. The typical energy spectrum was used also. [4]
3. Energy bands (i. e g, β, γ -bands)

Table 1 shows each isotope which have been studied in this work the best fitted interaction parameters values of equivalent Hamiltonian operators function of equation (1) for the energies in(MeV)units and show dynamical symmetry for each isotope.

Table 2 shows the values of parameters of the Hamiltonian operator functions, which are fitted to the data for special symmetries of these isotopes. Table 3 shows the relation between the experimental and calculated energy ratios as a function of neutron number for (Nd¹⁴⁸ – Nd¹⁵²) respectivley. The nuclear structures of even-even nuclei in this mass region A (=148, 150, 152). We have finding the dynamical symmetry of each isotope by comparing the energy ratios with

their identical and experimental values as shown in Table 3.

We used the (IBM-1)) Hamiltonian to determain theoretical energy levels compared with the experimental values of of the even – even isotopes ¹⁴⁸⁻¹⁵⁰⁻¹⁵² Nd.

Table 3 clarify that the energy ratios E(4₁⁺)/E(2₁⁺), E(6₁⁺)/E(2₁⁺) and E(8₁⁺)/E(2₁⁺) for the theoretical and experimental values for Nd(A =148–152) isotopes, there is a good agreement.

Figures 1, 2, and 3 are display the comparisons between theoretical and experimental energy levels for selected isotopes ¹⁴⁸⁻¹⁵⁰⁻¹⁵² Nd. [8]

Figures 1, 2, and 3 indicate the values of bands energies (g, β , γ) for each isotope (¹⁴⁸Nd₈₈, ¹⁵⁰Nd₉₀, ¹⁵²Nd₉₂) rapprochement with the experimental.

From the calculated energy rates E(4₁⁺)/E(2₁⁺), E(6₁⁺)/E(2₁⁺) and E(8₁⁺)/E(2₁⁺), it becomes clear that (¹⁴⁸Nd₈₈, ¹⁵⁰Nd₉₀, ¹⁵²Nd₉₂) tend to symmetry O(6) and, ¹⁵²Nd₉₂ tend to symmetry SU(3). [9]

Figures A, B, and C show the relation between the energy ratios as a function of number of neutron (N) for the even-even Nd (A=148-152) isotopes.

Conclsoions

The Interacting Boson Model, version one (IBM-1), gives a good values for the energy levels as compare with the experimental values. Since the energy levels depends on the overall bosons number so that only the ground state band will appear.

From above it can be seen that when the number of bosons increase the symmetry is translate from O(6) to SU(3). The value of the energy levels is increase when the number of bosons decreases.

Energy levels of even-even isotopes (¹⁴⁸Nd₈₈, ¹⁵⁰Nd₉₀, ¹⁵²Nd₉₂) have been labeled according to the three bands (g, β , γ).

The β band is wider than γ band for dunamical symmetry SU(3) but γ band for isotopes of dynamical symmetry O(6) appears increasind. [10]

Table 1: Theoretical energy levels and energy transitions compared with experimental data for chosen even- even isotopes. [11, 12].

Isotop	I^π	Energy level(MeV)		Isotop	I^π	Energy level(MeV)		Isotop	I^π	Energy level(MeV)	
		Exp ⁰	IBM-1 (pw)			Exp ⁰	IBM-1 (pw)			EXP ⁽¹⁾	IBM-1 (pw)
${}^{148}_{60}\text{Nd}$	2^+_{1+}	0.3017	0.323	${}^{150}_{60}\text{Nd}$	2^+_{1+}	0.1301	0.12	${}^{152}_{60}\text{Nd}$	2^+_{1+}	0.0759	0.075
	4^+_{1+}	0.7575	0.688		4^+_{1+}	0.3815	0.397		4^+_{1+}	0.2406	0.237
	6^+_{1+}	1.275	1.095		6^+_{1+}	0.7212	0.825		6^+_{1+}	0.4879	0.47
	8^+_{1+}		1.544		8^+_{1+}	1.1307	1.399		8^+_{1+}	0.81	0.764
	0^+_{2+}	0.7237	0.724		0^+_{2+}	0.6767	0.672		0^+_{2+}	1.139	1.211
	2^+_{2+}	1.171	0.767		2^+_{2+}	0.8514	0.802		2^+_{2+}	1.251	1.331
	4^+_{2+}	1.8586	1.217		4^+_{2+}	1.1386	1.095		4^+_{2+}		1.521
	6^+_{2+}		1.708		6^+_{2+}		1.542		6^+_{2+}		1.774
	8^+_{2+}		2.24		8^+_{2+}		2.132		8^+_{2+}		2.078
	0^+_{3+}	0.9167	1.324		2^+_{3+}	1.0624	1.394		2^+_{3+}		0.93
	2^+_{3+}		1.762		3^+_{1+}		1.536		3^+_{1+}		1.065
	4^+_{3+}		1.831		4^+_{3+}		1.703		4^+_{3+}		1.156
	6^+_{3+}		2.405		5^+_{1+}		1.929		5^+_{1+}		1.346
	8^+_{3+}		3.641		6^+_{3+}		2.167		6^+_{3+}		1.43
	2^+_{4+}	1.2486	1.185		7^+_{1+}		2.477		7^+_{1+}		1.691
	3^+_{1+}	1.5124	1.263		8^+_{3+}		2.776		8^+_{3+}		1.752
	4^+_{4+}	1.6875	1.686								
	5^+_{1+}		1.776								
6^+_{4+}		2.229									
7^+_{1+}		2.33									
8^+_{4+}		2.814									

Table 2: The parameters of Hamiltonian function operator for Nd (A = 148-152) isotopes.

Isotopes	N_x	N_y	N_{Tot}	ESP MeV	$\hat{p}\hat{p}$ MeV	$\hat{i}\hat{j}$ MeV	$\hat{Q}\hat{Q}$ MeV	(\hat{i}, \hat{i}_x) MeV	(\hat{i}, \hat{i}_y) MeV	CHI
${}^{148}_{60}\text{Nd}$	5	3	8	0.0010	0.0000	0.0048	0.0030	0.0501	0.0738	1.3000
${}^{150}_{60}\text{Nd}$	5	4	9	0.5500	0.0000	0.0080	-0.0087	0.0311	-0.0312	-1.2400
${}^{152}_{60}\text{Nd}$	5	5	10	0.0001	0.0600	0.0009	-0.1300	0.0576	0.0000	-1.1680

Table 3 : show the relation between the experimental and calculated energy ratios as a function of neutron number for (Nd¹⁴⁸ – Nd¹⁵²) respectively. [13]

Isotopes	E(4 ₁ ⁺) / E(2 ₁ ⁺)		E(6 ₁ ⁺) / E(2 ₁ ⁺)		E(8 ₁ ⁺) / E(2 ₁ ⁺)	
	EXP.	IBM-1 (pw)	EXP.	IBM-1 (pw)	EXP.	IBM-1 (pw)
¹⁴⁸ ₆₀ Nd ₈₈	2.5107	2.1300	4.2260	3.3900	0.0000	4.7801
¹⁵⁰ ₆₀ Nd ₉₀	2.9323	3.3033	5.5434	6.8750	8.6910	9.6580
¹⁵² ₆₀ Nd ₉₂	3.1699	3.1225	6.4281	6.2666	10.8719	10.1866

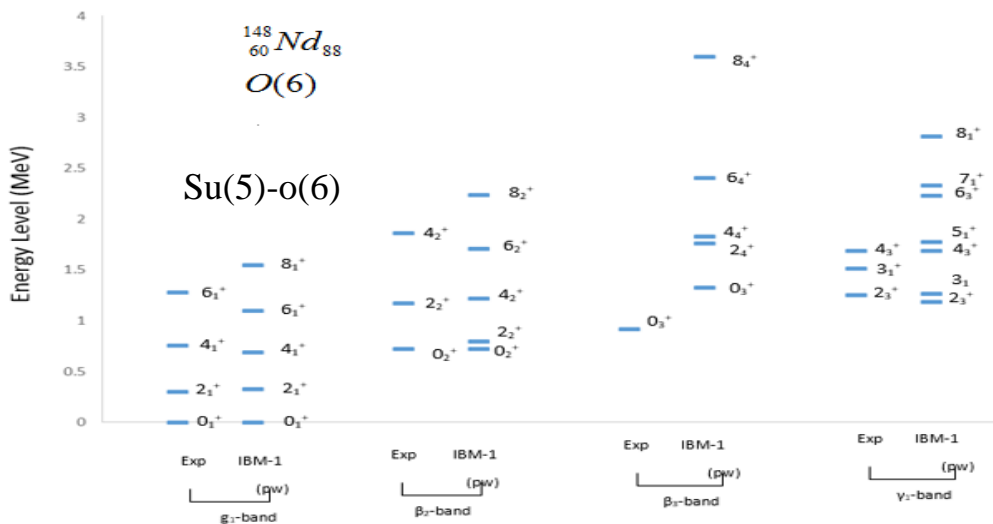


Figure 1: Comparison between calculated IBM (pw) and experimental energy levels states g, β, γ in isotope ¹⁴⁸₆₀Nd₈₈ of the dynamical symmetry su(5)-o(6).

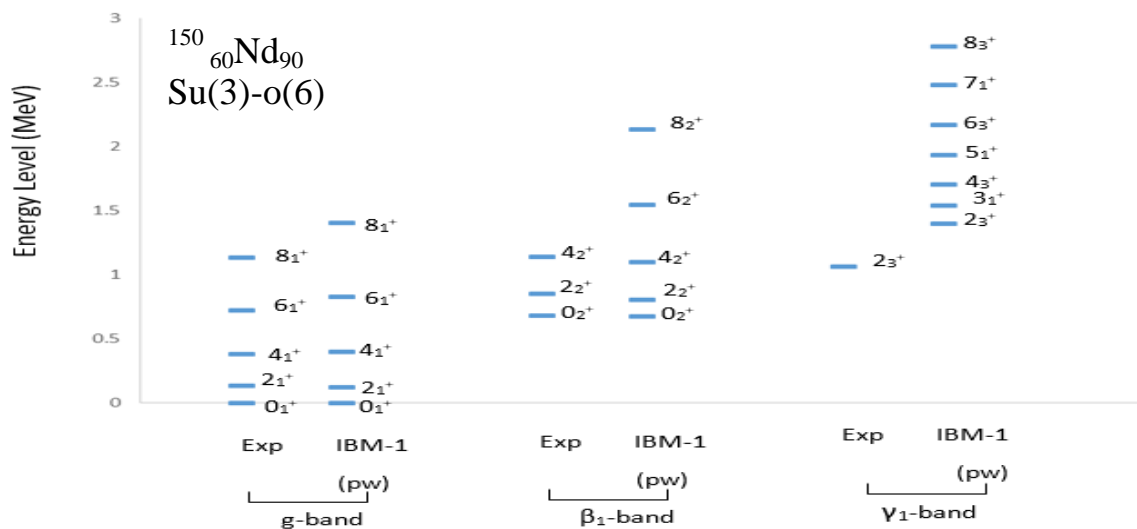


Figure 2: Comparison between calculated IBM (pw) and experimental energy levels states g, β, γ in isotope ¹⁵⁰₆₀Nd₉₀ of the dynamical symmetry su(3)-o(6).

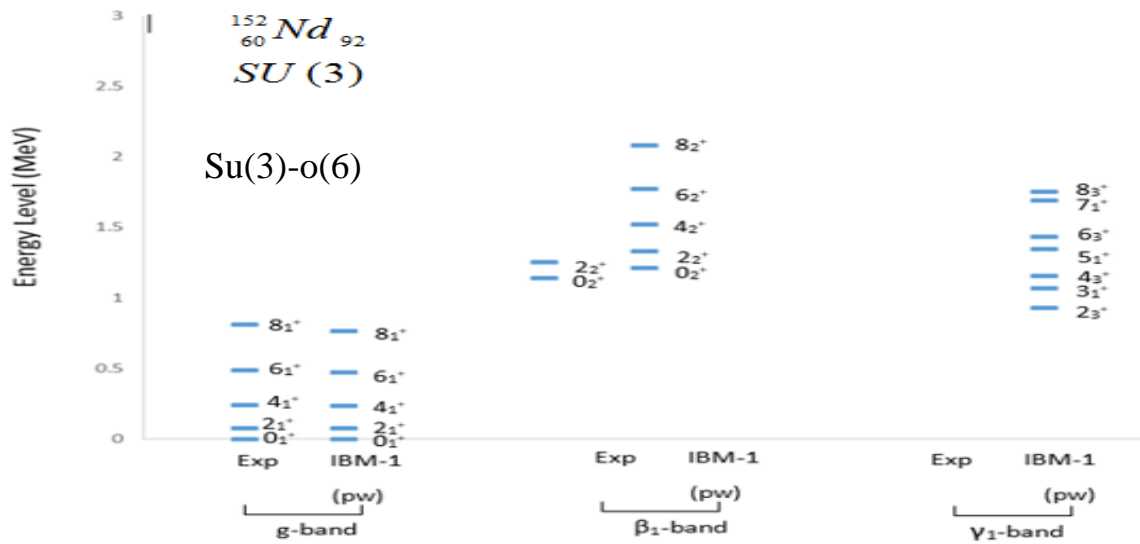
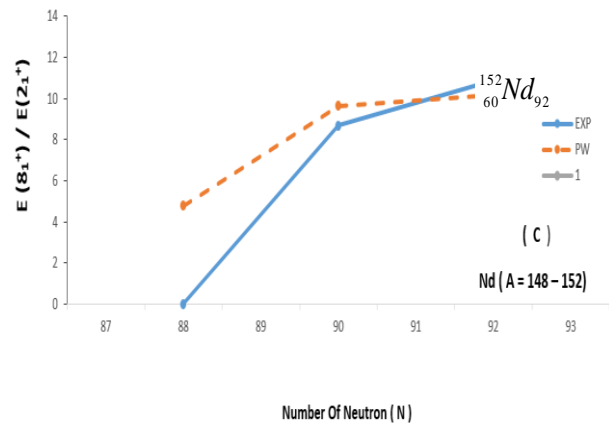
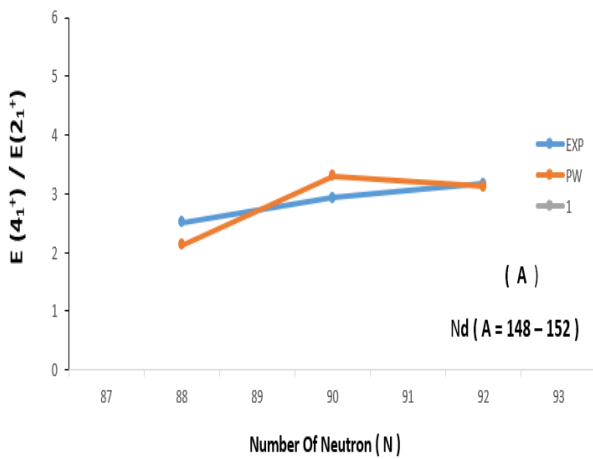
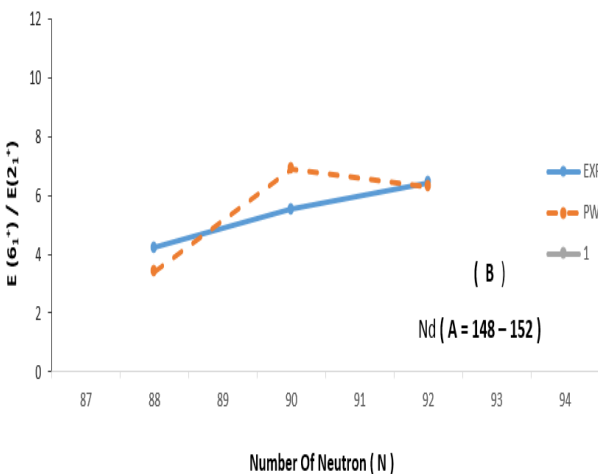


Figure 3: Comparison between calculated IBM (pw) and experimental energy levels states g, β, γ in isotope of the dynamical symmetry $SU(3)-o(6)$



Figures A, B, C: The relation between the energy ratios as a function of number of neutron N for the even-even Nd ($A=148-152$) isotopes.



References

- [1] Abdul-Ameer A.: Ph. D thesis "Investigations of nuclear energy levels in ^{82}Kr , ^{76}Se and ^{194}Pt " submitted to University of London, 1991.
- [2] Bonatsos D.: Interacting boson model of nuclear structure, Ed. David Stanford, Pub. In the Unites states by Oxford university press, New York. 7th priting, PP.1-50, 1988.

- [3] Omar Ahmed M.: phd thesis Nuclear structure calculations of some even A (even-even) and odd A Nuclei, using IBM-1 and
- [4] John L.: Nuclear physics (principles and application), Pub. Willey and Sons, PP.45-61, (2001).
- [5] Arima A. and Iachello F.: the interacting boson model, Ed. Iachello F., Pub. The press syndicate of a university of Cambridge, England, PP.1-133, 1987.
- [6] Casten R. F. and Warner D. D.: Rev. Mod. Phys., vol.60, P.391, 1988.
- [7] Yoshiaga N.: nud. Phys. A. Vol.522, 99C.1991.
- [8] Mitsuo Sakai, Atomic Data and Nuclear Data Tables, 31,399-432, (1984).
- [9] H. C. Wu, A. E. L. Dieperink: Physical Review C Volume 38, Number 4 P.1638-1648 ,1988.
- [10] Z. P. Li, * T. Nikšić, and D.: Vretenar. Physics Department, Faculty of Science, University of Zagreb, Croatia. Microscopic Analysis of Nuclear Quantum Phase Transitions in the $N \approx 90$ region P.17, 18(October 28, 2013).
- [11] Raja 'a S. N., M. Sc. Thesis Submitted to the Council of College of Science Baghdad University (1981).
- [12] Pietralla N. ,Fransen C. ,Belic D. ,Von Brentano P. ,FrieBner C. ,Kneissl V. ,Linnemann A. ,Nord A. ,Pitz H. H. ,Otsuka T. ,Schneider I. , Werner V. ,and Wiedenhover I. ,Phys. Rev. Lett. Vol.83, 1303(1999).
- [13] Casten R. F. and Warner D. D.: Rev. Mod. Phys., vol.60, P.391, (1988).

IBFM-1 submitted to

Research Article

Study Stopping Power Collision in one of Nuclear Element

Sanar G. Hassan

Department of Physics, College of Science, Mustansiriyah University, IRAQ.

*Email: sanargasid@gmail.com

Article Info

Received
29/05/2016

Accepted
18/01/2017

Abstract

The retarding force of the charged particles when interacts with matter causing loss of particle energy, this physical phenomenon in nuclear physics called stopping power. It has a lot of important applications such as in nuclear medicine and privation effects of radiations. The charge particles are alpha and beta particles. In this paper we studies the stopping power, collision and the stopping power of radioactivity of nuclear elements and to find the relationship between stopping power collision and stopping power of radioactivity, with arrange of CSDA range for the low energy electrons data of element F. The CSDA range he CSDA range it is an average distant length of the moving charge particles when it is path slows to stop. By using approximation of CSDA range we can calculate the rate of the loss in the energy at any point along the path of the travel by assuming these energies loss at points of the track are equal to whole stopping power loss. The CSDA range can be found by reciprocal integration of the total stopping power. from the Figures (3),(4),(5) and(6)we can get good results

الخلاصة

ان إعاقة الجسيمات المشحونة عند تفاعلها مع المادة بسبب خسارة في طاقة الجسيمات، هذه الظاهرة الفيزيائية في الفيزياء الذرية والفيزياء النووية تسمى قدرة الايقاف. ان قدرة الايقاف لها الكثير من التطبيقات الهامة في مجال التأثيرات الذرية، الطب النووي ومجال الإشعاعية. ان الجسيمات المسؤولة تتمثل بجسيمات ألفا وجسيمات بيتا. في هذا البحث، قمنا بدراسة قدرة الايقاف، التصادم وقدرة الايقاف للنشاط الإشعاعي في العناصر النووية وإيجاد العلاقة بين قدرة الايقاف التصادمية وقدرة الايقاف في النشاط الإشعاعي، مع ترتيب لمجموعة CSDA (التباطا المستمر لتقريب المدى) لبيانات طاقة الإلكترونات الواطنة للعنصر F. أن نطاق CSDA يمثل متوسط طول الازاحة للجسيمات المشحونة المتحركة عندما يكون المسار مؤديا إلى حالة الإبطاء. وباستخدام تقريب مدى CSDA يمكننا حساب معدل الخسارة في الطاقة في أي نقطة على طول مسار الانتقال على افتراض ان خسارة الطاقة في نقاط المسار تساوي كل فقدان قدرة الايقاف. من التكمال المتبادل الإجمالي لقدرة الايقاف يمكن أيجاد مدى CSDA.

Introduction

Charged particles when passing through can ionize the atom of the matter, the speed of the charge particles loss energy in many stopping point. The stopping power of the particles can be estimated for Avery unites of the track length by $-dE/dx$.

The stopping power is determined by the nature of the matter and the particle energy.

The ion pair needs an amount of energy and the amount of ionization along the tracts is related to stopping power of the matter. The property of the matter determent the stopping power, the loss of the energy for Avery points along the track describes the event of the particles during its travel. Both units and numerical values are identical.

Collision Stopping Power

The collision stopping power is resulted from energy of incident of electrons on the atoms of matter. The differential cross-section per atomic electron $d\sigma/dW$ for inelastic collisions leading to an energy transfer of W , the stopping power of mass collision can be denoted as:

$$\frac{1}{\rho} S_{coll} = \frac{N_A}{A} Z \int W \frac{d\sigma}{dW} dW \quad (1)$$

Where Z the atomic number of the medium, ρ its density N_A is Avogadro's number, A the atomic weight of the medium. The ionised energy loss is estimated from Bethe-Bloch formula [2]:

$$S_{coll} = \frac{2\pi r_e^2 m_0 c^2}{\beta^2} \frac{Z}{A} \left\{ \ln \left[\frac{\tau^2 (\tau + 2)}{2(I/m_e)^2} \right] + (1 - \beta^2) + \frac{\tau^2/8 - (2\tau + 1)\ln 2}{(\tau + 1)^2} - \delta \right\} \quad (2)$$

Where r_e the radius of the electron, $m_0 c^2$ is rest energy of the electron, δ is the density effect, β the electron velocity, I is the mean excitation energy and τ is the energy of the incident electron on its rest energy. The polarization of the atoms of the matter is result when an electron passing through it. This leads to decreases of electric field of the electron. The extent is in turn leading to decrease in the stopping power. For high energy value, the density can be approximated as [3]:

$$\delta \approx 2 \ln \left[\frac{28.816}{I} \sqrt{\frac{\rho Z}{A}} \right] + 2 \ln(\tau + 1) - 1$$

The mean excitation energy values can be seen in the following table 1 for various matterles

Element	Atomic number	Mean Excitation Energy I [eV]
Beryllium	4	63.7
Carbon (graphite)	6	78
Aluminum	13	166
Iron	26	286
Copper	29	322
Germanium	32	350
Tungsten	74	727
Lead	82	823
Uranium	92	890

Stopping Power of Radiative

The deflection of the electron path when passing electron through electric field Causing radiative energy loss, this phenomenon is called bremsstrahlung. The collision occurs in electron, emitted photon and the value of the scattering of nucleus can be neglected because of it high mass. The deflection of the electron path will be more when the nucleus charge is high; therefore the energy loss is significant especially when the atomic number of the matter is high. The deflection of an electron path can occur even at low energies. And this of the deflection is proportionate with electron energy. So the collision losses decrees when energy electron increase.

The energy loss becomes significant for contribution of the Bremsstrahlung phenomenon especially above 10 MeV for high atomic number and about 100 MeV for low-atomic number of the matter. The radiation photons of the incident electrons have a wide spectrum starting from zero to kinetic energy and the photons number proportionate inversely with there energy. The increase in the electron energy causing increase in the forward peaked of the emitted photons. In the following Figure the bremsstrahlung cross-sections differential is function of the photon energy for 4 values of electron energy for the lead and Copper [4].

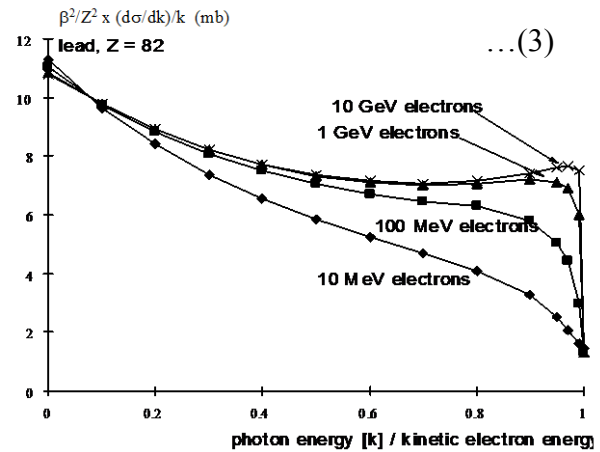


Figure (1. a) bremsstrahlung cross-sections for Lead (for 4 different electron energies) [4].

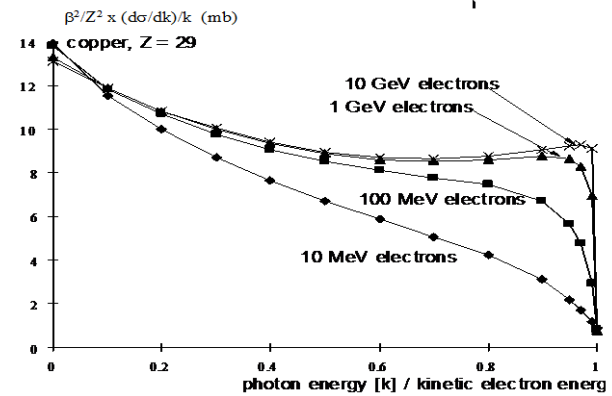


Figure (1. b): Bremsstrahlung cross-sections of Copper element (4 different electron energies) [4].

Total Stopping Power

Its total stopping power of electron and positron means the energy loss for every unit of the path length as a loss of ionization, excitation and the

radiations. And this is can be revealed by analytical expressions involving the use of these energy loss. a lot of works has been conducted now a days [5-8], the total stopping power in nuclear physics has a lot of application like in nuclear spectroscopy, surface layer analysis and semiconductor detectors[9,10]. The collision losses of electrons and positron are depends on the natures and properties of the materials. By using spatial formula to evaluate this loss of the electron [11]. in the last few years there have been some important development in the techniques and theories that inside the physical properties in solid concept like ionic charge, atomic number [12-18], valence electrons and these inside has relation with property of the chemical bond that explain and to categorize a lot of essential properties of the solid. Although this relation does not give an accurate hints for every matter but we can get benefit to study the properties of the materials. Below the two Figures show the total stopping power of collision for Lead and Graphite

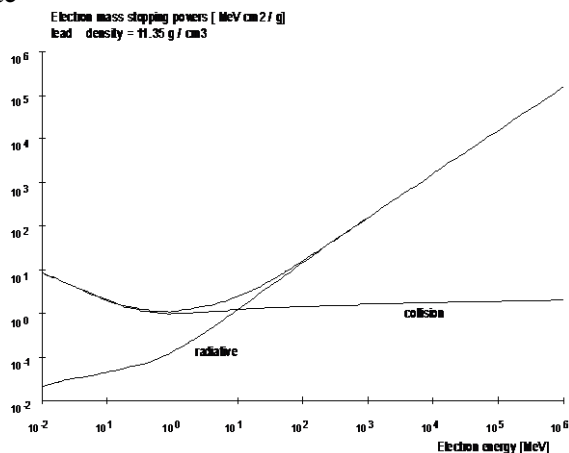


Figure (2a) stopping powers as an energy function (Graphite element) [2].

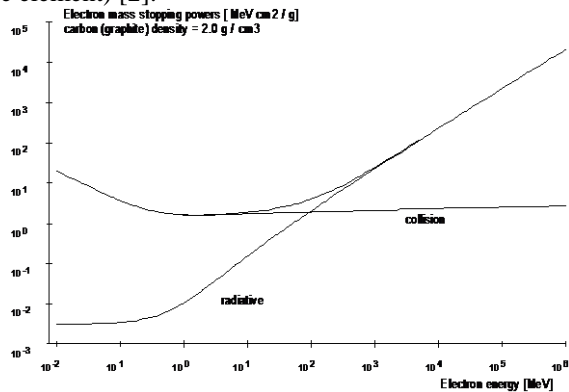


Figure (2b) stopping powers of Electron for lead as energy function [2].

Results and Discussions

From Theoretical point the results can be found by calculating stopping power collision and radiative stopping power together with CSDA data for F element. In the Figures 3a and 3b, the calculations represent a function of stopping powers to kinetic energy, for both sets Lin/Loge electron value after and before for F element.

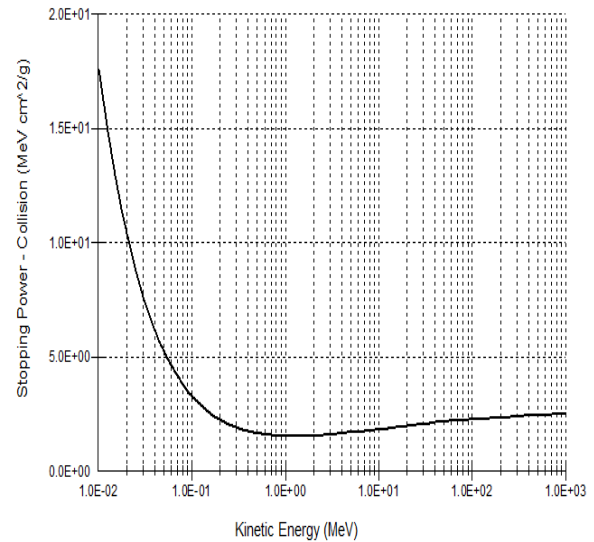


Figure (3a) shows total powers collision as a function to kinetic energy.

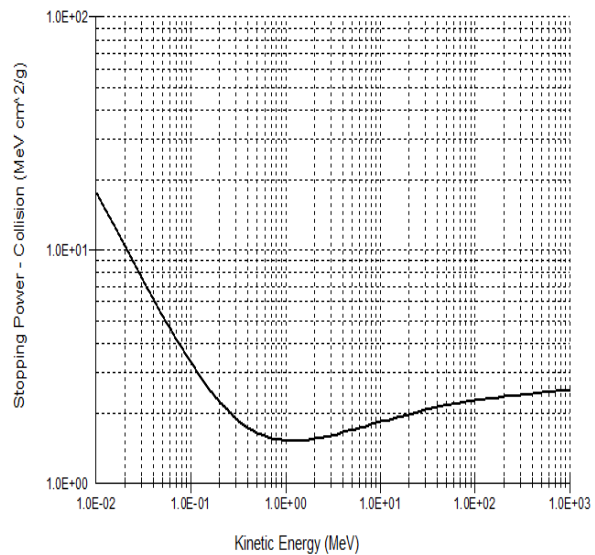


Figure (3b) the function Sets Lin/Log electron data of F element

Figures 4a and 4b denote to the stopping powers recitatives as a kinetic energy function after and before set Lin/Log electron data of F element.

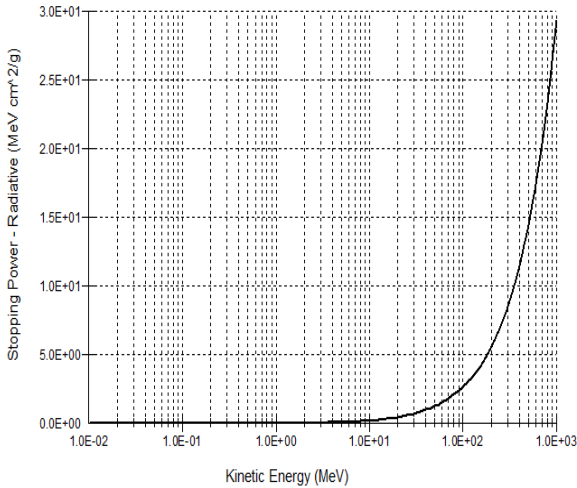


Figure (4a) radiative Stopping power as a kinetic energy function.

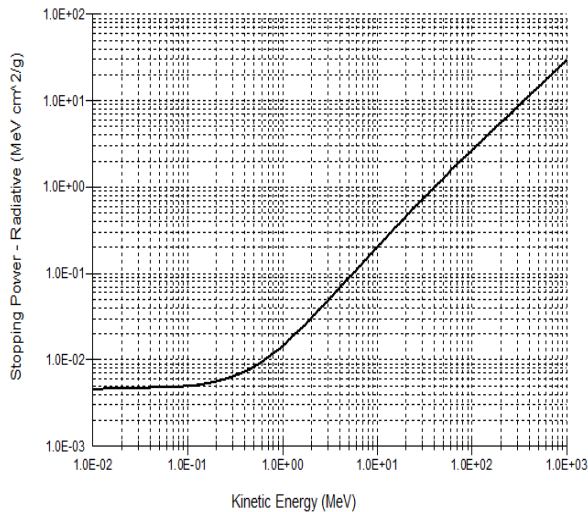


Figure (4b) Set Lin/Log data of radiative stopping power as a kinetic energy function.

Figures 5a and 5b for the total stopping powers function of kinetic energy after and before Lin/Log electron data for F element.

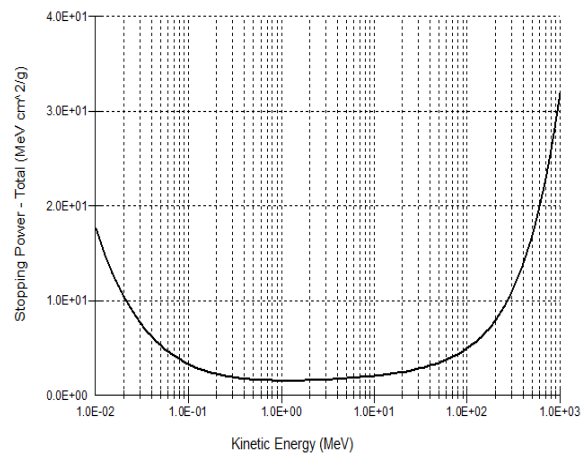


Figure (5a) the sum of stopping power as a kinetic energy function.

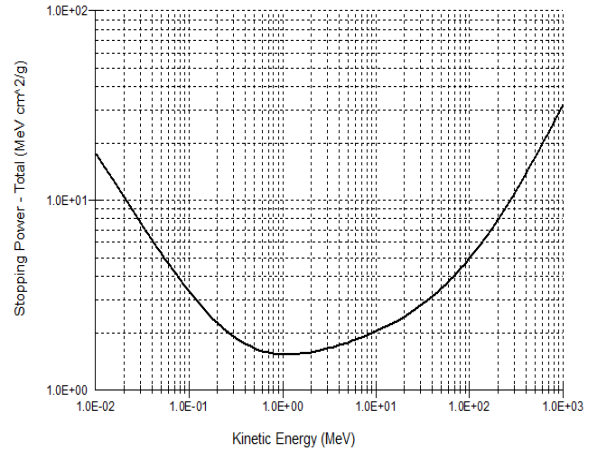


Figure (5b) Lin/Log the sum of stopping power as kinetic energy function.

The CSDA approximation for the range tracks the distance for charging all particles travelling when become to rest. The rate of losing energy in CSDA approximation, in every point of its path, is assuming equal losses to total stopping power. We can obtain it from the integrating of total stopping power reciprocal to energy. Figures 6a and 6b show the CSDA range the result of calculations.

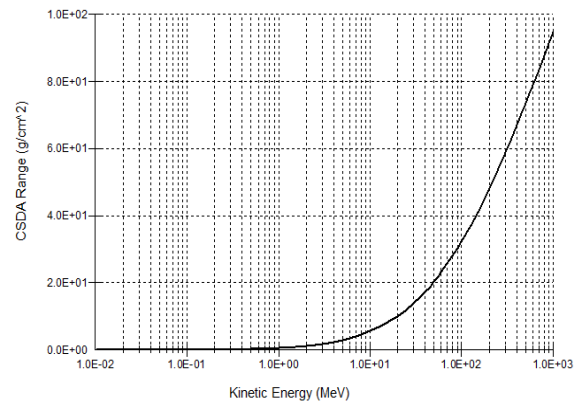


Figure (6a) CSDA calculations as a function of kinetic energy.

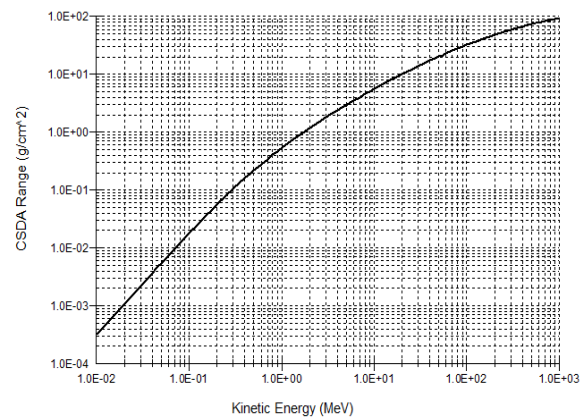


Figure (6b) Lin/Log CSDA range function to kinetic energy.

Conclusions

From the study of the total power we conclude that the collision of stopping power of electrons proportionate inversely with energy, it means for lower energies of electrons we can obtain height result of collision of stopping power.

The stopping power of radiative electrons increases when the energy increases. While the loss of the energy at any point on the path of the charge particle equals to the sum of stopping power in CSDA approximation.

References

- [1] VibhutiYadav, S. N. L. Sirisha, Sonali Bhatnagar, "Study for Stopping Power of Proton in Different materials–A Geant4 Simulation", Proceedings of the DAE Symp. On Nucl. Phys. 57, pp.734-735, 2012.
- [2] M. J. Berger, S. M. Seltzer, "Stopping powers and ranges of electrons and positron", National Bureau of Standards report NBSIR 82-2550, (1982).
- [3] Shielding against high energy radiation, Landolt-Börnstein new series, volume I/11, Editor H. Schopper, Springer-Verlag, 1990.
- [4] P. Berkvens, "Radiation Safety", Joint University, Accelerator School, 2007.
- [5] Batra, R. K., Sehgal, M. L., "Empirical relation for total stopping power of positrons and electrons", Nuclear Physics A., 156, 314, 1970.
- [6] Batra, R. K., Sehgal, M. L., "Approximate stopping power law of electrons and Positrons", Nucl. Inst. Methods, 109, 565, 1973.
- [7] Gupta, S. K., Govil, J. C., Gupta, K. K., Tyagi, R. K. and Verma, O. P., "Empirical equations for the stopping power and c. s. d. a. range difference of 0.2 to 10 MeV positrons", Int. J. Appl. Radiat. Isot., 33, 773, 1982.
- [8] Unak, T. Ongun, B., Unak, P., and Kumru, M. N., "Comparison of the calculated and measured stopping powers of low-energy electrons in different metals", Appl Radiat. Isot. 46, 561, 1995.
- [9] Berger, M. J. and Seltzer, S. M., "Nat. Bur. Stand. Report", No. NBSIR, 82-2550-A, 1983.
- [10] Seltzer, S. M. and Berger, M. J., "Procedure for calculating the radiation stopping power for electrons", Int. J. Appl. Radiat. Isot., 33, 1219, 1982.
- [11] Paul, H. and Schinner, A., "Atomic Data and Nucl Data Tables", 85, 377, 2003.
- [12] Akar, A. and Gumus, H., "Electron stopping power in biological compounds for low and intermediate energies with the generalized oscillator strength (GOS) model", Raditation Phys. Chem., 73, 196, 2005.
- [13] Gumus, H., "Simple stopping power formula for low and intermediate energy electrons", Raditation Phys. Chem., 72, 7, 2005.
- [14] Oller, J. C., Munoz, A., Percz, J. M., Blanco, F., Vieira, P. L. and Garcia, G., "Inelastic scattering and stopping power of electrons in methane based tissue equivalent materials at intermediate and high energies", 10–10 000 eV., Chem. Phys. Letts., 421, 439, 2006.
- [15] Tanuma, S., Powell, C. J. and Penn, D. R., "Calculations of stopping powers of 100 eV-30 keV electrons in 31 elemental solids", J. Appl. Phys., 063707, 103, 2008.
- [16] Pauling, L., "The Nature of the Chemical Bond", 3rd ed., Cornell University Press, Ithaca, 1960.
- [17] Verma, A. S., "Bond-stretching and bond-bending force constant of binary tetrahedral (AIII BV and AII BVI) semiconductors", Phys. Letts. A., 372, 7196, 2008.
- [18] Verma, A. S., "Thermal properties of chalcopyrite semiconductors", Phil. Mag., 89, 183, 2009.